COMPUTATIONAL STUDIES OF SHEAR-DEPENDENT NON-NEWTONIAN DROPLET FORMATION AT MICROFLUIDICS T-JUNCTION WITH EXPERIMENTAL JUSTIFICATION

WONG VOON LOONG

THESIS SUBMITTED TO THE UNIVERSITY OF NOTTINGHAM FOR THE DEGREE OF DOCTOR OF PHILOSOPHY

JULY 2015

Abstract

When Reynolds number (Re) is typically small, the dominant forces governing droplet formation in a microfluidic system includes surface tension, viscous, adhesion, and inertial forces, and the rheology of fluid becomes significantly important when non-Newtonian fluids are involved. The aim of this thesis is to systematically investigate the non-Newtonian shear-thinning effect of sodium carboxymethylcellulose (CMC) on the physical process of droplet formation. A two-phase conservative level-set formulation is adopted to capture the droplets breakup dynamics and relevant hydrodynamics. Detailed two-dimensional (2D) computational microfluidics flow simulations were carried out to examine systematically the influence of different controlling parameters such as degree of shear-thinning (η_o/η_∞), relaxation time (λ_{CY}), flow rates (Q_c, Q_d), viscosities (η_c, η_d), surface wettability (θ), and interfacial tensions (σ) on CMC microdroplets formation in a Newtonian continuum. Experimental tests and numerical model justification were performed in conjunction with grid refinement to support the computational analysis and ensure its accuracy and numerical stability. The breakup process of CMC microdroplets in the cross-flowing immiscible liquids in microfluidic device with T-shaped geometry was predicted well. Data for the rheological and physical properties obeying the Carreau-Yasuda stress model were experimentally obtained to support the computational work. In present study, it is worth noting that the dynamics of shear-thinning breakup process is very sensitive to the rheological quantities (η_o/η_∞, λ_{CY}) under a range of typical shear rate that associated with microchannel. The systematic variation in these rheological quantities has demonstrated different velocity profile and droplet properties. This variation significantly affects the size of droplet and breakup regime, which has never been studied previously. In contrast to previous

findings based on Newtonian solutions, the dependence of flow regimes, breakup time and generation frequency on CMC polymer concentration is distinctly different in dilute and semi-dilute concentration regimes, which only exists in polymer solutions. In dilute regimes, the breakup dynamics is similar to pure Newtonian solutions, which is droplet breakup sharply at the corner of T-Junction, as the polymers are at sufficiently low concentration. Conversely, in semi-dilute regime, the presence of highly polymer molecules leads to an elongated fluid thread, a delay in breakup time, and lower production rate of droplet. Interestingly, the existence of thin polymeric filament can be observed prior to breakup for shear-thinning solution. This feature is rarely observed in Newtonian solution, but a similar phenomenon that was previously attributed to elastic effects in the fluid. Besides, the instabilities in the filament leading to the formation and breakup of satellite droplets. In the view of essential role of interfacial tension, adhesion, viscous and inertial forces, the size of shear-thinning CMC droplets is always found to be smaller than the size of Newtonian droplets as it is believed that the shear-thinning thread encounter less resistance, resulting in rapid breakup phenomenon. Present investigations enhance the understanding of the polymer structural features that govern the droplet behaviour in different flow condition. This may contributes a conceptual framework to rheological application in pharmaceutical field, especially drug delivery system, which focuses on the stability and diffusion of drug particles in dispersion into the outer fluid.

Keywords: Emulsification, microfluidics T-junction, fluid dynamics, controlling parameters, non-Newtonian, sodium carboxymethylcellulose, shear-thinning, Carreau-Yasuda, level-set simulation, CFD.

List of Publications

The work presented in this thesis is, to the best of my knowledge, original, except for citations and quotations which have been duly acknowledged. The presented research work has not been previously and concurrently submitted for any other degree or award at other institutions. The research described was carried out in the Department of Chemical and Environmental Engineering at the University of Nottingham, Malaysia campus (March 2011-June 2012, September 2013-March 2014) and UK campus (July 2012-August 2013), respectively. The following publications and presentation have been partially based on the work reported in this thesis:

Wong, V.L, Loizou, K., Lau, P.L, Graham, R.S., and Hewakandamby, B.N. (2014). A CFD Based Parametric Study on Droplet Formation of Non-Newtonian Fluids at Microfluidics T-Junction. *Journal of Procedia Engineering*. Accepted.

Wong, V.L, Loizou, K., Lau, P.L, Graham, R.S., and Hewakandamby, B.N. (2014). Parametric Studies of Non-Newtonian Microdroplet Formation in a T-Junction Microchannel using Level-Set Method. *American Institute of Chemical Engineering* (*AIChe*) *Journal*, revising for submission.

Wong, V.L, Loizou, K., Lau, P.L, Graham, R.S., and Hewakandamby, B.N. (2014). Impact of Physical Properties on Non-Newtonian Polymeric Microdroplets Formation. *American Institute of Chemical Engineering* (*AIChe*) *Journal,* revising for submission.

Loizou, K., **Wong, V.L.**, Thielemans, W. and Hewakandamby, B.N. (2014). Squeezing and dripping at constant Capillary numbers: Effect of flow rate ratio on volume of droplets generated, revising for submission.

Wong, V.L, Loizou, K., Lau, P.L, Graham, R.S., and Hewakandamby, B.N. (2014). *Numerical Simulations of the Effect of Rheological Parameters on Shear-Thinning Droplet Formation*. Proceedings of the ASME 4th Joint US-European Fluids Engineering Division Summer Meeting, Chicago, Illinois, August 3-8, 9pp.doi:10.1115/FEDSM2014-21363.

Wong, V.L, Loizou, K., Lau, P.L, Graham, R.S., and Hewakandamby, B.N. (2014). *A CFD Based Parametric Study on Droplet Formation of Non-Newtonian Fluids at Microfluidics T-Junction*. Proceedings of the SOMChe 27th Symposium of Malaysian Chemical Engineers, Kuala Lumpur, Malaysia, October 29-30, vol. 1, 1-11, *Conference Proceedings Special Issues*.

Loizou, K., **Wong, V.L.**, Thielemans, W., and Hewakandamby, B.N. (2014). *Effect of Fluid Properties on Droplet Generation in a Microfluidic T-junction*. Proceedings of the ASME 4th Joint US-European Fluids Engineering Division Summer Meeting, Chicago, Illinois, August 3-8, 9pp.doi:10.1115/FEDSM2014-21274.

Acknowledgement

First and foremost I would like to express my deepest gratitude to University of Nottingham for awarding me the Malaysia Intercampus Doctoral Award Scheme (MIDAS) Scholarship. This invaluable financial support has enabled me to pursue my Doctoral Degree of Chemical and Environmental Engineering in the University of Nottingham.

I would like to offer my sincerest sense of gratitude towards my three principal supervisors, Dr. Buddhika N. Hewakandamby (UK campus), Dr. Richard S. Graham (UK campus), and Dr. Phei-Li Lau (Malaysia campus), who have supported me throughout my thesis with his patience and knowledge whilst allowing me to do my research in my own way. I attribute the level of my Doctoral Degree of Philosophy to their encouragement and effort and without them this thesis, too, would not have been completed or written. Their willingness to motivate me contributes tremendously in this project. Without invaluable advice, inspiration, guidance and enormous patience, I would face many difficulties while completing the modelling project and laboratory. I would also like to take the opportunity to thank Dr. Jit-Kai Chin (Malaysia Campus) who always lend a helping hand by providing me some useful measuring instruments. Special thanks also go to my former supervisor, Dr. David Hassell (Malaysia campus) who used to give me advices or kind words when needed during the first year of my postgraduate research study.

I am very fortunate to be blessed with the guidance and encouragement from the former researchers, colleagues and fellow graduates in multiphase flow research group from both UK and Malaysia campus, especially Dr. Kanu Aime, Dr. Kean-How Cheah, Dr. Kai-Seng Koh, and Dr. Nabeel Kadhim Abbood Alghaffari,

Dr. Vicky Lange, Mr. Pepe Escrig, Ms. Shara Kamal, and Mrs. Zoe Rose-Higgins who have the excellent attitude and the excitement in regard to teaching and gave the useful information during my research. This group has been a source of friendship as well as good advice and collaboration. In our microfluidics research group, I am particularly grateful to my group mate who is also one of my closest friends, Ms. Katerina Loizou for her constant support, kindness, helpfulness and the precious advice in my research work during my stay in UK campus. As well as keeping me stocked with general supplies, she has also inadvertently, and without fail, provided something much greater in the year I've known her: a friendly smile. And, I would like to express gratitude to her for providing me some of the useful experimental data and images in these modelling studies.

Last but not least, an honourable mention goes to my parents for their understanding and supports towards me without worrying and providing a home in which to complete my writing up. I would like to thank everyone who had contributed to the successful completion of this research project. Thank you for encouraging me, supporting me and making me realise that I should never let being dyslexic hold me back from what I want to do

Table of Contents

ABSTRACT I

LIST OF PUBLICATIONS III

ACKNOWLEDGEMENT V

TABLE OF CONTENTS VII

LIST OF TABLES XI

LIST OF FIGURES XII

NOMENCLATURE XXIV

CHAPTER 1 1

MOTIVATION AND ORGANIZATION 1

1.1 Research Background 1
1.2 Research Objectives 6
1.3 Organisation of Thesis 7

CHAPTER 2 9

ROLE OF MICROFLUIDIC DEVICE AND DROPLET FORMATION 9

2.1 Microfluidic Devices 9
2.2 Basic Principles in Microfluidics 11
2.2.1 Fluid Mechanics in Microfluidics 11
2.2.2 The Physics of Microdroplets 21
2.3 Droplet Formation in a Microchannel Network 28
2.4 Non-Newtonian Microdroplets Formation 36
2.5 Numerical Modelling Approaches 39
2.5.1 Two-Phase Flow Simulation 40
2.5.2 Numerical Models for Interface Representative 41
2.6 Summary 44

CHAPTER 3 46

MATERIALS, METHODS, AND EXPERIMENTAL TECHNIQUES 46

3.1 Introduction 46
3.2 Material and Sample Preparation 46
3.3 Refractive Index Measurements 47
3.4 Fluid Density Measurement 48

3.5 Rheological Characterisation 48
3.5.1 Newtonian Fluid Viscosity Measurement 48
3.5.2 Non-Newtonian Fluid Viscosity Measurement 49
3.6 Surface and Interfacial Tension Measurement 52
3.6.1 MATLAB Algorithm Development 54
3.7 Contact Angle Measurement 54
3.7.1 MATLAB Algorithm Development 57
3.8 PDMS Microfluidic Devices Fabrication 60
3.8.1 Photolithography 61
3.8.2 Soft-Lithography 62
3.9 Droplet Formation Experimental Setup 64
3.9.1 Effective Droplet Diameter Measurement 64
3.9.2 MATLAB Algorithm Development 65
3.10 Summary 67

CHAPTER 4 69

NUMERICAL STUDIES AND EXPERIMENTAL MODEL JUSTIFICATION 69

4.1 Introduction 69
4.2 CFD Modelling and Simulation: Conservative Level-Set Method 71
4.3 Numerical Model Implementation and Algorithm 77
4.3.1 Domain Discretisation and Mesh Dependency Analysis 77
4.3.2 Numerical Model Implementation 81
4.4 COMSOL Simulation Overview 95
4.5 Experimental Model: Droplet Formation at T-Junction 95
4.6 Numerical and Experimental Model Comparison 98
4.7 Droplet Formation and Breakup Mechanism 102
4.8 Summary 105

CHAPTER 5 107

THE EFFECT OF RHEOLOGICAL PARAMETERS OF CARREAU-YASUDA MODEL ON SHEAR-THINNING MICRODROPLETS FORMATION AND BREAKUP DYNAMICS 107

5.1 Introduction 107
5.2 Parametric Studies of the Effect of Rheological Parameters 108
5.2.1 Effect of Degree of Shear-Thinning on Effective Droplet Diameter 108
5.2.2 Effect of Relaxation Time on Effective Droplet Diameter 123
5.3 Summary 126

CHAPTER 6 128

THE EFFECT OF FLUID PHYSICAL PROPERTIES ON SHEAR-THINNING MICRODROPLETS FORMATION AND BREAKUP DYNAMICS 128

6.1 Introduction 128
6.2 Parametric Studies of the Effect of Physical Properties 128
6.2.1 Effect of Fixed Dispersed to Continuous Phase Viscosity Ratio on Effective Droplet Diameter 129
6.2.2 Effect of Fixed Dispersed to Continuous Phase Viscosity Ratio on Droplet Formation Time 132
6.2.3 Effect of Fixed Dispersed to Continuous Phase Viscosity Ratio on Droplet Generation Frequency 135
6.2.4 Satellite Droplets Formation 135
6.2.5 Effect of Contact Angle on Effective Droplet Diameter 138
6.2.6 Effect of Contact Angle on Droplet Formation Time 145
6.2.7 Effect of Contact Angle on Droplet Generation Frequency 150
6.2.8 Effect of Interfacial Tension on Effective Droplet Diameter 151
6.2.9 Effect of Interfacial Tension on Droplet Formation Time 155
6.2.10 Effect of Interfacial Tension on Droplet Generation Frequency 163
6.3 Summary 165

CHAPTER 7 168

THE EFFECT OF FLUID FLOW CHARACTERISTICS ON SHEAR-THINNING MICRODROPLETS FORMATION AND BREAKUP DYNAMICS 168

7.1 Introduction 168
7.2 Parametric Studies of the Variations in Controlling Flow Rate and Concentration of Continuous and Dispersed Phase 169
7.2.1 Effect of Dispersed Phase Flow Rate on Effective Droplet Diameter 170
7.2.2 Effect of Dispersed Phase Flow Rate on Droplet Formation Time 175
7.2.3 Effect of Dispersed Phase Flow Rate on Droplet Generation Frequency 176
7.2.4 Effect of Continuous Phase Flow Rate on Effective Droplet Diameter 176
7.2.5 Effect of Continuous Phase Flow Rate on Droplet Formation Time 182
7.2.6 Effect of Continuous Phase Flow Rate on Droplet Generation Frequency 184
7.2.7 Effect of Sodium Carboxymethylcellulose (CMC) Concentration on Effective Droplet Diameter 186
7.2.8 Effect of Sodium Carboxymethylcellulose (CMC) Concentration on Droplet Formation Time 190

7.2.9 Effect of Sodium Carboxymethylcellulose (CMC) Concentration on Droplet Generation Frequency 192
7.2.10 Effect of Continuous Phase Viscosity on Effective Droplet Diameter 193
7.2.11 Effect of Continuous Phase Viscosity on Droplet Formation Time 198
7.2.12 Effect of Continuous Phase Viscosity on Droplet Generation Frequency 200
7.3 Summary 202

CHAPTER 8 206

CONCLUSION AND RECOMMENDATION 206

8.1 Conclusion and Summary of Key Findings 206
8.2 Recommendation and Future Works 213
REFERENCES 216

APPENDIX A.1: TABLE DATA FOR CHAPTER 5 229

APPENDIX A.2: TABLE DATA FOR CHAPTER 6 236

APPENDIX A.3: TABLE DATA FOR CHAPTER 7 239

APPENDIX A.4: MATLAB CODE FUNCTION FOR SURFACE AND INTERFACIAL TENSION MEASUREMENT 243

APPENDIX A.5: MATLAB CODE FUNCTION FOR CONTACT ANGLE MEASUREMENT 247

APPENDIX A.6: MATLAB CODE FUNCTION FOR THRESHOLD DETECTION MEASUREMENT 251

APPENDIX A.7: MATLAB CODE FUNCTION FOR DROPLET DIAMETER MEASUREMENT 254

List of Tables

Table 2.1: Values of a_i and β_i constant (Schechter, 1961; Cho and Hartnett, 1985).....18
Table 2.2: Computed result for the flow in rectangular duct (Schechter, 1961; Cho and Hartnett, 1985).....18
Table 2.3: Dimensionless numbers for Newtonian and non-Newtonian fluids flow in microfluidics (Square and Quakes, 2005; Berthier and Silberzan, 2009).....20
Table 2.4: Main approaches for droplet breakup in microchannel (Anna and Mayer, 2006; Utada *et al*., 2007; Baroud *et al*., 2010; Nunes *et al*., 2013). 33
Table 3.1: Standard specifications of BS/U Tube viscometer (ASTM International, 2012).....49
Table 3.2: Empirical constants (Source: Misak, 1968). 53
Table 3.3: Physical properties of distilled water and CMC solution with olive oil phase at room temperature (20 ± 2^{o}C). 59
Table 4.1: General settings for the variables and parameter in COMSOL. The colour bar specifies the dispersed phase as the area where colour distinction is from 0 to 0.5 and continuous phase the area from 0.5 to 1.0. 79
Table 4.2: Mesh statistics for grid convergence analysis. 81
Table 4.3: Variables for the strong form in the computational domain, Ω_k.....87
Table 4.4: *R* Variables for the domain boundaries in COMSOL. 89
Table 4.5: General settings for the variables and parameter in COMSOL (for system: flow rate ratio, *Q*: 0.05). 93
Table 4.6: Averaged Newtonian droplet diameter at different dispersed rate by using cross-flowing rupture techniques. 96
Table A.1: Data for Figure 5.2. 229
Table A.2: Data for Figure 5.10. 231
Table A.3: Data for Figure 5.12. 233
Table A.4: Data for Figure 5.14. 234
Table A.5: Data for Figure 6.1, 6.3 and 6.6 at fixed viscosity ratio (λ) of 1. ..236
Table A.6: Data for Figure 6.8, 6.13 to 6.15, and Figure 6.19 to 6.20. 236
Table A.7: Data for Figure 6.21, 6.23 to 6.25, and Figure 6.33 to 6.34.....237
Table A.8: Data for Figure 7.1 and Figure 7.4 to 7.5. 239
Table A.9: Data for Figure 7.6 to 7.7 and Figure 7.10 to 7.13. 240
Table A.10: Data for Figure 7.14 to 7.15 and Figure 7.18 to 7.20. 241
Table A.11: Data for Figure 7.21 to 7.23 and Figure 7.27 to 7.29. 241

List of Figures

Figure 2.1: Fluid flow with characteristic velocity scale *u* through the standard (a) rectangular circular microchannels; (b) SEM image of a rectangular microchannel. The coordinate x point downstream, z spans the width and y spans the height (*l*: channel length; *w*: channel width; *h*: channel height) (Figures adapted from Squires and Quake, 2005; Abate *et al*., 2008).....14

Figure 2.2: Velocity profile for laminar Newtonian flow: (a) Two-dimensional (2D) plot with velocity height expression, (b) One-dimensional (1D) plot with parabolic velocity profilein rectangular microchannel. 14

Figure 2.3: Comparison of shear-rate profile between Newtonian and purely viscous fluids: (a) Newtonian fluid; (b) Shear-thinning; (c) Shear-thickening; and, (d) Viscoplastic fluid (Chhabra and Richardson, 2008). 15

Figure 2.4: Velocity profile for laminar non-Newtonian shear-thinning flow: (a) Two-dimensional (2D) plot with velocity height expression, (b) One-dimensional (1D) plot with blunted velocity profile in rectangular microchannel. 16

Figure 2.5: Schematic velocity profile for fluids exhibit shear-thinning behaviour in microchannel. 19

Figure 2.6: Schematic velocity profile for fluids exhibit shear-thickening behaviour in microchannel. 19

Figure 2.7: Illustration of interfaces (Γ) between two immiscible fluids: (a) Microscopic view of interface at the molecular size; macroscopic view of (b) pendant drop and (c) sessile drop. The region occupied by first fluid phase and region occupied by second fluid phase are denoted as $\Omega_1$and Ω_2,respectively. The red solid line represents the approximate location of the interface between two immiscible fluids. 22

Figure 2.8: Schematic diagram of (a) the shape of an emerging tip; (b) the postulated evolution of Laplace pressure during the droplet breakup process in a T-junction microchannel (Garstecki *et al*., 2006). 23

Figure 2.9: Microphotograph images of droplet formation behaviour in microfluidic devices: (a1) water-in-hexadecane emulsions with the addition of hydrophilic surfactant Tween 80, SDS and (a2) hydrophobic surfactant Span80 (Shui *et al*., 2009); (b) water-in-soybean oil with the addition of surfactant Tween 20 (Peng *et al*., 2011). 24

Figure 2.10: Illustration of fluid-solid interaction in wetting. Consider a liquid droplet resting on an ideal solid surface: (a) if wetting angle is greater than 90^{o}or (b) equal to 90^{o}a liquid said to be non-wetting (known as hydrophobic contact if water is used);and, (c) if wetting angle is lesser than $90^{o}$the liquid is

said to wet the solid (known as hydrophilic contact if water is used). A zero contact angle denotes complete wetting. 25
Figure 2.11: The influence of contact angle on the droplet breakup process in water-in-oil (W/O) emulsification system at: (a) different Ca (Liu and Zhang, 2009); (b) different viscosity ratio(Bashir *et al*., 2011).....26
Figure 2.12: Effect of concentration of surfactant in (a) anhydrous hexadecane and (b) deionised water, respectively on the contact angle and surface tension (Xu *et al*., 2006).....26
Figure 2.13: The size of aqueous water droplets plotted as function of flow rates of oil and aqueous phase at a microfluidics T-junction: (a) fixed oil phase rate; (b fixed aqueous phase rate (Garstecki *et al*., 2006). 27
Figure 2.14: Effect of viscosity ratio and flow rate ratio on the (b) frequency generation and (b) droplet volume at each flow rate ratio (Gupta and Kumar, 2010).....28
Figure 2.15: Schematic diagram of the injection of fluid configuration in a T-junction microchannel: (a) Cross-Flow; (b) Opposed-flow; (c) Perpendicular-flow. 30
Figure 2.16: Four different microsystems for droplet generation: (a) breakup in co-flowing streams; (b) breakup in cross-flowing streams; (c) breakup in elongational strained flows; (d) breakup in microchannel emulsification (MCE) (van der Zwan *et al*., 2009; Baroud *et al*., 2010).....31
Figure 2.17: Schematic diagram of different distinct flow regimes in (a) flow-focusing, (b) cross-flowing (c) co-flowing microfluidics devices. The solid black and white arrow denotes the continuous and dispersed phase flow direction, respectively. 32
Figure 2.18: Schematic diagram of the formation of a droplet (or bubble) in the squeezing regime at a microfluidics T-junction (van Steijn *et al*., 2010).....34
Figure 2.19: Transition from dripping to jetting regimes in a T-shaped microchannel. Fluid flow regimes as function of flow rate ratio (Q): (a) 1/8; (b) 1/4; (c) 1/2 at fixed Ca=0.056 (Liu and Zhang, 2009). 35
Figure 2.20: Schematic representative of a two-phase flow problem. Ω_1 denotes the region occupied by the first fluid; Ω_2 denotes the region occupied by the second fluid; Γ denotes the interface separates the two fluids that reside in region Ω_1 and Ω_2. 40
Figure 3.1: Standard curve of sodium carboxymethylcellulose (CMC) solution.47
Figure 3.2: Normalized shear viscosity plotted against normalized shear rate for a series of CMC shear-thinning solutions with different concentrations.....50

Figure 3.3: Log-log plot of specific viscosity versus the concentration of CMC shear-thinning solutions. 51
Figure 3.4: Schematic diagram of experimental setup for pendant drop analysis. 52
Figure 3.5: Definition of dimensions describing the pendant drop. The region occupied by first fluid phase and region occupied by second fluid phase are denoted as ρ_A and ρ_B, respectively. 53
Figure 3.6: Image profile of pendant drop analysis. 54
Figure 3.7: Schematic diagram of experimental setup for sessile drop analysis. 55
Figure 3.8: Definition of dimensions and coordinates describing the sessile drop. For a point $A(x,z)$ on the sessile drop profile, the lateral and vertical coordinate were denoted as x and z; respectively; φ is the angle subtended by the normal at point A to the axis of revolution; l_w is the maximum half-width of the drop; r is the radius of contact line; R is the radius of the drop; h_d is the height of the drop; and, θ^* (=max(φ)) is the contact angle of the drop at the three phase contact line. (Figure adapted from Srinivasan *et al*., 2011). 56
Figure 3.9: Image profile of sessile drop analysis. 57
Figure 3.10: Schematic diagram of microfluidics T-junction composed of rectangular channel. 60
Figure 3.11: Illustration of microfluidics T-junction composed of rectangular channels. 60
Figure 3.12: Scanning electron microscope (SEM) image of fabricated T-junction of the (a) SU-8 photoresist and (b) PDMS microchannel and the (c) cross section of PDMS microchannel (Reproduced with permission from Loizou *et al*., 2013). 61
Figure 3.13: Schematic diagram of photolithography and soft lithography process. (A) A transparency photo-mask was laid on SU-8 film for the generation of master by photolithography process. A master consists of a positive relief of photoresist was used as a mould for PDMS replica moulding (REM) process. (B) A PDMS pre-polymer mixture was poured over the master and cured for 1 hour and 45 minutes at 65°C. (C), (D) The PDMS replica was peeled from the master and sealed to a glass slide to enclose the channels. 63
Figure 3.14: Schematic diagram of experimental setup for flow experiments. .64
Figure 3.15: Schematic diagram of the shape of confined droplets and plugs in microchannel. The depth of the microchannel was denoted as h. 65
Figure 3.16: Image profile of (a) histogram threshold approach and (b) droplet size analysis.....66

Figure 4.1: Schematic diagram of microfluidics T-junction composed of rectangular channel. The width of the continuous-phase and dispersed phase inlet channel are denoted as w_c and w_d, respectively; while the depth of the microchannel is denoted as h. 70
Figure 4.2: Plot of the (a) Heaviside function and (b) smeared out Heaviside function.....73
Figure 4.3: Contour representation of interface location for a droplet formed in a model of the T-shaped in this simulation. 74
Figure 4.4: Typical finite element mesh for structured mesh of 2D Mapped Mesh. 78
Figure 4.5: The geometry of microfluidics T-junction composed of five subdomains with prescribed dimensions in COMSOL simulation. 78
Figure 4.6: The modelling domain of a T-junction: Ω_k (for k=1...5) denotes the computational domain, and $\partial\Omega_k$ (for k=1...16) denotes the domain boundary, respectively. 86
Figure 4.7: Steps in COMSOL simulation and modelling.....95
Figure 4.8: Graph of the effect of flow rate ratio Q ($=Q_d/Q_c$) on normalised droplet size (d_{eff}/w_c) of water at fixed continuous phase rate of 2.0 ml/hr. Error bars shown indicate the standard deviation in droplet size measurement of 30 droplets under fixed experimental condition. 97
Figure 4.9: Comparison of normalised effective droplet diameter (d_{eff}/w_c) between numerical and experimental result in the range of Q applied. Error bars indicate the standard deviation in droplet size measurement of 30 droplets under fixed experimental condition. 98
Figure 4.10: Snapshots of two-dimensional (2D) simulations of the water-in-oil droplet breakup process in microchannel and corresponding to experiments (for system: Q_c: 2.0 ml/hr and Q_d: 0.1ml/hr, Q=0.05).The colour bar specifies the dispersed phase as the area where colour distinction is from 0 to 0.5 and continuous phase the area from 0.5 to 1.0.....100
Figure 4.11: Snapshots of two-dimensional (2D) simulations and experiments of the water-in-olive oil droplet breakup process for various flow rate ratios. The colour bar specifies the dispersed phase as the area where colour distinction is from 0 to 0.5 and continuous phase the area from 0.5 to 1.0. 101
Figure 4.12: Evolution of the normalized pressure at point P during droplet breakup in a model of the T-shaped. P denotes the point at the junction and reflects the evolution of breakup mechanism. The droplet formation process can be divided into three stages: In the lag stage (I), pressure builds-up in the junction corner and continues to rise with the emergence of a dispersed thread

after the detachment of the first droplet. Due to the confinement, the pressure increases as a consequence of the increased resistance to flow of the continuous phase in the main channel. In the filling stage (II), the dispersed phase start penetrating into the main stream, the droplet grows downstream and the pressure decreases. In the necking stage (III), the hydrodynamics forces deform the forming droplet and the neck connecting the thread and droplet wake becomes thinner. Once equilibrium of the hydrodynamic forces is achieved, the neck of the thread collapses and a droplet is formed. As a result of this pinch-off, the pressure shows the peak values at the corner of side channel. The dispersed thread recedes back into the side channel and the whole generation process is continuously repeated. After the first droplet detaches, the pressure starts to build up again and decreases after the thread flows into the main channel. The colour bar specifies the dispersed phase as the area where colour distinction is from 0 to 0.5 and continuous phase the area from 0.5 to 1.0. 104

Figure 4.13: Streamline and normalized velocity vector field during droplet breakup in a model of the T-shaped in the case of 7644 mesh elements. Contour of 0.5 denotes the interface where the droplet is identified as solid blue line. .105

Figure 5.1: Schematic profile of degree of shear-thinning effect. Note that subscripts 1, 2, and 3 represent the variation in infinite shear-viscosity in Carreau-Yasuda model. 109

Figure 5.2: The influence of degree of shear-thinning on droplet diameter at flow rate ratio, Q of 0.05 (for system: Q_c: 2.0 ml/hr and Q_d: 0.1 ml/hr). 110

Figure 5.3: Axial velocity profile along the width of dispersed phase channel for various flow with different infinite shear viscosity (shown in legend) at fixed zero shear viscosity (4.113 kg/m.s). In each case, the velocity profile represents a fully-developed laminar flow. Dashed arrow denotes the direction of increasing infinite shear viscosity. 111

Figure 5.4: Shear rate profile for Newtonian flow along the continuous phase during the droplet breakup process (for system: η_c=0.068 kg/m.s (olive oil), Q_d/Q_c=0.05). 114

Figure 5.5: Shear rate profile for Newtonian flow along the dispersed phase during the droplet breakup process (for system: η_d=0.00093 kg/m.s (distilled water), Q_d/Q_c=0.05). 115

Figure 5.6: Shear rate profile for CMC concentration 0.40wt% along the continuous phase during the droplet breakup process (for system: η_o=0.19461 kg/m.s, η_∞=0.00448kg/m.s, Q_d/Q_c=0.05). 116

Figure 5.7: Shear rate profile for CMC concentration 0.40wt% along the dispersed phase during the droplet breakup process (for system: η_o=0.19461 kg/m.s, η_∞=0.00448 kg/m.s, Q_d/Q_c=0.05). 117

Figure 5.8: Shear rate profile for CMC concentration 1.00 wt% along the continuous phase during the droplet breakup process (for system: η_o=4.11430 kg/m.s, η_∞=0.00448 kg/m.s, Q_d/Q_c=0.05). 118

Figure 5.9: Shear rate profile for CMC concentration 1.00wt% along the dispersed phase during the droplet breakup process (for system: η_o=4.11430 kg/m.s, η_∞=0.00448 kg/m.s, Q_d/Q_c=0.05). 119

Figure 5.10: Onset rate for infinite shear viscosity over a range of degree of shear-thinning. The solid lines denote the approximated upper limit and lower limit values of estimated typical shear rate in present numerical model ($200<\gamma<7000$ 1/s). 120

Figure 5.11: Snapshots of two-dimensional (2D) simulation of CMC-in-olive oil droplet breakup process for different CMC concentration (for system:η_∞=0.00448 kg/m.s, Q_d/Q_c=0.05). 122

Figure 5.12: Effect of CMC viscosity on normalised effective droplet diameter (d_{eff}/w_c) during droplet breakup process for various flows with different infinite shear viscosity (shown in the legend). 123

Figure 5.13: Schematic profile of relaxation time effect. Note that subscripts 1, 2 and 3 represent the variation in relaxation time constant in Carreau-Yasuda model. 124

Figure 5.14: The effect of relaxation time constant against on normalised CMC effective droplet diameter at flow rate ratio, Q of 0.05 (for system: Q_c: 2.00 ml/hr and Q_d: 0.10 ml/hr). 125

Figure 5.15: Axial velocity profile along the width of dispersed phase channel for various flow with different relaxation time (shown in legend) for CMC concentration of 1.0wt% (η_o:4.1143 kg/m.s; η_∞:0.0031 kg/m.s). In each case, the velocity profile represents a fully-developed laminar flow. Dashed arrow denotes the direction of decreasing relaxation time constant. 125

Figure 6.1: Combined effects of both phases viscosity on the effective droplet diameter of CMC solutions for various CMC concentrations (for system: λ=1, Q_d/Q_c=0.05). 130

Figure 6.2: Normalised Pressure profile of (a) 0.04wt%, (b) 0.08wt%, (c) 0.20wt% CMC for the effect of fixed dispersed to continuous phase viscosity ratio on CMC droplet breakup process (for system: λ=1, Q_d/Q_c=0.05). P denotes the

pressure at the corner of T-junction. The sharp pressure peak in the given data corresponds to the droplet breakup at the corner of the side channel as shown in the extracted images. The maximum magnitudes of the pressure peak and the formation periods under different CMC concentration are listed above. 131
Figure 6.3: Combined effects of both phases viscosity on the droplet formation time of CMC solutions for various CMC concentrations (for system: λ=1, Q_d/Q_c=0.05). 133
Figure 6.4: Diameter growth of CMC droplet as function of time for various CMC concentrations during droplet formation process (for system: λ=1, Q_d/Q_c=0.05). 134
Figure 6.5: Snapshots of 2D simulation comparison of droplet growth of CMC droplet as function of time between (a) 0.06wt% and (b) 0.20wt% CMC solution (for system: λ=1, Q_d/Q_c=0.05). The growths of diameter were determined when the droplets grow downstream beyond the detachment point (dashed line)....134
Figure 6.6: Effect of fixed viscosity ratio on the droplet generation frequency of CMC solutions for various CMC concentrations (for system: λ=1, Q_d/Q_c=0.05). 135
Figure 6.7: Snapshots of two-dimensional (2D) simulation of the effect of continuous phase viscosity on CMC-in-olive oil droplet breakup process for different CMC concentration (for system: λ=1, Q_d/Q_c=0.05).....137
Figure 6.8: Effect of contact angle on the effective droplet diameter of CMC solutions.....140
Figure 6.9: Snapshots of two-dimensional (2D) simulation of the effect of contact angle on CMC-in-olive oil droplet breakup process for different CMC concentration (for system: θ=130°, Q_d/Q_c=0.05).....141
Figure 6.10: Snapshots of two-dimensional (2D) simulation of the effect of contact angle on CMC-in-olive oil droplet breakup process for different CMC concentration (for system: θ=150°, Q_d/Q_c=0.05).....142
Figure 6.11: Snapshots of two-dimensional (2D) simulation of the effect of contact angle on CMC-in-olive oil droplet breakup process for different CMC concentration (for system: θ=170°, Q_d/Q_c=0.05).....143
Figure 6.12: Jet and filament formation profile prior to pinch-off for CMC concentrations above 0.4wt% at contact angle: (a) 130°, (b) 150°, (c) 170°(for system: Q_d/Q_c=0.05).The dashed box denotes the region where the formation of thin filament. 144
Figure 6.13: Variation in normalised effective droplet diameter of CMC droplets for various CMC concentrations at each contact angle. 145

Figure 6.14: Effect of contact angle on the normalised droplet formation time of CMC solutions. 146
Figure 6.15: Variation in normalised droplet formation time of CMC droplets for various CMC concentrations at each contact angle. 148
Figure 6.16: Diameter growth of CMC droplet as function of time for various CMC concentrations during the droplet formation process (for system: θ=130^o, Q_d/Q_c=0.05). 149
Figure 6.17: Diameter growth of CMC droplet as function of time for various CMC concentrations during the droplet formation process (for system: θ=150^o, Q_d/Q_c=0.05). 149
Figure 6.18: Diameter growth of CMC droplet as function of time for various CMC concentrations during the droplet formation process (for system: θ=170^o, Q_d/Q_c=0.05). 150
Figure 6.19: Effect of contact angle on the normalised droplet generation frequency of CMC solutions. 151
Figure 6.20: Variation in normalised droplet generation frequency of CMC droplets for various CMC concentrations at each contact angle. 151
Figure 6.21: Effect of interfacial tension on the normalised effective droplet diameter of CMC solutions (σ_{wo} (=0.02074 N/m) denotes interfacial tension between de-ionized water and olive oil). 153
Figure 6.22: Pressure profile of 0.20wt% CMC droplet breakup for different interfacial tensions: (a) σ = 0.010 N/m, (b) σ = 0.020 N/m, (c) σ = 0.035 N/m (for system: Q_d/Q_c=0.05). P denotes the pressure at the corner of T-junction. The sharp pressure peak in the given data corresponds to droplet breakup point as shown in the extracted images. The maximum magnitudes of the pressure peak and the formation periods under different interfacial tension are listed above. 154
Figure 6.23: Variation in normalised effective droplet diameter of CMC droplets for various CMC concentrations at each interfacial tension. 155
Figure 6.24: Effect of interfacial tension on the normalised droplet formation time of CMC solutions (σ_{wo} =0.02074 N/m). 157
Figure 6.25: Variation in normalised droplet formation time of CMC droplets for various CMC concentrations at each interfacial tension. 157
Figure 6.26: Snapshots of two-dimensional (2D) simulation of the effect of interfacial tension on CMC-in-olive oil droplet breakup process for different CMC concentration (for system: σ=0.010 N/m, Q_d/Q_c=0.05). 158

Figure 6.27: Snapshots of two-dimensional (2D) simulation of the effect of interfacial tension on CMC-in-olive oil droplet breakup process for different CMC concentration (for system: σ=0.020 N/m, Q_d/Q_c=0.05). 159
Figure 6.28: Snapshots of two-dimensional (2D) simulation of the effect of interfacial tension on CMC-in-olive oil droplet breakup process for different CMC concentration (for system: σ=0.035 N/m, Q_d/Q_c=0.05). 160
Figure 6.29: Jet and filament formation profile prior to pinch-off for CMC concentrations above 0.4wt% at interfacial tension: (a) 0.010 N/m, (b) 0.020 N/m, (c) 0.035 N/m (for system: Q_d/Q_c=0.05). 161
Figure 6.30: Diameter growth of CMC droplet as function of time for various CMC concentrations during the droplet formation process (for system: σ=0.010 N/m, Q_d/Q_c=0.05). 162
Figure 6.31: Diameter growth of CMC droplet as function of time for various CMC concentrations during the droplet formation process (for system: σ=0.020 N/m, Q_d/Q_c=0.05). 162
Figure 6.32: Diameter growth of CMC droplet as function of time for various CMC concentrations during the droplet formation process (for system: σ=0.035 N/m, Q_d/Q_c=0.05). 163
Figure 6.33: Effect of interfacial tension on the normalised droplet generation frequency of CMC solutions (σ_{wo} (=0.02074 N/m) denotes the interfacial tension between de-ionized water and olive oil). 164
Figure 6.34: Variation in normalised droplet generation frequency of CMC droplets for various CMC concentrations at each interfacial tension. 164
Figure 7.1: Effect of dispersed phase flow rate on the effective droplet diameter of CMC solutions for various CMC concentrations at different flow rate ratio Q (=Q_d/Q_c) (for system: Q_c: fixed 2.00 ml/hr; Q_d: 0.05 ml/hr to 0.25ml/hr) 170
Figure 7.2: Pressure profile of 0.20wt% for the effects of dispersed phase rate on droplet breakup process at each flow rate ratio (for system: fixed Q_C=2.00 ml/hr). P denotes the pressure at the corner of T-junction. The sharp pressure peak in the given data values reflects the droplet breakup point as shown in the extracted images. The pressure profile demonstrated an abrupt fall in pressure caused by the balance of surface tension and viscous force dictates the droplet movement after the first droplet formation. This phenomenon is applied to all cases. The maximum magnitudes of the pressure peak and the formation periods under different dispersed phase rate are listed above. 173
Figure 7.3: Snapshots of two-dimensional (2D) simulation of the effect of dispersed phase rate on CMC-in-olive oil droplet breakup process for different CMC concentrations (for system: Q_c=2.00 ml/hr). 174

Figure 7.4: Effect of dispersed phase flow rate on the normalised droplet formation time of CMC solutions for various CMC concentrations at different flow rate ratio Q ($=Q_d/Q_c$) (for system: Q_c: fixed 2.00 ml/hr; Q_d: 0.05 ml/hr to 0.25ml/hr). 175
Figure 7.5: Effect of dispersed phase flow rate on normalised droplet generation frequency of CMC solutions for various CMC concentrations at different flow rate ratio Q ($=Q_d/Q_c$) (for system: Q_c: fixed 2.00 ml/hr; Q_d: 0.05 ml/hr to 0.25ml/hr). 176
Figure 7.6: Effect of continuous phase flow rate on effective droplet diameter of CMC solutions for various CMC concentrations (for system: fixed Q_d=0.20 ml/hr). 179
Figure 7.7: Effect of flow rate ratio Q ($=Q_d/Q_c$) on normalised effective droplet diameter of CMC solutions for various CMC concentrations (for system: fixed Q_d=0.20 ml/hr; Q_c=1.50 ml/hr to 4.00 ml/hr). 179
Figure 7.8: Snapshots of two-dimensional (2D) simulation of the effect of continuous phase flow rate on CMC-in-olive oil droplet breakup process for different CMC concentrations (for system: Q_d=0.20 ml/hr). 180
Figure 7.9: Pressure profile of 0.20wt% for the effects of continuous phase rate on droplet breakup process at each flow rate ratio Q (for system: Q_d=0.20 ml/hr). P denotes the pressure at the corner of T-junction. After the first droplet is pinched off, the pressure fluctuates abruptly and repeatedly. The insignificant sharp pressure peak reflects the detachment point is located downstream of the junction. The pressure profile demonstrated an abrupt fall in pressure caused by the balance of surface tension and viscous force dictates the droplet movement after the first droplet formation. This phenomenon is applied to all cases. 181
Figure 7.10: Effect of continuous phase flow rate on the droplet formation time of CMC solutions for various CMC concentrations (for system: fixed Q_d=0.20 ml/hr). 183
Figure 7.11: Effect of flow rate ratio Q ($=Q_d/Q_c$) on the normalised droplet formation time of CMC solutions for various CMC concentrations (for system: fixed Q_d=0.20 ml/hr; Q_c=1.50 ml/hr to 4.00 ml/hr). 183
Figure 7.12: Effect of continuous phase flow rate on the CMC droplet generation frequency for various CMC concentrations (for system: fixed Q_d=0.20 ml/hr). 185
Figure 7.13: Effect of flow rate ratio Q ($=Q_d/Q_c$) on the normalised droplet generation frequency of CMC solutions for various CMC concentrations (for system: fixed Q_d=0.20 ml/hr; Q_c=1.50 ml/hr to 4.00 ml/hr). 185
Figure 7.14: Effect of CMC Concentration on normalised effective droplet diameter of CMC droplets (for system: Q_d/Q_c=0.05).....186

Figure 7.15: Variation in normalised effective droplet diameter of CMC droplets for various CMC concentrations at each flow rate ratio.....187
Figure 7.16: Pressure profile of (a) 0.0wt%, (b) 0.20wt%, (c) 0.80wt%for droplet breakup process (for system: Q_d/Q_c=0.05). P denotes the pressure at the corner of T-junction. The sharp pressure peak in the given data values reflects the droplet breakup point as shown in the extracted images. The insignificant sharp pressure peak reflects the detachment point is located downstream of the junction. The pressure profile demonstrated an abrupt fall in pressure caused by the balance of surface tension and viscous force dictates the droplet movement after the first droplet formation. This phenomenon is applied to all cases. The maximum magnitudes of the pressure peak and the formation periods under different CMC concentration are listed above.....189
Figure 7.17: Effect of CMC Concentration on droplet formation time of CMC droplets (for system: Q_d/Q_c=0.05).....191
Figure 7.18: Variation in droplet formation time of CMC droplets for various CMC concentrations at each flow rate ratio. 191
Figure 7.19: Effect of CMC concentration on normalised droplet generation frequency of CMC droplets (for system: Q_d/Q_c=0.05). 192
Figure 7.20: Variation in normalised droplet generation frequency of CMC droplets for various CMC concentrations at each flow rate ratio. 193
Figure 7.21: Effect of continuous phase viscosity on effective droplet diameter of CMC droplets (for system: Q_d/Q_c=0.05).....194
Figure 7.22: Effect of continuous phase viscosity on effective droplet diameter for different CMC concentration (for system: Q_d/Q_c=0.05). 196
Figure 7.23: Effect of viscosity ratio on effective droplet diameter of CMC droplets for different continuous phase viscosity (for system: Q_d/Q_c=0.05). ...196
Figure 7.24: Pressure profile of 0.20wt% CMC droplets breakup at the system with different continuous phase viscosity: (a) 0.0354kg/m.s, (b) 0.068kg/m.s, (c) 0.0998 kg/m.s(for system: Q_d/Q_c=0.05). P denotes the pressure at the corner of T-junction. The sharp pressure peak in the given data values reflects the droplet breakup point as shown in the extracted images. The insignificant sharp pressure peak reflects the detachment point is located downstream of the junction. The pressure profile demonstrated an abrupt fall in pressure caused by the balance of surface tension and viscous force dictates the droplet movement after the first droplet formation. This phenomenon is applied to all cases. The maximum magnitudes of the pressure peak and the formation periods under different continuous phase viscosity are listed above. 197

Figure 7.25: Snapshots of two-dimensional (2D) simulation of the effect of continuous phase viscosity on CMC-in-olive oil droplet breakup process for different CMC concentration (for system: Q_d/Q_c=0.05). 198
Figure 7.26: Effect of continuous phase viscosity on normalised droplet formation time of CMC droplets for various CMC concentrations (for system: Q_d/Q_c=0.05). 199
Figure 7.27: Effect of continuous phase viscosity on droplet formation time of CMC droplets (for system: Q_d/Q_c=0.05).....200
Figure 7.28: Effect of continuous phase viscosity on normalised droplet generation frequency of CMC droplets for various CMC concentrations (for system: Q_d/Q_c=0.05). 201
Figure 7.29: Effect of continuous phase viscosity on droplet generation frequency of CMC droplets (for system: Q_d/Q_c=0.05). 202

Nomenclature

Roman Symbols

A	Constant in Equation 3.7	[μm^2]
A_c	Cross-sectional area of the channel	[μm^2]
A_{eff}	Projected area of the drop	[μm^2]
A_{mn}	Fourier coefficients	[dimensionless]
A_i	Constant in Equation 2.18	[dimensionless]
a	Fitting parameter in Carreau-Yasuda model	[dimensionless]
a_c	Capillary length of liquid	[µm]
Bo	Bond number	[dimensionless]
B_0	Constant in Equation 3.7	[dimensionless]
B_1	Constant in Equation 3.7	[dimensionless]
B_2	Constant in Equation 3.7	[dimensionless]
B_3	Constant in Equation 3.7	[dimensionless]
B_4	Constant in Equation 3.7	[dimensionless]
C	Nominal viscometer constant	[cSt/s]
C^*	Critical Overlap Concentration	[wt%]
C_D	Drag coefficient	[dimensionless]
Ca	Capillary number	[dimensionless]
Ca_{crit}	Critical capillary number	[dimensionless]
D	Diffusion coefficient	[m^2/s]
D_d	Drop diameter	[µm]
D_h	Hydraulic diameter of the channel	[µm]
D_N	Dispersed phase channel diameter	[µm]
De	Deborah number	[dimensionless]
d_e	Equatorial diameter of drop	[m]
d_s	Drop diameter at a distance d_e from the apex of the drop	[m]
d_{eff}	Effective droplet diameter	[µm]
d_{major}	Major droplet diameter	[µm]
d_{minor}	Minor droplet diameter	[µm]
d_{vi}	Damping (mass) coefficient	[dimensionless]
Ec	Elasto-capillary number	[dimensionless]
El	Elasticity number	[dimensionless]
F_{st}	Surface tension force acting on the interface	[N/m^3]
	Scalar coefficient	[dimensionless]

f	Body force/External force acting on fluid	[N/m^3]
$\mathbf{f}$	Artificial compressive flux	[N/m^2]
f_d	Droplet production rate/Frequency	[1/s]
Gr	Grashof number	[dimensionless]
F_{vi}	Scalar coefficients	[dimensionless]
g	Gravitational acceleration	[m/s^2]
h_d	Dimensionless height of the drop	[dimensionless]
H	Dimensionless height of the drop	[dimensionless]
H_s	Shape dependent parameter	[dimensionless]
H_{sm}	Smeared-out Heaviside function	[dimensionless]
h	Depth of the channel/Channel height	[μm]
h_d	Height of the drop	[μm]
I	Identity matrix	[dimensionless]
Kn	Knudsen number	[dimensionless]
k	Curvature of fluid-fluid interface	[dimensionless]
L	Characteristic length scale related to flow geometry	[μm]
l	Length of the channel	[μm]
l_d	Length of droplet	[μm]
l_w	Maximum half-width of the drop	[μm]
M	Drop mass	[g]
m	Fluid consistency index	[Pa.s^n]
$\mathbf{n}_\Gamma$	Unit normal vector at the interface	[dimensionless]
$\mathbf{n_b}$	Unit normal vector at the boundary	[dimensionless]
n	Fluid behavior index/ Power-law exponent	[dimensionless]
n_{Air}	Refractive index of air	[dimensionless]
Oh	Ohnesorge number	[dimensionless]
P	Pressure	[N/m^2]
P_{wet}	Wetted perimeter of the channel	[μm]
ΔP	Pressure drop	[N/m^2]
ΔP_L	Laplace Pressure	[N/m^2]
Pe	Peclet Number	[dimensionless]
Q	Flow rate ratio	[dimensionless]
Q_c	Flow rate of the continuous phase	[ml/hr]
Q_d	Flow rate of the dispersed phase	[ml/hr]
Re	Reynolds number	[dimensionless]
Ra	Rayleigh number	[dimensionless]
R	Radius of the drop	[μm]

R_i	Inner radii of capillary tube	[μm]
R_o	Outer radii of capillary tube	[μm]
R_1	First principal curvature radii of interface	[m]
R_2	Second principal curvature radii of interface	[m]
R_a	Radii of axial curvature	[m]
R_b	Radii of radial curvature	[m]
R	Radius of the channel	[μm]
R_{vi}	Scalar coefficient	[dimensionless]
r	Radial distance along cylindrical channel axis	[μm]
S	Shape factor	[dimensionless]
s	Moving distance of the drop	[μm]
t	Time/Real-time	[s]
t_d	Droplet Formation Time	[s]
$\mathbf{u}$	Velocity field	[m/s]
u	Superficial velocity characteristic of the flow	[m/s]
u_b	Bouyancy velocity	[m/s]
u_c	Inlet velocity of continuous phase	[m/s]
u_d	Inlet velocity of dispersed phase	[m/s]
u_{eff}	Effective average velocity in the microchannel	[m/s]
u_x	Average velocity characteristic of the flow in channel (x-direction)	[m/s]
u_y	Average velocity characteristic of the flow in channel (y-direction)	[m/s]
$\widetilde{u}_\iota$	Test function for velocity	[dimensionless]
$\mathbf{v}$	Solution vector	[dimensionless]
v_i	Solution dependent variable	[dimensionless]
We	Weber number	[dimensionless]
Wi	Weissenberg number	[dimensionless]
w	Width of the channel	[μm]
w_c	Width of the continuous phase channel	[μm]
w_d	Width of the dispersed phase channel	[μm]
X	Non-dimensional lateral coordinate	[dimensionless]
x	Lateral coordinate axes/Coordinate axes along the channel length	[μm]
y	Longitudinal coordinates axes/Coordinate axes along the channel width	[μm]
Z	Non-dimensional vertical coordinate	[dimensionless]
z	Vertical coordinate axes /Coordinate axes along	

	the channel height	[μm]

Greek Symbols

α	Aspect ratio	[dimensionless]
α_i	Constant in Equation 2.18	[dimensionless]
β	Slip length	[m]
β_i	Constant in Equation 2.18	[dimensionless]
$\dot{\gamma}$	Shear rate	[1/s]
$\dot{\gamma}_{\lambda_{CY}}$	Critical shear rate	[1/s]
$\dot{\gamma}_o$	Zero shear rate	[1/s]
$\dot{\gamma}_\infty$	Onset of infinite shear rate	[1/s]
γ	Reinitialization parameter	[m/s]
ν	Kinematic viscosity of fluid	[m^2/s]
τ_a	Artificial time	[s]
τ	Shear stress	[Pa]
τ_{xx}	Stress in the x-direction acting normal to the yz-plane	[Pa]
τ_{yy}	Stress in the x-direction acting normal to the xz-plane	[Pa]
τ_{zz}	Stress in the x-direction acting normal to the xy-plane	[Pa]
τ_{xz}	Stress in the z-direction acting on the plane normal to the x-direction (yz-plane)	[Pa]
τ_{xy}	Stress in the y-direction acting on the plane normal to the x-direction (yz-plane)	[Pa]
τ_{yz}	Stress in the z-direction acting on the plane normal to the y-direction (xz-plane)	[Pa]
τ_{zx}	Stress in the x-direction acting on the plane normal to the z-direction (xy-plane)	[Pa]
τ_{yx}	Stress in the x-direction acting on the plane normal to the y-direction (xz-plane)	[Pa]
τ_{zy}	Stress in the y-direction acting on the plane normal to the x-direction (yz-plane)	[Pa]
τ_D	Diffusional time	[s]
τ_I	Interfacial relaxation time	[s]
τ_R	Rayleigh Instability time	[s]
τ_T	Convective/viscous time	[s]
τ_w	Wall shear stress	[Pa]
τ_p	Relaxation time	[s]

τ_{flow}	Flow time of the fluid	[s]
θ	Contact angle	[dimensionless]
θ^*	Apparent Contact angle	[dimensionless]
ϕ	Level-set function	[dimensionless]
$\tilde{\phi}$	Test function for Level-set function	[dimensionless]
ϕ_θ	Deviation angle between droplet center and vertical channel center lines	[dimensionless]
δ_{sm}	Smeared-out Dirac delta function	[dimensionless]
φ	Angle subtended by the normal at certain point to the axis of revolution	[dimensionless]
η	Dynamic viscosity of fluid	[Pa.s]
η_d	Dynamic viscosity of the dispersed phase	[Pa.s]
η_c	Dynamic viscosity of the continuous phase	[Pa.s]
η_o	Zero shear viscosity	[Pa.s]
η_∞	Infinite shear viscosity	[Pa.s]
η_s	Solvent viscosity	[Pa.s]
η_{sp}	Specific viscosity	[Pa.s]
μ_{vi}	Lagrange multipliers	[dimensionless]
$\tilde{\mu}$	Test functions for Lagrange multiplier	[dimensionless]
λ	Viscosity ratio	[dimensionless]
λ_{CY}	Relaxation Time in Carreau-Yasuda Model	[s]
λ_D	Sodium D-line	[nm]
ρ	Fluid density	[kg/m^3]
ρ_c	Density of continuous phase	[kg/m^3]
ρ_d	Density of dispersed phase	[kg/m^3]
$\Delta\rho$	Density difference between fluid phases at interface	[kg/m^3]
ε	Maximum dimensionless half-width of the drop	[dimensionless]
ε_Γ	Half the thickness of the interface	[mm]
σ_{ik}	Cauchy stress tensor	[dimensionless]
σ	Surface/Interfacial surface tension	[N/m]
σ_{LG}	Liquid-gas surface/interfacial tension	[mN/m]
σ_{SG}	Solid-gas surface/interfacial tension	[mN/m]
σ_{SL}	Solid-liquid surface/interfacial tension	[mN/m]
$\prod_D$	Second invariant of strain tensor	[dimensionless]
Γ	Fluid interface	[dimensionless]
Γ_{vi}	Conservative flux vector	[dimensionless]
Ω_1	Region occupied by first fluid phase	[dimensionless]

Ω_2	Region occupied by second fluid phase	[dimensionless]
Ω	Domain	[dimensionless]
Ω_k	Computational domain	[dimensionless]
$\partial\Omega_k$	Domain boundary	[dimensionless]

Acronyms

CAD	Computer assisted design
CFD	Computational fluid dynamic
CMC	Carboxymethyl cellulose
DNA	Deoxyribonucleic acid
µTAS	Micro total analysis systems
DS	Degree of substitution
FDM	Finite difference method
FEM	Finite element method
FVM	Finite volume method
GC	Gas chromatograph
GNF	Generalized Newtonian fluids
IPA	Isopropyl alcohol
LBM	Lattice Boltzmann method
LSM	Level-set method
MCE	Microchannel emulsification
MW	Molecular weight
PAA	Polyacrylamide
PDMS	Polydimethylsiloxane
PEB	Post exposure bakes
PEO	Polyethylene oxide
PGMEA	Propylene glycol mono methyl ether acetate
PMMA	Polymethylmethacrylate
PTFE	Polytetrafluoroethylene
REM	Replica moulding
RI	Refractive index
SEM	Scanning electron microscopy
SDF	Signed distance function
SMCE	Straight-through microchannel emulsification
UV	Ultraviolet
VOF	Volume-of-fluid

CHAPTER 1

Motivation and Organization

1.1 Research Background

Over the past decade, research in the field of microscale devices has greatly accelerated (Kumar *et al*., 2010), and the promise of miniaturisation of large-scale laboratories to the size of a chip has attracted the attention of biologists and manufacturing engineers alike (Shilpiekandula *et al*., 2006). Researchers from a broad range of fields are intensively analysing the possibilities offered by the miniaturisation of equipment to achieve a fundamental change in design philosophy for chemical plants. The smaller characteristic dimensions in microscale devices have led to extremely high surface-to-volume ratios and compactness of unit operation devices (Kumar *et al*., 2010). This provides a number of useful capabilities over conventional system (Beebe *et al*., 2002; Weigl *et al*., 2003; Whitesides, 2006; Kumar *et al*., 2010), including:

- Higher heat and mass transport rates;
- Safer environment for hazardous or toxic sample and reagents due to the ability to work with small quantities of samples and reagent during the process and produce small amount of waste;
- Simplification of process control for effective processes/materials screening, due to extremely short response time;
- On-demand or on-site synthesis of critical chemicals such as H_2O_2 and ethylene oxide;
- No strict limit in size reduction or expansion of plant components due to the achievable production capacity in means of parallel operation;

- Integrated chemical analytic platform's development in micro-total analysis systems;
- Separations and detection can be carried out with high resolution and sensitivity.

In addition to the traditional advantages conferred by miniaturisation, the greatest potential lies in the physics of the microscale. Microtechnology has progressed a long way since its beginnings in the 1970s when Terry *et al*. (1979) first proposed the idea of a gas chromatograph air analyser integrated on a substrate silicon wafer based on a gas chromatograph (GC) principle. Initial progression from these pioneering studies by researchers was slow, but a dramatic increase in research activities has taken place within last two decades. Microfluidics system has been developed into an active research area (Moreno and Quero, 2010; Sin *et al*., 2011). By understanding and manipulating microscale phenomena, microfluidics can be used to perform tasks not possible on the macro scale, allowing new functionality and experimental paradigms to emerge (Beebe *et al*., 2002). Being multidisciplinary in nature, researchers active in this field are compelled to seek knowledge in a wide range of diverse disciplines.

Microfluidic devices are characterized by small length scales, laminar flow regimes and diffusion dominated mass transport (Webster *et al*., 2010). The first application of microfluidic technology was in the miniaturized total chemical analysis systems proposed by Manz *et al*. (1990). Microfluidics is a broad term used to describe the behaviour, precise control and manipulation of geometrically constrained fluids on a sub-millimetre scale. It has the potential to be powerful tool in a range of areas from chemical synthesis and biological analysis to optics and information technology (Whitesides, 2006). While still in an early stage of development, last decade has seen a tremendous increase in

research into integrated microfluidic devices, typically referred to as lab-on-a-chip devices or micro total analysis systems (μTAS), in a wide range of application areas such as sample preparation, fluid handling, micro-reactors, separation systems, cell handling, and cell culturing. The incorporation of these techniques has led to microfluidic devices that can be used to apply in a range of different research fields.

The development of microfluidic systems that allow for the formation of microdroplets inside microfluidic devices has gained greatly attention over the past 10 years (Xu *et al*., 2008). The droplet generation in microfluidic devices is a well-studied and understood phenomenon that has applications in biology, medicine, and chemistry (Mulligan and Rothstein, 2012). Liquid droplets dispersed in a second immiscible fluid are useful, particularly when the size and the size distribution of droplet can be prescribed on a micro or nanoscale (Anna *et al*., 2003). Microfluidic devices offer an alternate and versatile route to produce emulsions that are nearly monodispersed and have high formation frequencies in multiphase fluid systems (Sang *et al*., 2009).

Monodispersed droplets can be generated via a number of methods in microfluidic devices, including compound emulsions (Abate *et al*., 2011), geometry-dominated break-up, cross-flow shear in T-junction microchannels, hydrodynamic flow-focusing, membrane emulsification, and concentric injection (Cubaud and Manson, 2008; Xu *et al*., 2008). These methods have enabled the formation of dispersions with highly attractive features, particularly the control over droplet size and size distribution (Xu *et al*., 2008). Consequently, rapid development of droplet formation techniques in microfluidic devices has occurred as they provide robust and highly controllable platforms for droplet creation. These have been used in a diverse range of applications including the production of monodispersed microparticles (Nisisako *et al*., 2004; Kim *et al*., 2008; Zhao *et*

al., 2008; Kim *et al*., 2010), enhancement of mixing (Song *et al*., 2003), crystallization of proteins (Zheng *et al*., 2004), synthesis of nanoparticles (Takagi *et al*., 2004), and microchemical analysis (Sun *et al*., 2006).

While most fluids used in the previously mentioned work are Newtonian in nature, many fluids of interest to lab-on-chip devices in industrial practice exhibit complex micro-structure and non-Newtonian behaviour. Controlled formation of droplets with viscous non-Newtonian fluids in micro scaled channels is still remains challenging. The study of non-Newtonian flow is conventionally done with macro-scaled systems such as large pipes and channels, which allow observation at a relatively large scale and characterization with a mean-field approach. Recent advances in micro fabrication techniques have evolved in producing microscaled channels with arbitrary geometries and in high-speed imaging opens up new opportunities to investigate non-Newtonian multiphase flow microscopically.

An investigation into the behaviour of multiphase non-Newtonian/Newtonian systems in microdevices is of importance for microfluidic applications in the medical research and biological fields where non-Newtonian biological and pharmaceutical fluid is frequently encountered (Husny and Cooper-White, 2006). Current interest in these field is focused around understanding the effect of non-Newtonian fluid properties, including shear thinning (Gu and Liow, 2011) and elasticity (Tirtaatmadja *et al*., 2006; Steinhaus *et al*., 2007; Arratia *et al*., 2009), on liquid bridge breakup and on drop formation and breakup. Unlike Newtonian fluids, the non-Newtonian fluids are defined as materials which do not conform to a direct proportionality between shear stress and shear rate. The addition of colloids and polymers significantly modifies the rheological properties of the fluids and hence the dynamics of their flow. Examples of these include viscous polymeric emulsions, such as those encountered in polymer and plastic extrusion,

pharmaceuticals, cosmetics, food, petrochemical and hygiene product processing. In laminar flows, drop dynamics is governed by surface tension and viscous forces, and the rheology of the fluid is important in determining the behaviour of the fluids prior to and during droplet formation (Husny and Cooper-White, 2006;Tirtaatmadja *et al*., 2006;Arratia *et al*., 2009; Gu and Liow, 2011).

To form droplets in a microfluidic device, the flow conditions must be set such that the system operates in the dripping regime (Umbanhowar *et al*., 2000; Cramer *et al*., 2004; Utada *et al*., 2007; Abate *et al*., 2011). For Newtonian fluids, this regime generally occurs when the sum of the inner phase Weber number (We) and the continuous phase capillary number (Ca) is less than one, that conditions describe the formation of highly uniform droplets over a wide range of flow rates. On the contrary, non-Newtonian fluids normally do not suffice these conditions, and generally it is extremely difficult to achieve monodispersed dripping. The extensional viscosity of the fluids resists the pinching needed to form droplets, leading to the formation of long jets that break into droplets of uncontrolled sizes due to the Rayleigh–Plateau instability (Abate *et al*., 2011). The characteristic of Non-Newtonian fluids are having more complicated rheological behaviour than the conventional Newtonian fluids. Nevertheless, there is a dearth of published data in the study of non-Newtonian droplet formation in Newtonian-based continuous fluid system. Additionally, the difficulty of emulsifying non-Newtonian solutions in microfluidics in a controllable manner is a known and persistent problem (Abate *et al*., 2011), limiting the applicability of these techniques for industrial materials.

The rheological properties of non-Newtonian sodium carboxymethylcellulose (CMC), an anionic derivative of cellulose and water-soluble polymer solutions, are much documented in the aspect of polymer research and the subject of a great deal of experimental and theoretical work (Benchabane and Bekkour,

2008). The rheological characteristics of CMC solutions depend on the concentration. At higher concentrations, both non-Newtonian and viscoelastic properties of CMC have been found to be much more pronounced. Ghannam and Esmail (1997) have investigated the rheological properties of CMC solutions in the concentration range 1 to 5% and the results revealed that the solution with lowest concentrations show nearly Newtonian behaviour and become pseudoplastic, thixotropic, and viscoelastic responses at the higher concentrations. The work presented in this thesis attempts to predict numerically the influence of non-Newtonian behaviour of CMC fluid with a nominal molecular weight of 700,000 g/mol and a degree of substitution (DS) of 0.80-0.95 on droplet generation in a microfluidics T-junction. T-junction microchannel is the most widely researched microfluidic configuration for droplet formation and manipulation (Thorsen *et al*., 2001; Nisisako *et al*., 2002; Husny *et al*., 2003, Tice *et al*., 2004, Garteski *et al*, 2005; Xu *et al*., 2008). It has been used to produce monodispersed droplet among other's microfluidics geometry such as flow-focusing devices, co-flow devices and micro-channel terraces. In present study, experimental tests were conducted to provide data for the validation of the numerical modelling in microdroplets formation. For the numerical simulation of multiphase flow work in this thesis is undertaken using the commercial package COMSOL multiphysics based on the finite element method (FEM), used to analyse the fluid-structure interaction. These microscopic studies are complemented by computational and modelling techniques to provide a more complete understanding.

1.2 Research Objectives

Translating the problem area and research focus as described in the previous section into a clear objective, the major aims of the research are to evaluate the droplet formation and behaviour within microchannel geometries using both Newtonian and Non-Newtonian flows. The work includes:

i. To develop a numerical simulation model of two-phase flow with an interface capturing approach based on level-set function for simulating the fluid dynamics of CMC droplets with non-Newtonian properties using commercial software package COMSOL Multiphysics.

ii. To validate the developed numerical model with the experimental data, in order to acquire reliability on its usage. This validation process aims to assess the extent that the numerical model accurately represents the real case which it attempts to simulate.

iii. To understand how the behaviour of non-Newtonian material controls the formation and propagation of CMC droplets at a microfluidic T-junction. A series of numerical parametric studies will be performed to examine the effect of different operating parameters such as rheological parameters, flow rate, viscosity, interfacial tension, and surface wettability on the evolution of CMC droplet diameter, formation time, generation frequency, and pressure distribution during the CMC droplet breakup process.

1.3 Organisation of Thesis

This thesis is structured into seven chapters as follows:

Chapter 1 briefly introduces the scenario of research in the field of microscale devices, development of microfluidics system, and droplet formation in microchannel network.

Chapter 2 reviews the fundamentals and previous findings. This chapter is subdivided into four main sections; the first section introduces a general overview of microfluidics devices and the basic principle of microfluidics. Section two provides general ideas of the physical phenomena of the droplet flow behaviour under different flow conditions at microscale. Section three gives a review on the droplet formation in Newtonian and Non-Newtonian systems in microchannel networks. Finally, overview of numerical modelling approaches is presented in section four.

Chapter 3 presents the experimental procedures and analysis required in the droplet formation in shear-thinning non-Newtonian/Newtonian system. This section explains experimental procedures of droplet formation, various operating parameters and droplet size measurement with the application of MATLAB as a method of image processing analysis. These sets of values of parameters were used in the computations subsequently for the modelling studies.

Chapter 4 explains the Level-Set (LS) approach for the numerical modelling of droplet formation in the framework of Finite Element Method (FEM). This section mainly focuses on the validation of developed numerical prediction model with experimental data sets and visual observations.

Chapter 5 highlights the effect of rheological parameters in viscosity model on shear-thinning droplet formation in microchannel network. This section mainly explains the effect of degree of shear-thinning and relaxation time constant on droplet size.

Chapter 6 presents the numerical investigation on the effect of fixed dispersed to continuous phase viscosity ratio on droplet formation process. The variation in governing physical parameter: contact angle and interfacial tension on the formation of shear-thinning microdroplets at T-junction microfluidics has also been discussed extensively.

Chapter 7 presents the influence of flow rate and viscosity of both continuous and dispersed phases on shear-thinning droplet formation. This section presents the numerical result of the effect of the flow rate and the viscosity of continuous and CMC dispersed fluid on droplet diameter, droplet formation time and the frequency of droplet generation.

Chapter 8 gives the conclusions of the current investigations and recommendations for the future investigations. MATLAB codes function for image processing analysis used in this dissertation, are given in the appendices.

CHAPTER 2

Role of Microfluidic Device and Droplet Formation

2.1 Microfluidic Devices

Microfluidics is a multidisciplinary field stretch across engineering, physics, chemistry, micro-technology and biotechnology. Microfluidic devices generally have two of the three geometric length scales in the order of microns. Since the initiation in the early 1990s, microscale analytical chemistry techniques have gained popularity while microelectronic technology has been recognized as a way to fabricate miniaturised chromatographic and capillary electrophoresis-based systems. Considerable attention has been focused in this area and the development of complete lab-on-a-chip devices or micro-total analysis systems (μTAS) has grown significantly in recent years. This has been sustained by revolutionising conventional laboratory handling, processing, and analytical techniques (McDonald and Whitesides, 2002; Whitesides, 2006).

The micrometer length scale defines the most obvious but extremely important character of microfluidic devices especially their small size which allows small sample volumes, low cost and fast analysis, but with high resolution and sensitivity (Zhao and Middelberg, 2011). Key advantages of microfluidic device include the low manufacturing costs, economical use, and disposal; shorter time of analysis; minimal consumption of reagents and sample; minimal production of potentially harmful by-products; enhancement of separation efficiency; enhancement of portability for point of care testing; high surface-to-volume ratio and small laboratory footprint (Manz *et al*., 1990; Ãlvarez *et al*., 2008; Li *et al*., 2010). Additionally, they also provide the ability to integrate various transport

and processes steps, including sample preparation, mixing, reaction, separation, detection and manipulation of chemicals and particles (Manz *et al*., 1990; Ãlvarez *et al*., 2008; Li *et al*., 2010).

With the length scale associated with microfluidic devices, flow within them does not develop turbulences. In addition to this unique advantage, there are several other phenomena that occur at these typical dimensions that are not observed in larger-scale conventional devices (Weigl *et al*., 2003):

- Flow in the channels tends to be laminar which allows the parallel flow of different fluids. The design of the separation and detection devices is enabled based on the diffusion at interfaces between the different fluids.
- Diffusion distance can be made extremely small if the fluid streams are hydro-dynamically focused.
- Diffusion becomes a viable method to move particles, mix fluids and control the reaction rates.
- Active particle transportation and separation methods show greatly enhanced separation performance in small-scale channels.
- Sedimentation at standard gravity, unaided by centrifugation becomes a viable means to separation dispersed particles by density across small channel dimensions.

Recent advances and innovations could make microfluidics technology ubiquitous and create microfluidic devices that are more functional, efficient and cost effective than conventional techniques. This includes the use of new materials, augmented by the development of different fabrication techniques such as 3D printing.

2.2 Basic Principles in Microfluidics

2.2.1 Fluid Mechanics in Microfluidics

A fluid is a continuum that deforms continually under applied shear stress no matter how small the stress is. The flow of fluid is typically characterised as one of the two regimes; laminar (smooth and steady) or turbulent (chaotic and transient) regimes. The dimensionless, Reynolds number (Re) is interpreted as a measure of the ratio of inertial and viscous forces in any particular fluid flow (Nguyen and Wereley, 2002; Weigl *et al*., 2003) and the concept was first introduced by Stokes (1851). It was named after Osborne Reynolds who used the non-dimensional quantity in the late 1880's to describe the transition between the two regimes. Reynolds number is defined as:

$$\mathrm{Re} = \frac{\rho u L}{\eta} = \frac{uL}{\nu} \tag{2.1}$$

where u is the superficial velocity of the flow, L is the characteristic length, ρ is the fluid density, η is the dynamic viscosity of the fluid, and ν is the kinematic viscosity of the fluid. In microfluidics, the characteristic length is hydraulic diameter (D_h) which is introduced for approximating the flows through the different types of channel shape:

$$D_h = \frac{4A_c}{P_{wet}} \tag{2.2}$$

where A_c is the cross-sectional area of the channel occupied by the fluid and P_{wet} is the wetted perimeter of the channel.

In physics, the Navier-Stokes equation represents the momentum equations of fluid mechanics and is commonly used to describe the motion of the laminar flow. This equation arises from applying Newton's second law that satisfies the conservation of momentum to fluid motion by assuming the fluid stress is the sum of a diffusing viscous term (proportional to the gradient of velocity) plus a pressure term. Hence, the momentum equation states that the time rate of

change of linear momentum of a continuum is equal to the sum of the forces acting on the continuum. Three types of forces are typically present; body forces that act on the entire element inside the continuum due to gravity, rather than merely its surface; pressure force, a surface force which acts inward and normal to the surfaces of the element; a viscous force, a surface force due to friction which acts on the fluid element because of the viscosity of the fluid (Papautsky *et al*., 1999; Squires and Quake, 2005).

Laminar Newtonian Flow

The non-linear partial differential momentum Navier-Stokes equation that describes Newtonian fluid flowing in a channel is written as:

$$\rho\left[\frac{\partial \mathbf{u}}{\partial t} + (\mathbf{u}\cdot\nabla)\mathbf{u}\right] = -\nabla P + \eta\nabla^2\mathbf{u} + f \tag{2.3}$$

where **u** is average velocity characteristic of the flow, *t* is the time, fluid density and dynamic viscosity are given by ρ and η respectively, *P* is the pressure and *f* is the body force that acts on the entire element inside the continuum.

In microfluidic systems, the length scales demands that all flow to be laminar. Thus, both the inertial term which comprises the convective acceleration which is represented by the non-linear term $(\mathbf{u}\cdot\nabla)\mathbf{u}$ and unsteady-state acceleration which is represented by term of $\partial\mathbf{u}/\partial t$ can be neglected under this condition (Papautsky *et al*., 1999; Squires and Quake, 2005). In microfluidics systems, gravitational body forces and associated density differences are small and most separations are based on surface forces rather than body forces (Hessel *et al*., 2009). Thus, gravitational body forces are negligible in most microfluidic device. Consequently, these simplifications lead to the Navier-Stokes equation for steady-state, incompressible, constant viscosity and the flow without body forces is being presented as follows:

$$0 = -\nabla P + \eta\nabla^2\mathbf{u} \tag{2.4}$$

For laminar flow in parallel geometries, the velocity profile is a function of the *y* and *z*-coordinates normal to flow direction whereas the pressure is strictly a function of the *x*-coordinates direction. Thus, the Navier-Stokes equation with the associated boundary condition of zero velocity at the wall for a pressure-driven, steady-state incompressible flow in microchannel is expressed by (Nguyen and Wereley, 2002; Tanyeri *et al*., 2011):

$$0 = -\frac{\partial P}{\partial x} + \eta\left(\frac{\partial^2 u}{\partial y^2} + \frac{\partial^2 u}{\partial z^2}\right) \text{ for} -\frac{w}{2} < y < \frac{w}{2} \text{ and } 0 < z < h \tag{2.5}$$

Where *x* is the coordinate axes along the channel length, *y* is the coordinate axes along the channel width, *z* is the coordinate axes along the channel height, *w* is the channel width, and *h* is the channel height, respectively. With no-slip boundary condition, the geometry of the cross-section of the rectangular is fixed and an analytical solution solutions is possible (Nguyen and Wereley, 2002; Tanyeri *et al*., 2011).Figure 2.1 shows the standard rectangular microchannel cross section with practical application in microsystems. In applying the Navier-Stokes equation (Equation 2.4), the analytical solutions of the Poiseuille flow for rectangular cross-section are shown as follows:

Rectangular cross-section

$$\text{Velocity profile: } u_x(y,z) = \frac{4h^2\Delta P}{\eta\pi^3 l}\sum_{k=1,3,5\ldots}^{\infty}\frac{1}{k^3}\left[1 - \frac{\cosh(k\pi\frac{y}{h})}{\cosh(k\pi\frac{w}{2h})}\right]\sin(k\pi\frac{z}{h}) \tag{2.6}$$

$$\text{Flow rate: } Q = \frac{h^3 w\Delta P}{12\eta l\alpha}\left[1 - \sum_{k=1,3,5\ldots}^{\infty}\frac{192}{\pi^5 k^5}\alpha\tanh(k\pi\frac{w}{2h})\right] \tag{2.7}$$

where *l*, *w* and *h* are the length, width and height of the channel, respectively, ΔP is the driven pressure drop, η is the viscosity of liquid and α(=*h*/*w*) is the aspect ratio.

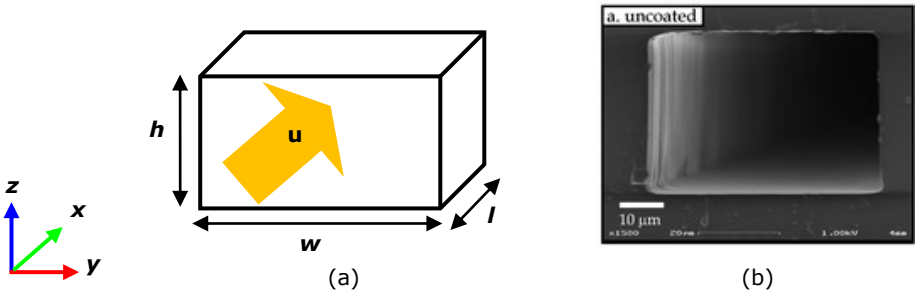


Figure 2.1: Fluid flow with characteristic velocity scale *u* through the standard (a) rectangular circular microchannels; (b) SEM image of a rectangular microchannel. The coordinate x point downstream, z spans the width and y spans the height (*l*: channel length; *w*: channel width; *h*: channel height) (Figures adapted from Squires and Quake, 2005; Abate *et al*., 2008).

Furthermore, an example for the diagram of the velocity profile for Newtonian flow in a rectangular microchannel is illustrated in Figure 2.2. These equations provide the velocity field as a function of location within the cross section of the channel and as a function of applied pressure difference. Apart from that, the flow rate across the cross section is also provided as a function of pressure drop (Nguyen and Wereley, 2002).

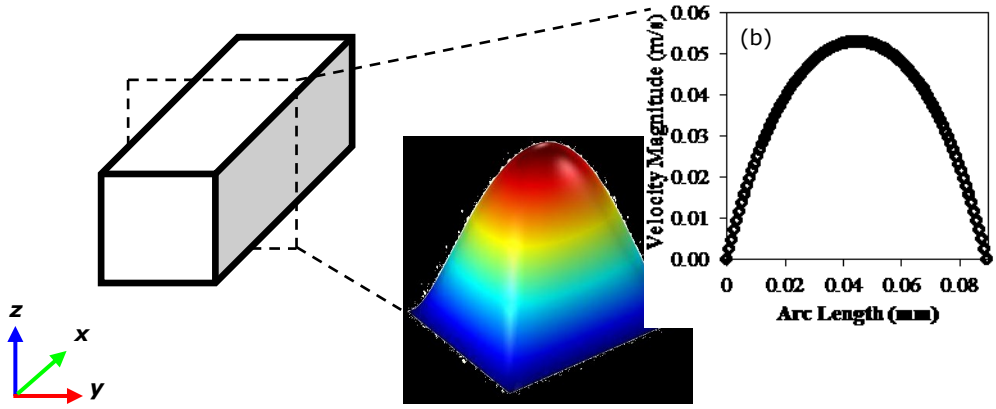


Figure 2.2: Velocity profile for laminar Newtonian flow: (a) Two-dimensional (2D) plot with velocity height expression, (b) One-dimensional (1D) plot with parabolic velocity profile in rectangular microchannel.

Laminar Non-Newtonian Flow

Most real fluids exhibit non-Newtonian behaviour, which means that the flow curve present a nonlinear relationship between shear stress and shear rate or does not pass through the origin. The apparent viscosity which is given by:

$$\eta = \frac{\tau}{\dot{\gamma}} = \frac{\text{shear stress}}{\text{shear rate}} \tag{2.8}$$

is not constant at a given temperature and pressure but is dependent on flow conditions such as flow geometry, shear rate and sometimes even the kinematic history of the fluid element (Kostic, 1993; Chhabra and Richardson, 2008). Non-Newtonian fluid exhibit various type of non-linearity and it can be classified into three general groups:

- *Purely viscous fluids*: The rate of shear at any point is determined only by the value of the shear stress at that point at that instant; it also can be known as or time-independent fluids or generalized Newtonian fluids (GNF).
- *Time-dependent fluids*: The relation between shear stress and shear rate further dependence on the duration of shearing and their kinematic history.
- *Viscoelastic fluids*: Substances exhibit characteristics of both viscous fluids and elastic solids and showing partial elastic recovery after deformation.

Purely viscous fluids are further subdivided into shear-thinning (pseudoplastic), viscoplastic and shear-thickening (dilatants). Figure 2.3 shows the types of time-independent fluid behaviour.

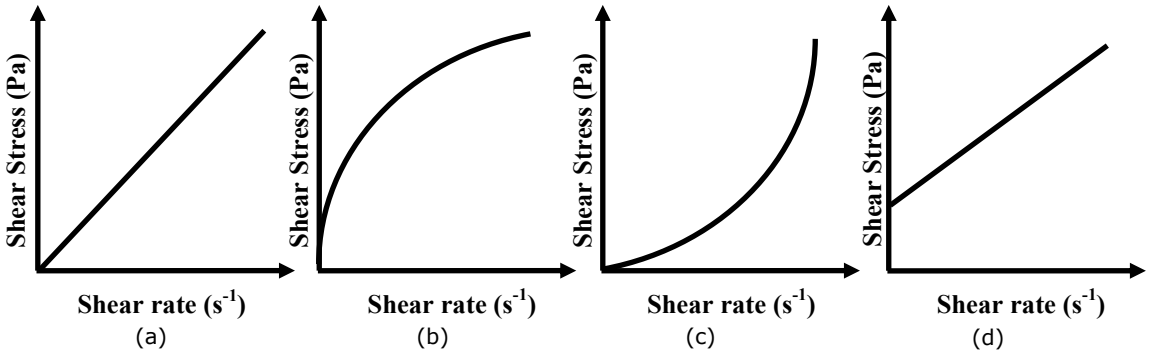


Figure 2.3: Comparison of shear-rate profile between Newtonian and purely viscous fluids: (a) Newtonian fluid; (b) Shear-thinning; (c) Shear-thickening; and, (d) Viscoplastic fluid (Chhabra and Richardson, 2008).

Based on the non-Newtonian flow through the microchannel with rectangular cross-section, the axial velocity in the fully developed region is a function of two independent variables and the study of the hydrodynamic behaviour in a rectangular microchannel requires a two-dimensional or three dimensional

analyses. An example for the diagram of the velocity profile for non-Newtonian flow in a rectangular microchannel is illustrated in Figure 2.4.

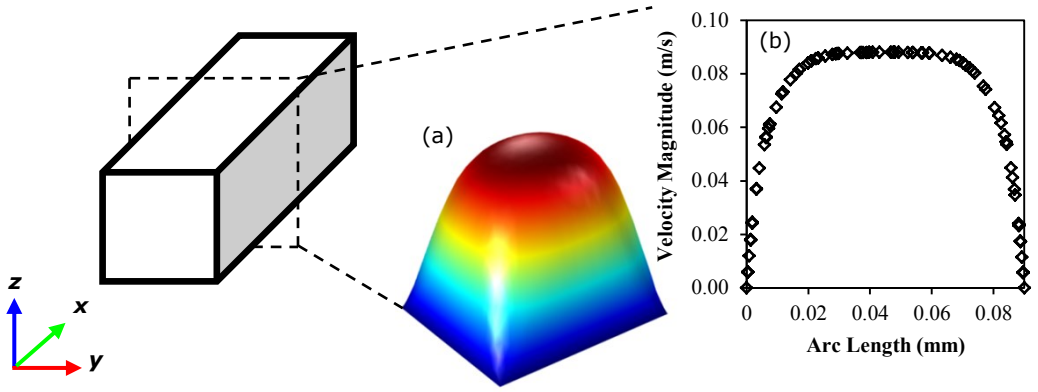


Figure 2.4: Velocity profile for laminar non-Newtonian shear-thinning flow: (a) Two-dimensional (2D) plot with velocity height expression, (b) One-dimensional (1D) plot with blunted velocity profile in rectangular microchannel.

The governing equations expressing conservation of mass and momentum in a rectangular coordinate system under the assumptions of steady-state condition, constant fluid properties, laminar non-Newtonian flow are given by (Cho and Hartnett, 1985):

$$\rho[(\mathbf{u}\cdot\nabla)\mathbf{u}] = -\nabla P + \nabla\cdot\boldsymbol{\tau} \tag{2.9}$$

The governing equation in Cartesian coordinates can be written as:

$$\frac{\partial u}{\partial x} + \frac{\partial v}{\partial y} + \frac{\partial w}{\partial z} = 0 \tag{2.10}$$

x-momentum

$$\rho\left(u\frac{\partial u}{\partial x} + v\frac{\partial u}{\partial y} + w\frac{\partial u}{\partial z}\right) = -\frac{\partial p}{\partial x} + \left(\frac{\partial \tau_{xx}}{\partial x} + \frac{\partial \tau_{xy}}{\partial y} + \frac{\partial \tau_{xz}}{\partial z}\right) \tag{2.11}$$

y-momentum

$$\rho\left(u\frac{\partial v}{\partial x} + v\frac{\partial v}{\partial y} + w\frac{\partial v}{\partial z}\right) = -\frac{\partial p}{\partial y} + \left(\frac{\partial \tau_{xy}}{\partial x} + \frac{\partial \tau_{yy}}{\partial y} + \frac{\partial \tau_{yz}}{\partial z}\right) \tag{2.12}$$

z-momentum

$$\rho\left(u\frac{\partial w}{\partial x} + v\frac{\partial w}{\partial y} + w\frac{\partial w}{\partial z}\right) = -\frac{\partial p}{\partial z} + \left(\frac{\partial \tau_{xz}}{\partial x} + \frac{\partial \tau_{yz}}{\partial y} + \frac{\partial \tau_{zz}}{\partial z}\right) \tag{2.13}$$

Generally, three common models: Power-Law model, Carreau-Yasuda model, and Cross model are used to describe fluid flow characteristics if a purely viscous

fluids with shear-thinning behaviour is assumed. For example, we have the generalized power-law or Ostwald-de Waele relationship that has been used to correlate the shear stress to shear rate with the following form:

$$\eta = \frac{\tau}{\dot{\gamma}} = m\left(\Pi_D\right)^{\frac{(n-1)}{2}} \tag{2.14}$$

$$\Pi_D = 2\left[\left(\frac{\partial u}{\partial x}\right)^2 + \left(\frac{\partial v}{\partial y}\right)^2 + \left(\frac{\partial w}{\partial z}\right)^2\right] + \left(\frac{\partial u}{\partial y} + \frac{\partial v}{\partial x}\right)^2 + \left(\frac{\partial u}{\partial z} + \frac{\partial w}{\partial x}\right)^2 + \left(\frac{\partial w}{\partial y} + \frac{\partial v}{\partial z}\right)^2 \tag{2.15}$$

where m is fluid consistency coefficient, n is fluid behaviour index (for n<1: shear-thinning; n=1: Newtonian; n>1: shear-thickening), and Π_D is the second invariant of the strain tensor. The velocity profile is a function of y and z-direction only whereas the pressure is strictly a function of x-direction and the flow must be in the direction of decreasing pressure. Thus, the Equation 2.15 reduces to:

$$\Pi_D = \left(\frac{\partial u}{\partial y}\right)^2 + \left(\frac{\partial u}{\partial z}\right)^2, \text{ for hydraulically fully developed flow.} \tag{2.16}$$

Thus, the laminar velocity profile of a power-law fluid flowing through a rectangular duct by substituting the Equation 2.16 to the governing equation is given by (Cho and Hartnett, 1985):

$$\frac{1}{m}\frac{\partial p}{\partial x} = \frac{\partial}{\partial y}\left\{\frac{\partial u}{\partial y}\left[\left(\frac{\partial u}{\partial y}\right)^2 + \left(\frac{\partial u}{\partial z}\right)^2\right]^{(n-1)/2}\right\} + \frac{\partial}{\partial z}\left\{\frac{\partial u}{\partial z}\left[\left(\frac{\partial u}{\partial y}\right)^2 + \left(\frac{\partial u}{\partial z}\right)^2\right]^{(n-1)/2}\right\} \tag{2.17}$$

Approximate velocity profile for the power-law fluid (α=0.25, 0.50, 0.75 and 1.00) flow in a rectangular microchannel is given by (Schechter, 1961; Cho and Hartnett, 1985):

$$\frac{u(y,z)}{U} = \sum_{i=1}^{6} A_i \sin\left[\alpha_i \pi \frac{(z/h)}{2} + 1\right] \sin\left[\beta_i \pi \frac{(y/w)+1}{2}\right] \tag{2.18}$$

where constant α_i and β_i are given in Table 2.1 and A_i is the constants selected to minimize an integral. Six constants (A_1= A_{11}; A_2= A_{21}; A_3= A_{12}; A_4= A_{22}; A_5= A_{31}; A_1= A_{13}) which are to be computed by the Ritz-Galerkin method are identical to

the corresponding Fourier coefficient and tabulated as a function of aspect ratio and fluid-behaviour index in Table 2.2.

Table 2.1: Values of α_i and β_i constant (Schechter, 1961; Cho and Hartnett, 1985).

i	α_i	β_i
1	π	π/α
2	3π	π/α
3	π	$3\pi/\alpha$
4	3π	$3\pi/\alpha$
5	5π	π/α
6	π	$5\pi/\alpha$

Table 2.2: Computed result for the flow in rectangular duct (Schechter, 1961; Cho and Hartnett, 1985).

Fluid behaviour index, *n*	**Aspect ratio, α**	A_1	A_2	A_3	A_4	A_5	A_6
1.00	1.00	2.346	0.156	0.156	0.0289	0.0360	0.0360
0.75	1.00	2.313	0.205	0.205	0.0007	0.0434	0.0434
0.50	1.00	2.263	0.278	0.278	-0.0285	0.0555	0.0555
1.00	0.75	2.341	0.204	0.119	0.0256	0.0498	0.0303
0.75	0.75	2.310	0.235	0.180	0.0001	0.0568	0.0364
0.50	0.75	2.263	0.286	0.267	-0.0277	0.0644	0.0505
1.00	0.50	2.311	0.296	0.104	0.0285	0.0795	0.0303
0.75	0.50	2.288	0.299	0.174	0.0120	0.0811	0.0364
0.50	0.50	2.249	0.312	0.274	-0.0101	0.0789	0.0501
1.00	0.25	2.227	0.503	0.0867	0.0274	0.184	0.0189
0.75	0.25	2.221	0.459	0.160	0.0312	0.160	0.0210
0.50	0.25	2.205	0.407	0.270	0.0257	0.131	0.0364

Nevertheless, there is no unique constitutive model to represent the different characteristic behaviours of non-Newtonian fluids which are characterized by the fact that the shear-stress is not linearly proportional to the rate of deformation. In present work, power-law model is not potentially selected to describe the behaviour of shear-thinning working fluid as it poses limitations on its range of applicability over a wide range of shear rate. In order to circumvent the drawback of the power-law model, alternative approaches such as Carreau-Yasuda model utilize viscosity functions that have finite values both at very low and high shear rate. On the contrary, the Navier-Stokes equations are almost generally accepted to be appropriate and unique representation of the flow behaviour for Newtonian fluids. Figure 2.5 and 2.6 illustrates the velocity profile

for the Newtonian and purely viscous fluids, respectively. In microchannels, the apparent viscosity of shear-thinning fluid decreases as the shear rate increase; moreover, the velocity profile in a microchannel becomes increasingly blunt as *n* decreases. It shows that the velocity profile of a shear-thickening fluids becoming more pointed as *n* increases, with larger velocity gradients throughout the flow domain.

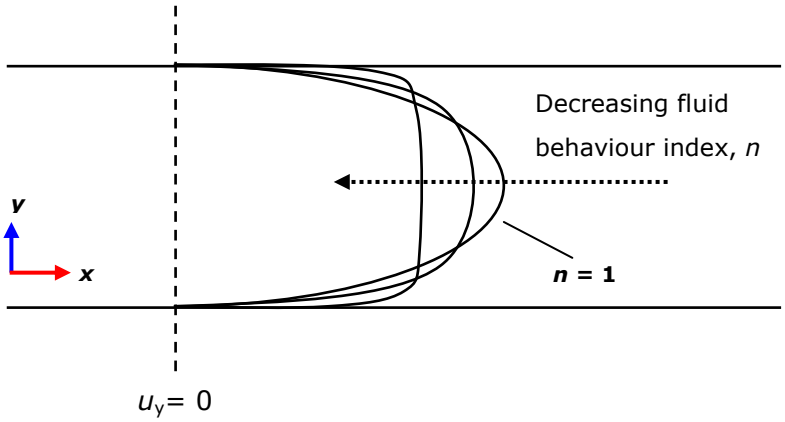


Figure 2.5: Schematic velocity profile for fluids exhibit shear-thinning behaviour in microchannel.

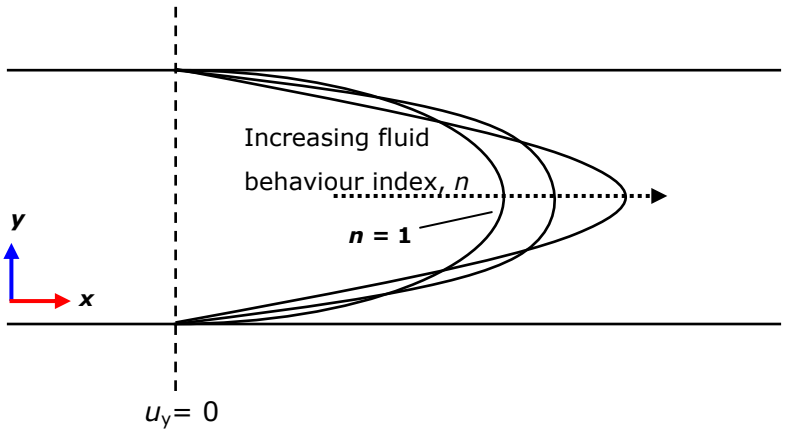


Figure 2.6: Schematic velocity profile for fluids exhibit shear-thickening behaviour in microchannel.

Dimensionless Group

Scaling analysis and dimensional analysis are of key importance in physics. A number of forces at various scales applied on a fluid flow through a microchannel where the importance of them has been judged against competing phenomena (Square and Quakes, 2005). Dimensionless numbers expressing the ratio of these physical phenomena indicating the relative importance of forces, energies,

and the time scales would lead the way to simplification of complex systems (Square and Quakes, 2005; Berthier and Silberzan, 2009). A list of most widely used dimensionless numbers in microfluidics for Newtonian and non-Newtonian is given in Table 2.3.

Table 2.3: Dimensionless numbers for Newtonian and non-Newtonian fluids flow in microfluidics (Square and Quakes, 2005; Berthier and Silberzan, 2009).

Dimensionless number		**Significance**	**Equation**	**Scaling Law**
Reynolds	Re	inertial/viscous	$\frac{\rho u L}{\eta}$	L^2
Pèclet	Pe	convection/diffusion	$\frac{uL}{D}$	L^2
Bond	Bo	gravitational/interfacial	$\frac{\rho g L^2}{\sigma}$	L^2
Capillary	Ca	viscous/interfacial	$\frac{u\eta}{\sigma}$	L
Ohnesorge	Oh	viscous/inertia**/**interfacial	$\frac{\eta}{\sqrt{\rho\sigma L}}$	$L^{-1/2}$
Weber	We	inertial/Interfacial	$\frac{\rho u^2 L}{\sigma}$	L^3
Weissenberg	Wi	polymer relaxation time/ shear rate time	$\tau_p \dot{\gamma}$	L
Deborah	De	polymer relaxation time/ flow time	$\frac{\tau_p}{\tau_{flow}}$	$L^{-3/2}$
Elasticity	El	elastic effects/ inertial effects	$\frac{\tau_p \eta}{\rho L^2}$	L^{-2}
Elasto-capillary	Ec	elastic and capillary effects/viscous	$\frac{\tau_p \sigma}{\eta L}$	L^{-2}
Grashof	Gr	Re for buoyant flow	$\frac{\rho u_b L}{\eta}$	L^2
Rayleigh	Ra	Pe for buoyant flow	$\frac{u_b L}{D}$	L^2
Knudsen	Kn	slip length/ macroscopic length	$\frac{\beta}{L}$	L^{-1}

*** Note:*

L	*= characteristic length scale related to flow geometry*
u	*= average velocity characteristic of the flow*
u_b	*= buoyancy velocity*
g	*= acceleration of gravity*
η	*= dynamic viscosity of the fluid*
ρ	*= density of the fluid*
$\dot{\gamma}$	*= shear rate*
σ	*= surface/interfacial tension of the fluid*
D	*= diffusion coefficient*
τ_p	*= relaxation time of the fluid*
τ_{flow}	*= flow time of the fluid*
β	*= slip length*

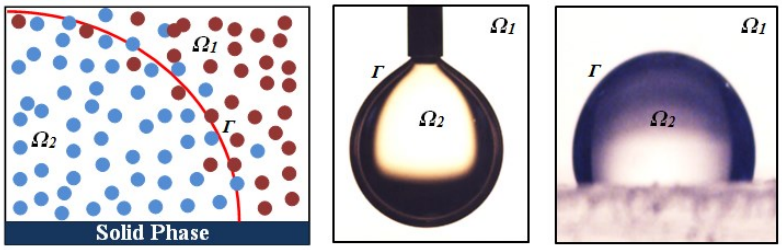
Reynolds number and the Pèclet number provide information on the flow characteristics and heat and mass transfer in a microfluidics system. The influence of the surface tension on the flow behaviour is characterised using a number of dimensionless groups. These include Ohnesorge number, Capillary number, Bond number, and Weber number. Weissenberg, Deborah, elasticity, and elastocapillary numbers are characteristic of non-Newtonian flow. These dimensionless numbers act especially when dealing with polymers that add an elastic component to the fluid. Finally, the Knudsen number, relating microscopic to macroscopic length scales.

2.2.2 The Physics of Microdroplets

Toward a deeper understanding of the role of droplet breakup inside a microfluidic device can be achieved by exploiting the physics of fluid flow at the microscale. Thus, the understanding of physical phenomena that control the fluid flow behaviour at microscale is necessary.

Interfaces and Surface Tension

An interface is the geometrical surface forming a common boundary that delimits two fluid domains. This definition implies that an interface has no thickness and is smooth. Mathematically speaking, surface/interfacial tension, σ(unit: J/m^2 or N/m) is a cohesive force between molecules or a function which rules interface processes involving fluids such as gas and liquids. Figure 2.7 illustrates the microscopic view of interfaces between two immiscible fluids.



(a) **(b)** **(c)**

Figure 2.7: Illustration of interfaces (Γ) between two immiscible fluids: (a) Microscopic view of interface at the molecular size; macroscopic view of (b) pendant drop and (c) sessile drop. The region occupied by first fluid phase and region occupied by second fluid phase are denoted as $\Omega_1$and Ω_2,respectively. The red solid line represents the approximate location of the interface between two immiscible fluids.

The shape of a pendant or sessile drop is used to be defined as a function of the surface tension. Due to the existence of surface tension effect in a case of liquid droplet, there is a pressure inside the droplet which is always greater than a continuous phase. As the radius of droplet become smaller, the pressure becomes larger on the concave side of liquid interface. A Young-Laplace equation is usually used to determine the pressure difference across a fluid interface as a function of curvature. And, the magnitude of this pressure differential (or termed as Laplace pressure) can be expressed in term of surface tension:

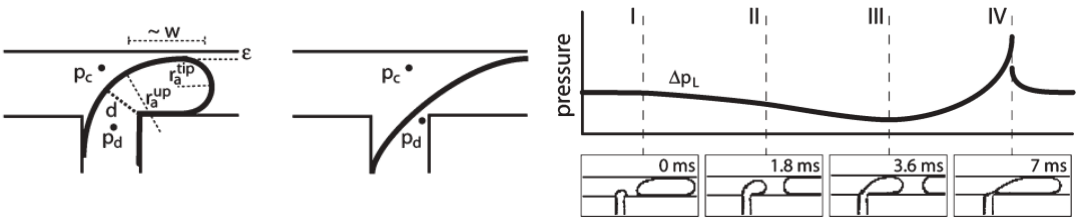
$$\Delta P_L = \sigma\left(\frac{1}{R_1} + \frac{1}{R_2}\right) \tag{2.19}$$

where σ is the surface tension of the respective liquid interface and $R_1$and $R_2$are the two principal curvature radii of the interface.

In microfluidic systems, as the dimension of the interest gets smaller, surfaces tension becomes dominant over not only the gravitational forces but others physical forces such as viscous and inertial forces. Due to the existence of a high surface-to-volume ratio within a microscaled device, the surface/interfacial tension becomes an important surface energy parameter that controls the stability of interfaces between the two phases when the droplets are forming.

Garstecki *et al*. (2006) approximated the magnitude of surface tension force, which has the stabilizing effect on the emerging tip, arising from ΔP_L ($=\sigma(r_a^{-1}+ r_r^{-1})$),where r_a and r_r are the radii of axial and radial curvature) across the interface in a squeezing regime (see section 2.3). Figure 2.8 illustrates a schematic diagram of the emerging shape of a thread in a T-shaped microchannel and the evolution of Laplace pressure at the interface.

Previous studies have focused in particular on the predominance of surface tension on characters of microfluidic droplet formations (Wang *et al*., 2009; Bashir *et al*., 2011; Glawdel *et al*., 2012; Wehking *et al*., 2014) and its changes in presence of surfactants in microfluidic systems (Shui *et al*., 2009; Peng *et al*., 2011). Figure 2.9 illustrates the several pattern formations of microdroplets and the droplet size variation as results of the effect of surface tension in the microfluidic T-junction and flow-focusing devices. Surface flows of surfactant can induce variations in surface tension (for instance, Marangoni effect), which can substantially alter the interfacial morphology and resulting droplets size (Cubaud and Manson, 2008). Apart from the presence of surfactant, depending on the fluid viscosity or concentration (Liu and Zhang, 2009; Gu and Liow, 2011), temperature (Murshed *et al*., 2008) and the presence of micro- or nanoparticles in the fluid (Murshed *et al*., 2008; Wang, 2013) can modify considerably the value of surface tension of the fluid in nature, and thus tailor the two-phase flow behaviour within the microfluidic system.



(a) **(b)**

Figure 2.8: Schematic diagram of (a) the shape of an emerging tip; (b) the postulated evolution of Laplace pressure during the droplet breakup process in a T-junction microchannel (Garstecki *et al*., 2006).

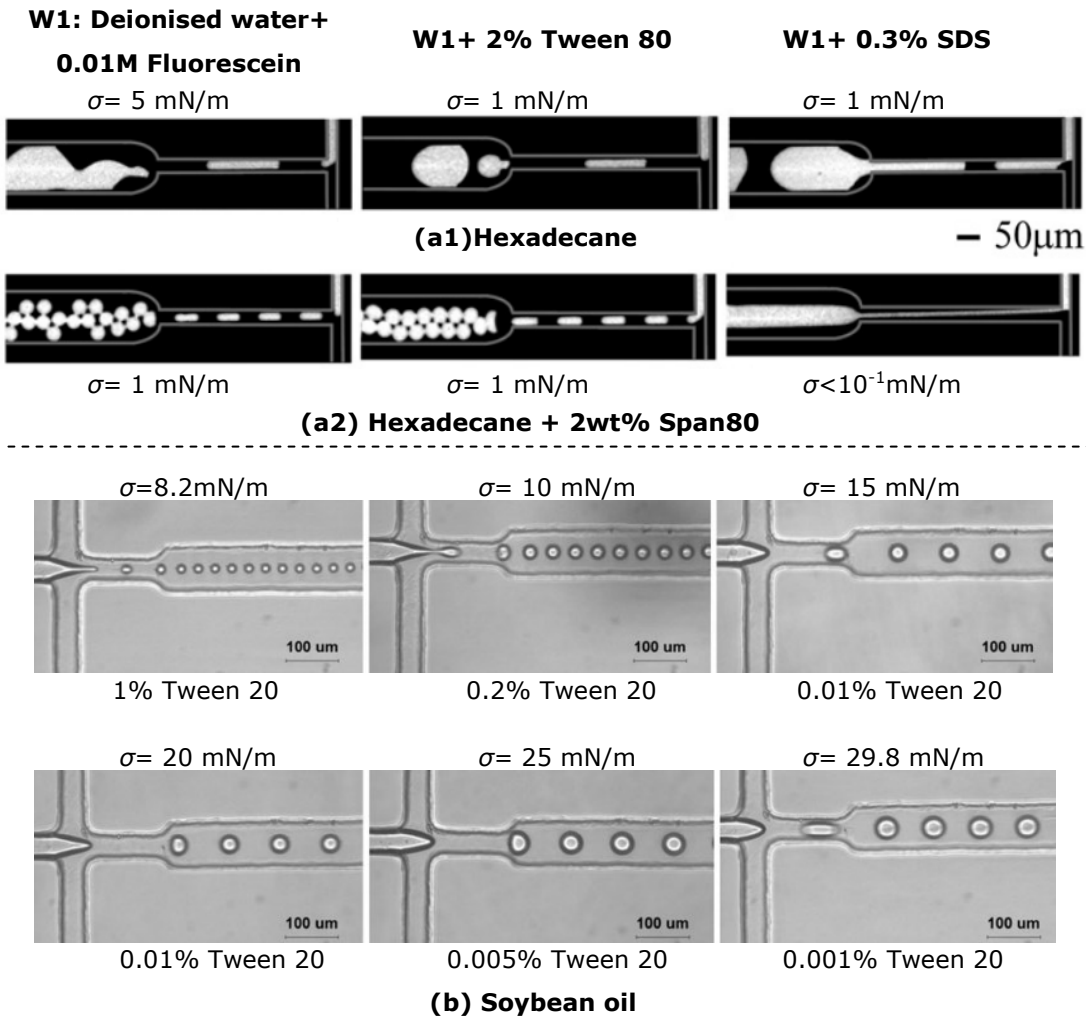


Figure 2.9: Microphotograph images of droplet formation behaviour in microfluidic devices: (a1) water-in-hexadecane emulsions with the addition of hydrophilic surfactant Tween 80, SDS and (a2) hydrophobic surfactant Span80 (Shui *et al*., 2009); (b) water-in-soybean oil with the addition of surfactant Tween 20 (Peng *et al*., 2011).

Contact Angle and Surface Wettability

Theoretically, contact angle (θ)is an angle formed by a liquid droplet at three phase boundary where a gas/liquid or liquid/liquid interface meets a solid surface, as illustrated in Figure 2.10. The Young equation, which is initially proposed by Young (1805), relates contact angle to the surface tension of liquid-gas, solid-gas and solid-liquid that are in equilibrium with one another is given by:

$$\sigma_{LG}\cos\theta = \sigma_{SG} - \sigma_{SL} \tag{2.20}$$

Where σ_{LG}, σ_{SG}, *and* σ_{SL} represent the liquid-gas, solid-gas, and solid-liquid surface tension, respectively, and θ is the contact angle.

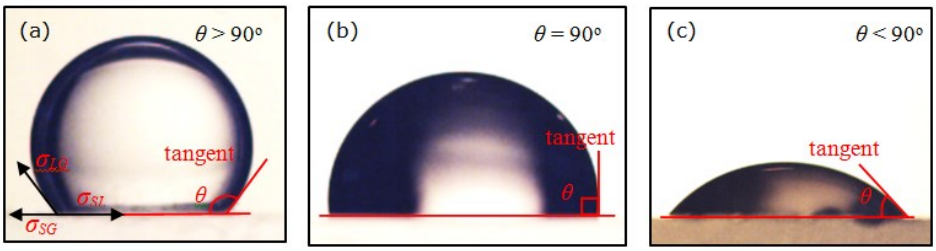


Figure 2.10: Illustration of fluid-solid interaction in wetting. Consider a liquid droplet resting on an ideal solid surface: (a) if wetting angle is greater than 90°or (b) equal to 90°a liquid said to be non-wetting (known as hydrophobic contact if water is used);and, (c) if wetting angle is lesser than 90°the liquid is said to wet the solid (known as hydrophilic contact if water is used). A zero contact angle denotes complete wetting.

The interaction between the solid surface of the microchannel and the fluid has been a major focal point in affecting the dynamics of the droplet formation process. Figure 2.11 illustrates the flow patterns for different wetting conditions in a T-shaped microchannel. Most studies of droplet generation in microfluidic devices involve the numerical studies of the contact angle effect on the shape, size, the distance between two neighbouring droplets, detachment point and the generation frequency of droplets in microfluidic system (Liu and Zhang, 2009; Bashir *et al*., 2011). Liu and Zhang (2009) reported that the channel wall surface plays significant role in generating larger droplets with smaller contact angle provide longer contact time with the surface, especially for small values of capillary number, which is in consistent with the numerical results from Bashir *et al*. (2011). Additionally, Bashir *et al*. (2011) further claimed that increasing of contact angle in the excess of 165° had a negligible impact on droplet size for all values of capillary number applied. Previous experimental work has also reported that the surfactants can alter the surface wettability. Xu *et al*. (2006) demonstrated the preparation of monodispersed O/W and W/O emulsions in a T-junction microchannel by adding the surfactant Tween 20 to water phase and Span 80 to oil phase, respectively, in changing the wetting characteristics of the PMMA channel wall (see Figure 2.12). The influence of surface wettability characteristics on flow behaviour has attracted further numerical and experimental studies (Raj *et al.*, 2010; Tostado *et al.*, 2011).

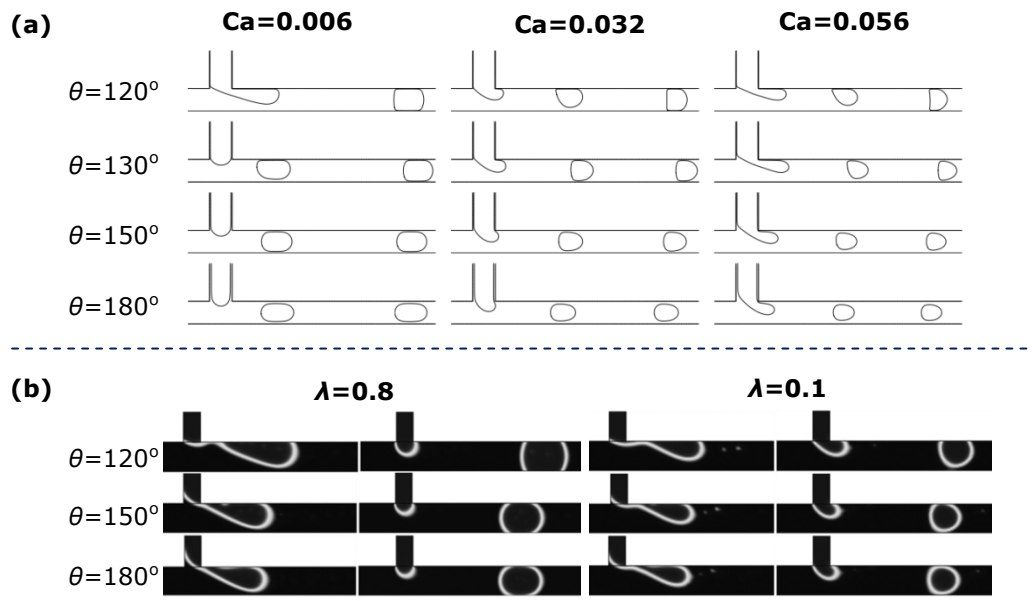


Figure 2.11: The influence of contact angle on the droplet breakup process in water-in-oil (W/O) emulsification system at: (a) different Ca (Liu and Zhang, 2009); (b) different viscosity ratio(Bashir *et al*., 2011).

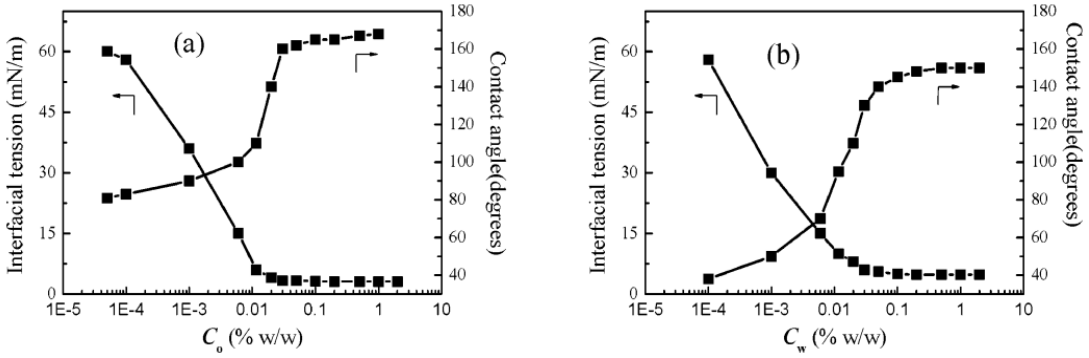


Figure 2.12: Effect of concentration of surfactant in (a) anhydrous hexadecane and (b) deionised water, respectively on the contact angle and surface tension (Xu *et al*., 2006).

Shear Stress in Microflows

One characteristic of microscale miniaturization is the large surface area to volume ratio. In previous sections, the flows in micro- or nanodevice naturally emphasize phenomena associated with interfacial tension and wetting properties. Additionally, inertial and viscosity effects are two important parameters in characterizing the role of the shear-stress exerted from the continuous phase acts to deform the interface during the droplet breakup process. Garstecki *et al*. (2006) demonstrated the influence of two phase flow rates and viscosities on the

size of aqueous water droplets in an oil phase at a T-shaped microfluidics (see Figure 2.13). They relates the shear stress and flow rate of continuous phase and quantifies the magnitude of shear stress ($\tau \propto \eta_c Q_{oil}$, where η_c is the viscosity of continuous phase) acting on the interface. As Q_{water} increases, the shear stress exerted by the continuous phase on the droplet is increased due to the difference of the flow rate of the two fluids decreases with increasing Q_{water} (Garstecki *et al*., 2006). Similar phenomena were found by Xu *et al*. (2006b) who studied on the effect of flow rates on the formation of oil droplets. The same tendency was also reported by Cramer *et al*. (2004), Hong and Wang (2007), Yeom and Lee (2011), and Mulligan and Rothstein (2012). These numerical and experimental results imply that the flow rate of the both phases considerably alter the droplet formation mechanisms under laminar flow in different microfluidic configurations.

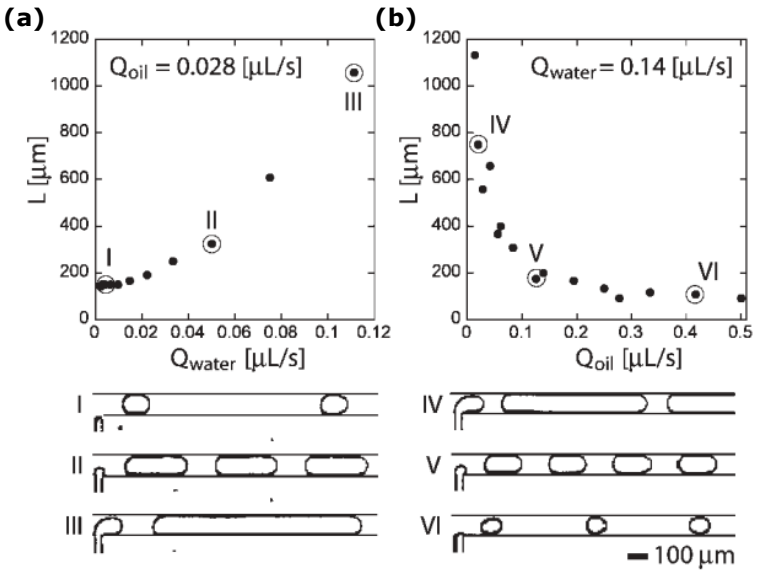


Figure 2.13: The size of aqueous water droplets plotted as function of flow rates of oil and aqueous phase at a microfluidics T-junction: (a) fixed oil phase rate; (b fixed aqueous phase rate (Garstecki *et al*., 2006).

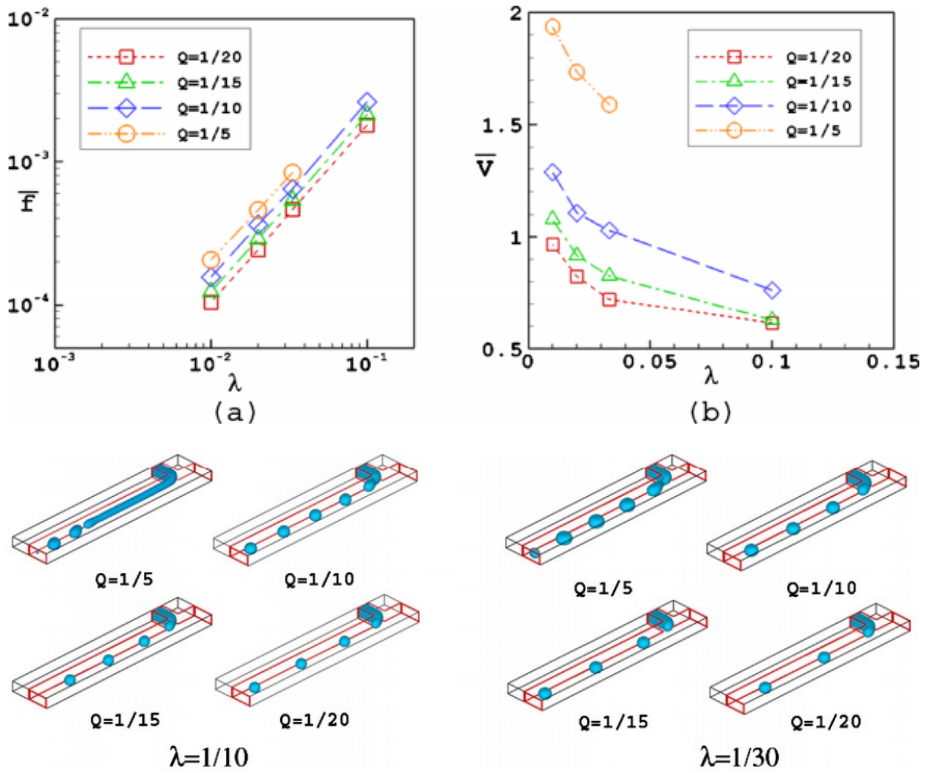


Figure 2.14: Effect of viscosity ratio and flow rate ratio on the (b) frequency generation and (b) droplet volume at each flow rate ratio (Gupta and Kumar, 2010).

Apart from the effect of two phase flow rates (or flow rate ratio, $Q=Q_d/Q_c$), the length of the droplet should also depend on the viscosity ratio ($\lambda=\eta_d/\eta_c$) (Garstecki *et al*., 2006). Previous investigations reported that an increase of the viscosity of continuous phase gives rise to the viscous stress added on the dispersed phase, and thus decreasing the droplet size and alter the flow pattern (Cramer *et al*., 2004; Husny and Cooper-White, 2006; DeMenech et al., 2008). Nevertheless, Gupta and Kumar (2010) numerically observed that the droplet volume deceases with decreasing viscosity of continuous phase, which indicates the smaller shear force acting on the droplet interface (see Figure 2.14).

2.3 Droplet Formation in a Microchannel Network

An emulsion contains a mixture of two immiscible liquids as one phase being dispersed throughout the other phase in small droplets. Most common emulsions include oil-in-water, or direct emulsions, and water-in-oil, or inverted emulsions

(Umbanhowar *et al*., 2000).Emulsions are typically made by fissioning droplets with shear or impact and the resulting suspensions possess a wide size distribution of drop sizes. The characteristics of emulsion products such as droplet size and distribution are the most important parameters that affect the stability, rheology, chemical reactivity, and physiological efficiency of any emulsion (Xu *et al*., 2006; Xu *et al*., 2008; Qiu *et al*., 2010).

Emulsions produced in the conventional processes are usually poly-disperse, unstable, and energy-intensive (Qiu *et al*., 2010). Conventional processes are in general continuous processes in which a disperse microstructure is generated under laminar and/or turbulent flow conditions. The conventional processes for emulsification including rotor-stator system, high pressure homogenizer and ultrasonic waves use droplet break-up as the dispersing mechanism and usually require considerable energy input and high shear stresses (Kobayashi *et al*., 2003; Aryanti *et al*., 2006). The resultant emulsions exhibit considerable polydispersity with droplet diameters of 0.1-100 μm (Kobayashi *et al*., 2003).

With the enhanced control available over more conventional systems, the formation of microdrops inside microfluidic devices has gained a great deal of attention over the past decade (see for instance, Xu *et al*., 2008) for emulsion generation and as a precursor for crystallization (Zheng *et al*., 2004), nanoparticle formation or chemical reaction (Hung and Lee, 2007).

Microfluidics Approaches to the Droplet Formation

Numerous researchers have investigated the potential of microfluidic device technology as a new generation methodology for the continuous and controlled production of droplets (Hong and Cooper-White, 2009). Monodispersed droplets have been generated by a number of methods in microfluidics devices, including breakup in co-flowing stream (Cramer *et al*., 2004; Utada *et al*., 2007, Moon *et*

al., 2014), breakup in-cross-flowing stream (Garstecki *et al*., 2006; Xu *et al*., 2008, Qiu *et al*., 2010), breakup in elongational strained flows (Anna and Mayer, 2006; Peng *et al*., 2011) and microchannel emulsification (Kobayashi *et al*., 2002; Kobayashi *et al*., 2005; van der Zwan *et al*., 2009). Figure 2.16illustrates four of the most common microfluidics configurations to microdroplets formation in microchannel network based on different physical mechanisms. There are four different microsystems for the droplet generation can be defined as follows:

- Co-flowing streams (see Figure 2.16a): A disperse phase is forced through an orifice into a continuous phase and it will ultimately break into droplets through one of two different drop formation mechanisms (Utada *et al*., 2007).
- Cross-flowing streams (see Figure 2.15a and 2.16b):The formation of droplet at a T-junction, at which viscous shear stresses from the continuous stream of the horizontal channel overcome surface tension at the liquid-liquid interface and pull off droplets of the dispersed phase entering from the vertical channel (Zhao and Middelberg, 2011). Monodispersed droplets with an equal spacing can be achieved by the high shear forces at the T-junction. The droplet size and frequency can be accurately controlled by modifying the relative pressures of the two immiscible liquid in order to enable the production of a wide range of vesicle shapes and patterns (Thorsen *et al*., 2001). Contrary to cross-flowing, opposed flowing (Shui *et al*., 2009) (see Figure 2.15b) and perpendicular flowing (Leshansky and Pismen, 2009) (see Figure 2.15c) are another operation modes producing monodispersed droplet formation in microchannel (Zhao and Middelberg, 2011).

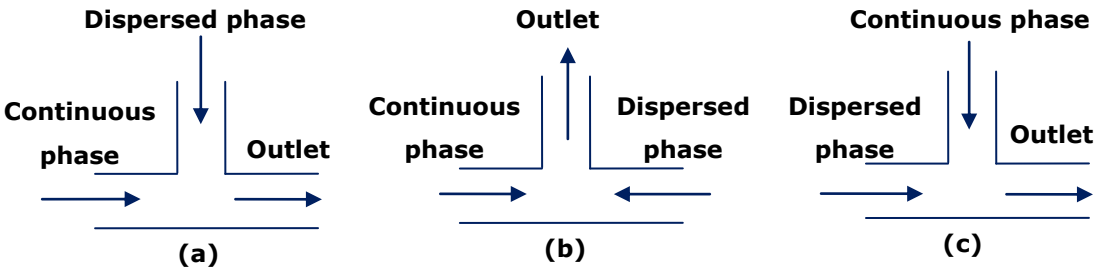


Figure 2.15: Schematic diagram of the injection of fluid configuration in a T-junction microchannel: (a) Cross-Flow; (b) Opposed-flow; (c) Perpendicular-flow.

- Elongational strained flows (see Figure 2.16c): A strong elongation flow of a continuous stream of one liquid flowing through a constriction draws a thin filament of the second immiscible liquid through the orifice, and the filament subsequently breaks into droplets (Anna and Mayer, 2006).
- Microchannel emulsification (see Figure 2.16d): Microchannel emulsification is a novel technique which was introduced by Sugiura *et al*. (2001) for producing monodispersed emulsions. A dispersed phase is dispensed through a microchannel onto a terrace where it assumes a disk-like shape. When the dispersed phase volume expands further, it eventually reaches into the well. A spherical dispersion is connected to the disk on the terrace with a neck. While the spherical dispersion continuously grows, the neck shrinks and this phenomenon eventually leads to break-up of the neck and droplet detachment (van der Zwan *et al*., 2009). A similar method to the MCE technique was also introduced by Kobayashi *et al* (2002) known as straight-through microchannel emulsification (SMCE) with an advantage of achieving a higher production rate by mass parallelization (van der Zwan *et al*., 2009; Kobayashi *et al*., 2005).

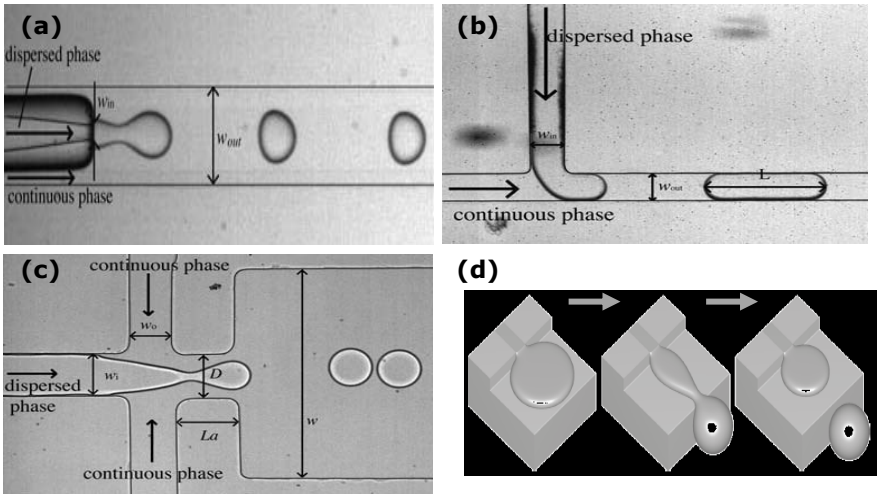


Figure 2.16: Four different microsystems for droplet generation: (a) breakup in co-flowing streams; (b) breakup in cross-flowing streams; (c) breakup in elongational strained flows; (d) breakup in microchannel emulsification (MCE) (van der Zwan *et al*., 2009; Baroud *et al*., 2010).

Droplet Formation Process in Various Flow Regimes

In two-phase flow microfluidics, dispersed and continuous phase fluids generally were dispensed separately into the microfluidic device. The continuous and dispersed phase channels typically meet at a junction which depends on the specific geometry of microfluidic device. Each shape of the junction helps to define the local flow fields that deform the interface between the two immiscible fluids (Gu *et al*., 2011; Nunes *et al*., 2013). When the instabilities of free surface between the phases are sufficiently large, drops emerge and eventually pinch-off from the dispersed phase. There are many controlling parameter scan affect the droplet generation regime such as, interfacial tension (Glawdel *et al*., 2012; Wehking *et al*., 2014), surface wettability/wall adhesion (Raj *et al.*, 2010), the volumetric flow rate (DeMenech *et al*., 2008; Liu and Zhang, 2009), viscosities of both immiscible fluids (Garstecki *et al*., 2006; Liu and Zhang, 2009;Wehking *et al*., 2014), and channel geometry (Gupta and Kumar, 2010).Table 2.4 describes the three main approaches for the droplet breakup in microchannel at different flow regimes. These configurations are also shown schematically in Figure 2.17.

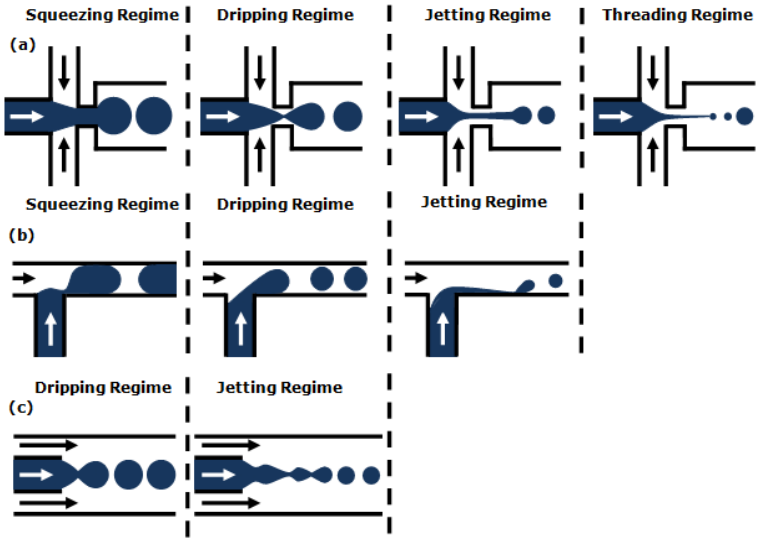


Figure 2.17: Schematic diagram of different distinct flow regimes in (a) flow-focusing, (b) cross-flowing (c) co-flowing microfluidics devices. The solid black and white arrow denotes the continuous and dispersed phase flow direction, respectively.

Table 2.4: Main approaches for droplet breakup in microchannel (Anna and Mayer, 2006; Utada *et al*., 2007; Baroud *et al*., 2010; Nunes *et al*., 2013).

Approaches	Distinct Breakup Regimes	Flow Regime Description
Breakup in co-flowing streams	Dripping	Droplet forms at the exit of the capillary tube tip and propagates downstream with the flow.
	Jetting	Droplets pinch off from an extended thread downstream of the capillary tube tip.
Breakup in cross-flowing streams	Squeezing	Dispersed threads block the outlet channel leads to dramatic increase in the dynamic pressure upstream of the droplet, thus forcing the interface to neck and pinch off into a droplet.
	Dripping	Dispersed thread does not touch the wall of the channel in the entire droplet formation process.
	Jetting	Droplet breakup point moves progressively downstream of the outlet channel.
Breakup in elongational strained flows	Squeezing	The tip of the droplet phase effectively blocks the cross-section of the orifice.
	Dripping	Droplets are periodically formed in the orifice.
	Jetting	The tip of the droplet phase extends downstream of the orifice and small droplets are formed at its terminus.
	Threading	Each droplet is formed a long and thin thread of the inner liquid is dragged behind the droplet. This thread subsequently breaks up into a group of tiny secondary droplets.

Various Flow Regimes in a T-Junction Microchannel Network

The T-junction microchannel, which is frequently used microfluidic configurations based on the physical mechanism of droplet breakup in cross-flowing stream, is employed in present work. Flow regimes have been investigated extensively for two phase flow in microfluidics T-junction. The previous works also showed that the interplay of capillary number (Ca), viscosity ratio (λ) or flow rate ratio (Q) is the important parameter that used to distinguish the two phase flow pattern and the mechanism of break up in a T-junction microchannel (Xu *et al*., 2008; Liu and Zhang, 2009; Gupta et al., 2009;Gupta and Kumar, 2010).There are three distinct flow regimes can be identified for droplet formation at a T-junction, namely squeezing, dripping, and jetting regimes (DeMenech *et al*., 2008; Yeom

and Lee, 2011), which corresponds to the primary driving forces acting on the system such as interfacial tension, tangential shear acting on the interface, pressure across the droplet and wetting properties of channel surface (Garstecki *et al*., 2006, Christopher *et al*., 2008; Cubaud and Manson, 2008).

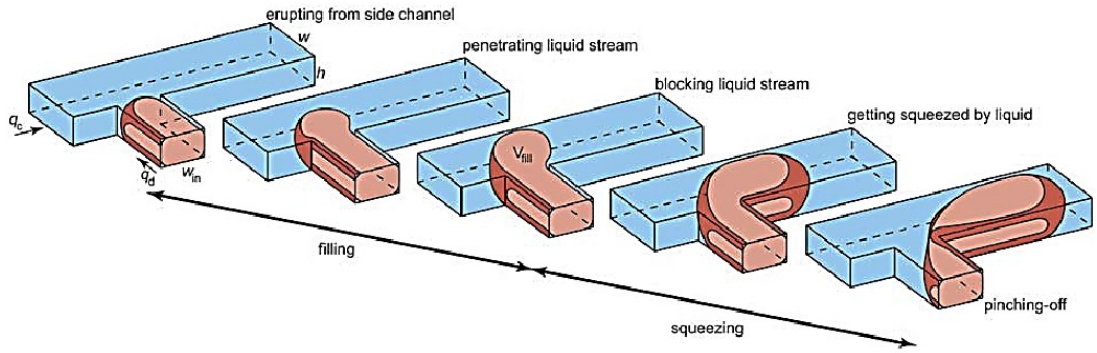


Figure 2.18: Schematic diagram of the formation of a droplet (or bubble) in the squeezing regime at a microfluidics T-junction (van Steijn *et al*., 2010).

Figure 2.18 illustrates the droplet breakup in the mode of "squeezing". In the squeezing regime, the evolution of pressure at the T-junction lies at the heart of the interfacial dynamics (DeMenech *et al*., 2009). When the stream of dispersed phase enters the main channel, the obstruction of the main channel leads to an increase in pressure upstream of the tip of the dispersed fluid. Once the dispersed phase pressure overcomes the ΔP_L across a static interface, the dispersed phase thread effectively block almost the entire cross-section of main channel and developed in the main channel, during which, it is confined by both the shape and size of channel. The pressure build-up in the upstream continues rises with the emerging droplet from orthogonal channel. The droplet deforms before detachment, and the necking of the dispersed phase is initiated once the continuous phase intrudes into the upstream of the lateral channel. The intrusion of the continuous phase accentuates the influence of the contact line dynamics, which is thought to be indispensable for the droplet detachment (Liu and Zhang, 2009). The necking occurs soon after the dispersed phase flows into the main channel and droplets are pinched-off (Garstecki *et al*., 2005; DeMenech *et al*., 2008; Xu *et al*., 2008; Fu *et al*., 2010).

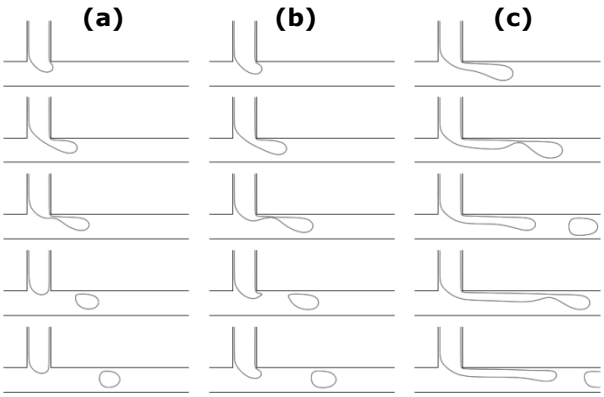


Figure 2.19: Transition from dripping to jetting regimes in a T-shaped microchannel. Fluid flow regimes as function of flow rate ratio (*Q*): (a) 1/8; (b) 1/4; (c) 1/2 at fixed Ca=0.056 (Liu and Zhang, 2009).

In dripping regime, the dispersed phase thread does not block the main channel in the entire process of droplet formation, as illustrated in Figure 2.19a and 2.19b. In dripping regime, the size of droplets is mainly controlled by the local shear force around the thread and the droplets are highly uniform in size but smaller than the channel width. While in jetting regime, droplet detachment point is moved from the T-junction to the downstream (see Figure 2.19c). This is due to the inertia effects when velocities of both phase is increased. Initially, the stream of the dispersed phase fluid intrudes and extends downstream of the T-junction and forms a long thread prior to formation of a droplet. Two immiscible fluids are in laminar flow side-by-side over lengths of the channel which are at least several times larger than its channel width (DeMenech *et al*., 2008).Some aspects, namely the parallel flow regime were observed where the protruding dispersed thread is become stable. Gupta *et al*. (2009) demonstrated that the influence of capillary number, viscosity ratio, and flow rate ratio on the flow regime transition from droplet flow to the stable parallel flow. No droplets formation was observed in this regime, which means that the two incoming streams flow in parallel downstream without any pinching process (Gupta *et al*., 2009).

2.4 Non-Newtonian Microdroplets Formation

Microfluidic device applications are commonly inclusive of coating flows, the formation of suspensions, emulsions and foams, heat transfer and fluid flow (Stone *et al*., 2004; Squires and Quake, 2005; Pipe and McKinley, 2009). However, many of these ultimate applications involve handling fluids that have a complex microstructure, and many materials of commercial interest would exhibit non-Newtonian phenomena, where the flow curve present a nonlinear relationship between shear-stress and shear rate (Tirtaatmadja *et al*., 2006; Pipe and McKinley, 2009). Most studies of drop formation in microchannels have focused on traditional Newtonian-Newtonian systems, and little experimental attention has been given to non-Newtonian fluids (Stone *et al*., 2004; Tirtaatmadja *et al*., 2006; Husny and Cooper-White, 2006; Arratia *et al*., 2009). An investigation into the behaviour of multiphase non-Newtonian–Newtonian systems in microdevices is highly relevant to many microfluidic technology applications, especially in the medical research and biotechnology fields. Biological fluids generally contain high molecular weight macromolecules such as DNA and proteins, and this will undoubtedly result in non-Newtonian behaviour being observed (Husny and Cooper-White, 2006; Qiu *et al*., 2010). Stone *et al*. (2004) identified this as one of the major areas of interest in microfluidics research in the near future. More research, both experimental and numerical, is necessity in such areas due to the rheological effect and the breakup mechanism of non-Newtonian droplets.

Drop dynamics is governed by diverse forces includes surface tension and viscous forces, and the rheology of the fluid can be important when non-Newtonian fluids are involved (Chhabra and Richardson, 2008). As general rule, non-Newtonian fluids can be classified intro three groups, namely purely viscous fluids, time-dependent fluids, and viscoelastic fluids. Each above mentioned non-Newtonian fluid possess distinct characteristic of their own; however, there is no

single constitutive equation has been established to describe the rheogram of all such fluids. Understanding the dynamical mechanisms of microdroplets formation of non-Newtonian fluids in microfluidic channels is essential to ensure the droplets can be created based on droplet size, patterns, and productivity.

Previously, many research efforts have been devoted to the analysis of the dynamics and deformation of droplets with viscoelastic properties in this area (Husny and Cooper-White, 2006; Steinhaus and Shen, 2007; Arratia *et al*., 2009), yet a thorough understanding of relevant physics behind their creation for other non-Newtonian fluid types is still limited. Husny and Cooper-White (2006) investigated the polymeric droplet creation and breakup dynamics of low viscosity, elastic polyethylene oxide (PEO) fluids and Newtonian fluids by cross-flow shear employing a T-shaped configuration. From the analysis of the necking dynamics of the dispersed phase filaments, the pre-stretch and exponential self-thinning regions were found. In the pre-stretch region, a breakup drop was strongly accelerated away from the outlet channel by the cross-flowing fluid stretching the drop filament. A linear increase in the length of filaments and linear decrease in the radius of filament can be identified. These elongated filaments resulted in the appearance of smaller size of secondary drops depending on flow rates of continuous phase and the viscosity ratio. Steinhaus and Shen (2007) investigated the effects of fluid elasticity on the pinch-off dynamics of PEO-based Boger fluids in the presence of flowing silicone oil as continuous phase. They observed that higher molecular weight of PEO-based Boger fluids possess longer relaxation times and exhibit more dominant elastic effects, leading to larger extensional viscosities, longer thread lengths and longer pinch-off times. Arratia *et al*. (2009) investigated the effect of elastic stresses of polyacrylamide (PAA) fluids on filament thinning and droplet breakup in cross-slot microchannel. The results revealed that the filament of PAA fluids becomes

longer and the time for droplet breakup increases as the molecular weight of PAA is increased.

Apart from microdroplets formation with viscoelastic properties, there are a very few studies have focused on other non-Newtonian fluids with shear-dependent viscosity. Hong and Cooper-White (2009) investigated the impact of Carbopol dispersions, which exhibited shear-thinning, elastic and yield stress, on the pinch-off behaviour in silicone oil phase. The results revealed that the resultant droplet size increases with increasing viscosity ratio. With further increase the flow rate of continuous phase, smaller size of droplets is generated with increasing the viscosity ratio. Gu and Liow (2011) studied the formation of shear-thinning xanthan gum droplets in oil phase under different flow conditions. As the flow rate ratio increases, the resultant droplet size is significantly affected by changes in the xanthan gum concentration, increasing with higher concentration of xanthan gum solution.

Apart from empirical works, Sang *et al*. (2009) developed both numerical and analytical models with interface capturing scheme to explore the material behaviour effect of the Newtonian, Bingham, and power-law fluid on the formation of Newtonian droplets. Effects of the generalized power law coefficient, the power law exponent and the yield stress on the mechanism of drop breakup, final drop size and frequency of drop formation were studied. Droplet coalescence in Bingham fluids was observed in the transient period upon flow start-up. The effect of the yield stress term in the apparent viscosity affected the droplet shape, where a larger yield stress caused elongation of the droplets due to the plug-like velocity profile. Besides, Qiu *et al*. (2010) numerically investigated the droplet formation in shear thinning nature fluid under the cross-flow condition in a T-junction microchannel using the volume-of-fluid (VOF)

formulation. They found that the rheology of the bulk liquid flow greatly affected the droplet formation process and its size.

Most of the previous available studies, especially the numerical ones, have focused on the Newtonian droplets formed in the non-Newtonian phase; however, there have been far fewer attempts to develop a predictive model for the relevant physics, evolution and formation of droplets with non-Newtonian characteristics in a microfluidic cell.

2.5 Numerical Modelling Approaches

A numerical simulation approach to the problem provides a detail comprehensive description of the formation of droplet since a number of statistical information can be extracted from the numerical model. For majority of micro-devices Re <<1, the effects of volume-based inertia and gravity do not play as important role as in the macroscale. The surface-based interfacial tension and the viscosity become more significant and play in controlling flow behaviour of multiphase flow in microscale. Numerical simulation becomes a powerful tool used for prediction and understanding these underlying complex multiphase phenomena and the dynamics of a microfluidic system.

In multiphase flow, one of the greatest difficulties in the study of two immiscible fluid flows is handling the domain of interest contains an unknown interface separating the fluids involved and its evolution over time (Li and Renardy, 2000). The interface shape deforms continuously as two phases significantly affect each other as well as the boundary conditions. The interface moves from one location to another and may sometimes undergo severe deformations, including even breakup; the interface plays a major role in defining the system and must be determined as part of the solution (Liu and Nguyen, 2010). At each computational step, the fluid flow field and the structure evolve as a coupled

system, and the interaction forces are immediately accounted for and their resultant motions enforced in each step (Saha and Mitra, 2008).

2.5.1 Two-Phase Flow Simulation

Two phase flow is a term covering the motion of two different interacting fluids or with fluids that are in different phases. Figure 2.20 illustrate the dynamics of two immiscible incompressible fluids separated by an interface, Γ. The motion of each fluid of two phase flow is described by the incompressible Navier-Stokes equations. In microfluidics, a laminar flow is assumed at low enough Re.

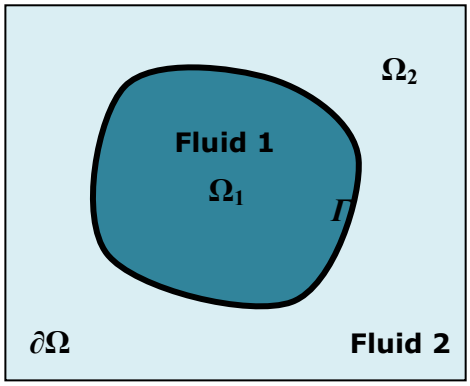


Figure 2.20: Schematic representative of a two-phase flow problem. Ω_1 denotes the region occupied by the first fluid; Ω_2 denotes the region occupied by the second fluid; Γ denotes the interface separates the two fluids that reside in region Ω_1 and Ω_2.

Limiting the discussion to two-phase flow, the two-phase modelling methods can be broadly classified into three categories: Eulerian method, Lagrangian method, and Combined Lagrangian-Eulerian method, based on how the interface is modelled. In Eulerian method (fixed-grid method), there is a predefined Cartesian grid that do not move with the interface. While in Lagrangian method (moving-grid method), an interface which is specified as a boundary between the two sub-domains of the grid is explicitly tracked by constructing a Lagrangian grid that is embedded in and moves with the interface. The interface then identifies, at the same order of approximation, with element boundaries. The governing equations are solved on this boundary fitted grid that moves in accordance with moving boundary. The moving boundary of separate flow

regions is constantly traced by deforming the elements. Moreover, the boundary is represented by continuously updated discretisation and remeshing. However, this method confronted with difficulties when the interfaces undergo large deformation. For geometrically complicated moving boundaries, this Lagrangian approach becomes computationally expensive and the numerical stability issues may encountered when the topology changes. In Combined Lagrangian-Eulerian method, the interface is tracked explicitly, while the actual computations are performed on fixed grid. These methods are specifically suitable for the problems involving moving rigid bodies with sharp and non-deformed interface. In addition to solving the incompressible Navier-Stokes equations, the representation of the interface is pointed out as the main aspects in the simulation of two-phase flow.

2.5.2 Numerical Models for Interface Representative

In microfluidic systems, interfaces between fluids play a significant role in many physical processes such as droplets collision, coalescence, and breakup (Christopher *et al*., 2009). In many applications, the geometry of the interface is usually complex and it can undergo large deformations or even topology changes such as the breakup and reconnection of bubbles. There are two approaches to represent the interface, Γ evolution problem either explicitly or implicitly to the NS equations discretised on a fixed grid: interface tracking and interface capturing. These methods are widely used in computation of flow problems with moving boundaries and interfaces.

Explicit Representative: Interface Tracking

Interface tracking the moving boundary is based on explicit description of the interface by the computational mesh. Interface tracking approaches requires the meshes that allowed tracking the evolving interfaces and these interface meshes are needed to be updated as the flow evolves for each time step. Boundary integral (Hou *et al*., 2001) and front tracking methods (Tryggvason *et al*., 2001)

are examples of the interface tracking methods. Interface tracking approaches provide great accuracy; however, their applicability is only valid for the limited physics of a Stokes flow.

Boundary integral methods discretised the points on interface and make it relatively efficient in locating interface. However, boundary integral method becomes difficult to implement when the interface undergoes merging, breaking and extreme topological changes (Hou *et al*., 2001). Front tracking methods are used to embed nodes or elements for representing the interface. The evolution of the interface in front tracking schemes is accomplished by Lagrangian advection of the nodes, making use of mesh nodes to follow the interfaces. The movement of interface has to be accounted for by adjusting the position of the nodes on the interface which means the nodes need to be redistributed for retaining accurate interface representations when interface is deformed by the flow. The adjustment of the inner mesh nodes is arbitrary while the movement of the interface nodes is prescribed. In addition, straight-forward implementations of tracking methods are prone to unphysical changes of the area or volume of the respective fluid (Tryggvason *et al*., 2001).

Implicit Representative: Interface Capturing

In contrast to interfacial tracking methods, interface motion can be simply obtained by the advection of the corresponding phase function in the interface capturing method. The interface capturing method uses a separate phase function discretised on the fixed grid to implicitly represent the interface (Bonometti and Magnaudat, 2007). In implicit approaches, there are three common interface capturing methods that have been developed to solve incompressible two-phase problems. These are the volume-of-fluid (VOF) (Rider and Kothe, 1998), level-set method (LSM) (Osher and Sethian, 1988), and

Lattice-Boltzmann method (LBM) (Takada *et al*., 2000). These approaches are computationally relatively simple and inherently able to deal transparently with the problems where the interface is subjected to severe motion, even topological changes can be considered. However, this flexible interface description provides challenges regarding mass conservation and the treatment of discontinuities across the interface.

The VOF method was first developed by Nichols and Hirt (1975) and more completely reported by Hirt and Nichols (1981). In the VOF methods, different fluid phases are defined on the fixed grid by the volume fraction of each fluid phase in a computational cell. The motion of the fluid-fluid interface is captured through the evolution of volume fraction. The main advantage of the VOF method is its superior volume conservation compared to any other fixed grid interface-tracking or volume-tracking methodology, because transport of the fluid phases is governed by a conservation equation for the phase indicator function. In addition, changes in interface topology are automatically dealt with. On the contrary, the solution of convection equation is not trivial as the volume fraction is a discontinuous function which varies abruptly across the interface. Thus, the main drawback of the VOF method is the complex extraction of interface topology as the volume fraction description only provides the ratio and not the distribution of fluid phases in a computational cell. In order to maintain the sharpness of the interface, geometric reconstruction is required to approximate the location of the interface. Therefore, the functional discontinuities of the VOF method present at the interface lead to low accuracy in the computation of the mean curvature, causing errors in the surface tension force.

Apart from the VOF method, the LBM, which is based on discrete equation derived from the well-known in kinetic theory Boltzmann equation, has become a

numerically robust and efficient technique for simulating multiphase fluids (Sankaranarayanan *et al*., 2002; Lee and Lin, 2005). Some popular LBM multiphase model, such as colour gradient, potential method, and free energy method, are recently proposed (Chen and Doolen, 1998; Zheng *et al*., 2006). The main drawback of these methods is the forcing term in LBM is not explicitly involved. In addition, the variation of surface tension has made difficulties in the application of LBM to this problem as this parameter cannot be adjusted independently of density ratio.

Nevertheless, the above mentioned limitations can be overcome by LSM as it allows any interfacial tension values to be chosen. The level-set method is a simple and versatile method for tracking moving interfaces and shapes. It permits numerical computations of such objects involving curves and surface to be performed on a fixed Cartesian grid without having to parameterize them. It is a robust scheme that is relatively easy to implement (Takada *et al*., 2000). Although the main drawback of classical LSM description is the difficulty of ensuring volume conserving advection of fluid phases, a conservative LSM has been devised to overcome this (Olsson and Kreiss, 2005; Olsson *et al*., 2007). A more comprehensive understanding of LSM is included in subsequent *Chapter 4*.

2.6 Summary

Microfluidic systems have been established as an alternate and versatile platform for microdroplets formation. In microfluidics system, all flow tends to be laminar where the viscous effects dominate the inertial effects. Incompressible Navier-Stokes equation represents the important momentum governing equations relating to physics of microfluidic dynamics that will be employed in present numerical modelling studies. This equation provides a mathematical model of the motion of laminar flow in micro- device. Fundamental principles and application of microfluidic systems were presented due to the selection and interpretation of

the subsequent numerical analysis will be based on these facts. A large number of experimental and numerical investigations on microdroplets formation process are mainly Newtonian in nature. However, most real fluids to lab-on-chip devices in industrial practice exhibit non-Newtonian behaviour. Hitherto, the emulsifying non-Newtonian solution in microfluidics in a controllable manner is still one of the most difficult and least understood emulsification problems. Most of the previously published works have been reported in the area of either experimental or numerical investigations on the effect of viscoelasticity and molecular weight on non-Newtonian droplet breakup process. Nevertheless, the experimental validation of a numerical predictive model for non-Newtonian fluids appears to be limited. Bridging the knowledge gap between the numerical and forthcoming experimental in this area is incredibly vital for non-Newtonian microdroplets formation in a microchannel network.

CHAPTER 3

Materials, Methods, and Experimental Techniques

3.1 Introduction

This chapter outlines the materials, methods, and experimental techniques used throughout the experimental work in this thesis. Prior to the numerical model setup, preliminary measurements such as fluid density, viscosity, interfacial tension, and contact angle were carried out. These parameters were used in the computation for the subsequent chapters. The measurement data of these physical properties for each Newtonian and non-Newtonian solution in two phase system were summarized in *Table 3.3*. The fabrication methods of T-junction microfluidic devices in one material, polydimethylsiloxane (PDMS) were also presented. The experimental model for the droplet formation in PDMS microchip was developed and outlined in detail, with an emphasis on the measurement of droplet diameter. This experimental model was used for the validation of the numerical model, which is presented in *Chapter 4*.

3.2 Material and Sample Preparation

Sodium carboxymethylcellulose is a typical non-Newtonian fluid that can be modelled as various types of non-Newtonian biological fluids such as blood, saliva, and mucus which are consistently met in many medical and biological systems due to their shear-thinning property. Sodium carboxymethylcellulose (CMC, $[C_6H_7O_2(OH)CH_2COONa]_n$, Sigma Aldrich) with a nominal molecular weight (MW) of 700,000 g/mol and a degree of substitution (DS) of 0.80-0.95 was selected as the key water-soluble polymer material in the present work. Without further purification, CMC stock solutions were prepared by dissolving CMC

powder sample in distilled water to obtain a concentration of 1.20wt% at room temperature (20 ± 2°C). Other working solutions (0.02wt% to 1.00wt%) used in the experiments were obtained by dilution. Additionally, the stock solution was stirred gently (600 rpm) for 48 hours in order to achieve complete hydration and avoiding air bubbles formation. The CMC stock solution was stored airtight in refrigerator at 4°C and used within one week. All working solutions were allowed to rest for 24 hours prior to being used due to their shear-sensitive behaviour. A fresh CMC stock solution was again prepared after a week.

3.3 Refractive Index Measurements

A calibration curve with concentration of CMC solutions ranging from 0.20wt% to 1.20wt% was constructed. Each sample solution was initially calibrated for concentration in terms of refractive index (RI). Figure 3.1 demonstrates the calibration curve of CMC aqueous solution.

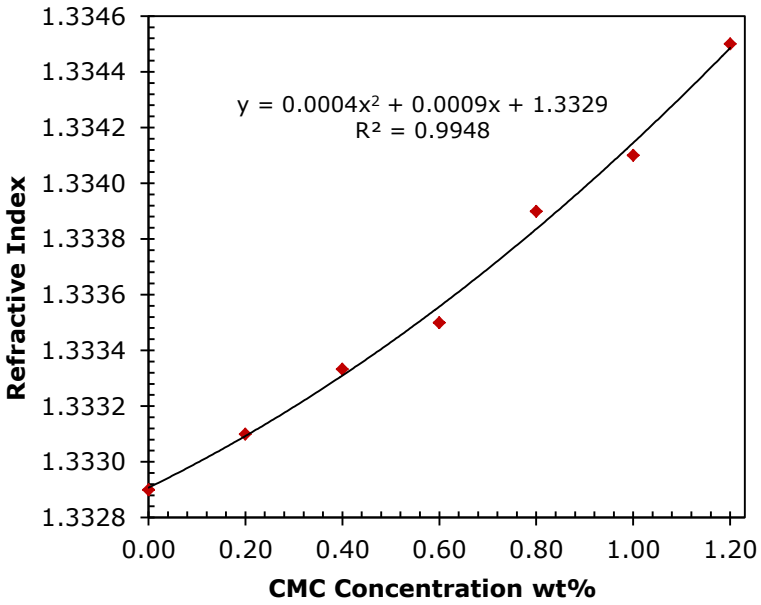


Figure 3.1: Calibration curve of sodium carboxymethylcellulose (CMC) solution.

The values of refractive index of each working solution were determined using a digital portable refractometer (Refracto 30PX) operating in the measurement range of 1.32 to 1.50 with the resolution of 0.0001. The refractive index of each

sample solution was measured using the angle of the total reflection and the known refractive index of air (n_{Air}=1.0). Since the refractive index depends on the temperature of measured sample solution as well as the wavelength of the light, the measurements were performed at the wavelength of the sodium D-line (λ_D=589.3nm) at room temperature of 20 ± 2°C.

3.4 Fluid Density Measurement

The density of each working solution was measured using a digital portable densitometer (Densito 30PX) operating in the measurement range of 0 to 2 g/cm^3 with the resolution of 0.0001 g/cm^3. Calibration and checks carried out on instrument using distilled water as a reference standard material before each density measurement.

3.5 Rheological Characterisation

3.5.1 Newtonian Fluid Viscosity Measurement

A calibrated BS/U-tube viscometer was used to perform the kinematic viscosity measurement for the transparent Newtonian liquid of distilled water and olive oil. The capillary diameter of BS/U-tube viscometer with 0.50 mm ± 0.01 mm was used. The specification for each size of BS/U tube viscometer is listed in Table 3.1. The viscometers were mounted upright in a beaker (2000 mL) of water at room temperature (20 ± 2°C). Each sample solutions were allowed to attain the water temperature for 10 minutes. The temperature was measured close to the capillary viscometer by a digital thermometer (ETI EcoTemp) with an accuracy of ±1°C. To determine the kinematic viscosity behaviour of sample solution, the flow time of sample solution with different concentrations was firstly measured by a thoroughly cleaned and dry viscometer. After the flow time of solution was measured, the sample solution was poured out and viscometer was rinsed completely with acetone (ACS reagent, ≥99.5%, 58.08 g/mol, 0.791 g/mL, CH3COCH$_3$, Sigma Aldrich) and dried in oven at 80°C. Having reset the

viscometer in the beaker of water after drying, the flow time of different concentration of solution were measured. All the viscosity measurements were conducted three times and the average values were taken for analysis. Equation 3.1 is used for determination of kinematic viscosity of working solution:

$$\nu = Ct \tag{3.1}$$

where ν is kinematic viscosity, C is nominal viscometer constant, and t is flow time. The dynamic viscosity of each concentration of solution was calculated using following equation:

$$\eta = \nu\rho \tag{3.2}$$

where η is dynamic viscosity, ν is kinematic viscosity, and ρ is fluid density.

Table 3.1: Standard specifications of BS/U Tube viscometer (ASTM International, 2012).

Size No.	Capillary Diameter (mm)	Nominal Viscometer Constant (mm^2/s)/s	Kinematic Viscosity Range (mm^2/s)
A	0.50	0.003	0.9 to 3
B	0.71	0.01	2 to 10
C	0.88	0.03	6 to 30
D	1.40	0.1	20 to100
E	2.00	0.3	60 to 300
F	2.50	1.0	200 to 1000
G	4.00	3.0	600 to 3000
H	6.10	10.0	2000 to 10000

3.5.2 Non-Newtonian Fluid Viscosity Measurement

All the rheological measurements were performed on controlled stress rheometer (MCR 302, Anton Paar) equipped with a cone-and-plate geometry (cone plate with diameter of 50 mm; angle 0.04 radian) at controlled temperature of 20^{o}C. The samples were carefully loaded onto the measuring plate of the rheometer and the measuring cone was lowered at a very slow speed in order to prevent the disruption of the solution structure. The samples were then left to rest for 10 minutes prior to the measurements. The normalized shear stress against normalized shear rate plot of CMC solutions at various concentrations has been plotted over a log-log scale that covers nearly six orders of magnitude of

normalized shear rate and is shown in Figure 3.2. All the measurement data were seen to be fitted well to the well-known Carreau-Yasuda model for all CMC concentration:

$$\frac{\eta - \eta_\infty}{\eta_o - \eta_\infty} = [1 + (\lambda_{CY}\dot{\gamma})^a]^{\frac{n-1}{a}} \tag{3.3}$$

Where η_o is zero shear viscosity, η_∞ is infinite shear viscosity, λ_{CY} is the relaxation time, $\dot{\gamma}$ is shear rate, *n* is power-law exponent for Carreau-Yasuda model and *a* is the fitting parameter.

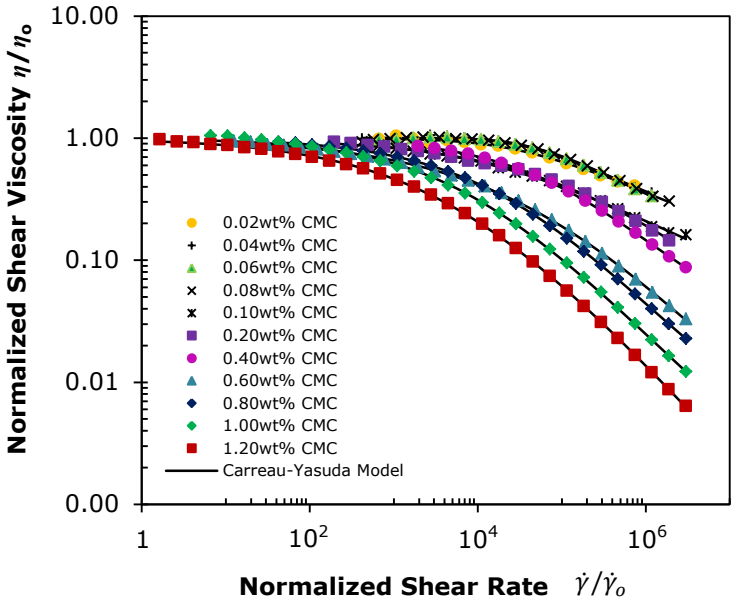


Figure 3.2: Normalized shear viscosity plotted against normalized shear rate for a series of CMC shear-thinning solutions with different concentrations.

Specific viscosity of CMC polymer in solution was measured according to the following equation:

$$\eta_{sp} = \frac{\eta_o - \eta_s}{\eta_s} \tag{3.4}$$

where η_o is zero shear viscosity and η_s is the solvent viscosity. The critical concentration of CMC polymer solution was measured using standard methods. Log-log plot of the specific viscosity versus the CMC concentration as shown in Figure 3.3 were analyzed to determine the concentration for the dilute and semi-dilute transitions at the intersection point of two straight lines from the plot. The

CMC polymer solution could be divided into two regions: dilute state and semi-dilute state according to the critical overlap concentration (see Figure 3.3):

- The CMC polymer solution with concentration less than C* (≈0.40wt%) was a totally dilute with only weak interactions being found in the solution. The increase in η_{sp} is attributable to the hydrodynamic interaction between the polymer coils behaving essentially as independent impermeable spheres (Sikorski, 2006).
- In the region of the concentration above C* (≈0.40wt%), the slope of the linear curve in semi-dilute regime appear to become steeper due to the development of entanglement coupling between the polymer molecular chains in the solution leading to the increased interaction between the molecules. All the polymer molecules in the solution effectively interpenetrate and become entangled as their total hydrodynamic volume appears greater than the solution volume, even without being stressed, so changing the solution behaviour from mainly viscous to mainly elastic with the viscosity (η_o at zero stress) is mainly governed by the mobility of the polymer molecules (Witten, 1998).

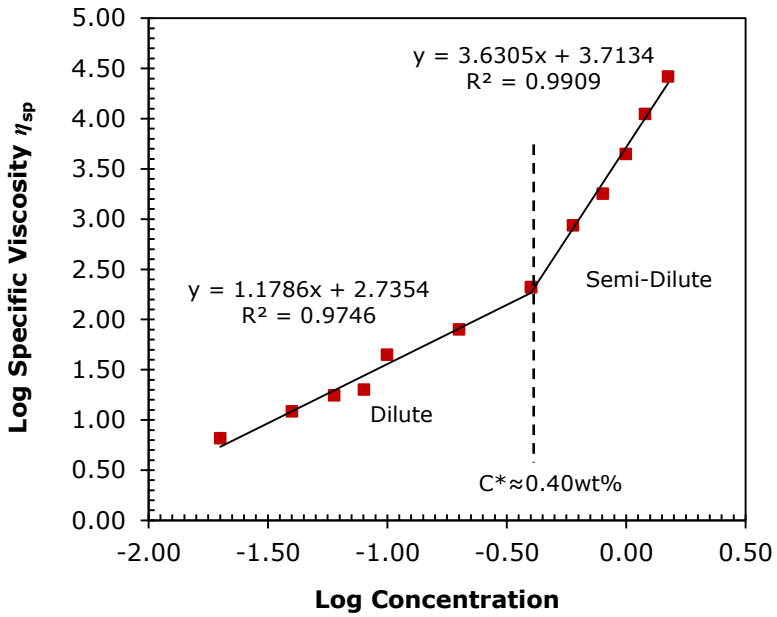


Figure 3.3: Log-log plot of specific viscosity versus the concentration of CMC shear-thinning solutions.

3.6 Surface and Interfacial Tension Measurement

Surface/interfacial tensions of each working solution were measured using pendant drop apparatus of which a schematic diagram is given in Figure 3.4. A maximum drop volume (11 to 15 µl) against the gravity that could be held at the tip of the needle was dispensed from a syringe with needle tip of size 20 gauge. The drop was then left to stabilize for 5 min in order to reach equilibrium before the images were captured using a high speed camera (MIC Hotshot 1280 cc). Images were analysed using MATLAB (R2012a, v7.12) to implement the correlations suggested by Misak (1968) (see Appendix A.4) to calculate the surface/interfacial tension of the sample drop in air-liquid or liquid-liquid system. All the surface/interfacial tension measurements were conducted in septuplicate and the average value were taken for analysis. The surface/interfacial tension by pendant drop method was explained according to the following equation (Misak, 1968; Arashiro and Demarquette, 1999; Drelich *et al*., 2002):

$$\sigma = \frac{\Delta\rho g {d_e}^2}{H_s} \tag{3.5}$$

where σ is the surface or interfacial tension, $\Delta\rho$ is the density difference between the fluid phases at the interface, g is the gravitational force, d_e is the equatorial diameter of the drop, and H_s is the shape dependent parameter.

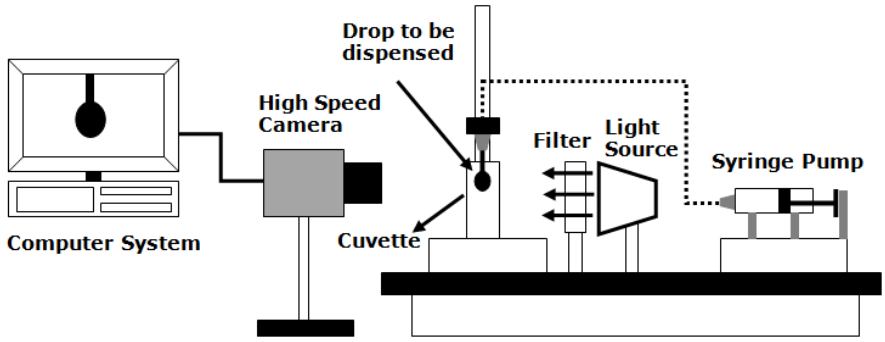


Figure 3.4: Schematic diagram of experimental setup for pendant drop analysis.

The shape dependent parameter (H_s) is related to the shape factor of the drop (S) which was defined as (Misak, 1968; Arashiro and Demarquette, 1999; Drelich *et al*., 2002):

$$S = \frac{d_s}{d_e} \tag{3.6}$$

where S is shape factor, d_s is drop diameter at a distance d_e from the apex of the drop, and d_e is equatorial diameter of drop. Figure 3.5 illustrates the details of pendant drop geometry.

Prior to the calculation of surface/interfacial tension, the values of $1/H_s$ are determined from the following equations based on the empirical constant (see Table 3.2) in a range of S value (Misak, 1968, Drelich *et al*., 2002):

$$\frac{1}{H_s} = \frac{B_4}{S^A} + B_3 S^3 - B_2 S^2 + B_1 S - B_0 \tag{3.7}$$

where$A$, B_0, B_1, B_2, B_3, and $B_4$are constant related to respective equations.

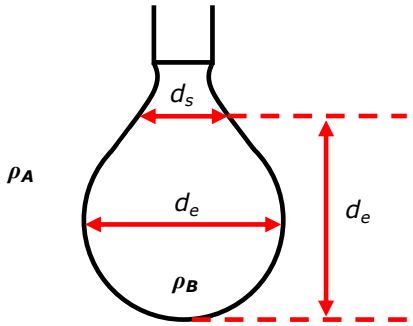


Figure 3.5: Definition of dimensions describing the pendant drop. The region occupied by first fluid phase and region occupied by second fluid phase are denoted as ρ_A and ρ_B, respectively.

Table 3.2: Empirical constants (Source: Misak, 1968).

***S* Range**	***A***	***B*$_4$**	***B*$_3$**	***B*$_2$**	***B*$_1$**	***B*$_0$**
0.401-0.46	2.56651	0.32720	0	0.97553	0.84059	0.18069
0.46-0.59	2.59725	0.31968	0	0.46898	0.50059	0.13261
0.59-0.68	2.62435	0.31522	0	0.11714	0.15756	0.05285
0.68-0.90	2.64267	0.31345	0	0.09155	0.14701	0.05877
0.90-1.00	2.84636	0.70715	-0.69116	-1.08315	-0.18341	0.20970

3.6.1 MATLAB Algorithm Development

An algorithm was developed for surface/interfacial tension measurement. It can locate the pendant drop and compute the surface tension with an adequate accuracy. Figure 3.6 illustrates an image profile of pendant drop analysis. Firstly, the images were organized uniformly and the colours of image were then inverted. The background of the image was estimated by minimization and interpolation for decreasing the illumination effect. Next, the region of interest was extracted to detect the edge of the drop using SOBEL method. This requires redistributing the intensity of the image colour to be binary. A contact point between the needle tip and drop was identified manually by user as a location where the polynomial-fit curve that matches the identified edge is needed. The shape factor, *S* was then determined by finding the length ratios (see Equation 3.7). Additional information such as density difference between two fluid phases and the needle tip diameter were manually entered by the user in order to calculate surface/interfacial tension using this algorithm.

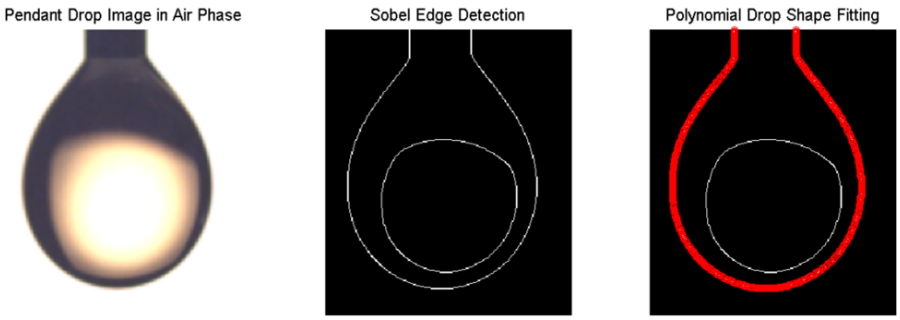


Figure 3.6: Image profile of pendant drop analysis.

3.7 Contact Angle Measurement

Contact angles of each solution between the two phases were measured using a sessile drop apparatus (see Figure 3.7). Contact angle measurement was performed by dispensing a sample drop (11 to 15 µl) from a syringe with needle tip of size 20 gauges on a clean and fresh polydimethylsiloxane (PDMS) surface in surrounding gas or liquid phase. Sample drop was then left on the substrate to stabilize for 5 min in order to reach equilibrium before the images were captured

by high speed camera (MIC Hotshot 1280 cc). The images of droplet formation were then collected and analysed using image processing tool by MATLAB (R2012a, v7.12) with generated code (see Appendix A.5) to measure the contact angle of sample drop on the substrate. All the contact angle measurements were conducted in septuplicate and the average value were taken for analysis.

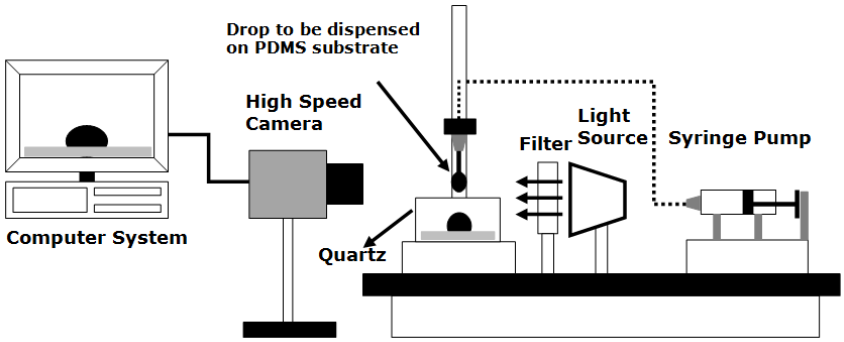


Figure 3.7: Schematic diagram of experimental setup for sessile drop analysis.

The contact angle measurement of sessile drop was explained according to the O'Brien's singular perturbation solution of Bashforth-Adams equation as shown below (Bashforth and Adams, 1883; Srinivasan *et al*., 2011):

Non-dimensional lateral coordinates, X

$$X = \varepsilon\left\{\sin\varphi - \frac{1}{2}(\pi-\varphi) + \frac{1}{2}(\pi-\varphi)\sqrt{1+\frac{8\varepsilon^2}{3(\pi-\varphi)^2}}\right\}$$

$$+\varepsilon^3\left\{\frac{1}{3}\cos^2\varphi\tan\frac{\varphi}{2} + \frac{2}{3(\pi-\varphi)}\right\} + O(\varepsilon^4) \qquad (3.8)$$

Non-dimensional vertical coordinates, Z

$$Z = \varepsilon\left\{1-\cos\varphi + (\frac{\pi-\varphi}{2})^2 - (\frac{\pi-\varphi}{2})^2\sqrt{1+\frac{8\varepsilon^2}{3(\pi-\varphi)^2}}\right\}$$

$$+\varepsilon^3\cdot\frac{1}{3}\left\{1+\cos\varphi-\cos^2\varphi+2\log\frac{\varepsilon}{2}+2\log\left[\sqrt{\frac{8}{3}+\frac{(\pi-\varphi)^2}{\varepsilon^2}}+\frac{\pi-\varphi}{\varepsilon}\right]\right.$$

$$\left.-2\log(\pi-\varphi)+2\log\left(\cos\frac{\varphi}{2}\right)\right\} + O(\varepsilon^4) \qquad (3.9)$$

where X ($=x/a_c$) is the non-dimensional lateral coordinate, Z ($=z/a_c$) is the non-dimensional vertical coordinate, ε ($=l_w/a_c$) is the maximum dimensionless half-

width of the drop, and φ is the angle subtended by the normal at certain point to the axis of revolution. An analytical profile of the sessile drop can be estimated from Equation 3.8 and 3.9. Thus, the apparent contact angle (θ^*=max(φ)) of investigated working solution was calculated by solving Equation 3.8 and 3.9 for φ numerically. The dimensionless sensitivity of the apparent contact angle to variations in the drop height is defined as:

$$\frac{\partial\theta^*}{\partial H} = \left\{ \frac{2\varepsilon^3}{3(\pi-\theta^*)} + \frac{4\varepsilon^3(\pi-\theta^*)}{8\varepsilon^2 + \left[3(\pi-\theta^*) - \sqrt{24\varepsilon^2 + 9(\pi-\theta^*)^2}\right](\pi-\theta^*)} \right\}$$
$$+ \varepsilon(\pi-\theta^*) + \varepsilon\sin\theta^* - \frac{\varepsilon^3}{3}\left[\sin\theta^* - \sin 2\theta^* + \tan\frac{\theta^*}{2}\right] \qquad (3.10)$$

where θ^* is the apparent contact angle and H ($=h_d/a_c$) is the dimensionless height of the drop at the three phase contact line. Figure 3.8 illustrates a schematic diagram of a sessile drop on a non-wetting substrate. The capillary length of the investigated working solution was used to non-dimensionalise the spatial coordinates and parameters as shown above:

$$a_c = \sqrt{\frac{\sigma_{LG}}{\rho g}} \qquad (3.11)$$

where σ_{LG} is the liquid-gas surface tension, ρ is the fluid density, and g is the gravitational acceleration.

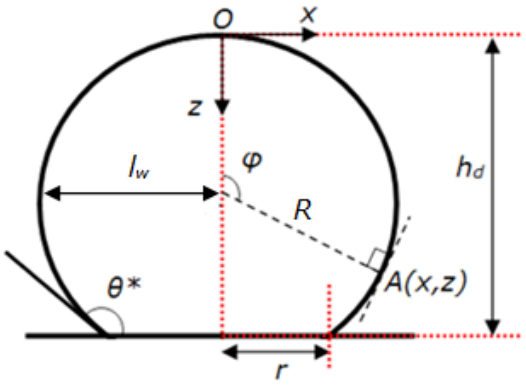


Figure 3.8: Definition of dimensions and coordinates describing the sessile drop. For a point $A(x,z)$ on the sessile drop profile, the lateral and vertical coordinate were denoted as x and z; respectively; φ is the angle subtended by the normal at point A to the axis of revolution; l_w is the maximum half-width of the drop; r is the radius of contact line; R is the radius of the drop; h_d is the height of the drop; and, θ^* (=max(φ)) is the contact angle of the drop at the three phase contact line. (Figure adapted from Srinivasan *et al*., 2011).

3.7.1 MATLAB Algorithm Development

An algorithm was developed to examine sessile drop image in order to deduce the contact angle. Figure 3.9 demonstrates the image profile of sessile drop on PDMS substrate. The algorithm can automatically locate the sessile drop and compute the contact angle with an adequate accuracy.

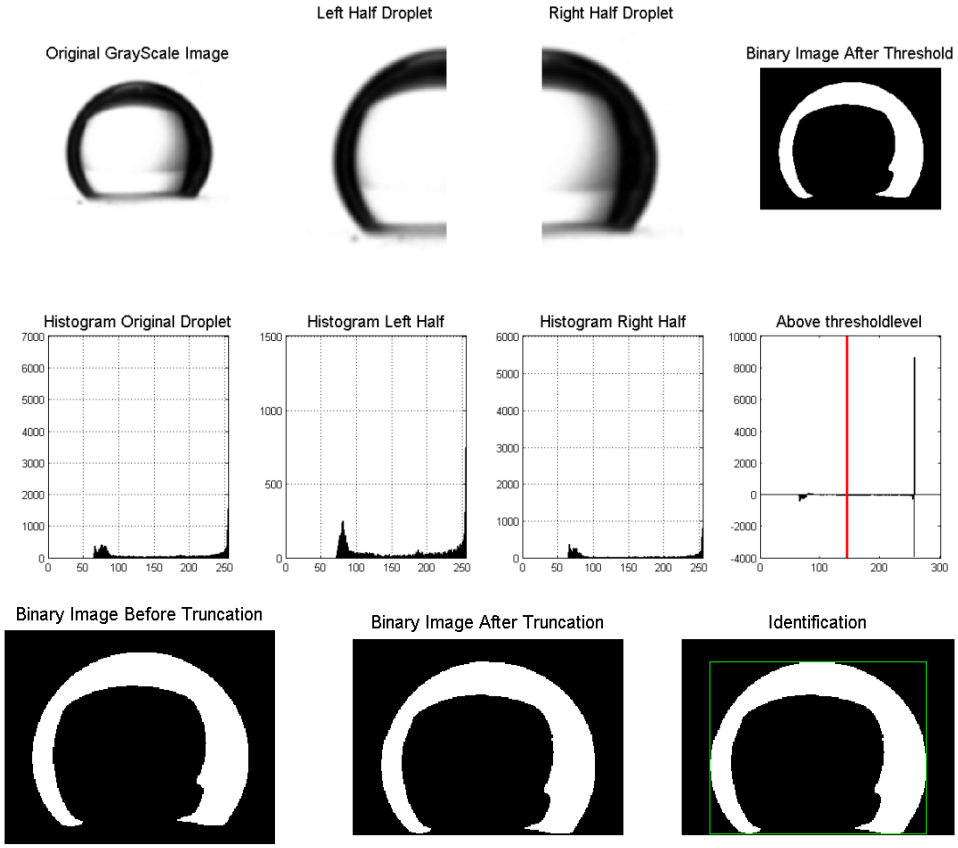


Figure 3.9: Image profile of sessile drop analysis.

Firstly, the images were organized sequentially, then the colours of the images were inverted, the background of the image estimated by minimization and interpolation for decreasing the illumination effect. Next, the images were adjusted by redistributing the intensity of colour within 0 to 1 ranges which to be represented in binary image. The value of 0 represented to droplet phase while value of 1 corresponds to the continuous phases. The edges are detected using appropriate threshold value via an automatic histogram threshold approach (see Appendix A.6).After obtaining this information, the left and right contact point

between the sessile drop and the substrate were identified manually by users as a location at the so-called tri-phase contact line. Once the contact points were determined, the image was truncated to the level of the substrate surface. Next, the drop image was rotated to make the substrate appear to be flat. Therefore, a binary image after truncation was then displayed (see Figure 3.9) and the apparent contact angle θ^* (=max(φ))was determined from the measurement of l_w and h_d by solving Equation 3.9 numerically using the 'fsolve' function from MATLAB optimization toolbox with a trust-region algorithm.

Table 3.3: Physical properties of distilled water and CMC solution with olive oil phase at room temperature (20 ± 2°C).

Solution	Density (kg/m^3)	Interfacial tension with olive oil (mN/m)	Contact angle (°)	Viscosity (kg/m.s) / Carreau-Yasuda Model Constant				
				η_o(kg/m.s)	η_∞(kg/m.s)	λ(s)	*n*	a
Olive oil	1090.9	-	-	0.06808 ± 0.01				
De-ionized water	998.2	20.74 ± 0.47	120.49 ± 9.19	0.00093 ± 0.01				
0.02wt% CMC	998.0	20.84 ± 3.04	125.73 ± 3.41	0.0070	0.0003	0.0400	0.7121	0.9653
0.04wt% CMC	998.1	21.70 ± 0.70	127.76 ± 4.30	0.0121	0.0000	0.0325	0.7102	1.6980
0.06wt% CMC	998.1	21.26 ± 0.78	127.57 ± 1.90	0.0171	0.0000	0.0256	0.6775	1.3728
0.08wt% CMC	998.3	22.14 ± 0.87	131.57 ± 2.31	0.0195	0.0028	0.0143	0.4886	1.1319
0.10wt% CMC	998.2	21.57 ± 0.87	132.00 ± 7.00	0.0420	0.0007	0.0572	0.6242	0.4734
0.20wt% CMC	999.1	20.64 ± 1.75	120.25 ± 4.46	0.0742	0.0006	0.0041	0.3528	0.3856
0.40wt% CMC	1000.1	18.87 ± 0.90	126.45 ± 7.10	0.1946	0.0040	0.0138	0.3157	0.5534
0.60wt% CMC	1000.9	16.84 ± 0.84	121.21 ± 1.57	0.7995	0.0022	0.0147	0.1995	0.3660
0.80wt% CMC	1001.7	18.90 ± 0.68	124.41 ± 2.87	1.6469	0.0057	0.0515	0.2444	0.4782
1.00wt% CMC	1002.6	18.93 ± 0.97	123.29 ± 3.80	4.1143	0.0031	0.1604	0.2869	0.5000
1.20wt% CMC	1003.3	19.41 ± 1.17	121.42 ± 7.38	10.2644	0.0000	0.2069	0.2297	0.4175

3.8 PDMS Microfluidic Devices Fabrication

A channel dimension of 221 µm (w_c) × 90 µm (w_d) × 73.5 µm (h) used in present studies was fabricated in-house by photolithography and soft lithography technique. These techniques have been discussed in the following sections (see section 3.8.1). Figure 3.10 illustrates the dimensions of a T-junction employed in the subsequent numerical and experimental studies. Prior to the start of fabrication process, an out sourced positive photolithographic mask (clear lines with a black background) was used for transfer of the photo-lithographically pattern onto the negative mould (see Figure 3.11). The photolithographic mask with the desired layout of microchannel structure was designed using standard computer assisted design (CAD) program (AutoCAD 2012). Besides, the SEM image of fabricated T-junction PDMS microchannel is illustrated in Figure 3.12.

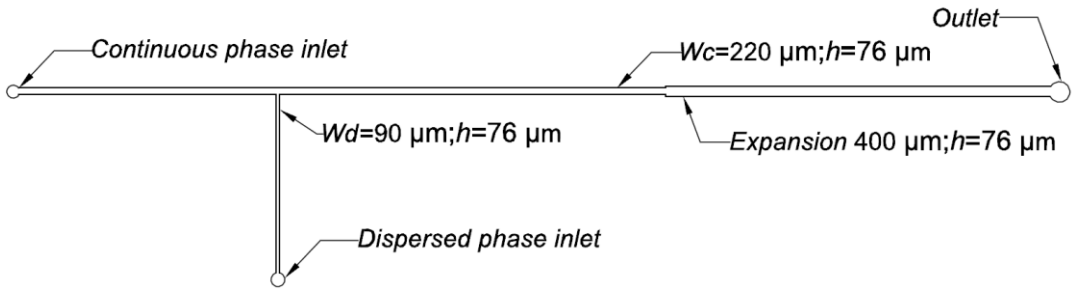
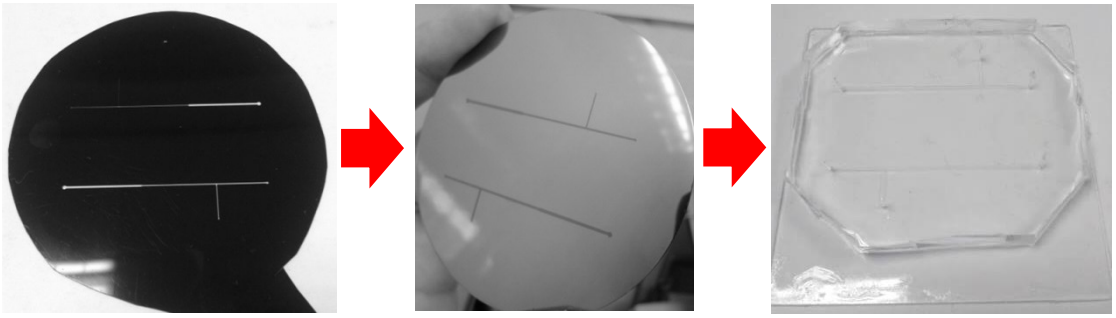
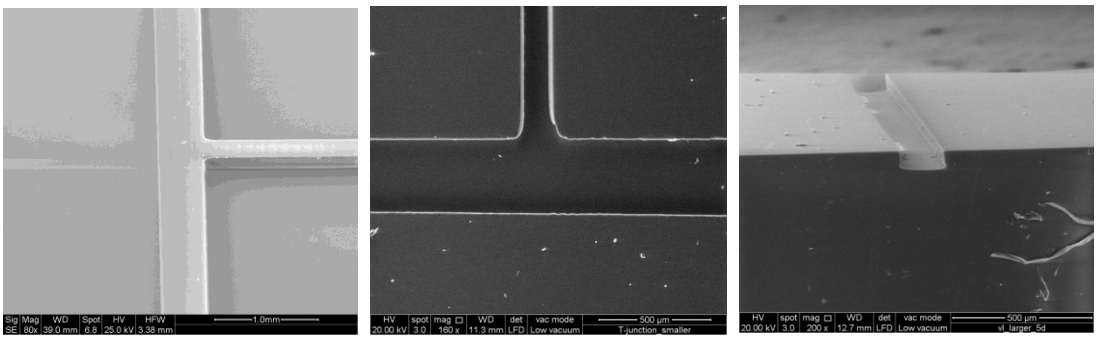


Figure 3.10: Schematic diagram of microfluidics T-junction composed of rectangular channel.



(a) Positive Photomask (b) SU-8 Mould (c) PDMS Microchip

Figure 3.11: Illustration of microfluidics T-junction composed of rectangular channels.



(a) (b) (c)

Figure 3.12: Scanning electron microscope (SEM) image of fabricated T-junction of the (a) SU-8 photoresist and (b) PDMS microchannel and the (c) cross section of PDMS microchannel (Reproduced with permission from Loizou *et al*., 2013).

3.8.1 Photolithography

A 63.5 mm p-type silicon (Si) wafer (Siltronix, France) was immersed in a concentrated sulphuric acid mixture with a H_2SO_4/H_2O_2 ratio of 3:1 (v/v) to clean any contaminations from the surfaces of the substrate. The wafer was subsequently rinsed thoroughly with distilled water and the residual water removed using compressed air and a dehydration bake at 200°C for 1 hour using a ceramic-topped hot plate. Before application of a polymer negative tone photoresist SU8-2025 (MicroChem Corporation, Newton, MA), the wafer was allowed to cool down to room temperature (20°C± 2^{o}C).

After pre-treating the Si wafer, SU8-2025 was prepared by a conventional spin-coating process in a spin coater (SCS P6700, United Kingdom). A volume 2.5 ml of SU8-2025 was poured onto the Si wafer and distributed across the wafer using the following spin cycle: spin to 500 rpm for 5 seconds with an acceleration ramp of 100 rpm/s, followed by 10 seconds at 500 rpm, followed by a spinning cycle at 1000 rpm for 4 seconds with acceleration ramp of 300 rpm/s and a hold for 15 seconds at 1000 rpm, respectively. After the spinning cycle, a SU8 film on the Si wafer was created. The Si wafer was then soft baked at 65°C

for 3 minutes and 95°C for 9 minutes on a ceramic-topped hot plate to evaporate the solvent and densify the polymer photoresist film.

After pre-baking, a few drops of glycerol were applied onto the film before the photolithographic mask was laid on the SU8-50 film and the pattern transferred by contact lithography. SU8-50 film was exposed to 564.6 mJ/cm^2 of ultraviolet (UV) energy at a wavelength of 365 nm for 3 minutes in a homemade UV box using a Vilber Lourmat UV Lamp (VL-215.L, France). Next, a post exposure bake (PEB) was conducted at 65°C for 2 minutes and 95°C for 7 minutes on the contact hot plate to selectively further cross link the exposed portion of the photoresist film. The SU8 2025 photoresist was finally developed in propylene glycol mono methyl ether acetate (PGMEA) solution (MicroChem Corporation, Newton, MA) with gentle agitation to remove the non-cross linked SU8 until a clear pattern of cross-linked SU-8 emerged. Following development, the SU8 master was rinsed with isopropyl alcohol (IPA) followed by distilled water and blow dried with a compress air gun. A hard bake could be conducted optionally at 200°C for 5 minutes on the hot plate to further increase the rigidity of the SU8 film. At last, SU-8 mould was placed in Petri dish and left for overnight before soft-lithography was conducted.

3.8.2 Soft-Lithography

The PDMS microfluidic device was fabricated by moulding a mixture of PDMS liquid pre-polymer onto the SU-8 mould. Sylgard 184 Silicone Elastomer (Dow Corning, USA) and Sylgard 184 curing agent (Dow Corning, USA) were mixed in a ratio of 10 parts base to 1 part curing agent (w/w) and then were poured over the SU8 mould wafer and degassed for 1 hour. Once the PDMS was completely degassed, the PDMS was cured on a ceramic-topped hot plate for 1 hour and 45 minutes at 65°C. After curing, the patterned PDMS was peeled off carefully from the SU8 mould. Holes into which the interconnecting poly-(tetrafluoroethylene)

(PTFE) tubing was inserted were created by using blunt tip needle with size of 20 gauges.

A glass slide was spin coated with a 10-50 µm thin layer of PDMS mixture and was placed in oven to cure for 15 minutes at 80°C. The glass slide with PDMS thin layer and the surface of the PDMS mould with the micropattern indent then brought into conformal contact and cured at 80°C for 2 hours to complete the irreversible sealing. PDSM microchannel was placed in Petri dish and left for overnight before flow experiment was conducted. Figure 3.13 demonstrates a flow chart of microfabrication process consist of photolithography and soft lithography process.

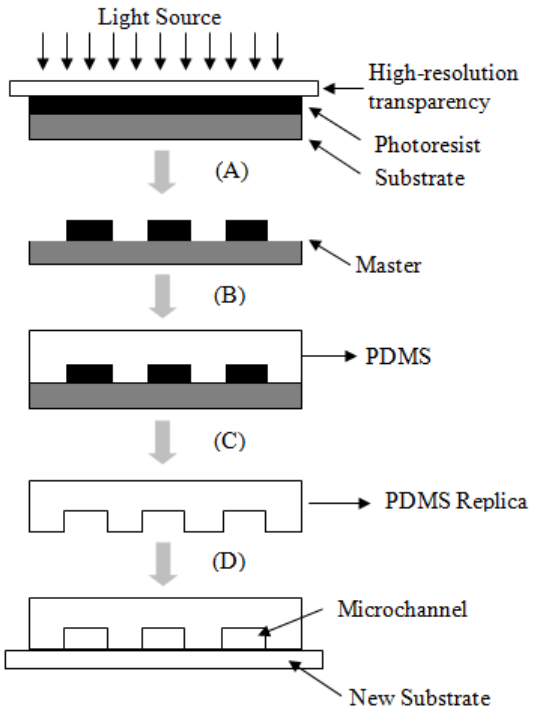


Figure 3.13: Schematic diagram of photolithography and soft lithography process. (A) A transparency photo-mask was laid on SU-8 film for the generation of master by photolithography process. A master consists of a positive relief of photoresist was used as a mould for PDMS replica moulding (REM) process. (B) A PDMS pre-polymer mixture was poured over the master and cured for 1 hour and 45 minutes at 65°C. (C), (D) The PDMS replica was peeled from the master and sealed to a glass slide to enclose the channels.

3.9 Droplet Formation Experimental Setup

The continuous and dispersed phase liquids were dispensed separately into the reservoirs of microchannel; each fluid was driven through microchannel at the desired continuous (Q_c) and dispersed flow rates (Q_d) using a separate syringe pump (AL-1000, Florida and NE-1000, Netherlands). The processes before and after droplet formation in microchannel were recorded using a high speed camera (MIC Hotshot 1280 cc) connected to an epifluorescence microscope (Olympus IX51, Japan). After allowing the system to reach steady state for predetermined time intervals (20 minutes), videos were recorded at 500 frames per second (fps) after each flow rates of either continuous or dispersed phase were adjusted. The average effective droplet diameter of 30 droplets (see section 3.9.1) under experimental condition was measured through an image processing routine using MATLAB (see section 3.9.2). Figure 3.14 illustrates the observation of droplet break-up process in the microchannel under the microscope.

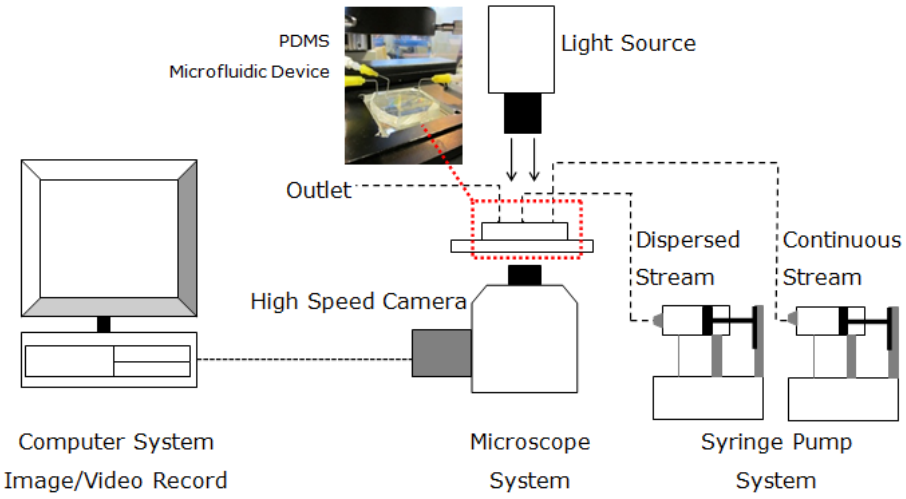


Figure 3.14: Schematic diagram of experimental setup for flow experiments.

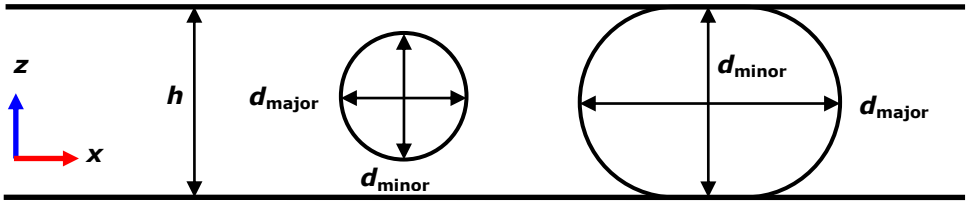
3.9.1 Effective Droplet Diameter Measurement

Each droplet size can be tuned by adjusting the flow rate of continuous phase and dispersed phase in microchannel. Since the formed droplets/plugs are almost always confined by channel walls and their interfaces may depart

significantly from a spherical shape, the droplet/plug size can be characterized using the major and minor droplet diameters. Major droplet diameter (d_{major}) denotes the longest dimension of the projected area of droplet/plug whereas the minor droplet diameter (d_{minor}) indicates the shortest dimension of the projected area of droplet/plug (see Figure 3.15). Apart from measuring d_{major} and d_{minor}, the effective droplet diameter (d_{eff}) denotes the diameter of a spherical droplet with the equivalent area as the formed droplets/plugs was used to determine the droplet size according to the following equation:

$$d_{eff} = 2\sqrt{\frac{1}{\pi} A_{eff}} \qquad (3.12)$$

where A_{eff} is the projected area of a spherical droplet.



(a) Droplet (b) Plug

Figure 3.15: Schematic diagram of the shape of confined droplets and plugs in microchannel. The depth of the microchannel was denoted as *h*.

3.9.2 MATLAB Algorithm Development

The droplet sizes in the experiment were measured by counting pixels using MATLAB software with the generated code function (see Appendix A.7)in images with displaying in a pixel screen of 1280 x 1024 grabbed from the microscope camera. Image processing is used to label the droplets on the photograph. An algorithm was developed for droplet counting and sizing with the capability of distinguishing droplets in microchannel from a large quantity of data. Consequently, the droplets can be automatically traced and the size of droplet can be computed with an adequate accuracy. Figure 3.16 demonstrates the profile of droplet size measurement. Firstly, the images were organized sequentially, then the colours of image were inverted, the background of the image estimated by minimization and interpolation for decreasing the

illumination effect. Next, the images were adjusted by redistributing the intensity of colour within 0 to 1 ranges which to be represented in binary image. The value of 0 represented to droplet phase while value of 1 corresponds to the continuous phases. The edges are detected using appropriate threshold value via an automatic histogram threshold approach (see Figure 3.16a, Appendix A.6), the unconnected droplets are fixed, and the gaps were filled. At last, the image was then cleaned from noises and was labelled in order to obtain the statistical properties from labelled image (see Figure 3.16b).

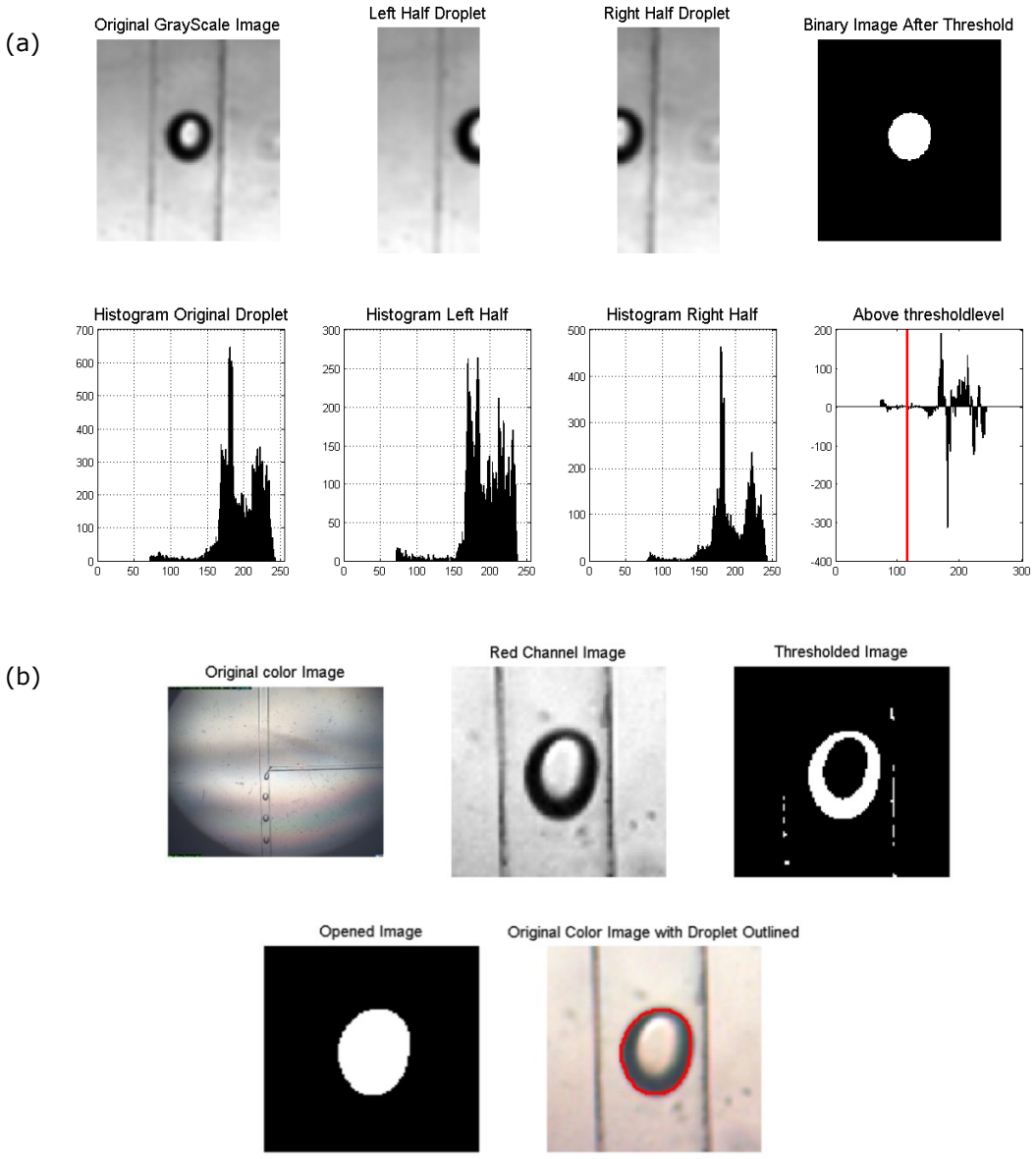


Figure 3.16: Image profile of (a) histogram threshold approach and (b) droplet size analysis.

3.10 Summary

In order to enable a more robust modelling assessment for the subsequent studies, laboratory experiments and physical properties measurements were conducted. The procedures and analysis of present experimental model required in the shear-thinning non-Newtonian/Newtonian system for microdroplets formation process were summarized in this chapter.

Prior to the start of the laboratory experiments, water-soluble polymer sodium carboxymethylcellulose (CMC), which exhibits non-Newtonian behaviour, with the concentration ranging from 0.02wt% to 1.20wt% were prepared. For an initial assessment of the calibration function, standards with seven different concentrations, including a blank as reference, were prepared for refractive index measurement. The values of refractive index were taken for the preparation of standard curve. Consequently, future preparations of the respective working solutions do not need to be verified. Next, the rheological properties and density of each working solutions were examined. Steady shear flow rheological measurements were performed using rheometer to characterise the behaviour of non-Newtonian liquids used in present studies.

Various operating parameters such as surface/interfacial tension and contact angle of each working solution between two phases were measured using the conventional pendant drop and sessile drop apparatus which were developed in our microfluidics laboratory. The images of pendant and sessile drop were captured using high speed camera and analysed with the application of MATLAB as a method of image processing analysis to perform automated analysis of image data. Image processing analysis involves the conversion of image data into quantitative information. Once the image processing routine is devised, it can be applied to a large number of microscopy images, facilitating the collection of large amounts of data for statistical analysis.

Owing to the low cost and easy handling of PDMS, PDMS becomes a primary material for the manufacturing of microfluidic device. This microdroplets generator was fabricated in-house via photolithography and soft lithography methods. Additionally, PDMS is by far dominant soft polymeric material utilized in academic and industrial research groups in microfluidics community due to its numerous salient features. For microdroplets formation in PDMS microchannel network, continuous and dispersed phase systems were employed. With olive oil as continuous phase and shear-thinning CMC solution as dispersed phase, CMC droplets were generated in the continuous phase flow. Various phenomena of droplet generation process in microchannel were captured to obtain qualitative information via image processing analysis. The size of the droplets in relation to the flow speed and channel size were then analyzed.

Last but not least, all these above sets of the values of operating parameters were eventually used in the computations to access the validity of the numerical model.

CHAPTER 4

Numerical Studies and Experimental Model Justification

4.1 Introduction

Since the start of micro total analysis system (μTAS), the manipulation of droplets in confined microfluidic channels has been highlighted as a useful technology platform for a broad range of application in many scientific fields such as biology, biomedical studies, chemistry, and synthesis and drug discovery. While much research effort has been devoted to the analysis of the dynamics and deformation of droplet in this area, there have been far fewer attempts to develop and validate predictive modelling for the microdroplets formation processes. This chapter describes a combined numerical and experimental effort to explain and develop a model for predicting the effect of different parameters on droplet generation. This objective is motivated by the need for a highly reliable numerical method and model that can forecast the performance of a module in terms of droplet size and frequency, as well as the functionality of the entire system. This will lead to a better understanding of the droplet generation process and relevant phenomena.

Interface capturing is a hot topic in current multiphase flow techniques used to model a multiphase flow and capture the position and motion of interfaces. Interface capturing techniques are typically used for free-surface and two-fluid interface flows. These techniques are formulated typically, over non-moving meshes, by using both the flow equations and the time-dependent advection equation that governs the evolution of an interface function, which marks the location of the interface. In the present work, the COMSOL computational fluid

dynamic (CFD) code was selected as the numerical backbone for solving the steady incompressible Navier-Stokes equation and evolution of droplet interface. The two-phase conservative level-set method (LSM) was chosen as a potential interface capturing scheme for analysing the interfacial phenomena including insight into the mechanism of non-Newtonian droplet formation in microchannel network. In order to establish that this simulation method provides qualitative information, visualization experiments were carried out and these laboratory experimental data were used to validate the simulation results. If a comparison of experimental data and numerical model results shows that the results produced by the model are close to those obtained from the experimental system, then the implemented numerical model is assumed to be reasonable with respect to the real system and a valid representation of the experimental system.

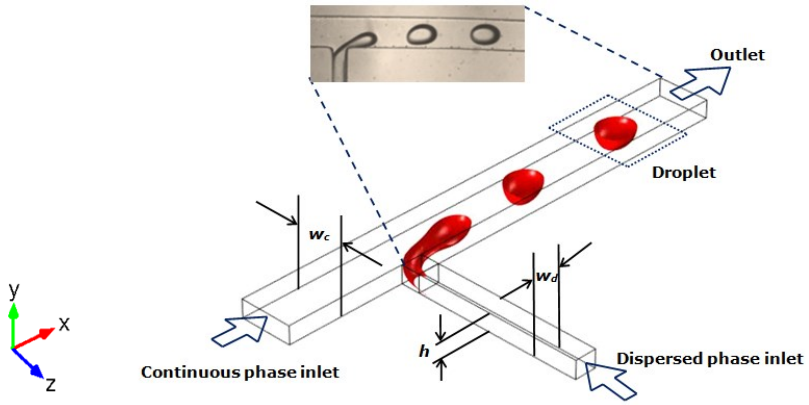


Figure 4.1: Schematic diagram of microfluidics T-junction composed of rectangular channel. The width of the continuous-phase and dispersed phase inlet channel are denoted as w_c and w_d, respectively; while the depth of the microchannel is denoted as h.

In preliminary stage, a two-dimensional (2D) numerical predictive model with the conservative LSM was developed using a Newtonian/Newtonian system. The processes of droplet generation was preliminarily investigated using deionised water as the dispersed phase and olive oil as the continuous phase in microfluidic device with a T-shaped geometry of aspect ratio 2:1 (221 μm width of continuous phase channel: 90 μm width of dispersed phase channel). The

proposed dimension of the T-junction microchannel was created based on the dimension of PDMS polymeric microfluidics which was fabricated in-house via soft-lithography technique. Figure 4.1 illustrates the schematic diagram of a microfluidics T-junction. As the predictive model is devised, the numerical model was later incorporated with a non-Newtonian stress model together with front-capturing scheme.

4.2 CFD Modelling and Simulation: Conservative Level-Set Method

The Level set Method (LSM) was initially developed in 1988 by Osher and Sethian (1988). It is a class of numerical techniques that deal with the motion of fluid interfaces. LSM rely on an implicit representation of the interface and the equation of motion is numerically approximated using schemes built from hyperbolic-conservation laws. LSM are particularly designed for problems in which the topology of the evolving interface changes during the course of events and for problems in which sharp corners and cusps are present. Classically, the LSM is defined as signed distance function. The basic idea behind this method is to consider a smooth continuous scalar function ϕ. The interface between two fluids is considered to be sharp and characterized by the zero contour of the level set function where ϕ>0 on one side of the interface and ϕ<0 on the other. The level set function ϕ is initialized as the signed minimum distance function to the interface, so $|\nabla\phi|$=1 on the whole domain. When solving the reinitialisation equation, $|\nabla\phi|$=1 is valid at the interface. In the case of an arbitrary initial interface, the reinitialisation equation needs to be solved at the beginning of the calculation to ensure that the level set function is a signed distance from the interface. When the interface is advected by a given external velocity field, $\mathbf{u}=(u_x,u_y)$, the evolution of the level set function corresponding to the interface motion is given by the following convection equation:

$$\frac{\partial\phi}{\partial t}+\mathbf{u}\cdot\nabla\phi=0 \tag{4.1}$$

where *t* is the real time. The convection equation only needs to be solved locally near the interface. If the flow is incompressible the velocity field will be divergence free, $\nabla \cdot \mathbf{u}=0$. The convection equation can be written as:

$$\frac{\partial \phi}{\partial t} + \nabla \cdot (\mathbf{u}\phi) = 0 \tag{4.2}$$

Equation 4.2 corresponds to a continuity equation for the level set function. The level set function is positive in one phase and negative in the other. In two phases, a Heaviside function is used to represent the density and viscosity of fluids:

$$H(\phi) = \begin{cases} 0, \phi < 0 \\ 1, \phi > 0 \end{cases} \tag{4.3}$$

where the level set function can be defined as signed distance function from the interface:

$$|\phi(x)| = d(x) = \min_{r_\Gamma \in \Gamma}(|x - x_\Gamma|), x \in \Omega \tag{4.4}$$

where *r* and r_Γ are a given point in the domain and the interface, respectively.

In numerical simulations, the step or Heaviside function (Equation 4.3) has isolated points of discontinuity where the forcing function jumps from one value to another value abruptly (see Figure 4.2a) and this abrupt jump will lead to numerical instabilities in the Finite Element Method (FEM). This also denotes that the area bounded by the zero level set is not conserved (Olsson and Kreiss, 2005). Consequently, a smeared out approach is used where the discretisation of the Heaviside function can be useful as it is better suited to numerical computations (Deshpande and Zimmerman, 2006):

$$H_{sm}(\phi) = \begin{cases} 0, & if\ \phi < -\varepsilon_\Gamma \\ \frac{1}{2} + \frac{\phi}{2\varepsilon_\Gamma} + \frac{1}{2\pi}\sin(\frac{\pi\phi}{\varepsilon_\Gamma}), & if -\varepsilon_\Gamma \le \phi \le \varepsilon_\Gamma \\ 1, & if\ \phi > \varepsilon_\Gamma \end{cases} \tag{4.5}$$

where ε_Γ corresponds to half the thickness of the interface.

Consequently, a new level set function can be expressed as:

$$\tilde{\phi}(x,t) = H_{sm}(\phi(x,t)) \tag{4.6}$$

The discontinuity of original Heaviside function is smeared out to a thickness proportional to ε_Γ in $H_{sm}(\phi)$. For instance, the smeared out Heaviside function with a transition zone with the size of 1 is shown in Figure 4.2b.

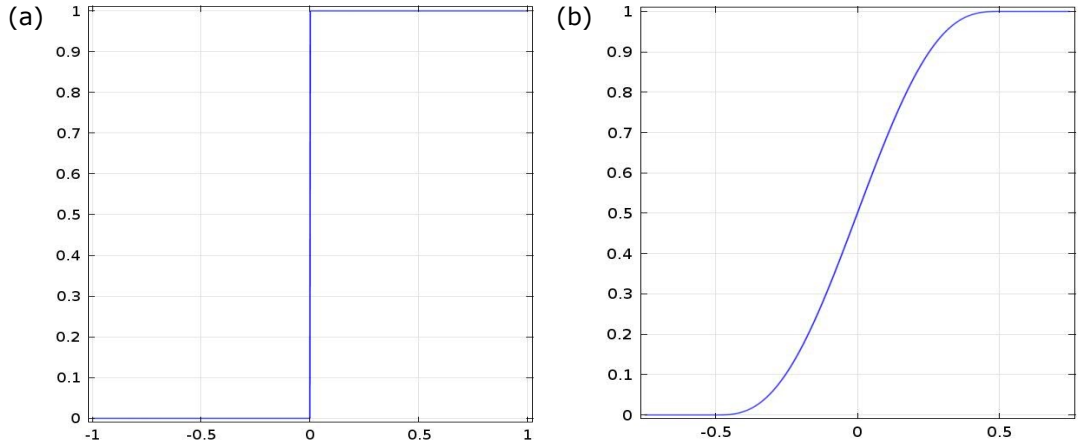


Figure 4.2: Plot of the (a) Heaviside function and (b) smeared out Heaviside function.

As previously mentioned, in standard LSM, the ϕ is a signed distance function which is smooth and continuous across the interface. Hence, the curvature of interface can be computed with high-order accuracy. However, this conventional method generally suffers from an excessive amount of mass loss or gain. As time evolves, these negligibly small errors will typically accumulate to a large value. To overcome this drawback, the advection step of ϕ including reinitialization step, which are formulated in conservative manner, are used to preserve the smooth nature of the signed distance function. In present study, a conservative LSM that was proposed by Olsson and Kreiss (2005) was adopted. It possesses a high-order accuracy and good mass conservation. In present work, this approach has been used to describe the interface between two immiscible fluids which is implicitly defined by the 0.5 contour of the new level set function, for instance, $\tilde{\phi}(x,t)$, where x denotes the coordinates of a point within that space at a time *t*. This function is given by values on an Eulerian grid. By using this

conservative numerical method, the area bounded by the sharp interface $\tilde{\phi}$= 0.5, $A_{\tilde{\phi}=0.5}$ can be conserved exactly since $A_{\tilde{\phi}=0.5} \approx \int_{\Omega} \tilde{\phi} dx$, with Ω being the domain of interest (Olsson and Kreiss, 2005). Figure 4.3 illustrates the model of the T-shaped junction in this simulation with tracking of the location of the droplet interface. The main channel is filled with the continuous phase ($\tilde{\phi}$=0) and the dispersed phase ($\tilde{\phi}$=1) is placed in the lateral channel.

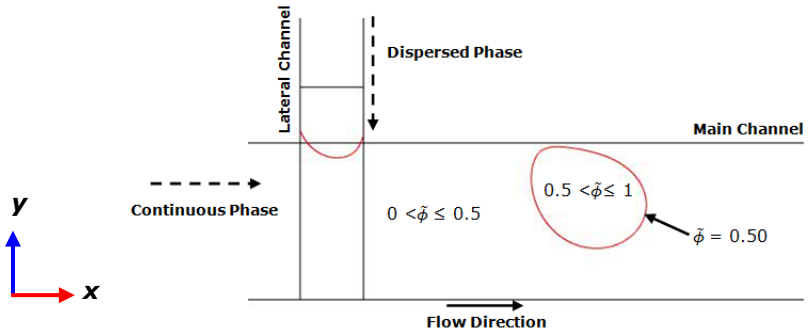


Figure 4.3: Contour representation of interface location for a droplet formed in a model of the T-shaped in this simulation.

The new level set function in equation 4.6 is used to smooth the fluid properties of density and the dynamic viscosity across the interface. These are calculated from the equation as follows:

$$\rho(x,t) = \rho_c + (\rho_c - \rho_d)\tilde{\phi} \tag{4.7}$$

$$\eta(x,t) = \eta_c + (\eta_c - \eta_d)\tilde{\phi} \tag{4.8}$$

where ρ_c and ρ_d denotes density of continuous and dispersed phase, in addition, η_c and η_d denote the dynamic viscosity of the continuous and dispersed phase, respectively. In simulating two-phase flows, the interface normal vector and interface curvature are two quantities needed for modelling surface tension. They can be computed from the gradient (Equation 4.9) and the divergence of the gradient of the unit normal vector to the front (Equation 4.10):

$$\mathbf{n}_\Gamma = \frac{\nabla\phi}{|\nabla\phi|} \tag{4.9}$$

$$k = \nabla \cdot \mathbf{n}_\Gamma \tag{4.10}$$

where $\mathbf{n}_\Gamma$ is the unit normal vector to the interface pointing into the droplet and k is the local interfacial curvature. In order to keep the thickness of the interface constant in the numerical simulation, an artificial compression is added and implemented by solving the conservation law of the form:

$$\frac{\partial \phi}{\partial \tau_a} + \nabla \cdot \mathbf{f}(\phi) = 0 \tag{4.11}$$

where τ_a denotes artificial time and $\mathbf{f}$ corresponds to the compressive flux. This artificial compressive flux acts in the regions where $0<\phi<1$ and in the normal direction of the interface. In the normal direction of the interface, the artificial compression flux is therefore defined as:

$$\mathbf{f} = \phi(1-\phi)\mathbf{n}_\Gamma = \phi(1-\phi)\frac{\nabla \phi}{|\nabla \phi|} \tag{4.12}$$

To avoid discontinuities at the interface, equation 4.11 is modified by adding a small amount of viscosity or diffusion:

$$\frac{\partial \phi}{\partial \tau_a} + \nabla \cdot \mathbf{f}(\phi) = \varepsilon_\Gamma \nabla^2 \phi \tag{4.13}$$

where ε_Γ is the artificial viscosity. Equation 4.1 and 4.13 can be combined into one equation, with the artificial time set equal to the real time. Thus, the resulting equation is modified as:

$$\frac{\partial \phi}{\partial t} + \nabla \cdot (\mathbf{u}\phi) = \varepsilon_\Gamma \nabla^2 \phi - \nabla \cdot \mathbf{f}(\phi) \tag{4.14}$$

The Laplacian term as shown in Equation 4.14 is a kind of artificial diffusion term that is trying to enlarge the width of the interface. The term with the divergence of flux counteracts the diffusion term. When the interface has a thickness of ε_Γ, these two terms are in equilibrium, keeping the interface thickness constant. Equation 4.14 can be defined in a conservative form as below:

$$\frac{\partial \phi}{\partial t} + \nabla \cdot \left(\mathbf{u}\phi + \phi(1-\phi)\frac{\nabla \phi}{|\nabla \phi|} - \varepsilon_\Gamma \nabla \phi \right) = 0 \tag{4.15}$$

To retain the level set function, a reinitialization procedure is required for the finite element approximation of the level set equation. Therefore, a reinitialized

and conservative level set method is used to describe and convect the fluid interface. The following equation describes the convection of the reinitialized level set function:

$$\frac{\partial \phi}{\partial t} + \mathbf{u} \cdot \nabla \phi = \gamma \nabla \cdot \left[\varepsilon_\Gamma \nabla \phi - \phi(1-\phi) \frac{\nabla \phi}{|\nabla \phi|} \right] \tag{4.16}$$

where γ and ε are numerical stabilization parameters, where the former denotes reinitialization parameter and latter parameter determines the thickness of the interface. The γ denotes reinitialization parameter which is approximated to the maximum speed occurring (Sethian, 1999). The ε_Γ denotes the thickness of the interface which is assumed to be the maximum mesh size in subdomains in the neighbourhood of the interface. Equation 4.16 is coupled to the governing equations, which consist of the incompressible Navier-Stokes equation (Equation 4.17), and the continuity equation (Equation 4.18) for the advection of the level set function, ϕ:

$$\rho \frac{\partial \mathbf{u}}{\partial t} + \rho(\mathbf{u} \cdot \nabla)\mathbf{u} = -\nabla p + \nabla \cdot \eta(\nabla \mathbf{u} + (\nabla \mathbf{u})^T) + F_{st} \tag{4.17}$$

$$\nabla \cdot \mathbf{u} = 0 \tag{4.18}$$

where ρ denotes density, η dynamic viscosity, and p denotes pressure. Naturally, the Navier-Stokes equation is solved on the fixed grid to control the motion of the multiphase system. The surface tension force, F_{st} term acting on the interface between two fluid phases can be calculated by Equation 4.19:

$$F_{st} = \sigma k \mathbf{n}_\Gamma \delta_{sm} \tag{4.19}$$

where σ denotes surface tension and δ_{sm} is the smooth Dirac delta function concentrated at the interface between the two fluids which can be approximated by Equation 4.20:

$$\delta_{sm}(\phi) = \begin{cases} 0, & \text{if } \phi < -\varepsilon_\Gamma \\ \frac{1}{2\varepsilon_\Gamma} + \frac{1}{2\varepsilon_\Gamma} \cos\left(\frac{\pi \phi}{\varepsilon_\Gamma}\right), & \text{if } -\varepsilon_\Gamma \le \phi \le \varepsilon_\Gamma \\ 0, & \text{if } \phi > \varepsilon_\Gamma \end{cases} \tag{4.20}$$

Since the surface tension term and the local interfacial curvature term are easily represented in terms of the level-set function as a surface tension force term (Equation 4.19), the LSM can be used to compute any changes in topology induced due to surface tension-driven flows. Surface tension and local curvature terms are implemented by second-order interpolation of Lagrange quadratic elements (Deshpande and Zimmerman, 2006, COMSOL Multiphysics 4.2a, 2011).

4.3 Numerical Model Implementation and Algorithm

The CFD modelling and numerical simulation is performed using COMSOL Multiphysics program, which numerical scheme is based on a FEM. The following sections describe the method of finite element approximates a partial differential equation (PDE) problem with a problem that has a finite number of unknown parameters, that is, a discretization of the original problem. This concept introduces finite elements or shape functions to describe the possible form of the approximate solution. COMSOL Multiphysics uses FEM, which first involves discretizing the spatial domain using a mesh. Once the physical discretisation of the flow domain is completed, the approximation is introduced to the dependent variables. The approximations are solved for small domains in space and time (Deshpande and Zimmerman, 2006).

4.3.1 Domain Discretisation and Mesh Dependency Analysis

The finite element method (FEM) represents a numerical approach by which general differential equations can be solved in an approximate manner. The arbitrary differential equations that are used to describe the physical problem considered are assumed to hold over a certain region (geometric domain). This region is divided into small units of a simple shape, so-called finite elements, and an approximation is then adopted over each element. The collection of finite elements is defined as a finite element mesh. There are different types of mesh elements, such as triangles or quadrilaterals in two-dimensional (2D) and

tetrahedral or hexahedral in three-dimensional (3D). Figure 4.4 illustrates typical finite element mesh for structured mesh of mapped mesh for 2D model in present study. When the type of approximation which is to be applied over each element has been selected, the corresponding behaviour of each element can be determined as the approximation made over each element is fairly simple.

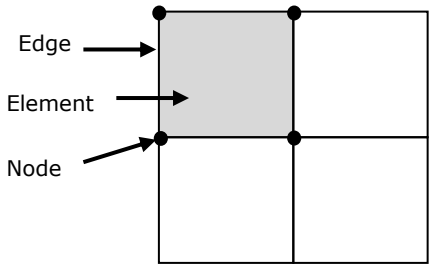


Figure 4.4: Typical finite element mesh for structured mesh of 2D Mapped Mesh.

Prior to the numerical and experimental model comparison, mesh refinement studies were performed to quantify the dependency of simulation results on the grid size and achieve an optimal grid resolution. COMSOL was used to create the geometry of a T-junction, as illustrated in Figure 4.5, and a corresponding mesh. This case was set up in two-dimensions (2D) and a 2D mapped (quads) mesh was generated. Meshes of varying degrees of resolution were set up for the domain with the same grid size of near-wall region in order to make the comparison easier, as shown in Table 4.1. Mesh can be arranged as to be clustered near the wall for the optimum grid resolution in order to resolve the boundary layer flow in future work.

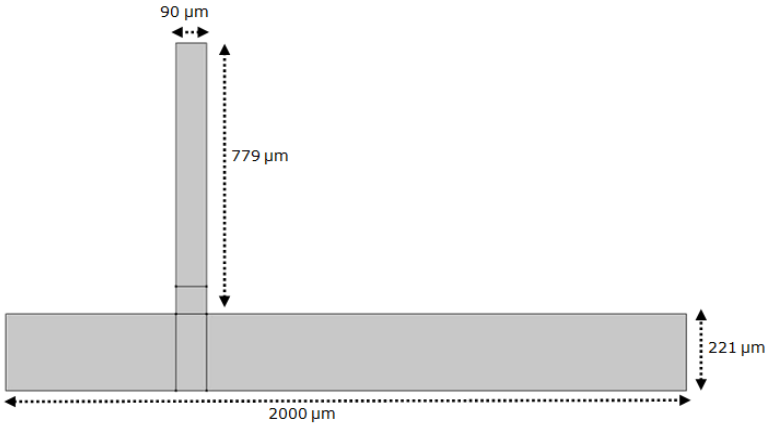
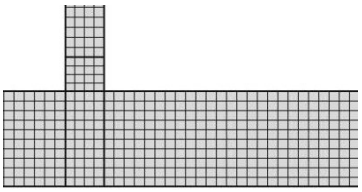
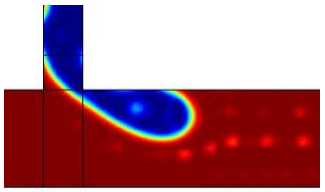
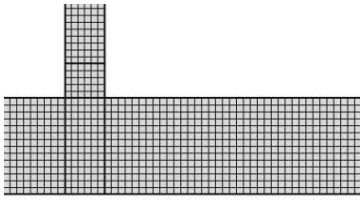
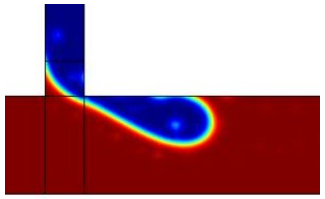
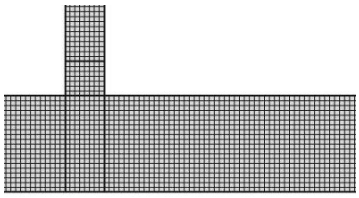
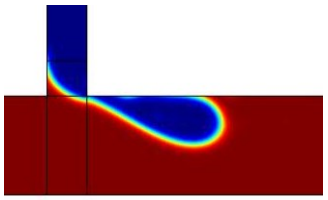
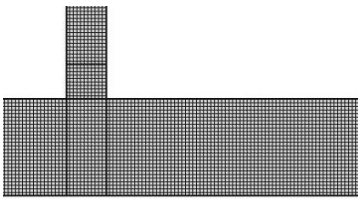
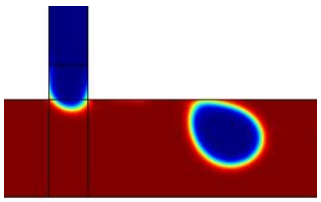
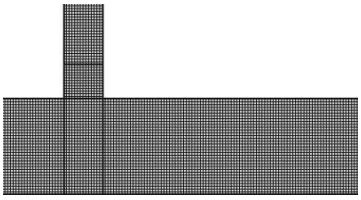
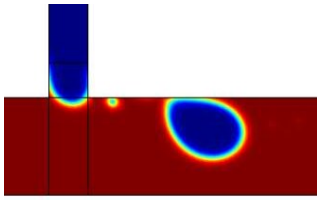
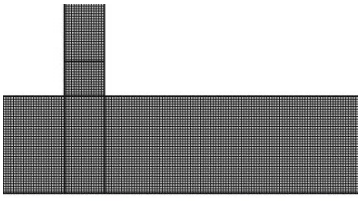
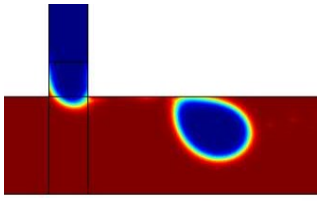
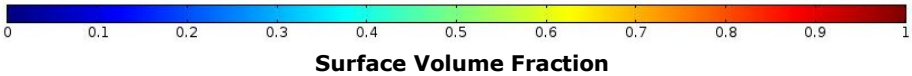


Figure 4.5: The geometry of microfluidics T-junction composed of five subdomains with prescribed dimensions in COMSOL simulation.

Table 4.1: General settings for the variables and parameter in COMSOL. The colour bar specifies the dispersed phase as the area where colour distinction is from 0 to 0.5 and continuous phase the area from 0.5 to 1.0.

No. of Mesh Elements	Two-Dimensional (2D) Structured Mapped Mesh	2D Two-Phase Flow at t = 0.05s
976 (coarsest)		
2072		
4024		
7644		
12166		
15963 (finest)		
	 **Surface Volume Fraction**	

A flow rate ratio, Q of 0.05 (where Q_c= 2.0 ml/hr and for the Q_d= 0.1 ml/hr) was applied. The data is recorded at 0.0005 seconds intervals, which were sufficiently small to capture the breakup phenomenon of the fluid-fluid interfaces. In

COMSOL, this model is set up for transient analysis which provides the time domain response of a system subjected to time-dependent loads. In present work, the numerical simulations were performed at a time-step size of 2.57×10^{-5} seconds calculated using the Courant number, which is also known as Courant-Friedrichs-Lewy (CFL) condition. It shows a relation between the computational cell size, the transient time-step size, and the fluid velocity within the cell. The Courant number is given as:

$$C = \frac{\Delta t \cdot u}{\Delta x} \tag{4.21}$$

where Δt is the time-step used during the simulations, u is the maximum fluid velocity and Δx is the computational cell size. The time-step size can be calculated using the CFL condition, which is done by identifying the specific value of Courant number to stabilize the numerical scheme. A Courant number of 0.25 is selected in the present study considering as robust value to maintain the stability of calculations.

The effect of mesh size was examined by increasing the number of mesh elements from 976 (coarsest grid) to 15963 (finest grid) as shown in Table 4.2. An acceptable relative error of 0.381% between the last two finer grids (see Table 4.2) was obtained. The relative error of the measurement shows the error deviation in relation to the measured values of the droplet diameter between two different mesh resolutions:

$$Relative \quad Error = \frac{\left|d_{eff\,,Mesh\,1} - d_{eff\,,Mesh\,2}\right|}{\left|d_{eff\,,Mesh\,2}\right|} \tag{4.22}$$

As all grid resolutions over 7644 elements give a relative error <0.5%, an optimal grid resolution containing 7644 elements was eventually chosen for the subsequent study.

Table 4.2: Mesh statistics for grid convergence analysis.

Number of Quadrilaterals Elements	Degree of Freedom	Effective Droplet Diameter	Relative Error%
976	13590	172.46	6.960
2072	28727	162.63	1.586
4024	54152	158.81	4.684
7644	101947	150.52	0.249
12166	161405	150.90	0.388
15963	207662	150.31	

4.3.2 Numerical Model Implementation

The fundamental concepts of the Level Set method are practically introduced, along with the numerical implementation of the physical equations, in COMSOL. The numerical model is firstly setup with the necessary numerical approximations for the problem of mathematical analysis. This attempts to provide a general framework for modelling the evolution of boundaries.

COMSOL Implementation: *Discretisation of PDEs Equation*

This section gives an overview of the basic concept for the discretisation scheme of PDE in COMSOL Multiphysics (Comsol Multiphysics 4.2a, 2011). Considering a 2D problem which is similar to the case of our numerical model, the starting point is the weak formulation of the problem. At first, the discretisation of the constraints is considered:

$$0 = R^{(2)} \text{on } \Omega \tag{4.23}$$

$$0 = R^{(1)} \text{on } B \tag{4.24}$$

$$0 = R^{(0)} \text{on } P_t \tag{4.25}$$

The constraints on domain Ω, boundaries B and point P_t are discretized in the same approach. Starting with the constraints on the boundaries B, the Largrange points of some order l (the order of the Lagrange element) is considered for each mesh edge in B and denoted by $x_{qj}{}^{(1)}$, where q is the index of the mesh elements. Therefore, the discretization of the constraints is described as:

$$0 = R^{(2)} x_{qj}{}^{(1)} \tag{4.26}$$

The above equation show that the constraints must hold pointwise at Lagrange points. The order of Lagrange element can be selected for various components of the constraint vector $R^{(1)}$ and varied in space (COMSOL Multiphysics 4.2a, 2011). All these pointwise constraints can be collected in one equation:

$$0 = M \tag{4.27}$$

where *M* is the vector consisting of all the constraints. COMSOL multiphysics approximate the dependent variables with functions in the chosen finite element spaces. The dependent variables are expressed in terms of the degree of freedom as (Galerkin Method):

$$v_n = \sum_i v_i \psi_i^{(n)} \tag{4.28}$$

where $\psi_i^{(n)}$ are the basis functions for variable v_n. Let the **v** be the vector with the degrees of freedoms v_i as its components. This vector is called the solution vector. The vector M depends on V so that the constraints can be written as:

$$0 = M(\mathbf{v}) \tag{4.29}$$

Now, considering a weak equation:

$$0 = \int_\Omega W^{(2)} dA + \int_B W^{(1)} ds + \sum_{Pt} W^{(0)} - \int_\Omega v \cdot h^{(2)^T} \mu^{(2)} dA - \int_B v \cdot h^{(1)^T} \mu^{(1)} ds - \sum_{Pt} v \cdot h^{(0)^T} \mu^{(0)} \tag{4.30}$$

where $\mu^{(i)}$ is the Lagrange multipliers. The treatment of the Lagrange multipliers as ordinary variables has thus produced a weak equation without constraints. In order to discretize the weak equation, the dependent variables are expressed in terms of the degree of freedom as described previously (Galerkin Method) (Comsol Multiphysics 4.2a, 2011):

$$u_n = \sum_i U_i \psi_i^{(n)} \tag{4.31}$$

As the test functions occur linearly in the integrands of the weak equation, it is sufficient to require that weak equation holds when the test functions is chosen as basis functions (Comsol Multiphysics 4.2a, 2011):

$$u_n = \psi_i^{(n)} \tag{4.32}$$

As the above equation is substituted into the weak equation, this shows one question for each *i* and becomes:

$$0 = \int_{\Omega} W^{(2)} dA + \int_{B} W^{(1)} ds + \sum_{Pt} W^{(0)} - \int_{\Omega} \psi_i \cdot h^{(2)^T} \mu^{(2)} dA - \int_{B} \psi_i \cdot h^{(1)^T} \mu^{(1)} ds - \sum_{Pt} \psi_i \cdot h^{(0)^T} \mu^{(0)} \tag{4.33}$$

Next, the Lagrange multiplier is discretized. Let:

$$\Lambda_{qj}^{(d)} = \mu^{(d)} x_{qj}^{(d)} w_{qj}^{(d)} \tag{4.34}$$

where $x_{qj}^{(d)}$ is the Lagrange point and $w_{qj}^{(d)}$ is certain weights. From Equation (4.28), the term $\int_{B} \psi_i \cdot h^{(1)^T} \mu^{(1)} ds$ is approximated as a sum over all the mesh elements in boundaries. The contribution from mesh element number *q* to this sum is approximated with the Riemann sum:

$$\sum_{j} \psi_i(x_{qj}^{(1)}) \cdot h^{(1)^T}(x_{qj}^{(1)}) \cdot \mu^{(0)}(x_{qj}^{(1)}) w_{qj}^{(1)} = \sum_{j} \psi_i(x_{qj}^{(1)}) \cdot h^{(1)^T}(x_{qj}^{(1)}) \cdot \Lambda_{qj}^{(1)} \tag{4.35}$$

where $w_{qj}^{(1)}$ is the length over the appropriate part of mesh element. The integral over Ω and the sum over P_t are approximated similarly. The objective of discretisation is to solve this system for the solution vector **v** containing all the discretized dependent variables and Lagrange multiplier vector $\boldsymbol{\Lambda}$ containing all the discretized Lagrange multipliers. The above discretisation approach has demonstrated how COMSOL multiphysics form the discretisation of the PDE.

In numerics, the solution of partial differential equation (PDE) can be formulated in a strong form or a weak form. The strong form is a description of the governing partial differential system equations and the relationship must be satisfied at every mathematical point in the domain. It is not always efficient to solve with the strong form, as there may not be classical solutions to a particular problem, especially in the case of complex domains. Besides, it is always a daunting task when the boundary conditions are enforced in the strong forms. In order to satisfy the requirement of continuity of field variables, weak formulations are being developed to solve these difficulties as it provides more

possibilities to control and enforces given constraints. Both strong and weak forms were used to solve the present numerical simulation model.

Simulation Model Setup

For the separated fluid elements to correspond to droplets, the geometry is modelled in 2D. The modelling domain of a T-junction microchannel is shown in Figure 4.6. A two-dimensional numerical model is implemented in COMSOL and there are four unknown field variables (dependent variables): the level set function, the two components of the velocity field and the pressure. These fields are shown as below:

$$\phi = \phi(x,y,t) \tag{4.36}$$

$$u_x = u_x(x,y,t) \tag{4.37}$$

$$u_y = u_y(x,y,t) \tag{4.38}$$

$$p = p(x,y,t) \tag{4.39}$$

Here, the fluid phase is described with respect to an Eulerian reference frame. The velocity vector field is defined as:

$$\mathbf{u} = (u_x(x,y,t), u_y(x,y,t)) \tag{4.40}$$

Each field has a corresponding governing equation. For instance, the level set function is governed by Equation 4.16 corresponding to the numerical extension of the convection equation. The two components of velocity field are governed by the Navier-Stokes equation (Equation 4.17). The pressure field is governed by the continuity equation (Equation 4.18) for mass conservation. All this gives a set of four coupled linear or non-linear differential equations.

In COMSOL, the software collects all the equations and boundary conditions formulated by the physics interface into one large system of PDEs and boundary conditions. Consequently, a general form of PDE interface is used by COMSOL

while solving the governing differential equations is written in the following coefficients equation system form (for time-dependent model):

$$d_{v_i}\partial_t v_i + \nabla \cdot \Gamma_{V_i} = F_{v_i} \text{ ,in } \Omega \tag{4.41}$$

with generalized Neumann boundary condition,

$$-\mathbf{n}_b \cdot \Gamma_{V_i} = G_{V_i} - (\partial_{v_i} R_{v_i})\mu_{v_i}, \text{ on } \partial\Omega \tag{4.42}$$

with Dirichlet boundary condition,

$$0 = R_{v_i}, \text{ on } \partial\Omega \tag{4.43}$$

where d_{vi} denotes damping (or mass) coefficient, F_{V_i}, G_{V_i}, and R_{V_i}denote scalar coefficients, Γ_{V_i} denotes conservative flux vector, μ_{V_i} denotes Lagrange multipliers, $\mathbf{n}_b$ denotes outward unit normal vector on the domain boundary, and the solution vector **v** contains:

$$\mathbf{v} = \begin{bmatrix} \phi \\ u_x \\ u_y \\ p \end{bmatrix} \tag{4.44}$$

These Lagrange multipliers are only relevant when the constraints boundary condition R_{V_i}s' are different from zero ($R_{V_i} \neq 0$).Generally speaking, one can create a Lagrange multiplier associated with each constraint the problem is subjected to. For instance, when R_{vi} is equal to one of the velocity components ($R_{V_i}=u_x$) on a specific boundary segment, the x-component of the velocity must be zero on that part of domain boundary. Referring to Equation 4.42, one observes that the derivative with respect to x-component of the velocity is different from zero. Therefore, COMSOL always adjusts the Lagrange multiplier on this special part of boundary such that Equation 4.42 fulfils the Neumann conditions. Therefore, the G_{V_i} become irrelevant if the Lagrange multiplier is introduced for a given constraint in the problem and can be left out of the treatment. One has thereby eliminated a constraint in the expense of another equation for the Lagrange multiplier (Bankorb and Anderson, 2007).

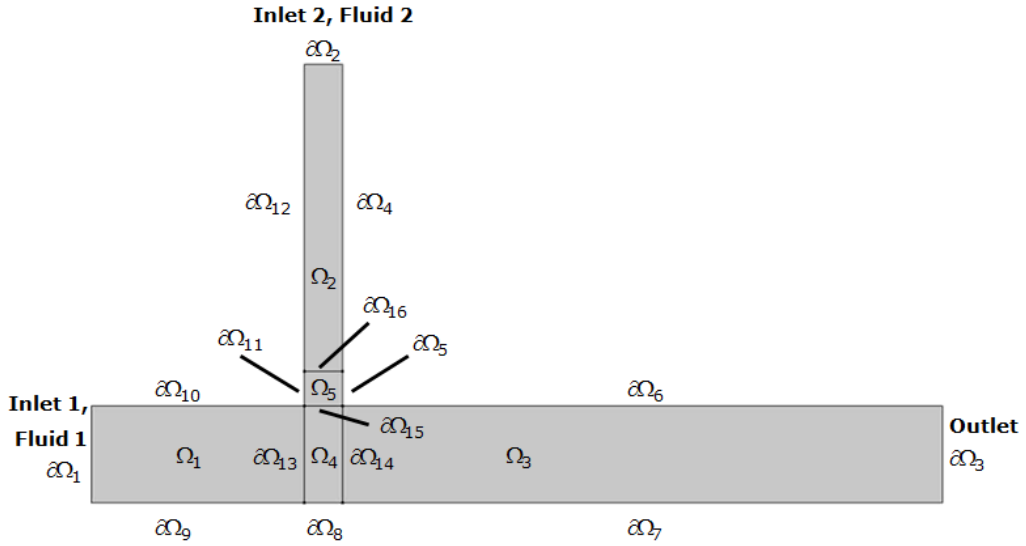


Figure 4.6: The modelling domain of a T-junction: Ω_k (for k=1...5) denotes the computational domain, and $\partial\Omega_k$ (for k=1...16) denotes the domain boundary, respectively.

Domain Variables: Strong and Weak Formulation

Strong Form:

In two-phase modelling, the surface tension force term in Navier-Stokes equation (see Equation 4.17) are introduced in a weak form. Thus, the remaining equation of strong from as:

$$\rho\partial_t\mathbf{u}+\nabla p-\eta\nabla\cdot(\nabla\mathbf{u}+(\nabla\mathbf{u})^T)=-\rho(\mathbf{u}\cdot\nabla)\mathbf{u} \tag{4.45}$$

For an incompressible Newtonian fluid flow, the stress tensor σ is decomposed as:

$$\sigma=-pI+\eta(\nabla\mathbf{u}+(\nabla\mathbf{u})^T) \tag{4.46}$$

Thus, Equation 4.30 can be rearranged and expressed as:

$$\rho\partial_t\mathbf{u}-\nabla\cdot\sigma=-\rho(\mathbf{u}\cdot\nabla)\mathbf{u} \tag{4.47}$$

Comparing with Equation 4.26, each coefficient is represented as:

$$\text{x-component:}\begin{cases}d_{ux}=\rho\\ \Gamma_{ux}=-[\sigma_{xx},\sigma_{xy}]^T\\ F_{ux}=-\rho(\mathbf{u}\cdot\nabla)u_x\end{cases} \tag{4.48}$$

$$\text{y-component:}\begin{cases}d_{uy}=\rho\\ \Gamma_{uy}=-[\sigma_{yx},\sigma_{yy}]^T\\ F_{uy}=-\rho(\mathbf{u}\cdot\nabla)u_y\end{cases} \tag{4.49}$$

For the pressure, comparing with the continuity equation (Equation 4.18), each coefficient is represented as:

$$\begin{cases} d_p = 0 \\ \Gamma_p = 0 \\ F_p = \nabla \cdot \mathbf{u} \end{cases} \tag{4.50}$$

For the level set function, comparing with the level-set equation (Equation 4.16), each coefficient is represented as:

$$\begin{cases} d_\phi = 1 \\ \Gamma_\phi = \mathbf{u}\phi + \phi(1-\phi)\dfrac{\nabla\phi}{|\nabla\phi|} - \varepsilon_\Gamma \nabla\phi \\ F_\phi = 0 \end{cases} \tag{4.51}$$

Consequently, the variables for the strong form of the modelling equations are the damping (or mass) coefficient, conservative flux vector, scalar coefficients and are summarized in Table 4.3.

Table 4.3: Variables for the strong form in the computational domain, Ω_k.

$\boldsymbol{v_i}$	u_x	u_y	p	ϕ
d_{V_i}	ρ	ρ	0	1
$\boldsymbol{\Gamma}_{V_i}$	$-\left[\sigma_{xx}, \sigma_{xy}\right]^T$	$-\left[\sigma_{yx}, \sigma_{yy}\right]^T$	0	$\mathbf{u}\phi + \phi(1-\phi)\dfrac{\nabla\phi}{\lvert\nabla\phi\rvert} - \varepsilon_\Gamma\nabla\phi$
F_{V_i}	$-\rho(\mathbf{u}\cdot\nabla)u_x$	$-\rho(\mathbf{u}\cdot\nabla)u_y$	$\nabla\cdot\mathbf{u}$	0

Weak Form:

For the domain, the only weak contribution is come from the Navier-Stokes equation. The weak contribution stems from the term includes the surface tension force, $\sigma k\,\delta(r-r_\Gamma)\mathbf{n}_\Gamma$ (where δ(r-r$_\Gamma$) denotes the Dirac delta function as a function of the smallest distance between a given point in the domain and the interface) (Bankorb and Anderson, 2007). To discretize it, approximate the surface tension force with a test/basis function and integrate over the domain by using Green's theorem. The test (arbitrary) functions are assumed to be smooth and compactly supported functions so as they vanish on the prescribed displacement boundary. Green's theorem gives the relationship between

boundary integral around a simple closed curve (domain boundary) and double integral over a plane region (computational domain). Thus, the integral can be divided up into an integral over the computational domain and an integral over the domain boundary. It is the integral over the domain that defines the weak contribution. Without going into the details, the weak contributions can be simply expressed as:

$$\sigma((\partial_x \tilde{u}_x)\mathbf{n}_{\Gamma x} + (\partial_y \tilde{u}_x)\mathbf{n}_{\Gamma y})|\nabla\phi|\mathbf{n}_{\Gamma x} \tag{4.52}$$

$$\sigma((\partial_x \tilde{u}_y)\mathbf{n}_{\Gamma x} + (\partial_y \tilde{u}_y)\mathbf{n}_{\Gamma y})|\nabla\phi|\mathbf{n}_{\Gamma y} \tag{4.53}$$

where $\tilde{u}_i$ is the test function. Note that subscript x and y are denoted as x-velocity component and y-velocity component, respectively.

Boundary Variables: Strong and Weak Formulation

Strong form

In present modelling, there are 16 parts of the domain boundary as shown in Figure 4.6. The boundary constraints of the variables are given by specifying the R_{V_i} in Equation 4.43 for each boundary division which gives a total of 84 variables (see Table 4.4):

$$R = R_{v_i}^{\partial\Omega_k}, \; i=1\ldots4; \; k=1\ldots16, \tag{4.54}$$

For the first boundary, $\partial\Omega_1$, the component of the velocity normal to the domain boundary, u_x is not zero ($u\cdot\mathbf{n}=u_o$) and a constant value of the level set function of zero is applied. This boundary is defined as the inlet for the continuous phase fluid. While for the second boundary, $\partial\Omega_2$, this boundary is defined as the inlet for the dispersed phase fluid. On this part of the domain boundary, the component of the velocity normal to the boundary, u_y is different from zero as $u\cdot\mathbf{n}=u_o$ and a constant value of the level set function of one is used. For the third boundary, a pressure of zero with no viscous stress $\eta\,(\nabla\mathbf{u} + (\nabla\mathbf{u})^{\mathrm{T}})\cdot\boldsymbol{n} = \mathbf{0}$ is applied. This boundary is defined as the outlet of the modelling domain. For the boundaries 4 to 12, a wetted wall boundary condition is applied to the wall of the

geometry used in the simulation. For boundaries 4 to 5 and 11 to 12, the component of the velocity normal to the wall, u_x has to be zero, while the component of the velocity (tangential velocity), u_y parallel to the wall is unrestricted. For boundaries 6 to 10, the component velocity normal to the wall, u_y has to be zero, while the component of the velocity (tangential velocity), u_x parallel to the wall is unrestricted. No pressure or level set function boundary conditions are applied on these particular domain boundaries. The boundaries 13 to 16 are not applicable since the program satisfies these boundaries without intervention by the user.

Table 4.4: *R* Variables for the domain boundaries in COMSOL.

$R_{V_i}^{\partial\Omega_k}$	Boundary Condition	u_x	u_y	p	ϕ
$\partial\Omega_1$	Inflow Velocity	$u\cdot\mathbf{n}=u_o$	$u_y=0$	-	$\phi=0$
$\partial\Omega_2$	Inflow Velocity	$u_x=0$	$u\cdot\mathbf{n}=u_o$	-	ϕ-1=0
$\partial\Omega_3$	Outlet Pressure	-	-	$p=0$	-
$\partial\Omega_4$	Wetted Wall	$u\cdot\mathbf{n}=0$	$u_y=0$	-	-
$\partial\Omega_5$	Wetted Wall	$u\cdot\mathbf{n}=0$	$u_y=0$	-	-
$\partial\Omega_6$	Wetted Wall	$u_x=0$	$u\cdot\mathbf{n}=0$	-	-
$\partial\Omega_7$	Wetted Wall	$u_x=0$	$u\cdot\mathbf{n}=0$	-	-
$\partial\Omega_8$	Wetted Wall	$u_x=0$	$u\cdot\mathbf{n}=0$	-	-
$\partial\Omega_9$	Wetted Wall	$u_x=0$	$u\cdot\mathbf{n}=0$	-	-
$\partial\Omega_{10}$	Wetted Wall	$u_x=0$	$u\cdot\mathbf{n}=0$	-	-
$\partial\Omega_{11}$	Wetted Wall	$u\cdot\mathbf{n}=0$	$u_y=0$	-	-
$\partial\Omega_{12}$	Wetted Wall	$u\cdot\mathbf{n}=0$	$u_y=0$	-	-
$\partial\Omega_{13}$	Open Curve	-	-	-	-
$\partial\Omega_{14}$	Open Curve	-	-	-	-
$\partial\Omega_{15}$	Open Curve	-	-	-	-
$\partial\Omega_{16}$	Initial Interface	-	-	-	-

***Note:"-" represents the variables are not applicable in respective boundary.*

Weak Form:

The Lagrange multiplier is introduced for domain boundary, $\partial\Omega_k$ (for k=4...12) in order to enforce the contact angle condition on this boundary. The integral along the boundary from the transformation of surface tension force, $\sigma k\mathbf{n}\delta(r-r_l)$ is

also implemented as a weak equation. In the weak formulation, Neumann boundary conditions are incorporated into the integration:

$$\int_{\partial\Omega} \tilde{V}_i G_{vi} d\mathbf{r} \tag{4.55}$$

On boundary segment four to twelve, $\partial\Omega_4$-$\partial\Omega_{12}$, a contact angle of θ has been employed. This boundary condition can be expressed by dot product between the normal vector of level set at the interface and the normal vector of level set at boundary:

$$\mathbf{n}_\Gamma \cdot \mathbf{n}_b = \cos\left(\theta\right) \tag{4.56}$$

In order to find the G_{vi} that fulfils the Neumann boundary conditions (Equation 4.42), the constraints are converted to the weak form by use of Equation 4.55 and they can be briefly expressed as:

$$-\sigma|\nabla\phi|\mathbf{n}_{\Gamma x}\tilde{u}_x \cos(\theta) \tag{4.57}$$

$$-\sigma|\nabla\phi|\mathbf{n}_{\Gamma y}\tilde{u}_y \cos(\theta) \tag{4.58}$$

where $\tilde{u}_i$ is the test function. Note that subscript x and y denote the x-velocity component and y-velocity component, respectively. For the Lagrange multiplier, there are two weak equations:

$$\begin{cases} \tilde{\mu}(\partial_y\phi - \cos(\theta)) \\ \tilde{\phi}\mu \end{cases} \tag{4.59}$$

where $\tilde{\mu}$ and $\tilde{\phi}$ are the test functions for Lagrange multiplier and the level set function.

Overall Simulation Setup

Table 4.5 lists the general settings for the variables and parameters used in the present simulation model. Under definition settings in COMSOL, the domain boundary of the continuous ($\partial\Omega_1$) and dispersed phase ($\partial\Omega_2$) was set up with laminar inflow boundary condition with the flow rate specified. The flow rates are multiplied by a unit step function. The step function ramps up the flow rates at

the start of the simulation. In the present work, all the parametric studies used, as key output, the effective droplet diameter. Therefore, an integration operator was added to find the area corresponding to the dispersed phase, where $\tilde{\phi}$>0.5, in order to calculate the effective droplet diameter by the following equation:

$$d_{eff} = 2 \cdot \sqrt{\frac{1}{\pi} \int_{\Omega} (\tilde{\phi} > 0.5) d\Omega} \tag{4.60}$$

This is the diameter of a spherical droplet that has equivalent volume of the formed droplet. For the fluid properties setting, viscosity and density of the fluids with Newtonian and non-Newtonian behaviour are set. These values can be obtained from Table 3.3. In the Newtonian/non-Newtonian system, a stress model known as the Carreau-Yasuda (Equation 3.3) is incorporated with a front capturing scheme used in the computational fluid dynamics. The front-capturing method that we introduced in this current work is based on the level-set formulation. This model expresses the shear-thinning behaviour of the non-Newtonian CMC used in present study. The model was generalized by replacing the shear rate, $\dot{\gamma}$ in the constitutive equation (relationship between stress and strains, $\tau=\eta\dot{\gamma}$) for Newtonian fluid by the second invariant of the strain rate tensor, $\prod_D$ in Cartesian coordinates:

$$\dot{\gamma} = \sqrt{\frac{1}{2}\left[4\left(\frac{\partial u}{\partial x}\right)^2 + 2\left(\frac{\partial u}{\partial y} + \frac{\partial v}{\partial x}\right)^2 + 4\left(\frac{\partial v}{\partial y}\right)^2\right]} \tag{4.61}$$

For wall settings, a wetted wall boundary condition was applied to all solid boundaries with the contact angle specified as 180° and a slip length equal to the mesh size parameter, h. The contact angle is the angle formed by the liquid/liquid interface as it attaches to the wall, while the slip length is defined as the distance between the fluid interfaces to the position outside the wall where the extrapolated tangential velocity component vanishes. For the inlet settings, at both inlets, laminar inflow conditions with prescribed volume flows were used. At the outflow boundary, the pressure (0 Pa) with no viscous stress condition

was set. The present computational works were implemented based on two-dimensional CFD simulations which can greatly reduce the computation cost and simplify the model. Although this case was modelled in 2D mode, an entrance thickness of 73.5 μm was employed in numerical system to define the depth (in the z-axis) of the channel.

Table 4.5: General settings for the variables and parameter in COMSOL (for system: flow rate ratio, *Q*: 0.05).

Name	Expression	Unit	Description
Definition Settings			
Q1	2e-6/3600*step1(t[1/s])[m^3/s]	m^3/s	Volume Inlet 1
Q2	0.1e-6/3600*step1(t[1/s])[m^3/s]	m^3/s	Volume Inlet 2
deff	2*(intop1((phils>0.5)*(x>0.15[mm]))/pi)^(1/2)	mm	Effective Droplet Diameter
Fluid Properties Settings			
tpf.mu1	0.068	kg/m.s	Viscosity Fluid 1
tpf.mu2**	0.00093	kg/m.s	Viscosity Fluid 2(Water)
or	tpf.mu_inf2+(tpf.mu02-tpf.mu_inf2)* (1+(tpf.lam_car2*tpf.sr)^0.9653)^((-1+tpf.n_car2)/0.9653)	kg/m.s	Viscosity Fluid 2 (Non-Newtonian)
tpf.mu_inf2**	Refer to Table 3.3	kg/m.s	Infinite shear viscosity
tpf.mu02**	Refer to Table 3.3	kg/m.s	Zero shear viscosity
tpf.lam_car2**	Refer to Table 3.3	s	Relaxation time constant
tpf.sr	sqrt(0.5*(4*ux^2+2*(uy+vx)^2+4*vy^2)+eps)	1/s	Shear rate
tpf.n_car2**	Refer to Table 3.3	1	Fluid behaviour index
tpf.rho1	908.9	kg/m^3	Density Fluid 1
tpf.rho2**	998.2	kg/m^3	Density Fluid 2 (Water)
or	Refer to Table 3.3		Density Fluid 2 (Non-Newtonian)
tpf.sigma**	0.02074	N/m	Surface Tension (Water)
tpf.sigma**	Refer to Table 3.3		Surface Tension (Non-Newtonian)
tpf.epsilon_ls	$5.8e^{-6}$	m	Parameter controlling interface thickness
tpf.gamma	0.065	m/s	Reinitialization parameter
Wall Settings			
tpf.thetaw	pi	rad	Contact angle
tpf.beta	h	m	Slip length
Inlet 1 Settings			
tpf.phi0	0	1	Level set function values
tpf.V0inl1	Q1	m^3/s	Flow rate
tpf.Dzentrinl1	$7.35e^{-5}$	m	Entrance thickness
tpf.Letr	$3.34e^{-7}$	m	Entrance length
Inlet 2 Settings			
tpf.phi0	1	1	Level set function values
tpf.V0inl1	Q2	m^3/s	Flow rate
tpf.Dzentrinl1	$7.35e^{-5}$	m	Entrance thickness
tpf.Letr	$3.34e^{-7}$	m	Entrance length

Table 4.3: (Continued)

Name	Expression	Unit	Description
Outlet Settings			
tpf.p0	0	Pa	Pressure

*Note:"**" represent the values of the parameter can be obtained from Table 3.3 accordingly. A Carreau-Yasuda viscosity model is incorporated with the simulation if a non-Newtonian CMC (for Fluid 2: dispersed phase fluid) is employed in the system.*

4.4 COMSOL Simulation Overview

To summarize, modelling with FEM for the LS computations require pre-processing, the solving phase, and the analysis of the results. These proceed following the steps reported below in COMSOL (see Figure 4.7):

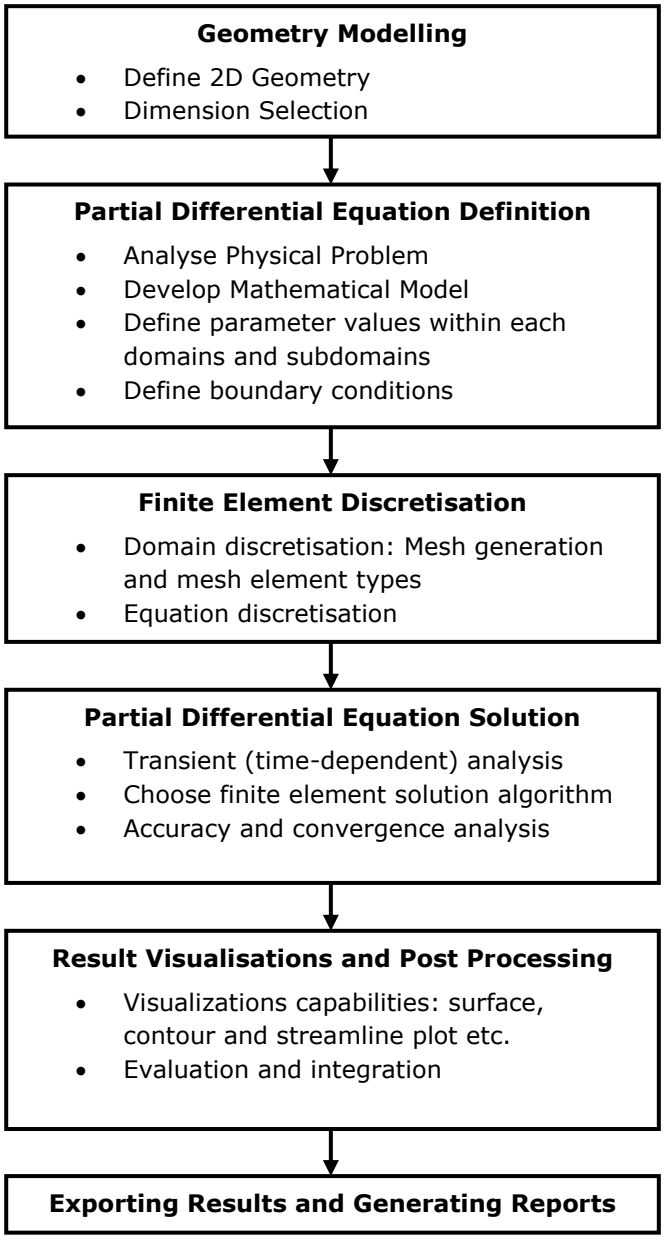


Figure 4.7: Steps in COMSOL simulation and modelling.

4.5 Experimental Model: Droplet Formation at T-Junction

In order to validate the proposed numerical model, experiments were set up to measure the droplet diameter (see section 3.9.1). The process of droplet formation in the microchannel was recorded using a high speed camera

connected to an epifluorescence microscope. After allowing the system to reach steady state for predetermined time intervals (20 minutes), videos were recorded at 500 fps for each flow rate of either continuous or dispersed phase. The droplet sizes in the experiment were measured through an image processing routine using MATLAB (see section 3.9.2).

In the first series of experiments, the effect of the dispersed phase rate on droplet diameter was examined for different flow rate ratios of 0wt% CMC (deionised water, η_d=0.00093kg/m.s). Olive oil (η_c=0.068 kg/m.s) was selected as the carrier fluid in the continuous phase. Both continuous and dispersed phases behave as Newtonian fluids. For a constant continuous phase flow rate, Q_c at 2.0ml/hr, the droplet size was measured with the variation in dispersed phase flow rate, Q_d (0.08 ml/hr to 1.0 ml/hr), with results of the observed droplet diameter outlined in Table 4.6. When Q_c>Q_d, Bashir *et al*. (2011) reported the droplet does not have time to elongate and breakup occurs immediately after a droplet major diameter (d_{major}) is formed and the droplet detachment occurs at the junction. Tan *et al*. (2008) also reported that shear force from the continuous phase is sufficiently high to induce the dispersed phase to form droplets at the T- junction of the microchannel at low dispersed phase rates.

Table 4.6: Averaged Newtonian droplet diameter at different dispersed rate by using cross-flowing rupture techniques.

Q_c (ml/hr)	Q_d (ml/hr)	Q	d_{major} (µm)	d_{minor} (µm)	d_{eff} (µm)
2.00	0.08	0.04	156.57±1.93	136.71±0.80	146.19±1.23
2.00	0.10	0.05	158.13±2.96	141.53±1.81	149.50±2.26
2.00	0.135	0.0675	165.72±2.12	139.86±0.88	152.12±1.35
2.00	0.20	0.10	176.26±1.78	143.76±0.72	159.06±0.93
2.00	0.25	0.125	191.59±5.19	152.01±1.89	170.51±3.32
2.00	0.40	0.20	205.22±2.05	152.44±0.40	176.76±1.06
2.00	0.50	0.25	210.01±4.49	158.13±1.36	182.10±2.54
2.00	0.80	0.40	237.43±2.76	160.04±0.50	194.80±1.40
2.00	1.00	0.50	267.60±7.37	169.42±1.29	212.77±3.34

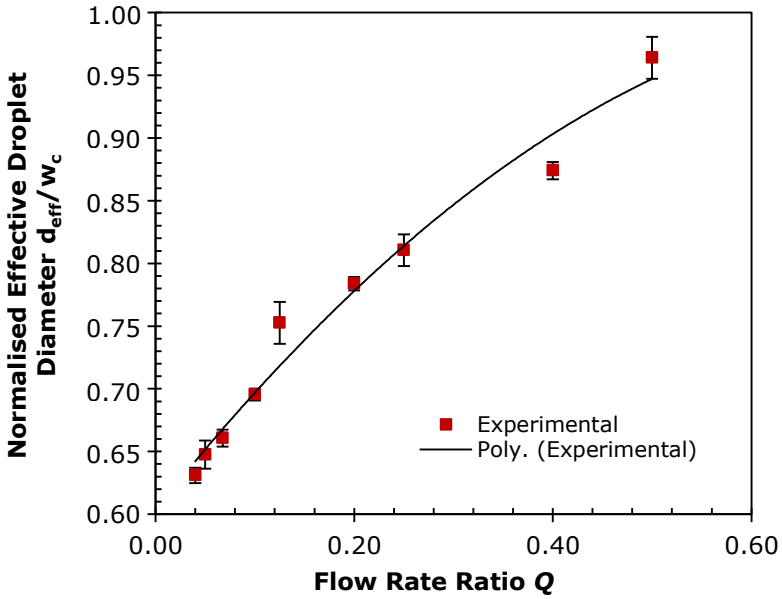


Figure 4.8: Graph of the effect of flow rate ratio Q ($=Q_d/Q_c$) on normalised droplet size (d_{eff}/w_c) of water at fixed continuous phase rate of 2.0 ml/hr. Error bars shown indicate the standard deviation in droplet size measurement of 30 droplets under fixed experimental condition.

Figure 4.8 reveals that the droplet size observed downstream of the T-junction microchannel, which illustrates the effect of Q_d on droplet diameter. The error bars added to markers show the standard deviation in droplet size measurement of 30 droplets under fixed experimental condition. The results reveal the diameter of the dispersed droplets increased when the dispersed flow rate increased. As elucidated in Figure 4.8, it can be seen that as the rate of Q_d increases, the inertial force of the dispersed phase generated during the droplet formation process are great enough to resist the opposing shear force which moves the interfacial boundary of the two liquids towards the T-junction corner pinch point resulting in formation of a droplet. As Q_d increases, more dispersed phase fluids enter the main channel before the dispersed thread is pinched off at the outlet corner and, as a result, the size of droplet increases with increasing Q_d. The experiment was repeated with the same operating parameters on the droplet size to assure the repeatability of the experiment. The variations in droplet size are most likely due to uncertainty in the threshold during droplet size measurement by counting pixels using the MATLAB software. When images

are converted into binary image, the edges of the droplet boundary are detected using an appropriate threshold value; however, the threshold decision step can be quite critical in that it will add uncertainty to the location of edge.

4.6 Numerical and Experimental Model Comparison

At a very preliminary stage, the justification of the numerical model of the formation of deionised water droplets (0wt% CMC) in olive oil (highly refined, low acidity, Sigma Aldrich) in a T-junction microchannel was carried out using the Level-Set method. This gave agreement with laboratory experimental data (see Figure 4.9) with reasonable precision in the range of flow rate ratio, Q ($=Q_d/Q_c$) applied. Additionally, the present comparison also gives an estimate of the discrepancy between the experimental measurements of the flow system and the predicted simulation results from its mathematical model.

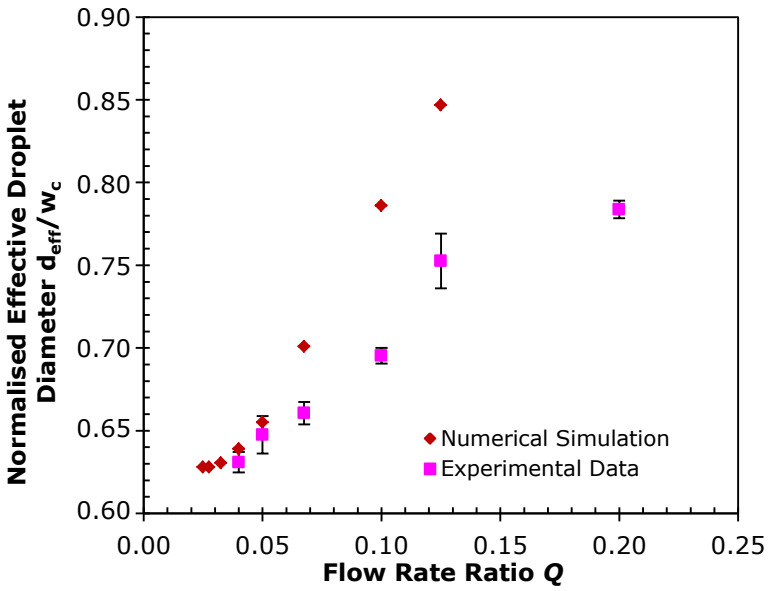


Figure 4.9: Comparison of normalised effective droplet diameter (d_{eff}/w_c) between numerical and experimental result in the range of Q applied. Error bars indicate the standard deviation in droplet size measurement of 30 droplets under fixed experimental condition.

As elucidated in Figure 4.9, in comparison with experimental data, a similar trend has been numerically evidenced for the evolution in the normalised effective droplet diameter over a range of flow rate ratios. Numerical results

revealed that the dispersed phase droplet diameter increases with increasing dispersed flow rate as in our experiments. Only a very slight discrepancy in effective droplet diameter between experimental and simulation was found at lower flow rate ratios. However, these differences in droplet diameter become more significant at higher flow rate ratios. The temperature dependence of the physical and rheological properties of each working fluid in experiments may have contributed to the deviation in droplet diameter from numerical simulation as they were assumed to remain constant in the numerical model. Additionally, syringe pump induced oscillation of flow rate implied a source of fluctuation in the microfluidic flow, which might also affect the droplet diameter. Besides, the difficulties of numerical dissipation in advection step of fluid simulation for Equation 4.17 may arise for larger flow rate ratio. When the flow rate ratio used in the simulation exceeds a certain limit, the convergence using the optimal grid resolution may not trustworthy and therefore a finer grid resolution for the higher flow rate ratio parameter may be necessary.

To reduce the numerical dissipation of the scheme, the Q of 0.05 was ultimately chosen for all subsequent parametric simulation studies in order to ensure higher accuracy of the numerical approach. Figure 4.10 illustrates a sequence of snapshot of droplet formation for model validation against laboratory experiments for Q of 0.05. The snapshots of the droplet formation process for other flow rate ratios are illustrated in Figure 4.11, for visual support. At the higher range of flow rate ratios (Q> 0.0675), the differences of the dynamics of droplet formation process between experimental and numerical data can be seen in Figure 4.11.

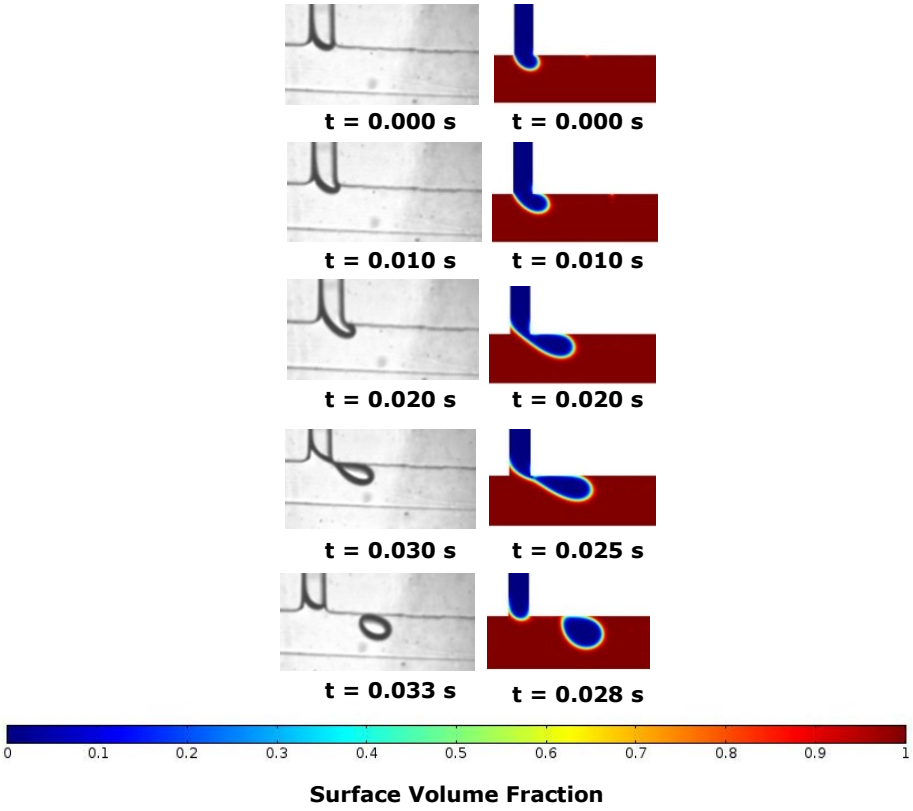


Figure 4.10: Snapshots of two-dimensional (2D) simulations of the water-in-oil droplet breakup process in microchannel and corresponding to experiments (for system: Q_c: 2.0 ml/hr and Q_d: 0.1ml/hr, Q=0.05).The colour bar specifies the dispersed phase as the area where colour distinction is from 0 to 0.5 and continuous phase the area from 0.5 to 1.0.

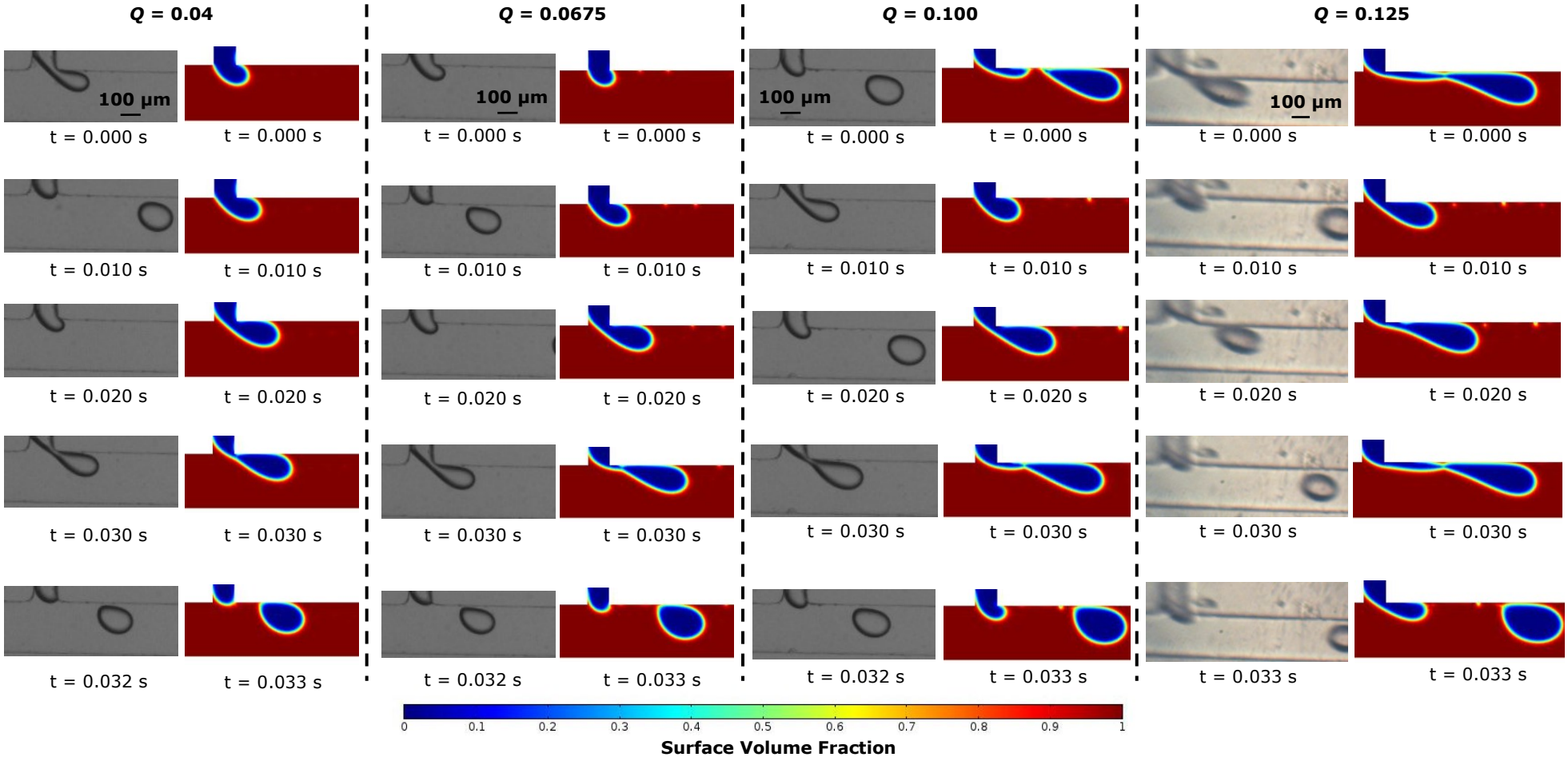


Figure 4.11: Snapshots of two-dimensional (2D) simulations and experiments of the water-in-olive oil droplet breakup process for various flow rate ratios. The colour bar specifies the dispersed phase as the area where colour distinction is from 0 to 0.5 and continuous phase the area from 0.5 to 1.0.

4.7 Droplet Formation and Breakup Mechanism

The typical process of the formation of a droplet in a microfluidics T-junction in the present simulation can be described from numerical data as follows. In the T-junction configuration, the inlet channel containing the dispersed phase perpendicularly intersects the main channel, which contains the continuous phase. The two phases form an interface at the junction. As fluid flow continues (Thorsen *et al*., 2001; Nisisako *et al*., 2002;Teh *et al*., 2008; Xu *et al*., 2008),at first, the tip of the dispersed phase enters the main channel and partially blocks the channel, which results in the continuous phase having to flow through a smaller cross-sectional area at the T-junction. This results in higher shear stresses at the interface between the two phases, and over time the disperse phase entering the T-junction is slowly convected downstream. This results in a pressure increase in the continuous phase, which squeezes the neck of the dispersed thread as the interface approaches the downstream edge of the inlet for the dispersed phase. The pressure gradient and shear stresses in the main channel further distort the droplet in the downstream direction until they overcome the surface tension and a droplet is formed (Garstecki *et al*., 2005; Garstecki *et al*., 2006). The fully detached deionised-water droplet flows downstream in the main channel, while the tip of the stream of the dispersed phase retracts to the end of the inlet channel. This break-up process is continuously repeated. Figure 4.12 illustrate the evolution of the pressure during the droplet formation process. Glawdel *et al*. (2012) have reported that the droplets formation process could be divided into three sequential stages known as the lag, filling, and necking stages. In the lag stage, the interface recedes back into the side channel after the detachment of the previous droplet. In the filling stage, the dispersed phase penetrates into the cross-flowing stream and the droplet grows downstream. Meanwhile, the hydrodynamic forces deform the droplet before its detachment. Once the forces overwhelm the droplet, the necking of the dispersed phase is initiated and the droplets are pinched off.

Figure 4.13 exhibits the pattern of a droplet growth and detachment, with streamline overlaid on vectors. The arrows were added showing the magnitude and direction of the velocity. The streamline is the line that is instantaneously tangential to the velocity vector of the field. In Figure 4.13, at the start of the formation process, a recirculation flow is generated close to the interface. This region expands gradually when the dispersed phase enters the main stream and elongates downstream. Due to the local loss of equilibrium between the hydrodynamics forces, the recirculation flow no longer exists when the droplet is pinched off.

Variations of pressure during the growth of the dispersed phase filament and the detachment of the drop given in Figure 4.12 show a sudden drop followed by the detachment of the first drop. This sudden pressure drop indicates the droplets exiting the computational domain. It should be noted that the pressure inside the droplet is higher than that of the continuous phase in the neighbourhood. Since the boundary condition applied assumes the droplets to be entering the constant pressure as they leave the domain, the pressure field shows a sudden reduction spread over the time it takes a droplet to cross the outlet boundary completely. This phenomenon is applied to all cases in subsequent chapters.

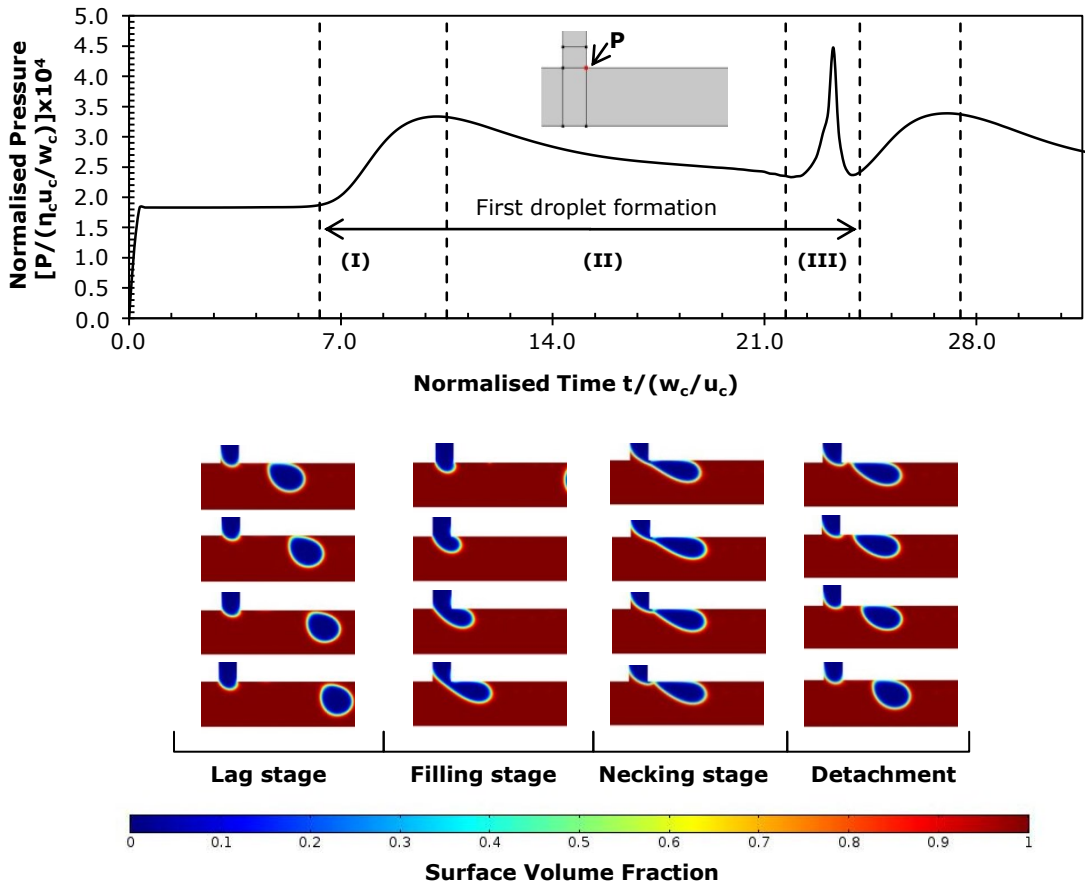


Figure 4.12: Evolution of the normalized pressure at point P during droplet breakup in a model of the T-shaped. P denotes the point at the junction and reflects the evolution of breakup mechanism. The droplet formation process can be divided into three stages: In the lag stage (I), pressure builds-up in the junction corner and continues to rise with the emergence of a dispersed thread after the detachment of the first droplet. Due to the confinement, the pressure increases as a consequence of the increased resistance to flow of the continuous phase in the main channel. In the filling stage (II), the dispersed phase start penetrating into the main stream, the droplet grows downstream and the pressure decreases. In the necking stage (III), the hydrodynamics forces deform the forming droplet and the neck connecting the thread and droplet wake becomes thinner. Once equilibrium of the hydrodynamic forces is achieved, the neck of the thread collapses and a droplet is formed. As a result of this pinch-off, the pressure shows the peak values at the corner of side channel. The dispersed thread recedes back into the side channel and the whole generation process is continuously repeated. After the first droplet detaches, the pressure starts to build up again and decreases after the thread flows into the main channel. The colour bar specifies the dispersed phase as the area where colour distinction is from 0 to 0.5 and continuous phase the area from 0.5 to 1.0.

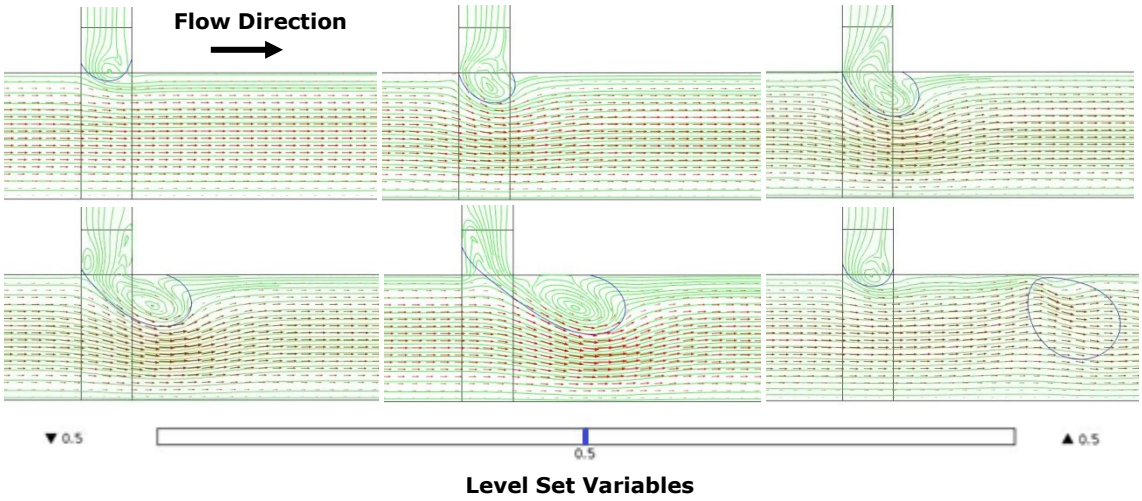


Figure 4.13: Streamline and normalized velocity vector field during droplet breakup in a model of the T-shaped in the case of 7644 mesh elements. Contour of 0.5 denotes the interface where the droplet is identified as solid blue line.

4.8 Summary

Modelling has become an essential tool for visualizing the dynamic behaviour of droplet breakup. In the present chapter, a numerical model was proposed and developed to track the fluid-fluid interfaces between two fluid phases of different density and viscosity. This applied the conservative level set method using COMSOL Multiphysics. The mathematical model used in the computational simulation utilized a numerical time-stepping procedure to obtain the model behaviour over time. The present numerical modelling approach can be subdivided into five phases: (a) modelling the dynamics and relevant hydrodynamics of the region or domain, (b) generating mesh elements, (c) simulating the interfaces in two phases, (d) interpreting the model output, and (e) extracting the useful information. In order to achieve reliable numerical results, a grid convergence assessment was conducted to describe the improvement of results by refining the grid size for calculation. As the mesh becomes finer, the model eventually approaches the final value for the droplet size and an acceptable solution was presented. Initially, numerical simulations of the Newtonian microdroplets formation in an oil-based continuous phase were

carried out. Microfluidic geometry with a T-junction configuration is employed and the predicted droplet size was computed. This allows benchmarking of the simulations against existing experimental data. The numerical model was validated by comparison with laboratory experiments and good agreement was found between experimental and simulation at lower flow rate ratios especially, Q=0.05 and below. With the modelling technique finalized, the numerical model was incorporated with a non-Newtonian stress model by modifying the viscosity expression to the Carreau-Yasuda viscosity model. These results will be employed in the subsequent parametric studies that focus on non-Newtonian fluid in the following chapters.

CHAPTER 5

The Effect of Rheological Parameters of Carreau-Yasuda Model on Shear-Thinning Microdroplets Formation and Breakup Dynamics

5.1 Introduction

The motion and formation of shear-thinning CMC droplets comprising of 0.02wt% to 1.20wt% at a microfluidic T-junction has been investigated numerically. Due to the shear-thinning behaviour of CMC droplets, a Carreau-Yasuda stress model (see Equation 3.3) was incorporated together with front-capturing scheme used in CFD. This shear-dependent constitutive model fitted well to our steady state non-linear shear measurements for polymeric CMC solutions, with asymptotic viscosities at zero and infinite shear rates, and with different degrees of shear thinning (η_o/η_∞) in steady state. Although a number of published works on numerical investigations have been reported in the area of non-Newtonian droplets formation (Sang *et al*., 2009; Qiu *et al*., 2010), none of the models take into account of the effect of rheological parameters on non-Newtonian shear-thinning fluids in microfluidics system. The particular focus of this chapter was to systematically undergo parametric studies on the influence of rheological parameters of the specified stress model, such as zero (η_o) and infinite shear viscosity (η_∞), and relaxation time (λ_{CY}), on the droplet formation processes. Systematic sets of numerical simulations were computed to monitor the evolution of CMC droplet size, which turns out to be effectively governed by the effect of λ_{CY} and η_o/η_∞. The sizes of each generated droplet are numerically determined according to Equation 4.45 (see section 4.2.2). The present work is achieved by performing a detailed investigation on the influence of these

rheological parameters in Carreau-Yasuda viscosity model. This ultimately helps to understand the physical phenomenon responsible for the changes induced by the shear-thinning properties of CMC solutions.

5.2 Parametric Studies of the Effect of Rheological Parameters

Prior to the start of a series of parametric studies, channel dimensions used in the numerical model were setup in COMSOL to match our PDMS microchips with a geometry size of 221 μm (w_c) × 90 μm (w_d) which was fabricated in-house by photolithography and soft lithography technique (see Section 3.8.1 and 3.8.2). In the present simulation, Newtonian olive oil was selected as the carrier fluid in the continuous phase along the main channel while the shear-thinning CMC polymer (applied in aqueous solution) was used as the dispersed phase fluid supplied from the lateral channel. Preliminary measurements such as fluid density, viscosity, and interfacial tension were carried out (see Section 3.4-3.6). These measured values were used in the computations subsequently. A contact angle of 180^o, representing complete repulsions of working liquid by the PDMS surface was applied. The droplet formation process was captured at a time step of 0.005 seconds which is sufficient to adequately capture the breakup phenomenon of the fluid-fluid interfaces.

5.2.1 Effect of Degree of Shear-Thinning on Effective Droplet Diameter

The rheological behavior of the shear-thinning solution plays a key role in microfluidic flow and it needs to be well-understood in order to validate any forthcoming experimental model. In the first series of parametric studies, using our numerical model, the role of degree of shear-thinning (η_o/η_∞) on droplet diameter was investigated systematically for CMC concentration ranging from 0.02wt% to 1.20wt%. For each concentration of CMC mixture, we adjusted the model parameters so that zero shear viscosity was held constant and the infinite shear viscosity was varied (see Figure 5.1). Changes in infinite shear viscosity

represent changes in the degree of shear-thinning. This aims to determine the potential of the degree of shear-thinning solution to control the droplet size and flow behavior. For a prescribed flow rate ratio (Q_d/Q_c=0.05), the droplet diameter was measured as the degree of shear-thinning was varied, with results depicted in Figure 5.2. The effect of the degree of shear-thinning on droplet diameter is found to be of considerable significance for the Carreau-Yasuda fluid used. The results reveal that the droplet diameter increased for an increase in degree of shear-thinning for all CMC concentrations. In addition, a more prominent impact on droplet diameter is found for the CMC concentration above 0.10wt%.

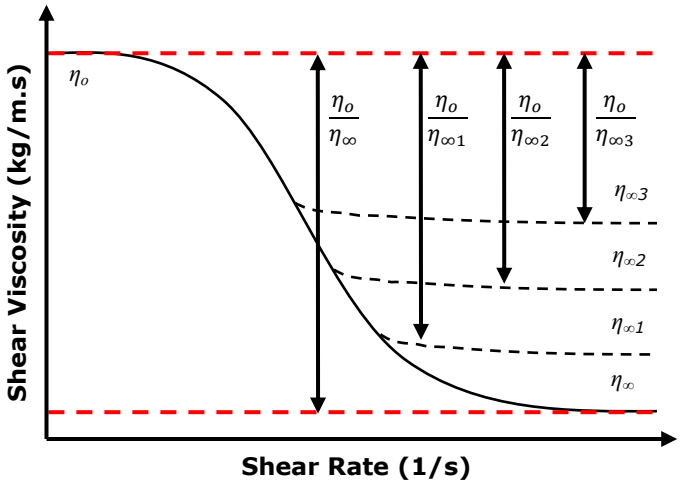


Figure 5.1: Schematic profile of degree of shear-thinning effect. Note that subscripts 1, 2, and 3 represent the variation in infinite shear-viscosity in Carreau-Yasuda model.

As elucidated in Figure 5.2, for the CMC concentration above 0.10wt%, the steep slopes reflect a sharp change in droplet diameter when the degree of shear thinning becomes smaller**.** According to Figure 5.1, as the infinite shear viscosity increases, there is a rapid approach of the shear viscosity to its limiting value.

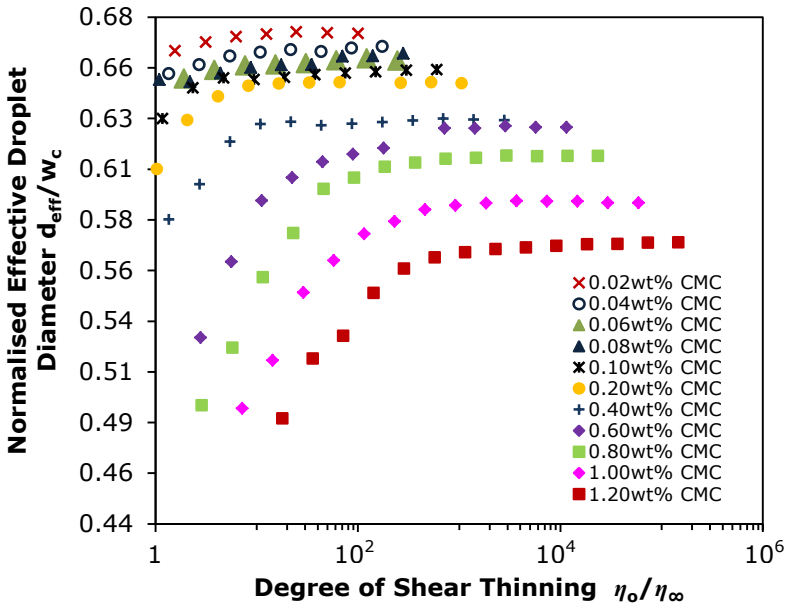


Figure 5.2: The influence of degree of shear-thinning on droplet diameter at flow rate ratio, Q of 0.05 (for system: Q_c: 2.0 ml/hr and Q_d: 0.1 ml/hr).

Due to the smaller onset values of infinite shear rate, a decrease in degree of shear-thinning causes less shear-thinning fluid behavior. The shear-thinning fluid behavior is related to the shape of the axial velocity profile depicted in Figure 5.3. As the degree of shear-thinning decreases, the axial velocity in the center of the channel increases, this causes a nearly parabolic velocity profile. On the contrary, a blunted (plug-shaped) velocity profile is found for the dispersed phase fluid with smaller infinite shear viscosity because the fluid flow encounters less resistance to high shear close to the wall. As the shear-thinning effect is greater, an increase in pressure along the neck of the dispersed threads tends to accelerate the droplet breakup process. This will inhibit the elongation of dispersed threads that contributes to the generation of smaller droplets. An interpretation made by Davidson and Cooper-White (2006) has reported that the limiting length of the drop decreases due the neck of the drop draining more rapidly as the infinite shear viscosity decreases. Moreover, decreasing the infinite shear viscosity reduces the normal viscous stresses leading to a further increase in pressure at the neck of drop prior to pinch-off. Therefore, larger droplet

diameters are generated at higher degree of shear-thinning due to the shear-thinning effects.

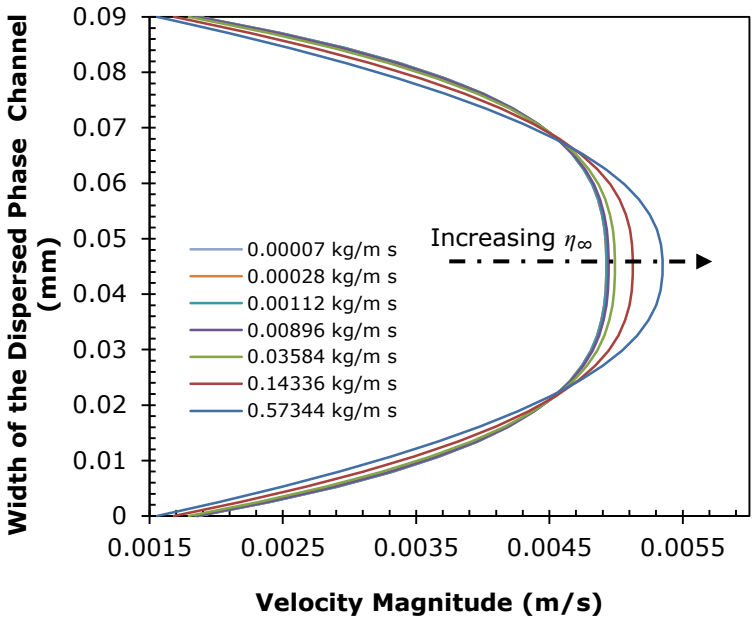


Figure 5.3: Axial velocity profile along the width of dispersed phase channel for various flow with different infinite shear viscosity (shown in legend) at fixed zero shear viscosity (4.113 kg/m.s). In each case, the velocity profile represents a fully-developed laminar flow. Dashed arrow denotes the direction of increasing infinite shear viscosity.

As the infinite shear viscosity is further reduced, a plateau region in the evolution of droplet diameter appears in a higher degree of shear-thinning (see Figure 5.2). This phenomenon could be interpreted in terms of the estimated range of typical shear rate (10^2 to 10^3 1/s) associated with the microfluidic channel, as shown in Figure 5.4 to 5.9. Higher shear rates occur adjacent to the channel wall in the channel flow for different CMC concentrations. The typical shear rate was seen in an approximate range of 200 1/s to 70001/s induced mostly in the fluid flow by the microfluidic device. However, as the dispersed fluid was forced to turn the corner of T-junction, the largest shear rate occurs at the corner edge of T-junction and thus shear-induced destabilization of the dispersed thread cause the breakup of thread leading to the formation of droplets. These highest shear rates are not indicative values of typical shear rate. As elucidated in Figure 5.4 to 5.9, it can be observed that the non-

Newtonian wall shear-rate is decreased as compared to the Newtonian wall shear rate profile. While in the lower wall shear rate range, the CMC solutions exhibited a significant increase in viscosity. This means the low shear rate viscosity occurs at the high concentration of CMC content.

Any changes made to the infinite shear viscosity parameter lead to a new onset rate of infinite shear viscosity. This variation in onset rate of infinite shear viscosity may fall within or outside the range of typical shear rate associated with microfluidic channel. The smaller onset values of infinite shear rate may be expected fall within the range of typical shear rate. Nevertheless, the smaller onset value of infinite shear rate limits the value of dispersed phase viscosity. Thus, the high-end values of the typical shear rate range may appear negligible in controlling the dispersed phase viscosity. In contrast, as the infinite shear viscosity decreases, the changes in onset values of infinite shear rate occur beyond the range of typical shear rate. Hence, dispersed phase viscosity in the entire fluid flow is purely influenced by the range of typical shear rate. The typical shear rate limits the shear-thinning effect during the droplet formation process and therefore the generated droplets diameters are observed to become almost constant at higher end degree of shear-thinning. Given the above discussion, it lead us to suggest that the onset values of infinite shear rate should be evaluated for examining the validity of the underlying assumptions.

In order to determine the onset values of infinite shear rate at each infinite shear viscosity (η_∞), the Carreau-Yasuda (Equation 3.3, see section 3.5.2) model equation was rearranged into an expression for the measurement of the onset rate of infinite shear viscosity. This will allow us to determine how the estimated typical shear rates in the present simulations compare to the onset rate for infinite shear viscosity. When the shear rate approaches infinity, $\dot{\gamma} \to \dot{\gamma}_\infty$, the magnitude of the apparent shear viscosity of the CMC solution will be equivalent

to the infinite shear viscosity ($\eta(\dot{\gamma}_\infty) \approx \eta_\infty$). The Carreau-Yasuda model contains two terms. A shear-thinning term and a constant infinite shear viscosity. We seek the shear rate at which these terms are equally balance. Equating these two terms gives:

$$\eta_\infty = [1 + (\lambda_{CY}\dot{\gamma}_\infty)^a]^{\frac{n-1}{a}} \eta_o \tag{5.1}$$

On rearranging Equation 5.2, the $\dot{\gamma}_\infty$ can be determined according to the following equation:

$$\dot{\gamma}_\infty = \frac{\left[\left(\frac{\eta_\infty}{\eta_o}\right)^{\frac{a}{n-1}} - 1\right]^{1/a}}{\lambda_{CY}} \tag{5.2}$$

For all the CMC concentrations, the values of $\dot{\gamma}_\infty$ wasreadily calculated from Equation 5.2. It has been plotted graphically against the η_o/η_∞ in Figure 5.10 on logarithmic scale with base 10. The upper and lower limits for the estimated typical shear rate range are indicated in solid black lines. As elucidated in Figure 5.10, the measured $\dot{\gamma}_\infty$ increases gradually with increasing η_o/η_∞. Additionally, for the larger η_o/η_∞, the measured $\dot{\gamma}_\infty$ are at least ten times greater than the estimated maximum typical shear rate. Comparing Figure 5.2 with Figure 5.10 shows that the effect of degree of shear-thinning on effective droplet diameter is significant only when $\dot{\gamma}_\infty$ falls in the range of typical shear rate. Once the $\dot{\gamma}_\infty$ goes beyond the upper limit of typical shear rate, the measured droplet diameter reaches systematically a plateau for larger η_o/η_∞. These findings have presented adequate information to interpret the above numerical observations for the role of typical shear rate in controlling the CMC droplet breakup process.

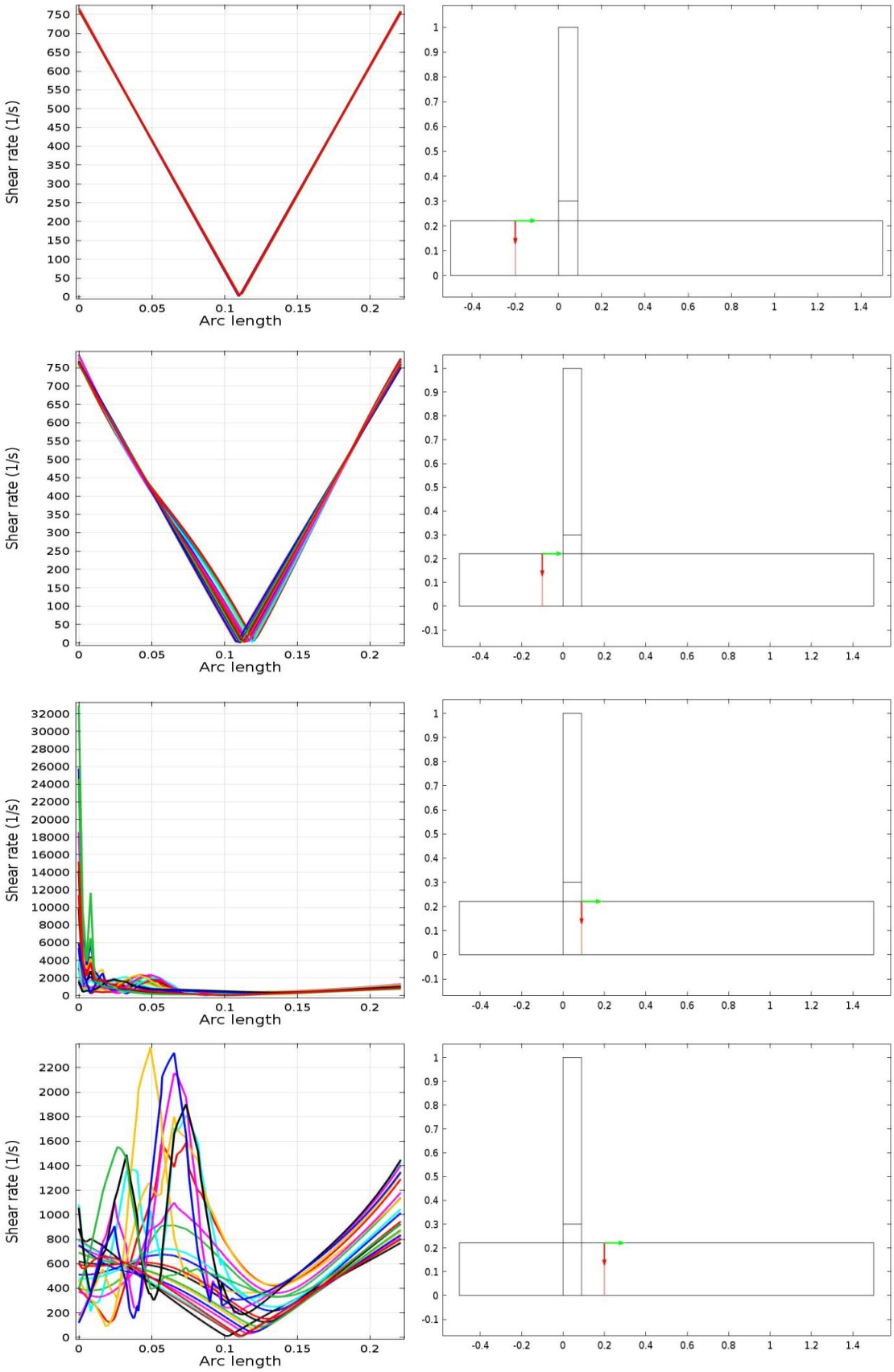


Figure 5.4: Shear rate profile for Newtonian flow along the continuous phase during the droplet breakup process (for system: η_c=0.068 kg/m.s (olive oil), Q_d/Q_c=0.05).

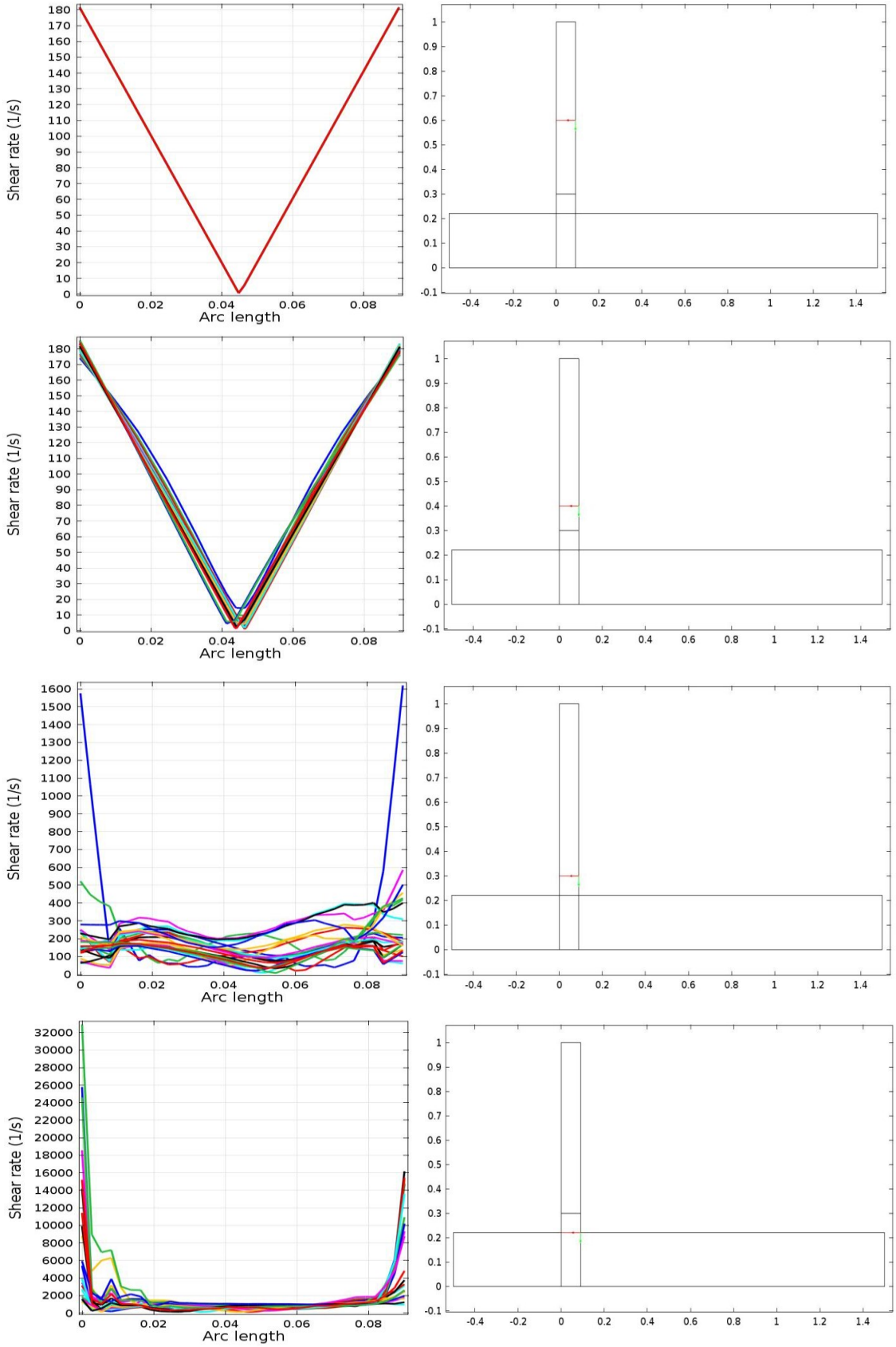


Figure 5.5: Shear rate profile for Newtonian flow along the dispersed phase during the droplet breakup process (for system: η_d=0.00093 kg/m.s (distilled water), Q_d/Q_c=0.05).

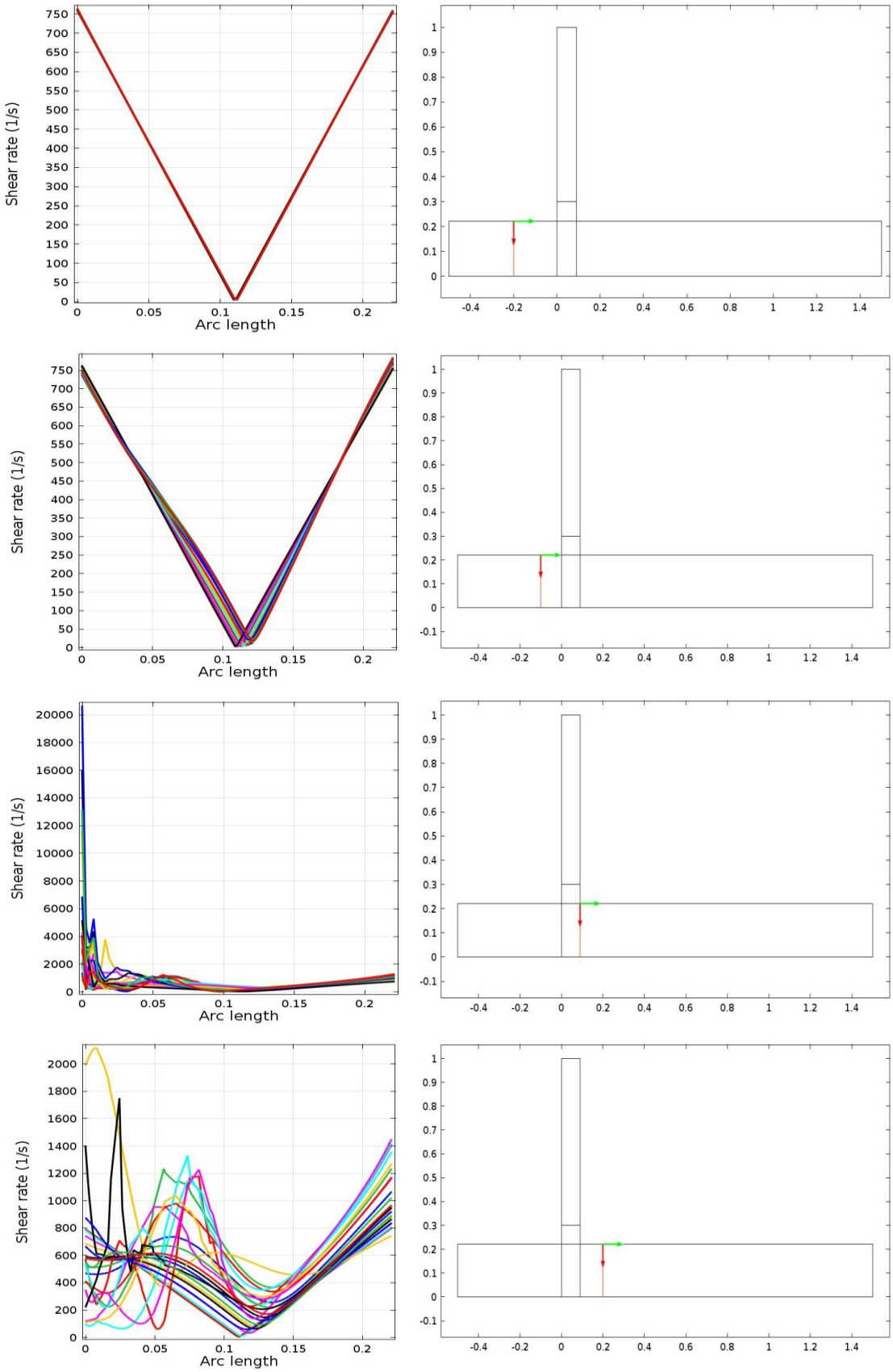


Figure 5.6: Shear rate profile for CMC concentration 0.40wt% along the continuous phase during the droplet breakup process (for system: η_o=0.19461 kg/m.s, η_∞=0.00448kg/m.s, Q_d/Q_c=0.05).

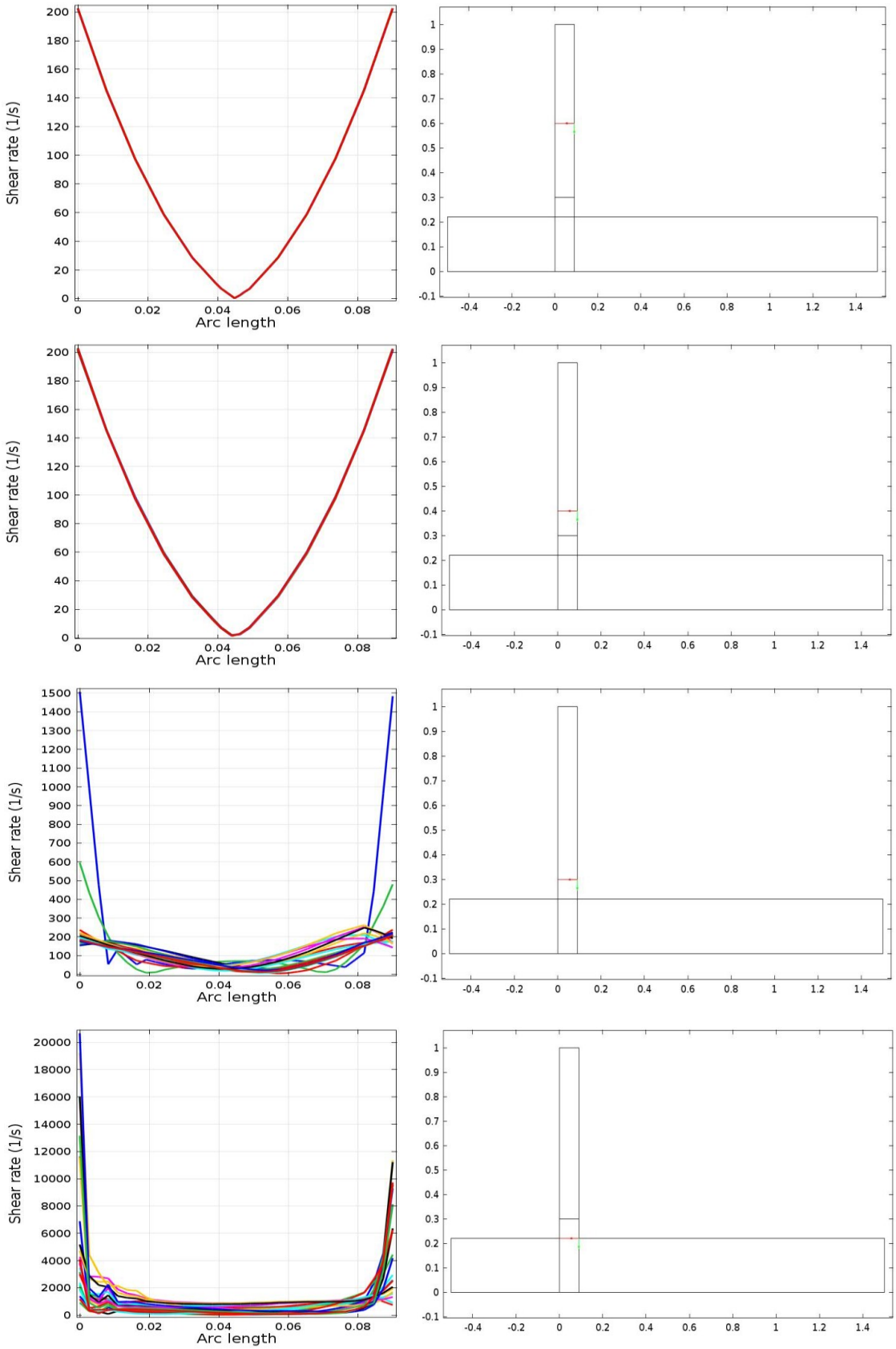


Figure 5.7: Shear rate profile for CMC concentration 0.40wt% along the dispersed phase during the droplet breakup process (for system: η_o=0.19461 kg/m.s, η_∞=0.00448 kg/m.s, Q_d/Q_c=0.05).

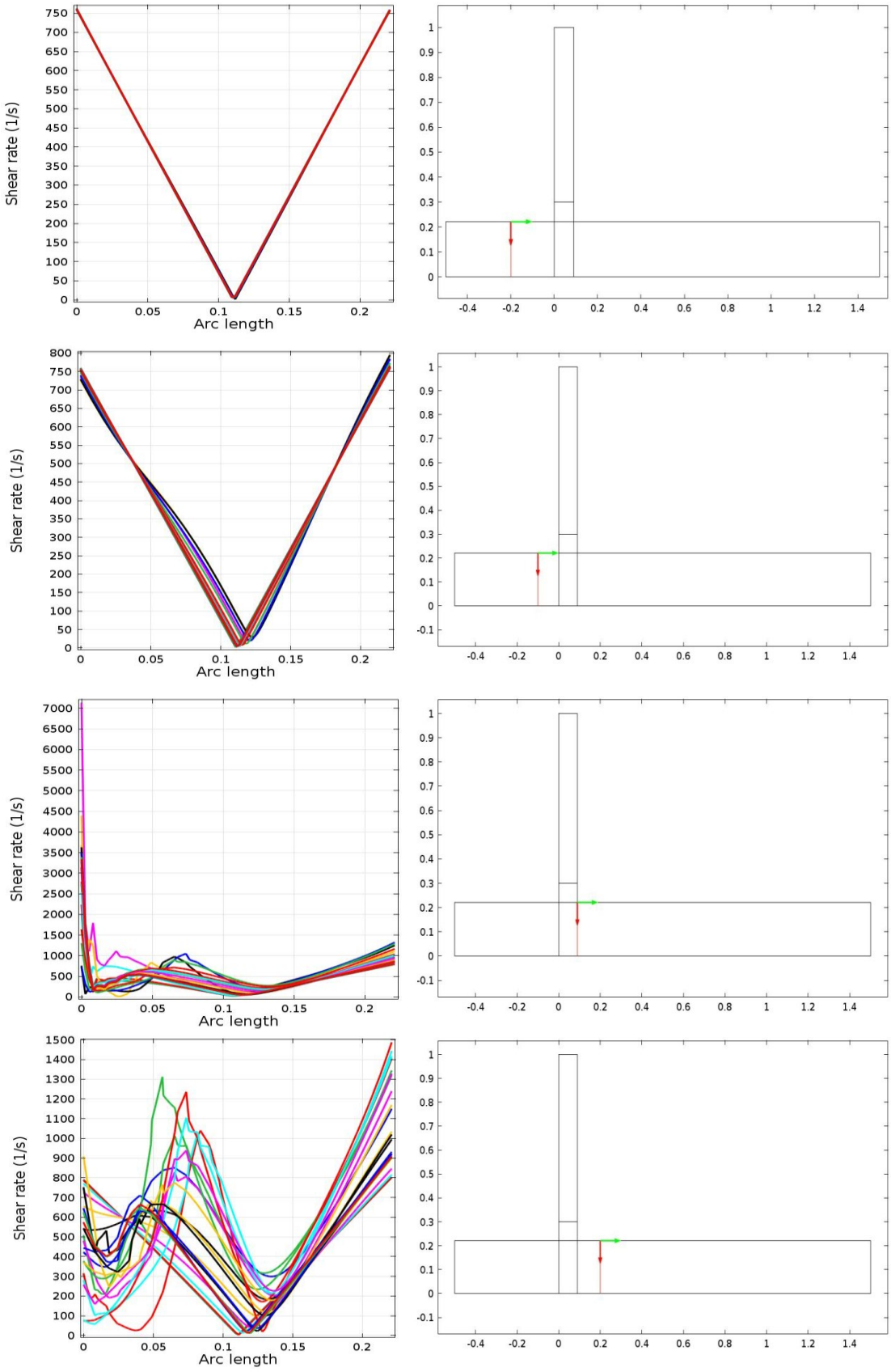


Figure 5.8: Shear rate profile for CMC concentration 1.00 wt% along the continuous phase during the droplet breakup process (for system: η_o=4.11430 kg/m.s, η_∞=0.00448 kg/m.s, Q_d/Q_c=0.05).

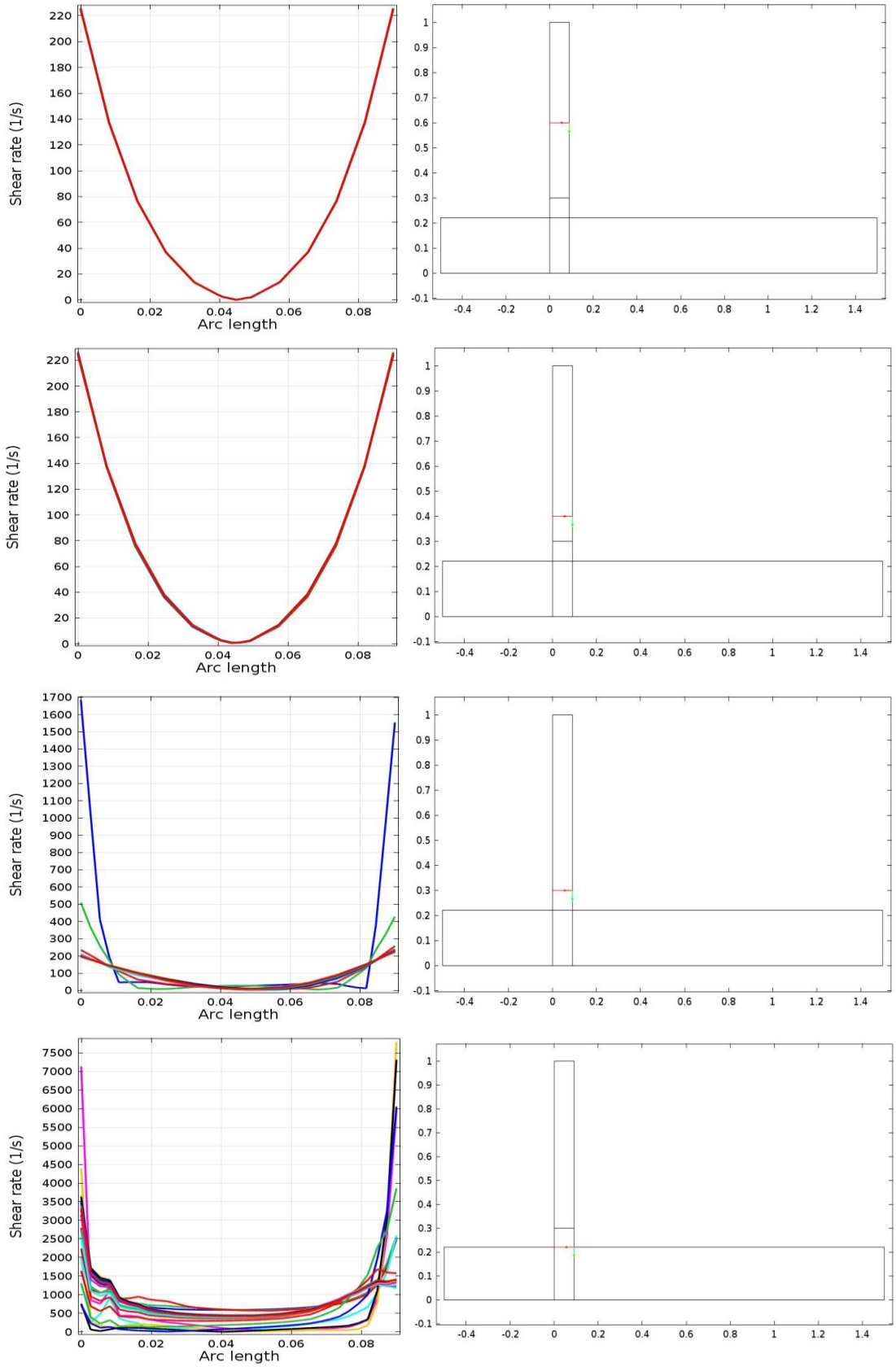


Figure 5.9: Shear rate profile for CMC concentration 1.00wt% along the dispersed phase during the droplet breakup process (for system: η_o=4.11430 kg/m.s, η_∞=0.00448 kg/m.s, Q_d/Q_c=0.05).

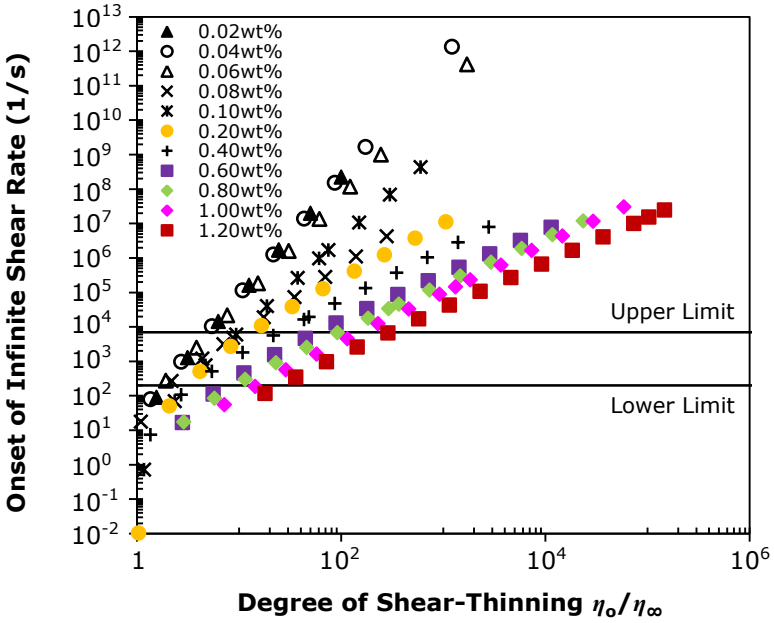


Figure 5.10: Onset rate for infinite shear viscosity over a range of degree of shear-thinning. The solid lines denote the approximated upper limit and lower limit values of estimated typical shear rate in present numerical model ($200<\dot{\gamma}<7000$ 1/s).

Figure 5.11 illustrates the sequence of snapshots of the concentration's effect on the droplet breakup process for a fixed infinite shear viscosity. Increasing the concentration of CMC solution generally gives rise to increasing viscosity. Depending on the CMC concentration, different flow patterns are observed. As the CMC concentration increases, the detachment point gradually moves from the corner of the side channel to a point downstream and forms a long neck before droplets are sheared off. This phenomenon is more significant when the concentration of CMC dispersed phase fluid is above 0.40wt% (see Figure 5.10). As the concentration rises, an increase in dispersed phase viscosity tends to increase the fluid resistance and therefore increase the viscous pressure in microfluidic channel. This causes a longer thread to be formed due to the larger resistance to flow. A higher viscous pressure overcomes the opposing capillary pressure and leads to a laminar elongated dispersed thread further downstream of the main channel. A study has made by Zhang and Basaran (1995) reported that an increase in dispersed phase viscosity contributes to an increase in the flow resistance, resulting in longer threads being formed which greatly stabilize

the growing drop. Also, reductions in droplet diameter are observed when the dispersed phase viscosity increases. The monotonic decreases in droplet diameter with CMC concentration is shown in Figure 5.12. As CMC concentration increases, a longer dispersed thread is formed due to the larger resistance to flow, which has been discussed previously. When the dispersed thread undergoes breakup, smaller droplets are generated because the high viscous effects tempers the onset of the Rayleigh-Plateau instability.

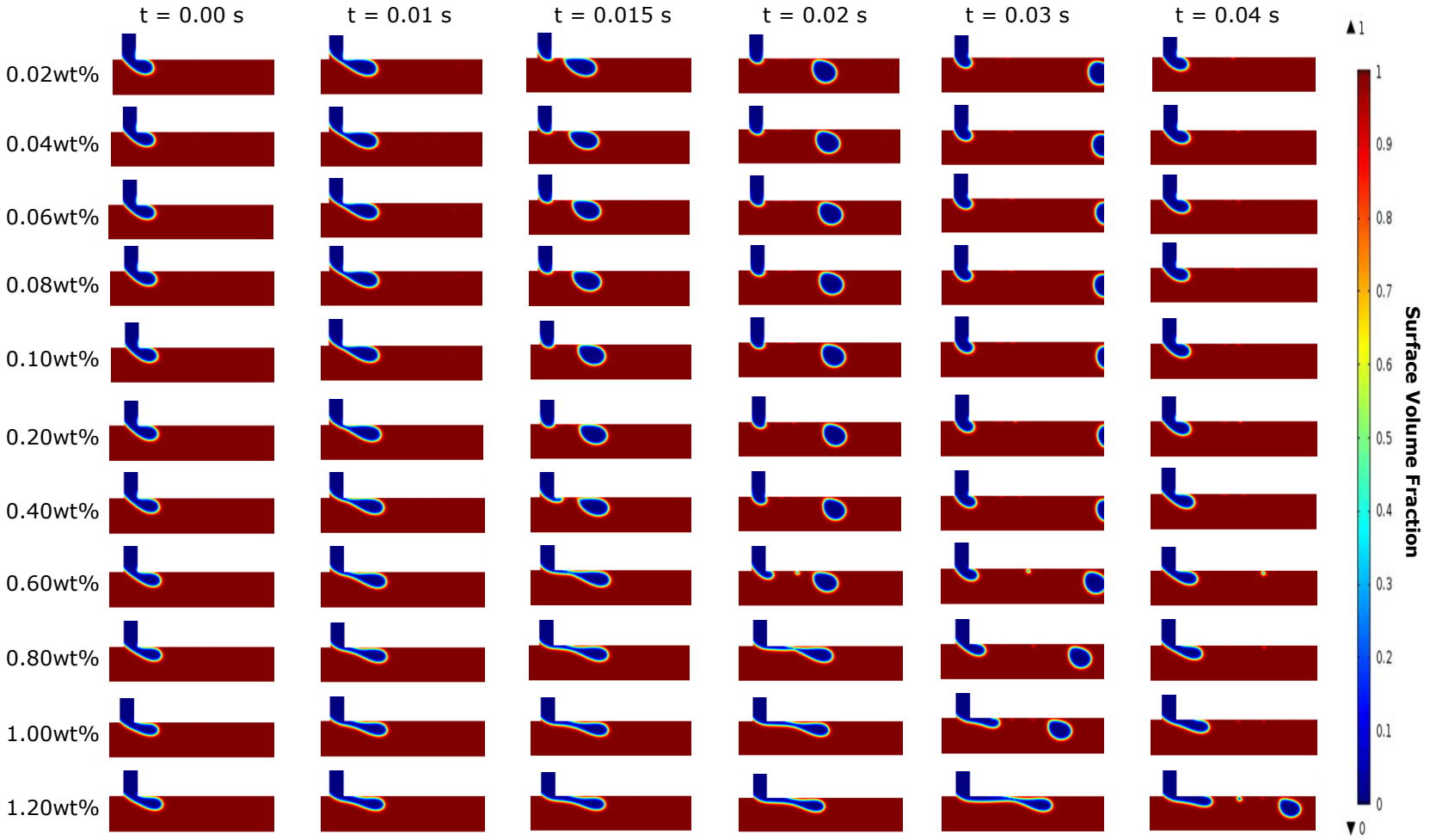


Figure 5.11: Snapshots of two-dimensional (2D) simulation of CMC-in-olive oil droplet breakup process for different CMC concentration (for system:η_∞=0.00448 kg/m.s, Q_d/Q_c=0.05).

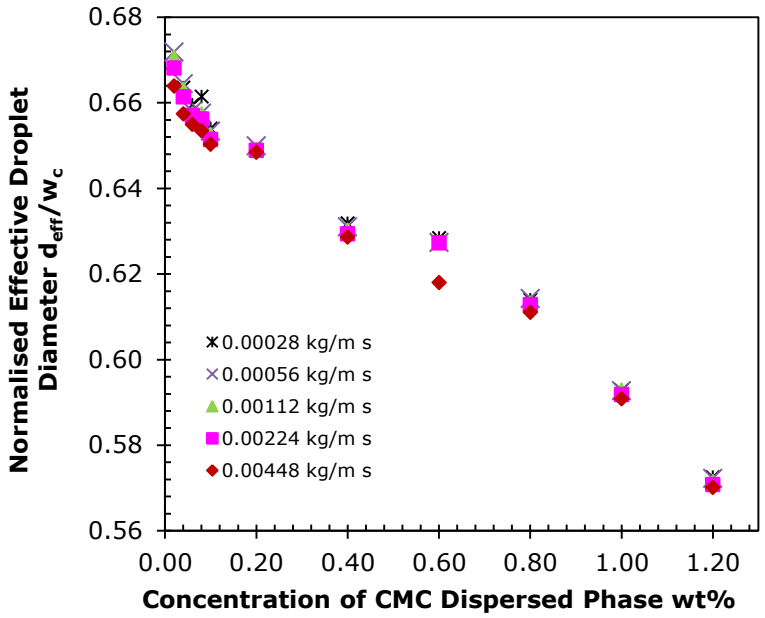


Figure 5.12: Effect of CMC viscosity on normalised effective droplet diameter (d_{eff}/w_c) during droplet breakup process for various flows with different infinite shear viscosity (shown in the legend).

5.2.2 Effect of Relaxation Time on Effective Droplet Diameter

A schematic profile of the relaxation time's effect on the rheological properties of a Carreau-Yasuda fluid is illustrated in Figure 5.13. The reciprocal of relaxation time ($1/\lambda_{CY}$) corresponds to a critical shear rate that provides a useful indicator of the onset shear rate for shear-thinning (Benchabane and Bekkour, 2008). Our rheological measurement revealed that the shear-thinning behavior of each CMC concentrations is seen above a critical shear rate (see Figure 3.3). Benchabane and Bekkour (2008) have reported that the fluid resistance to flow is reduced at higher shear rates for shear-thinning polymer solution. This is mainly due to the disentanglement of the polymer coils in solution or increased orientation of the polymer coils in the flow direction by internal shear stress (Benchabane and Bekkour, 2008). The role of the relaxation time on the droplet diameter is quantified systematically in present study. This aims to understand how the variation in relaxation time affects droplet diameter during the droplet breakup process. In the present simulation, any changes made to the polymer relaxation time leads to a new-onset value of shear-thinning. For a prescribed flow rate ratio (Q_d/Q_c=0.05), the droplet diameter is plotted graphically against relaxation

time in Figure 5.14. As depicted in Figure 5.14, results reveal that droplet size increases as the relaxation time increases (critical shear rate decreases). Moreover, a plateau region in the evolution of droplet diameter is found as the critical shear rate is further decreased. This phenomenon for the variation in droplet diameter is found to be more significant for higher CMC concentration.

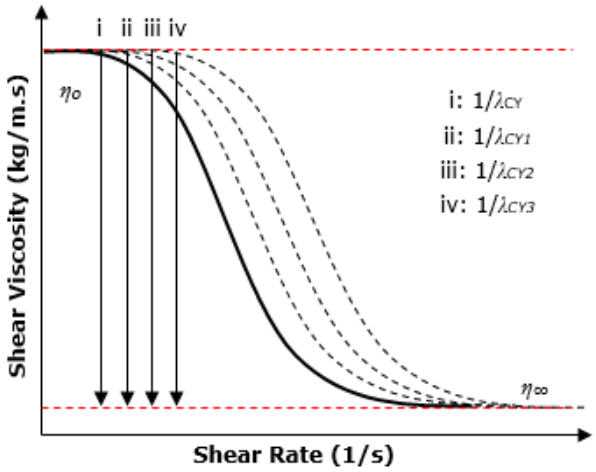


Figure 5.13: Schematic profile of relaxation time effect. Note that subscripts 1, 2 and 3 represent the variation in relaxation time constant in Carreau-Yasuda model.

A longer relaxation time indicates an earlier onset shear rate for shear-thinning region. Before a critical shear rate is reached, the alignment of polymer molecules to the flow field remains in an equilibrium condition. Once the shear rate exceeds the critical relaxation time, deformation of polymer molecules starts to occur and the alignment of molecules no longer stays in the equilibrium condition. Hence, the viscosity of dispersed phase begins to decrease and the shear-thinning nature becomes pronounced. The longer the relaxation time constant, the smaller the critical shear rate is. This contributes the rapid deformation of the polymer molecules and causes a highly shear-thinning profile. The characteristic of the shear-thinning fluid determines the shape of the axial velocity profile depicted in Figure 5.15. As the relaxation time increases, shear-thinning nature of the dispersed phase becomes dominant which causes a blunted velocity profile in the core region of dispersed phase flow. Therefore, the dispersed phase encounters less resistance. This will hinder the incoming

dispersed phase thread as it elongates some distance downstream, thus the pressure drop across the emerging droplet increases. This rise in pressure causes breakup at the corner of the T-junction, resulting in the formation of larger droplets.

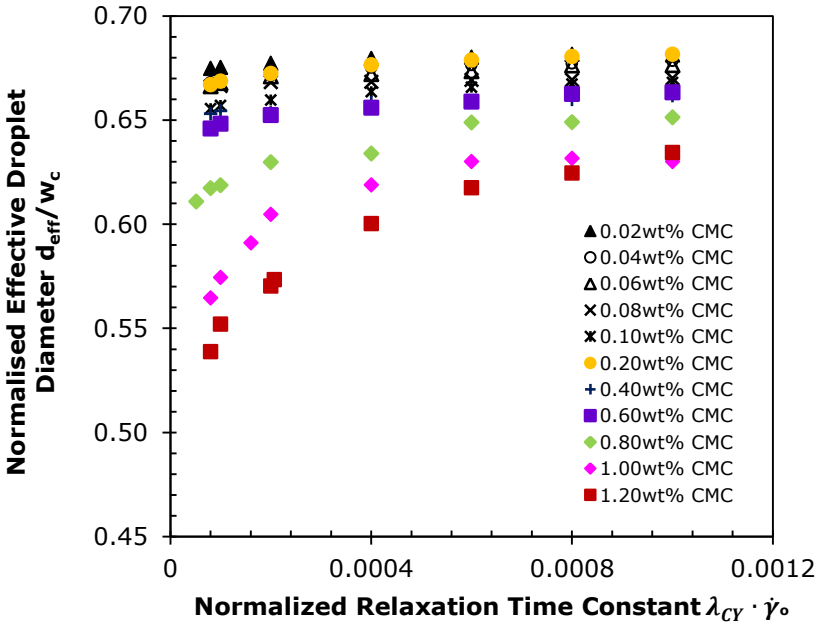


Figure 5.14: The effect of relaxation time constant against on normalised CMC effective droplet diameter at flow rate ratio, Q of 0.05 (for system: Q_c: 2.00 ml/hr and Q_d: 0.10 ml/hr).

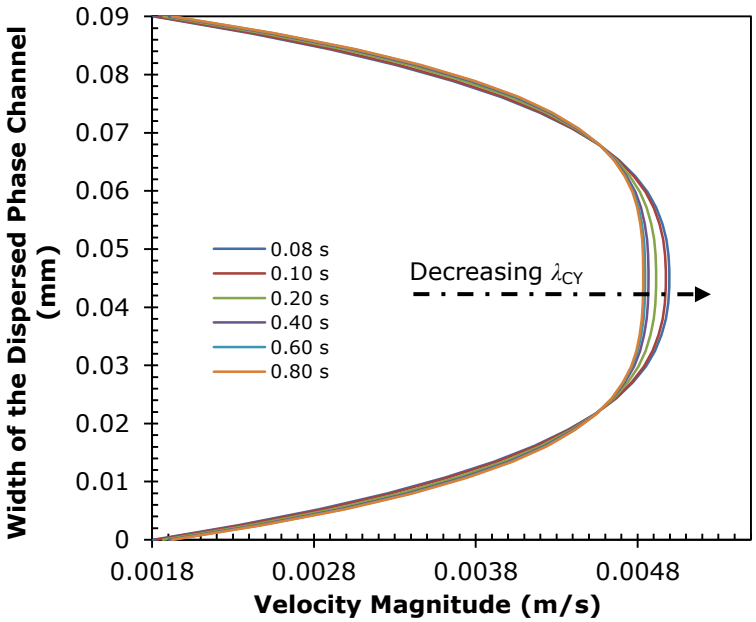


Figure 5.15: Axial velocity profile along the width of dispersed phase channel for various flow with different relaxation time (shown in legend) for CMC concentration of 1.0wt% (η_o:4.1143 kg/m.s; η_∞:0.0031 kg/m.s). In each case, the velocity profile represents a fully-developed laminar flow. Dashed arrow denotes the direction of decreasing relaxation time constant.

5.3 Summary

In our present numerical model, the effect of independently varying two Carreau-Yasuda model parameters, namely degree of shear-thinning (η_o/η_∞) and relaxation time constant (λ_{CY}), on the evolution of CMC droplet diameter have been demonstrated. The potential of the η_o/η_∞ and λ_{CY} in controlling the droplet diameter and flow behaviour has never been systematically determined in microfluidic context. Thus, these calculations aim to develop a comprehensive understanding on the impact of varying rheological quantities on shear-thinning microdroplets formation. For the numerical computations, the variation in η_o/η_∞ and λ_{CY} exhibits a major impact on the evolution of CMC droplet diameter. Nevertheless, the effective droplet diameter dependence on these rheological parameter effects becomes less marked at the high end values. Some conclusions are summarized as follows:

(1) At fixed η_o, an increase in η_∞ will cause a decrease in η_o/η_∞. When the η_o/η_∞ is reduced, the resulting axial velocity profile is approximately parabolic in shape. While an increase in η_o/η_∞ will cause the velocity profile to become flatter and blunted in front. For this reason, it shows that the shear-thinning effect is greater for larger η_o/η_∞. Due to the more pronounced shear-thinning behaviour, larger droplet sizes are generated. Nevertheless, the typical shear-rate associated with microfluidic channel was found to limit the shear-thinning effect on CMC droplet breakup process for the larger η_o/η_∞. Once onset rate for infinite shear viscosity approaches a value beyond the upper limit of the typical shear rate, the CMC droplet diameter reaches a plateau and no longer continues to increase with further increase in η_o/η_∞.

(2) For shear rate above $\dot{\gamma}_{\lambda_{CY}}$, the CMC dispersed phase viscosity steadily decreases with increasing shear rate. At each CMC concentration, the shear-thinning behaviour is enhanced by increasing the λ_{CY} or decreasing the critical shear rate. The axial velocity profile changes from parabolic shape to a more blunted shape for the longer λ_{CY} due to earlier onset rate for shear-thinning

region. Such behaviour is a characteristic of the highly shear-thinning nature of the CMC dispersed phase. For the lower CMC concentration, variation in λ_{CY} does not exhibit a significant effect on droplet sizes. Droplet sizes are strongly influenced by λ_{CY} for the larger CMC concentration.

Consequently, the present study reveals the interesting shear-thinning droplet formation phenomena during the systematic variation in rheological parameters. These results showed that the dynamics of shear-thinning breakup process can be very sensitive to the rheological quantities. From previous studies, the rheological characteristics of CMC solution are strongly depending on the concentration. Previous findings also found that different behaviours such as thixotropic and viscoelasticity can be found at the higher concentrations (Ghannam and Esmail, 1997). There are available constitutive equations can be applied to represent different non-Newtonian characteristics. Apart from η_o/η_∞ and λ_{CY}, these equations involve others rheological parameters such as yield stress, critical shear-stress and shear modulus (Chhabra and Richardson, 2008). Hence, the impact of these rheological parameters can be the future works which are great of interest to understand more the droplet formation process of CMC solutionwith different non-Newtonian behaviourin the microfluidics system.

CHAPTER 6

The Effect of Fluid Physical Properties on Shear-Thinning Microdroplets Formation and Breakup Dynamics

6.1 Introduction

There are a limited number of investigations that focused on the effect of physical properties of non-Newtonian shear-thinning fluids on droplet formation dynamics. The governing physical parameters play a significant role in the motion and shape evolution of droplets in microfluidic flow. It is imperative to better understand the dynamics and relevant hydrodynamic flow in microfluidics. The main focus of this chapter is on parametric studies of the influence of governing parameters: viscosity ratio (λ), contact angle (θ), and interfacial tension (σ) upon the physical processes of non-Newtonian shear-thinning CMC microdroplets formation at a microfluidic T-junction. A series of parametric studies were performed to establish the variation of physical properties that can be ultimately used to tailor the breakup dynamics of the CMC microdroplets in microfluidics researches.

6.2 Parametric Studies of the Effect of Physical Properties

The dispersed phases simulated have a range of viscosities similar to that of aqueous solutions. They comprise of 0.02wt% to 1.20wt% CMC solution in an olive oil phase which serves as the continuous phase. In the subsequent sections, the effects of CMC concentration at fixed dispersed to continuous phase viscosity ratio, interfacial tension and wetting properties were numerically studied to predict the effective droplet diameter, formation time, and generation frequency. The resultant droplet formation time and generation frequency are measured

between the breakup of the previous and current CMC microdroplets. The droplet formation process was captured at a time step of 0.0005 seconds and constant flow rate ratio of 0.05.A contact angle of 180°, representing the complete repulsions of working liquid by the channel wall surface, was applied in the computation.

6.2.1 Effect of Fixed Dispersed to Continuous Phase Viscosity Ratio on Effective Droplet Diameter

Earlier numerical and experimental investigations in Newtonian microfluidic flow revealed that the viscosity of the liquid phase is one of the dominant factors influencing the physical droplet breakup process (Garteski *et al*., 2006; Liu and Zhang, 2009; Bashir *et al*., 2011; Fu *et al*., 2012; Wehking *et al*., 2014). Viscosity ratio of the continuous and dispersed phases becomes a key factor for the control of the droplet size in the emulsification process. The present study focuses on the effect of viscosity ratio ($\lambda=\eta_o/\eta_c$) on the evolution of CMC microdroplets diameter. The λ is defined as the quotient of zero shear viscosity of dispersed phase (η_o) with the viscosity of continuous phase (η_c). Changing the CMC concentration changes both the zero shear viscosity and the degree of shear-thinning in the dispersed phase. In order to observe the effect of changes in shear-thinning in isolation, the viscosity of the continuous phase is varied to always match the η_o of the dispersed phase. Thus, a constant λ of 1 is maintained for all CMC concentrations. Figure 6.1 illustrates the plot of the effects of fixed dispersed to continuous viscosity ratio on the normalised droplet diameter of CMC solutions with concentrations ranging from 0.04wt% to 0.40wt%. By considering the aforementioned state with λ=1, the resulting droplet diameter decreases as the CMC concentration increases.

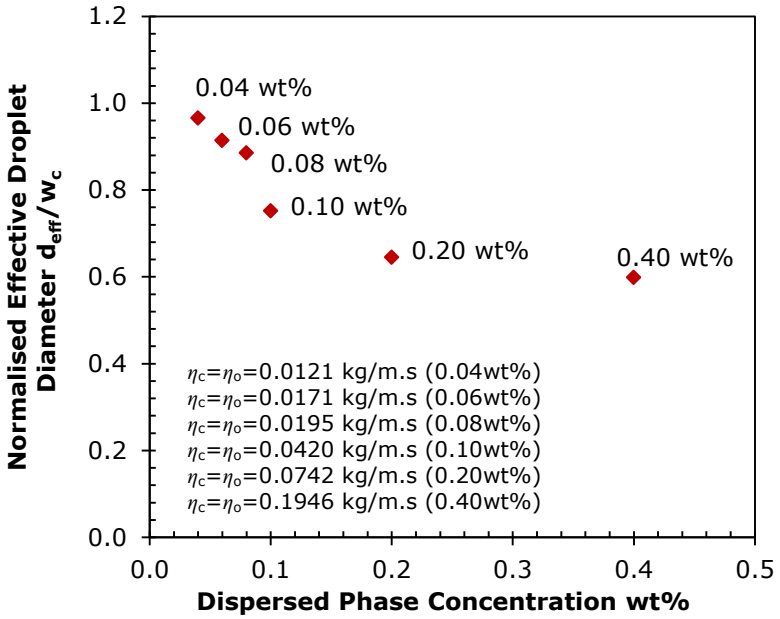
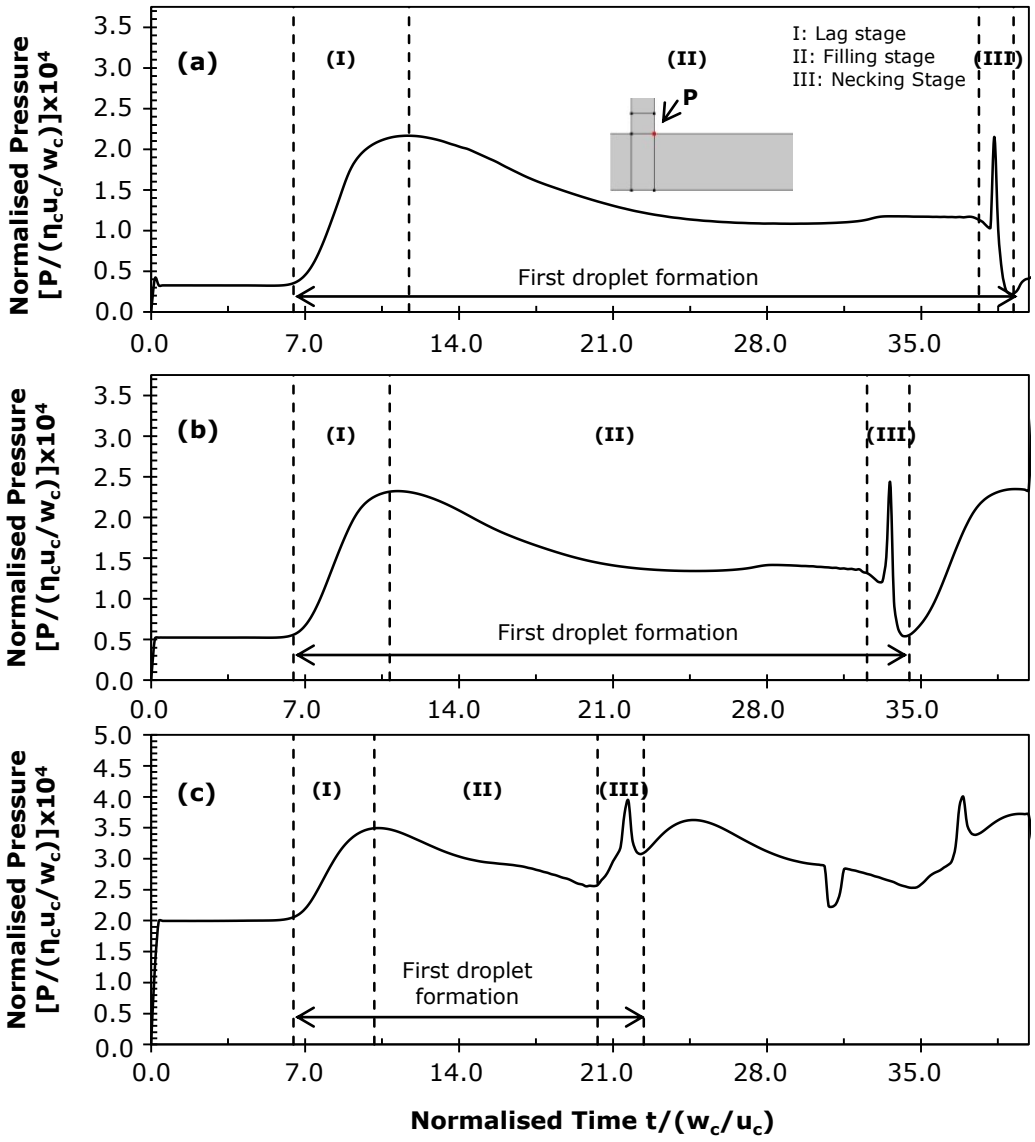


Figure 6.1: Combined effects of both phases viscosity on the effective droplet diameter of CMC solutions for various CMC concentrations (for system: λ=1, Q_d/Q_c=0.05).

At very low shear, the CMC dispersed phase fluid is completely structured without any disruption. Due to the shear-thinning character of CMC solution, as the flow develops, the dispersed phase viscosity (η_d) decreases with the rate of the shear strain and thus the η_c dominates. This dominance of η_c is increasingly important for the breakup of the neck of the dispersed thread. For the higher concentration of CMC fluid, the shear-thinning effect is more pronounced. The more strongly shear-thinning the fluid, the earlier in time $\eta_c >> \eta_d(\dot{\gamma})$, leading to earlier droplet breakup. As the η_c effect becomes greater, the neck of droplets will drain more rapidly as the pressure acting along the neck of the dispersed threads increases, as illustrated in Figure 6.2. This will tend to accelerate the droplet breakup process resulting in the formation of smaller shear-thinning CMC droplets (see figure 6.1).



CMC Concentration	Pressure Peak (Pa)	Periods (s)	Snapshots
0.04wt%	860.88	0.0950	
0.08wt%	973.13	0.0805	
0.20wt%	1575.70	0.0430	

Figure 6.2: Normalised Pressure profile of (a) 0.04wt%, (b) 0.08wt%, (c) 0.20wt% CMC for the effect of fixed dispersed to continuous phase viscosity ratio on CMC droplet breakup process (for system: λ=1, Q_d/Q_c=0.05). P denotes the pressure at the corner of T-junction. The sharp pressure peak in the given data corresponds to the droplet breakup at the corner of the side channel as shown in the extracted images. The maximum magnitudes of the pressure peak and the formation periods under different CMC concentration are listed above.

6.2.2 Effect of Fixed Dispersed to Continuous Phase Viscosity Ratio on Droplet Formation Time

The shape of the fluid interface of the upstream side of the neck joining the droplet with the inlet evolves with time when the tip enters the main channel and develops in the downstream direction. Over a short period of time, the neck thins and finally pinches off after the continuous phase fluid has fully entered the main channel (Garstecki *et al*., 2006). The time (t_d) taken by a droplet to grow and pinch off is an important factor to the dynamics of droplet formation process. Moreover, it is a key consequence of the different governing parameters such as viscosity, as we discussed.

Figure 6.3 illustrates the plot of the combined effects of both phases viscosity on the normalised droplet formation time of CMC solutions in the case of λ=1. The results revealed that droplet formation time decreases with increasing the viscosity of the continuous phase at different dispersed phase concentration. The breakup is caused by the large shear stress exerted on the interface by the continuous phase. At λ of 1, η_d decreases with flow and the shear stress acting on the interface becomes prevalent. This will further increase the pressure along the neck of the dispersed threads and leads to droplet breakup. Thus, for more strongly shear-thinning fluids, η_d becomes dominant earlier, leading to faster droplet breakup. Thus, Husny and Cooper-White (2006) has also reported that the droplet breakup time can be easily tailored by changing the viscosity ratio between the continuous and dispersed phase fluid. Here we show that the shear-thinning can be used to obtain the similar result at fixed viscosity ratio.

The effect of shear-thinning on the droplet diameter growth at fixed λ of 1 was examined. Figure 6.4 shows the evolution of the CMC droplet diameter during the droplet formation process. As seen in Figure 6.4, the emerging droplet grows in size linearly when the tip of dispersed phase thread enters the main channel.

The diameter grows until certain limiting size, at which the droplet is finally pinched off due to the complex balance between the shear stress and interfacial tension. For CMC concentration at 0.40wt%, the dispersed phase droplet starts growing later than other dispersed phase concentrations. This is mainly due to the viscous drag force imposed by the continuous phase is sufficiently large to cause the flow moves downstream prior to pinch-off. It is important to notice that for the system analysed in present study, the viscous drag is usually the dominant force acting on the emerging droplet since η_d decreases with flow, as discussed previously. Hence, after a small overshoot, a constant size of an isolated droplet is attained. We determined the size using the circular area equivalent diameter over time and the evolution of the diameter is investigated beyond the tracking point at the corner of T-junction as illustrated in Figure 6.5.

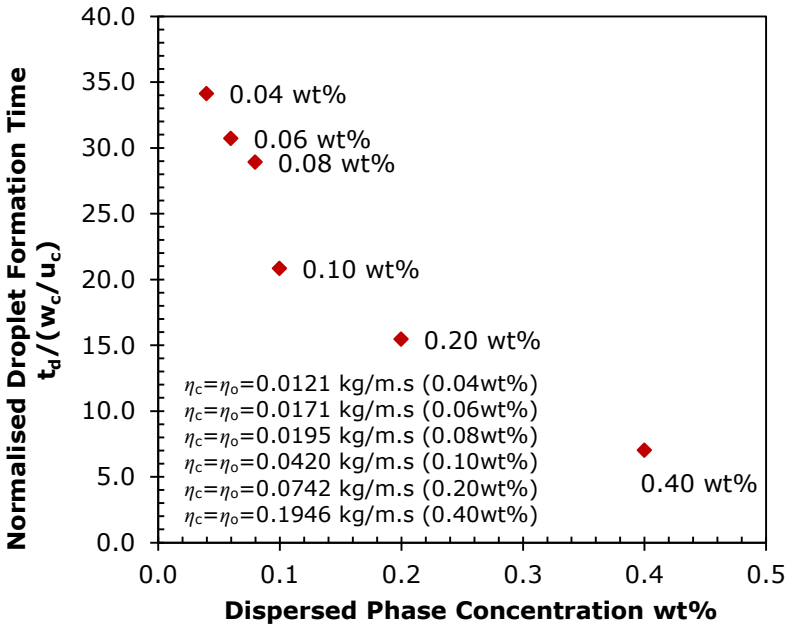


Figure 6.3: Combined effects of both phases viscosity on the droplet formation time of CMC solutions for various CMC concentrations (for system: λ=1, Q_d/Q_c=0.05).

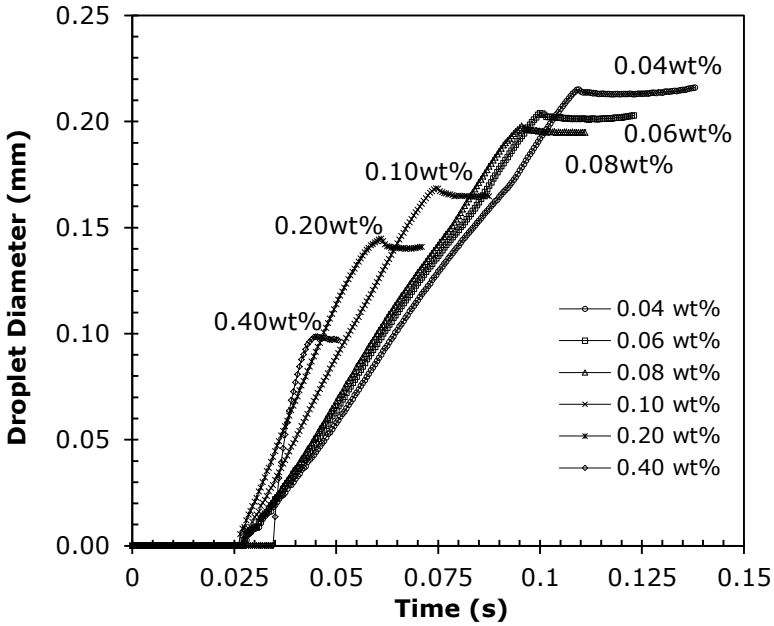


Figure 6.4: Diameter growth of CMC droplet as function of time for various CMC concentrations during droplet formation process (for system: λ=1, Q_d/Q_c=0.05).

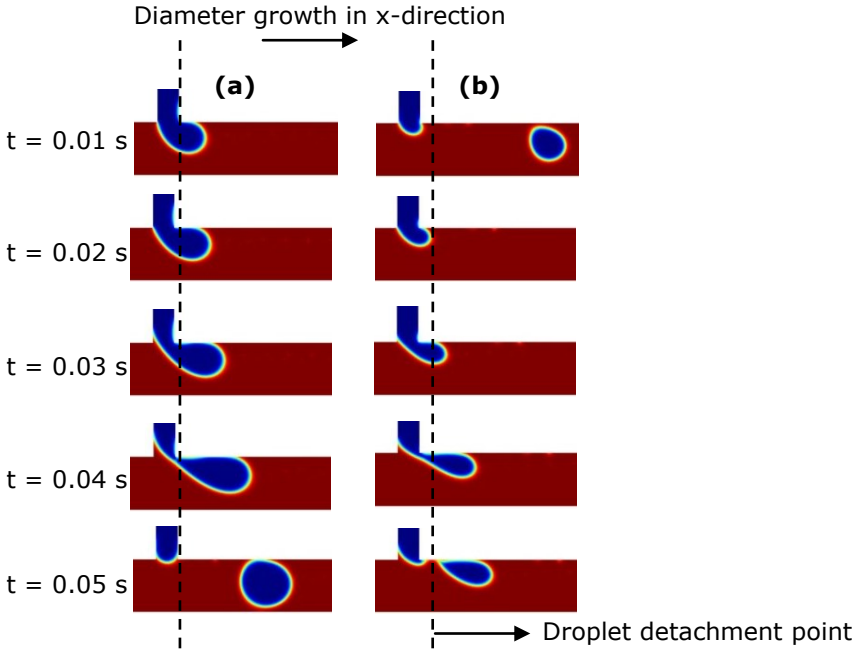


Figure 6.5: Snapshots of 2D simulation comparison of droplet growth of CMC droplet as function of time between (a) 0.06wt% and (b) 0.20wt% CMC solution (for system: λ=1, Q_d/Q_c=0.05). The growths of diameter were determined when the droplets grow downstream beyond the detachment point (dashed line).

6.2.3 Effect of Fixed Dispersed to Continuous Phase Viscosity Ratio on Droplet Generation Frequency

The droplet generation frequency (f_d) can be defined as the number of the complete droplet formation cycles per unit time. It means the droplet generation frequency is determined by the measurement of the inverse of droplet formation time ($f_d=1/t_d$). Figure 6.6 illustrates the plot of the effect of continuous phase viscosity on the normalised droplet generation frequency at fixed λ of 1. As elucidated in Figure 6.6, the generation frequency of droplet increases as the η_c increases. This is because the formation process is accelerated by the shear stress and so tends to produce greater amounts of droplets when $\eta_c >> \eta_d(\dot{\gamma})$, as discussed in section 6.2.2.

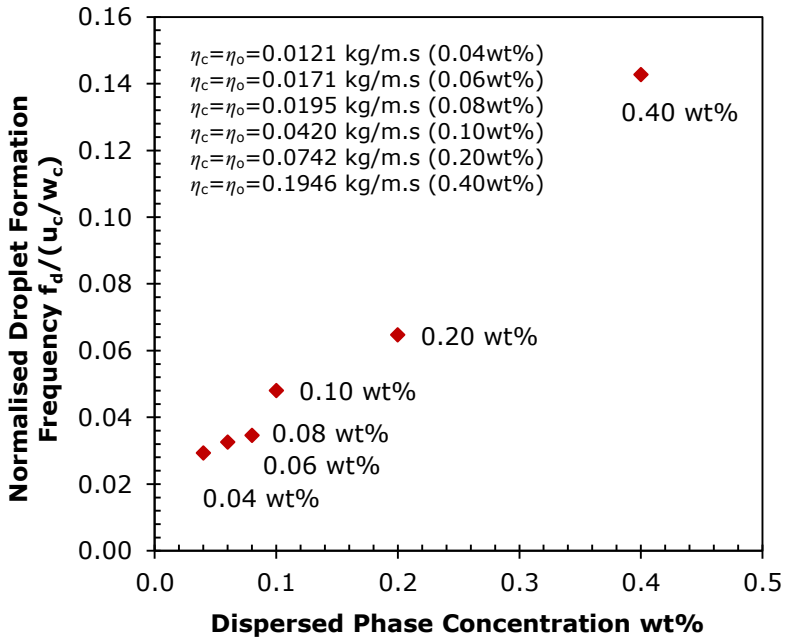


Figure 6.6: Effect of fixed viscosity ratio on the droplet generation frequency of CMC solutions for various CMC concentrations (for system: λ=1, Q_d/Q_c=0.05).

6.2.4 Satellite Droplets Formation

As the η_c increases relative to $\eta_d(\dot{\gamma})$, the viscous effects dominate over interfacial ones. Thus, η_c resists the pinching and will cause some fluid to get trapped in the thread becoming satellite droplet (Abate and Weitz, 2011). At the higher concentration of CMC (>0.10wt%), we found that instabilities in microfluidic flow

produced satellite droplets less than a micron in size behind the large primary drop. The satellites droplets increased in size for higher dispersed phase concentration. A sequence of snapshots of droplet formation at various concentration of CMC solution were taken and illustrated in Figure 6.7. The presence of satellite drops during the final pinching of shear-thinning CMC droplets was observed and illustrated in Figure 6.7. Zhang and Basaran (1995) reported that secondary satellite drops were formed due to the sudden acceleration created by the unbalanced force of surface tension after the formation of the primary droplets. As seen from Figure 6.7, the satellite drops tend to move near the wall of the microchannel, while the primary drops move away some distance from the wall. Yang *et al*. (2008) reported that, due to their large volume, the primary drops breakup due to the higher velocity flow of the main channel, whereas the smaller surface area of satellite droplets are only exposed to the flow projected from the side branch; thus, the primary drop and the satellite droplet are located in different streamlines at the moment of breakup.

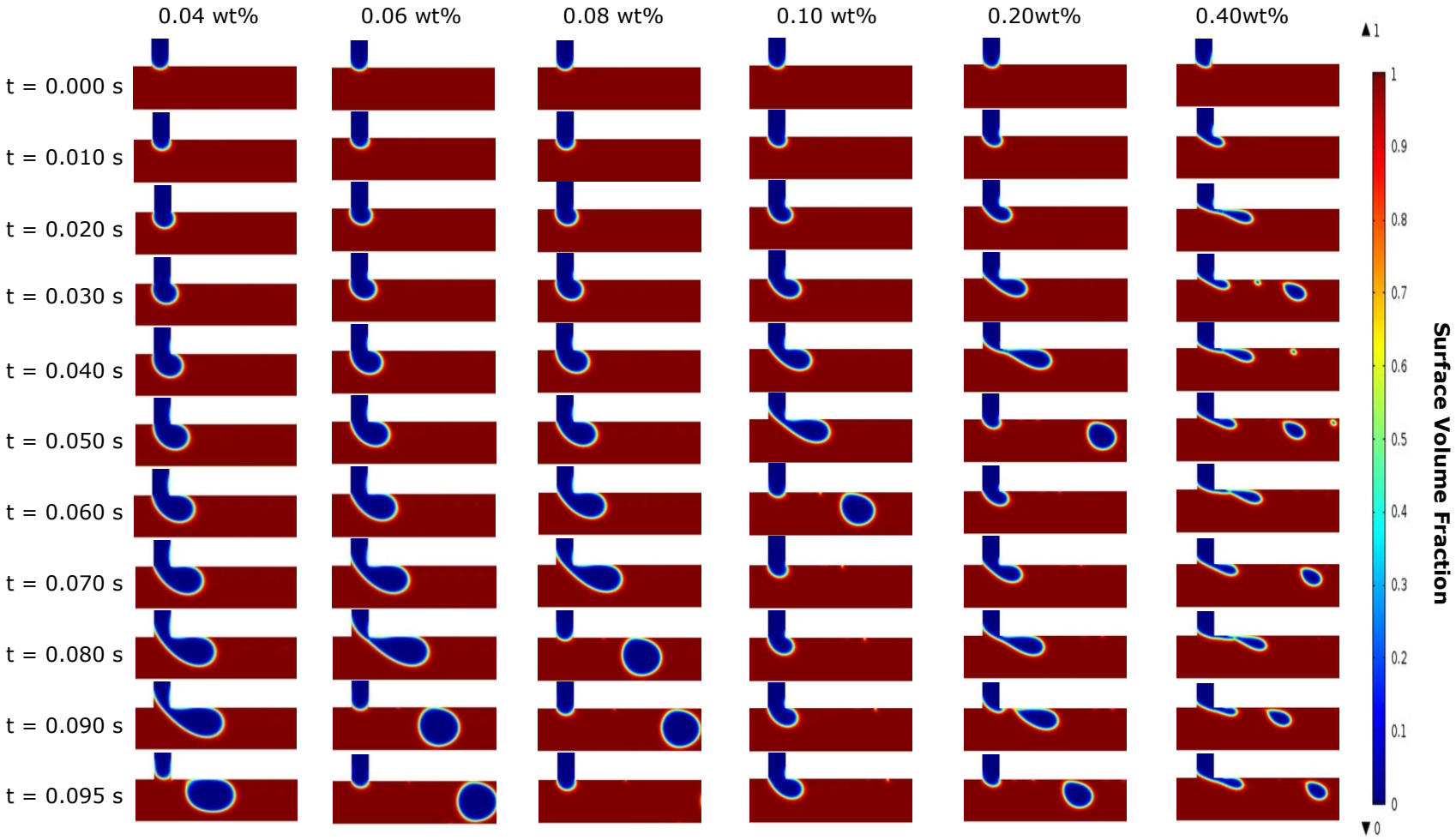


Figure 6.7: Snapshots of two-dimensional (2D) simulation of the effect of continuous phase viscosity on CMC-in-olive oil droplet breakup process for different CMC concentration (for system: λ=1, Q_d/Q_c=0.05).

6.2.5 Effect of Contact Angle on Effective Droplet Diameter

Most studies of droplet generation in microfluidic devices involve the study of the contact angle (θ) effect on the shape, size and the generation frequency of droplets with Newtonian properties (Liu and Zhang, 2009; Bashir *et al*., 2011). In this preceding analysis, the effect of non-Newtonian droplets with shear-thinning behaviour in nature was not been available. Due to the resulting high surface area to volume ratios of microsized devices, the interaction between the solid surface of the microchannel and the fluid has been a major focal point in affecting the dynamics of the droplet formation process. In microfluidic geometry with a T-junction configuration, the continuous phase and dispersed phase were initially dispensed separately at desired flow rates through the microchannel with a hydrophobic solid surface. The continuous phase needs to wet the channel walls preferentially in order to separate the dispersed phase, which tends to be non-wetting, from the walls and eventually break it into droplets. The wetting properties of the channels wall with two flowing immiscible liquids are of utmost importance for the stability of the droplets formation process in microfluidic devices (Kumacheva and Garstecki, 2011). The magnitudes of surface wettability can be characterized by static contact angles, and the dynamic effects are not explicitly taken into account. Neglecting the impact of fluid property on surface wettability, the alterations in contact angle for the same fluid is mainly studied for different concentration of CMC solutions.

The primary focus of the present study is to highlight the role of the wetting characteristic of the channel walls on the non-Newtonian droplet formation process. The contact angle of the CMC droplets at the channel walls was varied from 130^{o} to $180^{o}$and implemented in the simulation. Considering a three-phase coexisting system, this range of contact angles covers partial wetting behaviour to complete wetting behaviour. In this present simulation, olive oil (η_c=0.068 kg/m.s) was selected as the continuous phase fluid in the main channel while the

CMC polymer was used as the dispersed phase fluid, supplied from the orthogonal channel. Figure 6.8 illustrates the plot of the effect of different wetting conditions on the normalised effective droplet diameter of each CMC concentration. As elucidated in Figure 6.8, the droplet diameter decreases as the θ increases for most concentrations. However, θ has major impact on the droplet size for the concentration from 0.02wt% to 0.80wt%, causing a step change in droplet diameter at about 150^{o}. Interestingly, the effect of θ on the droplet diameter was found to be opposite at higher concentration of CMC solution (≥1.00wt%).

The numerical simulation predicts that the droplet diameter is independent of θ when it is larger than 150^{o}, which is in agreement with numerical results from Sang *et al*. (2009) and Bashir *et al*. (2011). Sang *et al*. (2009) reported that larger contact angles ($\theta \geq 165^{o}$), corresponding to the poor wettability of the dispersed phase to the channels wall, had a negligible effect on the resulting diameter of 1,6-hexanediol diacrylate droplet in polyvinyl aqueous solution based on VOF formulation. Bashir *et al*. (2011) also reported that the length of the resulting water droplets in n-Dodecane oil solution remains constant in the super-hydrophobic ($\theta \geq 165^{o}$) regime using the LS approach. For smaller θ, Liu and Zhang (2009) reported that the droplet interfaces are prone to be normal to the channel walls. This phenomenon is seen in Figure 6.9, 6.10 and 6.11, clearly demonstrating that the dispersed thread has strong tendency to attach to the wall surface at smaller θ for CMC concentration below 0.80wt%. As θ increases, the channel wall surface becomes unfavourable to the CMC dispersed fluid. This implies that the larger contact angle tends to minimize the adhesion force between the dispersed fluids with the channels wall, causing a larger shear force to be exerted on the thread by the continuous stream. The shearing force is more efficient and sufficient to overcome the adhesion force, resulting in rapid deformation of the droplet and thus a smaller droplet diameter was generated

(Rosengarten *et al.*, 2006; Bashir *et al.*, 2011). When the concentration increases above 0.80wt%, the droplet diameter increases with increasing θ, but the dependence was very slight (see Figure 6.8). Figure 6.12 illustrates a profile of jet formation prior to pinch-off for the CMC concentrations above 0.4wt% at different wetting conditions. As elucidated in Figure 6.12, above 0.80wt% CMC, it is clearly seen that the tip of the thread is repelled from the wall when the dispersed thread moves from the corner of the side channel to a point downstream. This can be explained as the resistance to flow reduces at the wall surface when the shear-thinning effect is more pronounced. Hence, the greater velocity in the center of the mainstream will direct the flow of the thread away from the wall, causing a significant reduction in the wall adhesion on the fluid interface. Therefore, the impact of contact angle is less important to the breakup process.

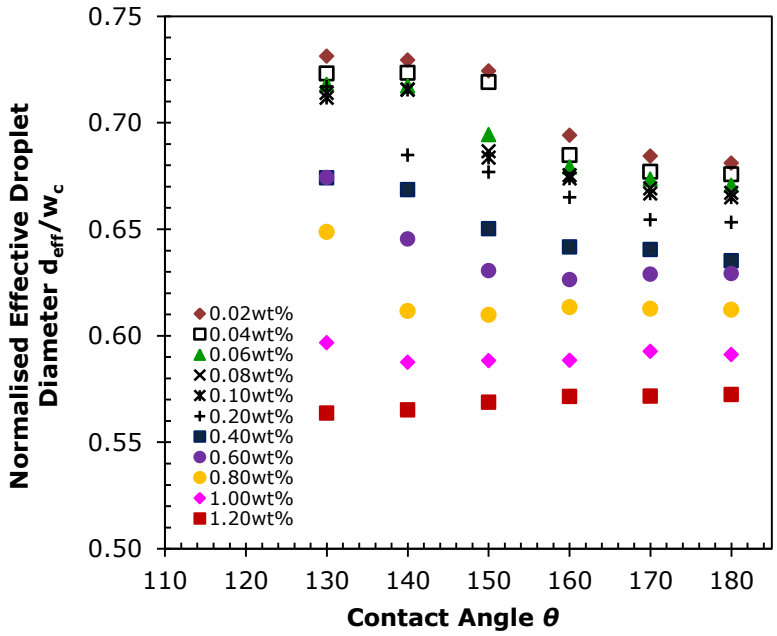


Figure 6.8: Effect of contact angle on the effective droplet diameter of CMC solutions.

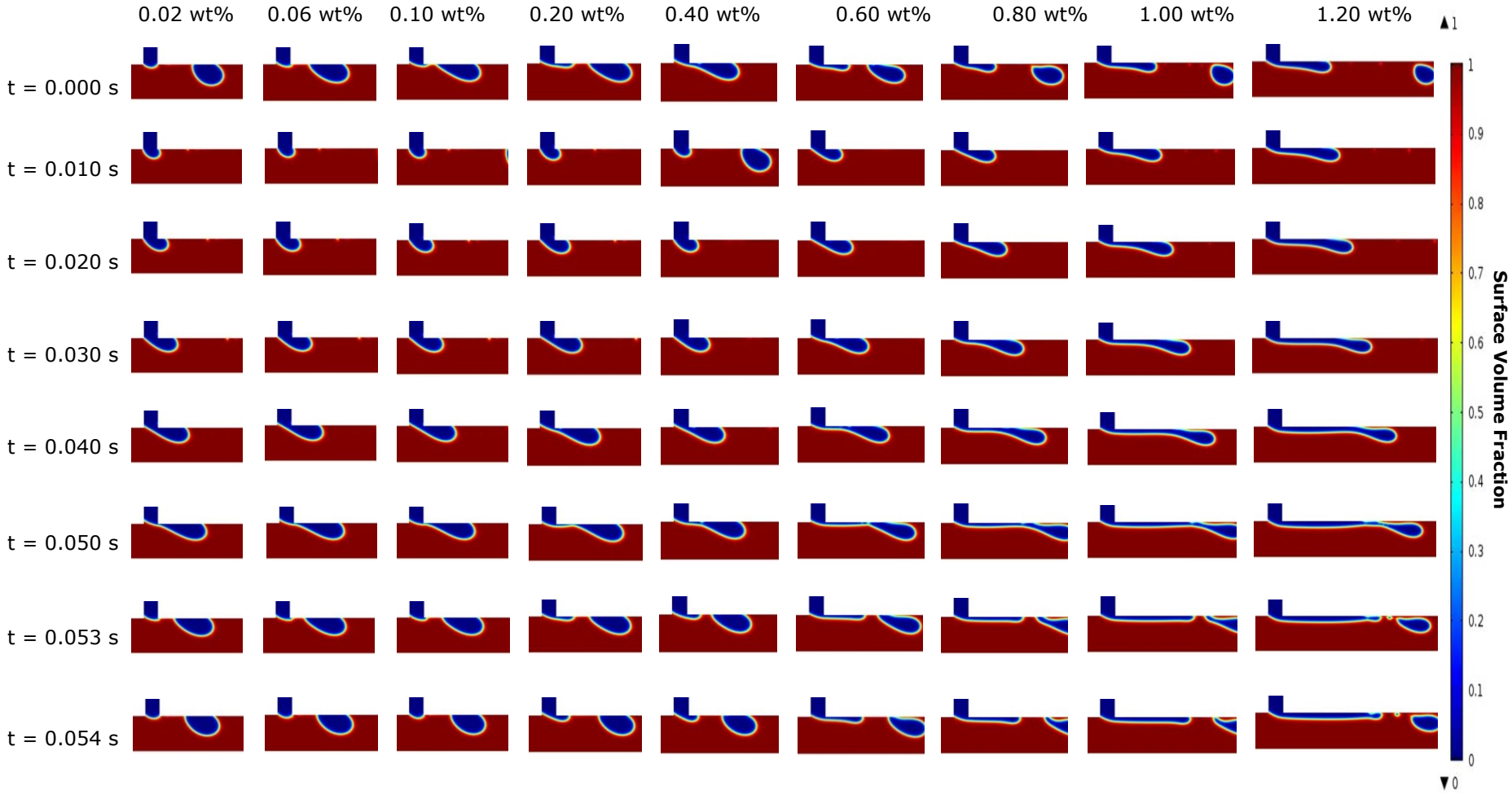


Figure 6.9: Snapshots of two-dimensional (2D) simulation of the effect of contact angle on CMC-in-olive oil droplet breakup process for different CMC concentration (for system: θ=130°, Q_d/Q_c=0.05).

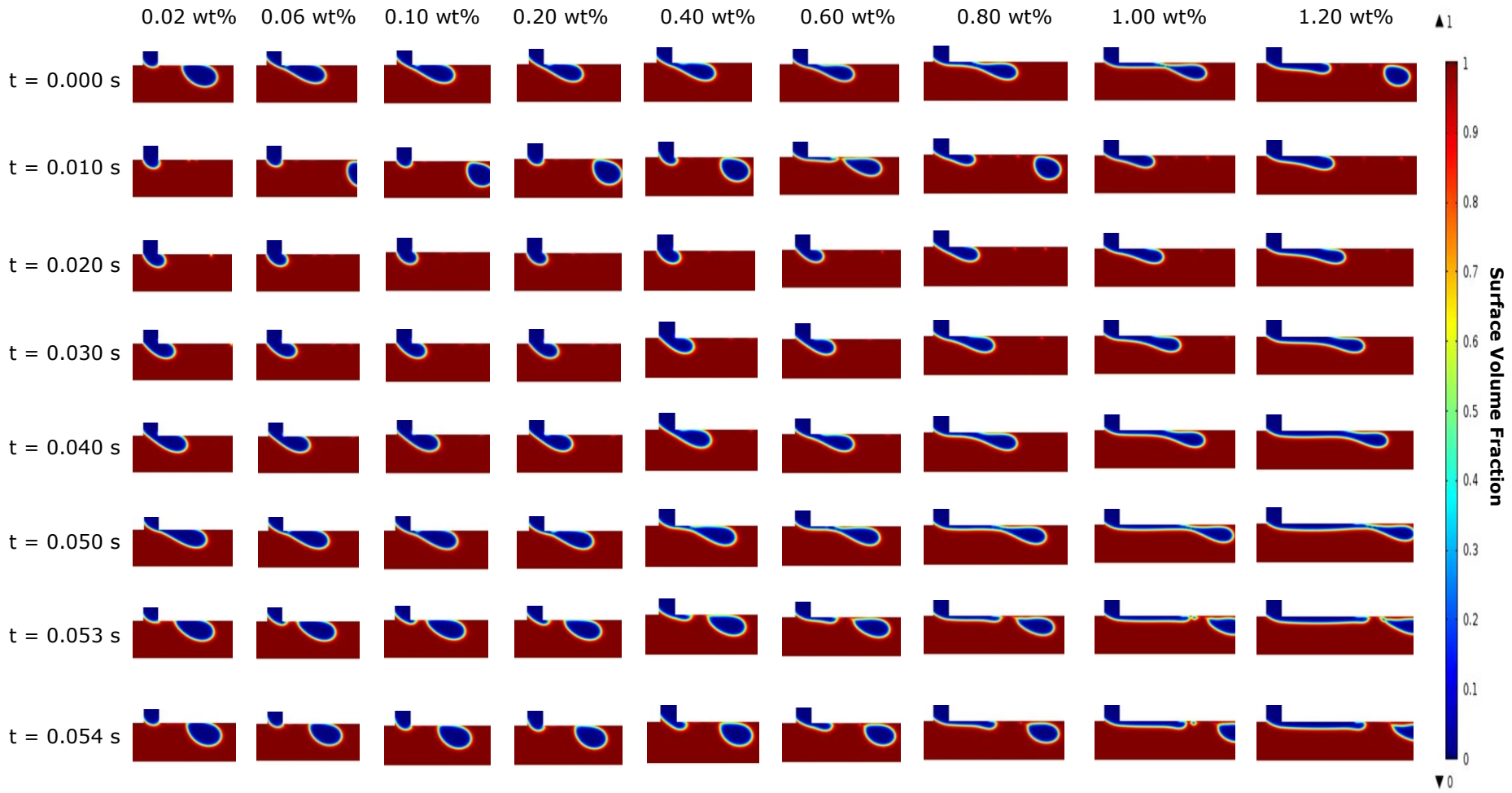


Figure 6.10: Snapshots of two-dimensional (2D) simulation of the effect of contact angle on CMC-in-olive oil droplet breakup process for different CMC concentration (for system: θ=150°, Q_d/Q_c=0.05).

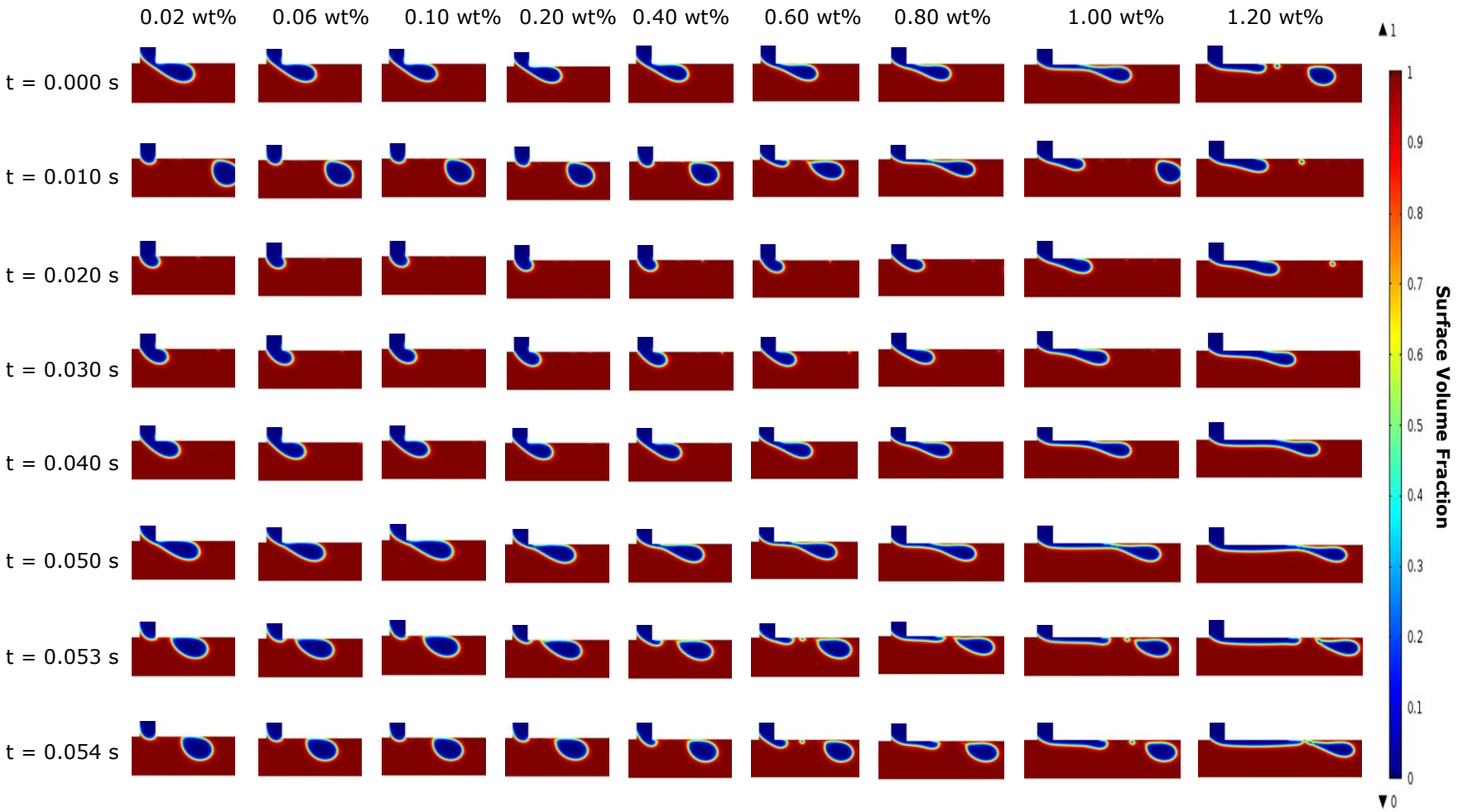


Figure 6.11: Snapshots of two-dimensional (2D) simulation of the effect of contact angle on CMC-in-olive oil droplet breakup process for different CMC concentration (for system: θ=170°, Q_d/Q_c=0.05).

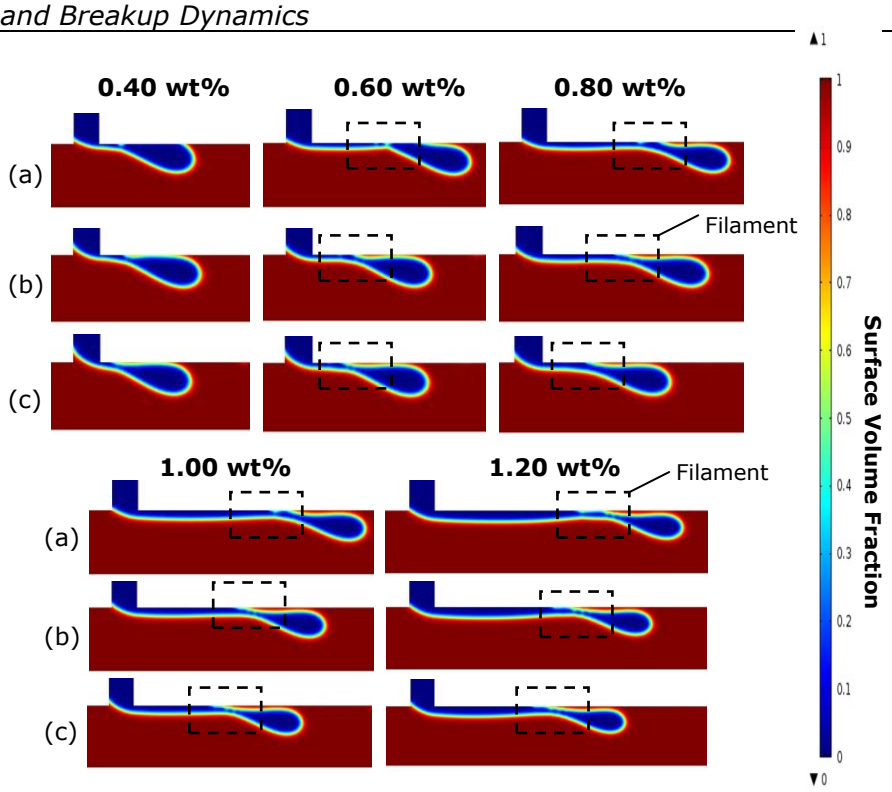


Figure 6.12: Jet and filament formation profile prior to pinch-off for CMC concentrations above 0.4wt% at contact angle: (a) 130°, (b) 150°, (c) 170°(for system: Q_d/Q_c=0.05).The dashed box denotes the region where the formation of thin filament.

The variation in droplet diameter for various concentrations at fixed θ is shown in Figure 6.13. For a fixed value of θ, the droplet diameter decreases monotonically as the CMC concentration increases. This is mainly due to the fact that the decreasing of the viscosity is enhanced by the shear-thinning behaviour under shear flow, which increases the pressure at the neck leading to acceleration of droplet breakup at higher CMC concentration. This is consistent with the related theory of interface dynamics (Davidson *et al*., 2004; Davidson and Cooper-White, 2006). Apart from this qualitative consideration, a smaller diameter of CMC droplets was generated when there was a longer thread during breakup. This may be due to the Rayleigh-Plateau instability.

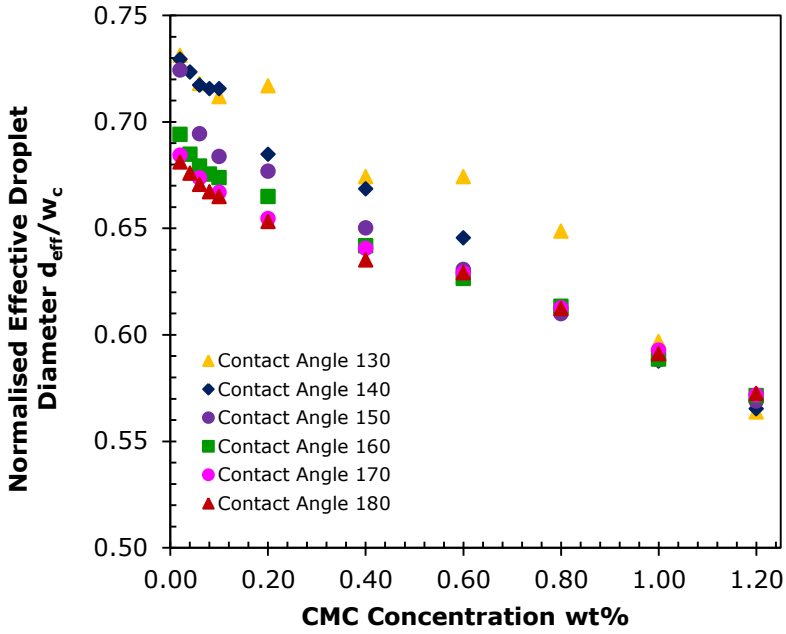


Figure 6.13: Variation in normalised effective droplet diameter of CMC droplets for various CMC concentrations at each contact angle.

6.2.6 Effect of Contact Angle on Droplet Formation Time

The influence of surface wettability on the total droplet formation time, that is the transition between a growing droplet and a detached droplet, was discussed. The results are plotted graphically in Figure 6.14, which illustrates the effect of contact angle on the normalised droplet formation time. As a result, the predicted droplet breakup process occurs at shorter times as the θ increases. The inertial force, shear force and surface wettability are competing effects influencing the dynamics of the droplet breakup process. For the smaller θ, the wettability driving the fluid toward the surface and the contact area between the droplets and solid surface increases. The smaller θ reduces the droplet deformation and postpones the breakup process to later times. As θ increases, the thread are no longer flowing close to the wall because their adhesion strength to the wall reduces, causing less resistance to the flow. Therefore, the inertial force driving the flow of thread is faster in the microchannel. The time for the formation of droplet is also essentially dependent of the strength of shear force acting on the interface, because it dominates over the adhesion force for larger θ. Bashir *et al*. (2011) also reported that the degree of confinement of the

droplets reduces when the shear forces dominates the breakup process. For larger θ, the degree of confinement promotes the breakup; whereas for smaller θ, the degree of confinement suppresses the breakup.

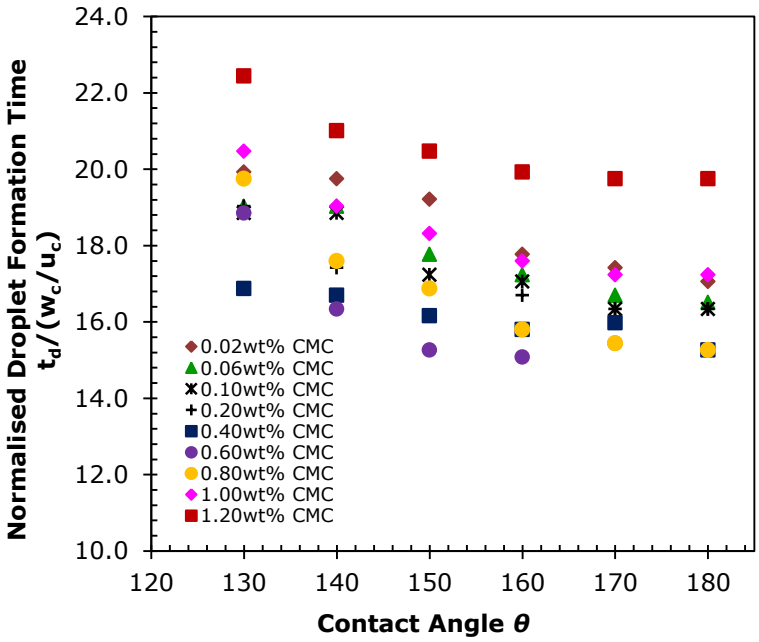


Figure 6.14: Effect of contact angle on the normalised droplet formation time of CMC solutions.

The variation in normalised droplet formation time for various concentrations at fixed θ is shown in Figure 6.15. For a fixed value of θ, the numerical simulation clearly reveals that the droplet formation time decreases as the concentration of the dispersed phase increases from 0.02wt% to 0.40wt%. Interestingly, a similar phenomenon does not happen at larger CMC concentration (>0.40wt%). This can be explained by the fact that the critical overlap concentration of the polymer solution exerts an influence on the droplet formation time. At CMC concentration below C*~0.4wt%, direct intermolecular interactions can be neglected. In this dilute regime, as the CMC concentration increases, the shear-thinning fluids result in rapid pinch-off due to the high shear stress induced by the continuous phase. As concentration increases above C*, the rheological behaviour of CMC solution is governed by the development of entanglement coupling between the chains; thus, the intermolecular interactions become

predominant and contribute significantly to the increasing of viscosity. In the semi-dilute regime, the dispersed systems are always more viscous than the pure continuous phase as the more polymer molecules are presented in the fluid solution. Hence, the viscous fluid thread is then stretched by the mainstream flow to the downstream region and the breakup event is delayed substantially. Hong and Cooper-White (2009) investigated the impact of non-Newtonian Carbopol dispersions on the pinch-off behaviour in silicone oil phase. They found that the droplet formation time increases with increasing viscosity of dispersed phase. Besides, Arratia *et al*. (2009) also claimed that the time for droplet breakup increases as the molecular weight of PAA is increased, under a fixed *Q*. However, there is dearth of information about the effect of dispersed phase concentration on droplet formation time at the transition between the two different regimes for the fixed value of θ.

At fixed θ, the filament exists for CMC concentration above C*~0.40wt%, where the elongation of the necked fluid forms a thin filament connecting the primary droplet and the upper dispersed phase thread, as illustrated in Figure 6.12 (see section 6.2.5). The dynamics of the thinning filament is governed by the shear stress and viscous pressure, by which the filament is elongated drastically and resists the droplet pinch-off. Husny and Cooper-White (2006) claimed that pinch-off occurred rapidly without any significant filament formation during necking for Newtonian droplet formation; but, this rapid necking event was retarded with the formation of a thinning filament for all PEO solutions. On the other hand, the delayed pinch-off may be also due to the retardation effect of the fluid elasticity, which it can be increased by increasing the polymer concentration. However, in our present study, the entire phenomena are observed from the model with no elastic stress applied. Hence, we conclude that shear-thinning alone is sufficient to induce a filament and that elasticity is not

necessary. Future work is suggested to determine the elastic properties of CMC solution and consider the elastic effect in present model.

The growth of CMC droplet diameter as function of time for various CMC concentrations at different contact angles are illustrated in Figure 6.16 to 6.18. A similar interpretation of the time evolution of the droplet diameter during the droplet formation process was discussed in section 6.2.2. As can be seen in those figures, there is a time delay in growth of CMC droplets, which the growth curves begin to drift further from the origin, caused by the viscosity effect due to an increase in CMC concentration. This phenomenon is more significant when the CMC concentration is increased above a critical concentration C*. A rapid increase in dispersed phase concentration tends to an increase in the fluid viscosity and resistance to flow that can cause a longer thread to be formed in axial direction of the microchannel (see Figure 6.9 to 6.11). Therefore, the elongation of the dispersed thread delays droplet growth before the breakup happens.

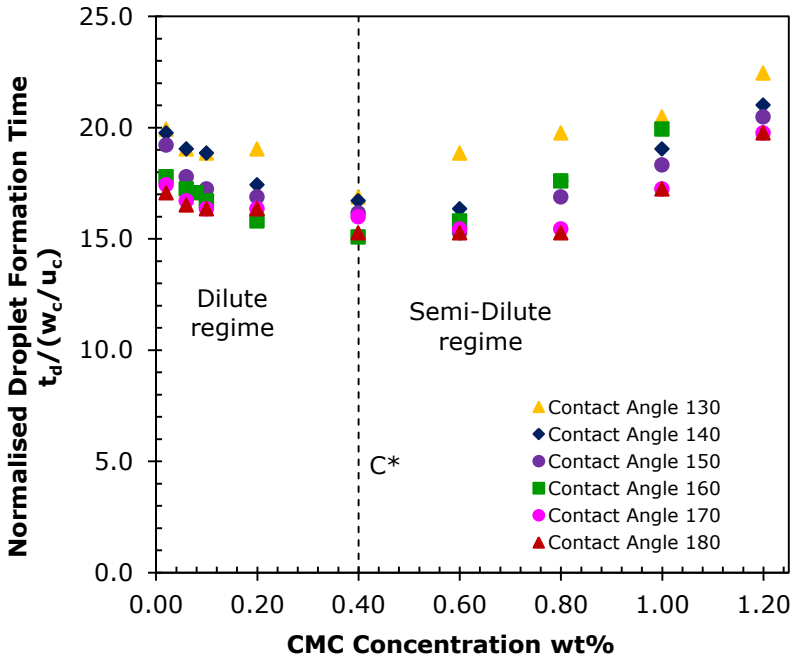


Figure 6.15: Variation in normalised droplet formation time of CMC droplets for various CMC concentrations at each contact angle.

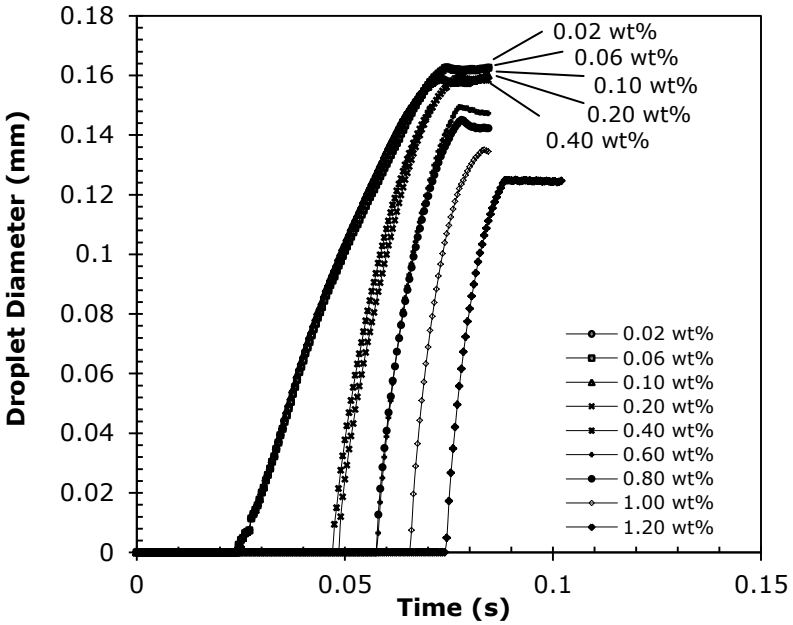


Figure 6.16: Diameter growth of CMC droplet as function of time for various CMC concentrations during the droplet formation process (for system: θ=130°, Q_d/Q_c=0.05).

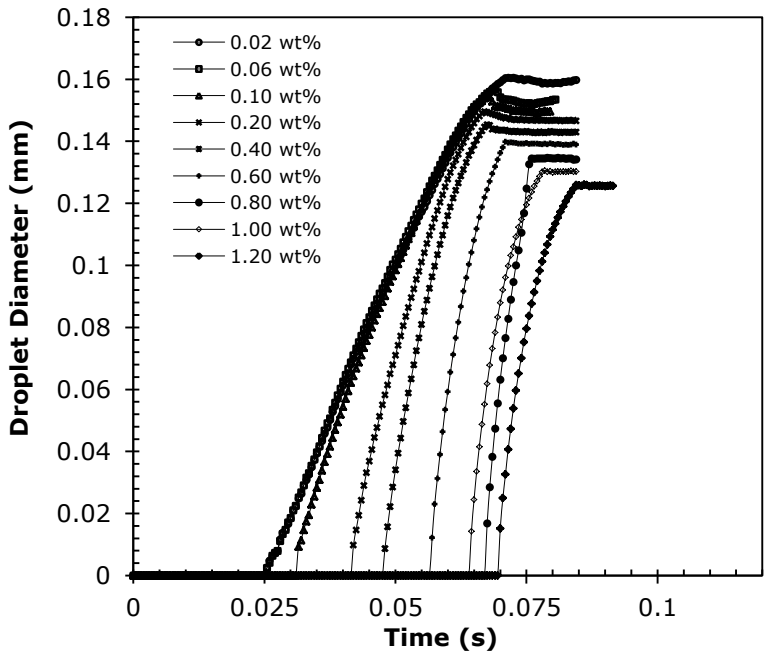


Figure 6.17: Diameter growth of CMC droplet as function of time for various CMC concentrations during the droplet formation process (for system: θ=150°, Q_d/Q_c=0.05).

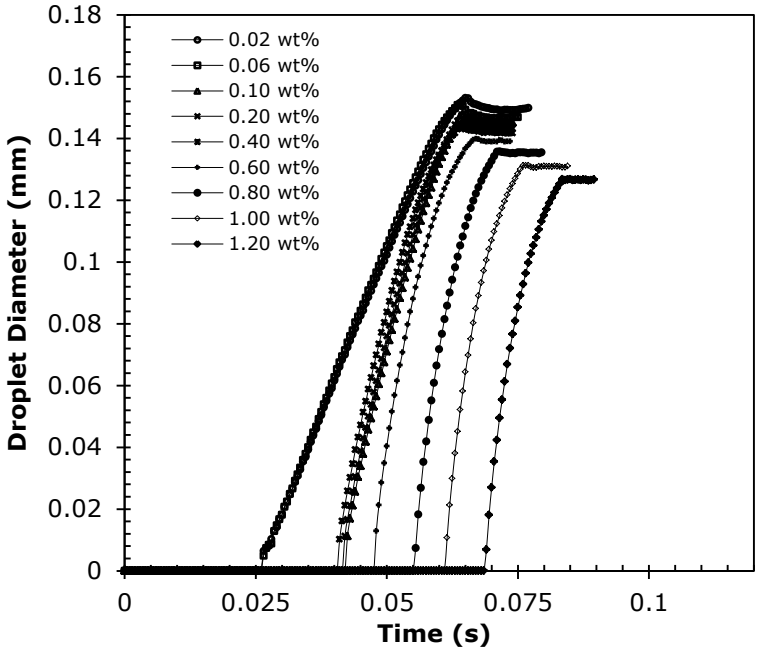


Figure 6.18: Diameter growth of CMC droplet as function of time for various CMC concentrations during the droplet formation process (for system: θ=170^{o}, Q_d/Q_c=0.05).

6.2.7 Effect of Contact Angle on Droplet Generation Frequency

The droplet generation frequency, which is defined as the number of droplets generated within a set period of time, has been also explored with variation of the contact angle. Figure 6.19 illustrates the effect of contact angle on the rate of droplet production. Numerical simulation predicts that the frequency of the droplet formation increases with enhanced surface wettability. As previously discussed in section 6.2.5, a reduction in the droplet formation time was observed for increasing contact angle, which is in agreement with the published literature for Newtonian systems (Bashir *et al*., 2011). The variation in frequency of droplet formation for various concentrations at fixed θ is shown in Figure 6.20. The droplet generation frequency increases with dispersed phase concentration over the range of 0.02wt% to 0.40wt% when the contact angle was held constant at each wetting condition. However, the rate of droplet production begins to decrease with increasing the concentration of CMC fluid when larger than C*, as noted in the previous section.

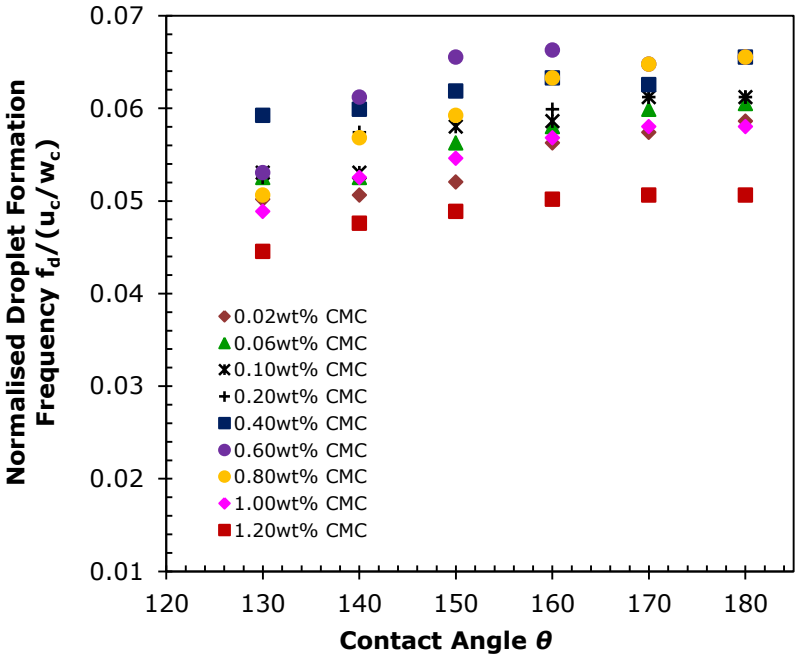


Figure 6.19: Effect of contact angle on the normalised droplet generation frequency of CMC solutions.

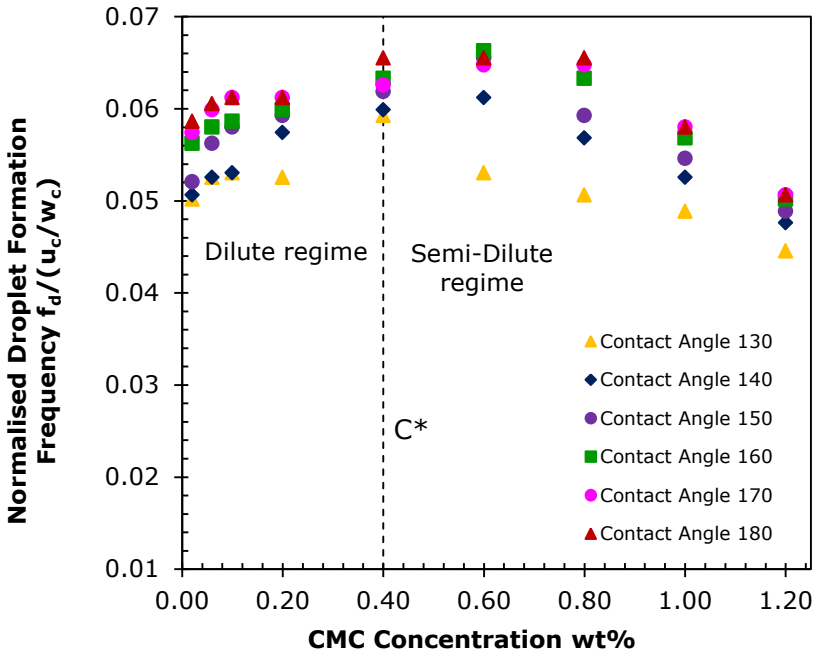


Figure 6.20: Variation in normalised droplet generation frequency of CMC droplets for various CMC concentrations at each contact angle.

6.2.8 Effect of Interfacial Tension on Effective Droplet Diameter

In a confined T-junction microchannel, the dispersed phase droplet grows, deforms and detaches under a series of forces which can be divided into two groups: resisting force (stabilizing the forming droplet, e.g. interfacial tension)

and driving force (tending to detach the forming droplet, e.g. viscous force). These forces are of great importance in control of the droplet breakup process. By considering the resisting force in the process of emulsification, it is generally accepted that interfacial tension is a significant element that markedly influences the evolution of the interface when droplets are shaping (Bashir *et al*., 2011; Peng *et al*., 2011; Wehking *et al*., 2014). When immiscible liquids interact with each other, the Gibbs-Marangoni effect, which is based on interfacial tension gradients, may be established if one liquid phase has much greater surface tension than the others. The interfacial tension gradient enables the interface to resist tangential stresses from the adjoining flowing liquid. Nevertheless, Gibbs-Marangoni effect is not sufficiently strong and can be omitted in present studies, due to the employment of pure solutions as well as the absence of emulsifier or surfactant that contributes significantly to the emulsions stability. Consequently, mass diffusion between two immiscible liquids, due to the change in interfacial tension, has less practical importance. Six systems with increasing values of interfacial tension from 0.010 N/m to 0.035 N/m were simulated. The dispersed phase contact angle of 180^{O} was a conservative estimate for PDMS devices.

Figure 6.21 illustrates the interfacial tension effect on the CMC droplet diameter. The simulations predict that the CMC droplet diameter increases when the interfacial tension is increased, which is in agreement with the numerical results from Bashir *et al*. (2011) and Peng *et al*. (2011).A larger interfacial tension gives rise to intermolecular attraction or a cohesive force between the liquid molecules, caused by a high dissymmetry of attractive forces. This results in a large excess free surface energy at the interface and this force drives minimization of the surface area. These larger intermolecular forces tend to delay the droplet formation process and resist the detachment of the droplets at higher surface tension. Consequently, a larger droplet diameter is generated after the complex balance between the shear stress and interfacial tension completely reaches

equilibrium. According to Laplace's law, the interfacial tension forces necessitate a pressure drop to maintain the interface at equilibrium against collapse. As described by the Young-Laplace equation (see Equation 2.19), the pressure difference across a fluid interface is directly proportional to the interfacial tension and inversely proportional to the radius of curvature. Therefore, the higher the surface tension, the larger the pressure difference across the interface. Figure 6.22 illustrates the plot of pressure profile of the CMC solution with a concentration of 0.20wt% at the corner of the T-junction at different interfacial tensions. A study made by Bashir *et al*. (2011) has reported that the pressure drop across the interface of the two phases may not be sufficient to detach the droplet at the junction for the lower interfacial tension. Besides, for higher values of the interfacial tension, the two-phase flow exhibits dominance of the interfacial tension forces over the viscous force, leading to the formation of larger droplets.

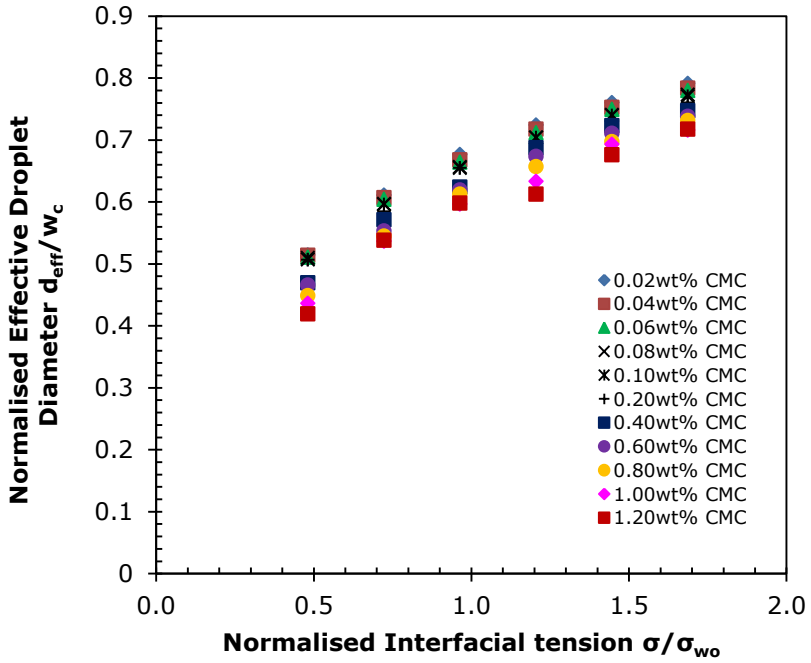
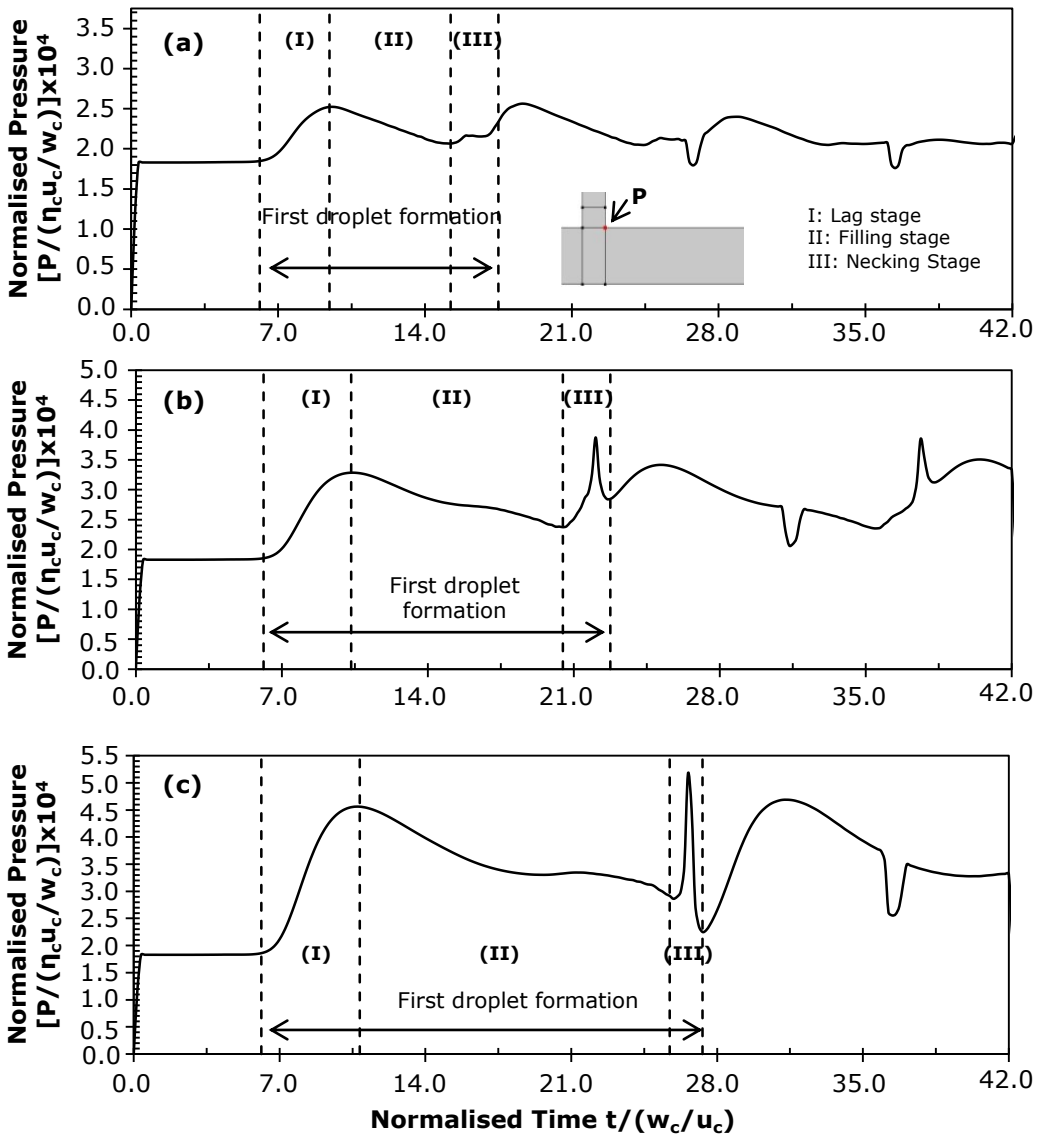


Figure 6.21: Effect of interfacial tension on the normalised effective droplet diameter of CMC solutions (σ_{wo} (=0.02074 N/m) denotes interfacial tension between de-ionized water and olive oil).



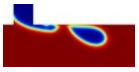
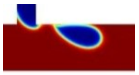
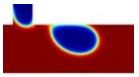
Interfacial Tension (N/m)	Pressure Peak (Pa)	Periods (s)	Snapshots
0.010	864.82	0.0285	
0.020	1550.18	0.0445	
0.035	2065.77	0.0595	

Figure 6.22: Pressure profile of 0.20wt% CMC droplet breakup for different interfacial tensions: (a) σ = 0.010 N/m, (b) σ = 0.020 N/m, (c) σ = 0.035 N/m (for system: Q_d/Q_c=0.05). P denotes the pressure at the corner of T-junction. The sharp pressure peak in the given data corresponds to droplet breakup point as shown in the extracted images. The maximum magnitudes of the pressure peak and the formation periods under different interfacial tension are listed above.

Figure 6.23 illustrates the interfacial tension effect on droplet diameter for different CMC concentrations. When the interfacial tension was held constant, the zero shear viscosity of the dispersed phase is increased as the concentration of dispersed phase increases. The shear viscosity is decreased by the shear-thinning behaviour under shear flow which contributes an increase in pressure along the neck. This will lead to the formation of smaller droplets. Besides, for the higher CMC concentration, the retraction of interface induced by the interfacial forces is not the only contributing factor. The viscous pressure induced by the dispersed phase begins to take effect, causing a downstream process which elongates the dispersed thread up to some distance downstream, prior to pinch-off.

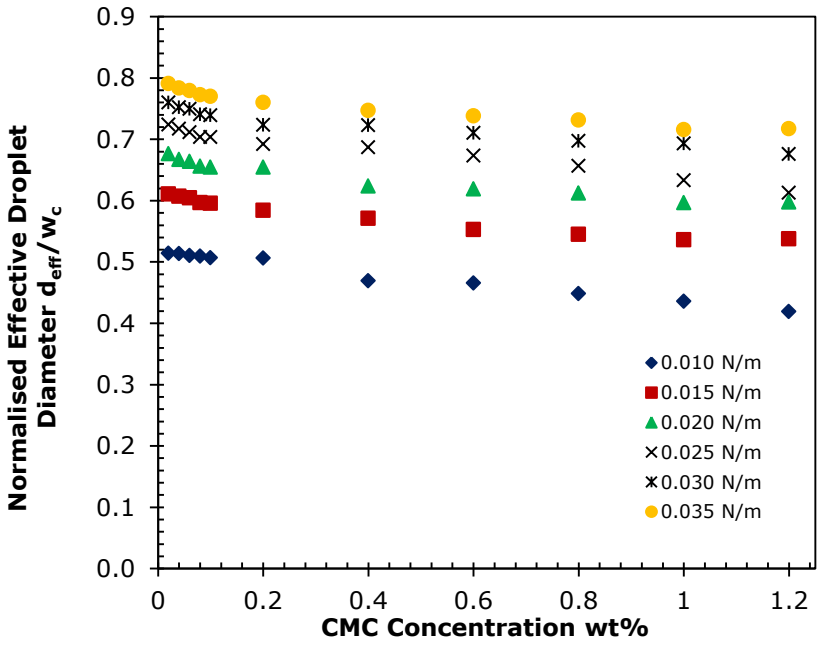


Figure 6.23: Variation in normalised effective droplet diameter of CMC droplets for various CMC concentrations at each interfacial tension.

6.2.9 Effect of Interfacial Tension on Droplet Formation Time

The time taken for the droplet growth, deformation and detachment can be markedly influenced by the interfacial tension. Figure 6.24 illustrates the effect of interfacial tension on the CMC droplet formation time. As elucidated in Figure 6.24, the droplet formation time increases with the increase of interfacial tension. At higher values of interfacial tension, the retraction of the interface induced by

interfacial tension becomes larger due to the relatively high surface free energy. This will tend to delay the droplet formation process as the CMC droplets take longer to approach equilibrium. However, in most case, when C<C*~0.4wt%, the droplet is pinched-off at the corner of T-junction and this breakup regime is driven chiefly by the build-up of pressure upstream due to the high degree of confinement of the droplet in the main stream.

To investigate the influence of the viscous stress combined with interfacial tension on the droplet, the influence of the CMC concentration on droplet breakup time at fixed interfacial tension was examined (see Figure 6.25). The droplet breakup time decreases as the CMC concentration is increased from 0.02wt% to 0.40wt%. In contrast to this phenomenon, the break-up time increases with increasing CMC concentration above C* of the polymer coils. A sequence of snapshots of droplet formation, with the interfacial tensions of 0.010 N/m, 0.020 N/m, and 0.035 N/m, were taken for various CMC concentrations and illustrated in Figure 6.26 to 6.28. For all the CMC concentrations below C*, the interfacial forces are more dominant than the dispersed phase viscous force, mainly due to insufficient polymer chain overlap. This leads to rapid formation of droplets. For CMC concentrations above C*, a higher viscosity gives rise to longer formation time which can be attributed to the higher magnitude of the dispersed thread pressure, similar to observations by Zhang and Basaran (1995) who studied high viscous pendant drops. Additionally, Tirtaatmadja*et al*. (2006) has also reported that the polymer molecules can be highly extended during their approach to pinch region and this contributes to the formation of filament. As the filament is formed, they can be further extended by stretching force at a constant rate until full extension of polymer coil is achieved (Tirtaatmadja*et al*., 2006). High stretching of polymer chains is associated with high elasticity. In the present study, the length of filament gets longer with increasing the CMC polymer concentration which presumably prevents the neck of dispersed thread

from pinching off (see Figure 6.29). Thus, the existence of a thin polymeric filament will tend to retard the formation time, especially for C>C*~0.4wt%. However, most available studies have reported that the filament is formed due to the impact of dispersed phase elasticity (Husny and Cooper-White, 2006; Steinhaus and Shen, 2007; Arratia *et al*., 2009). Here we see a similar effect even though our fluid is purely viscous and shear-thinning.

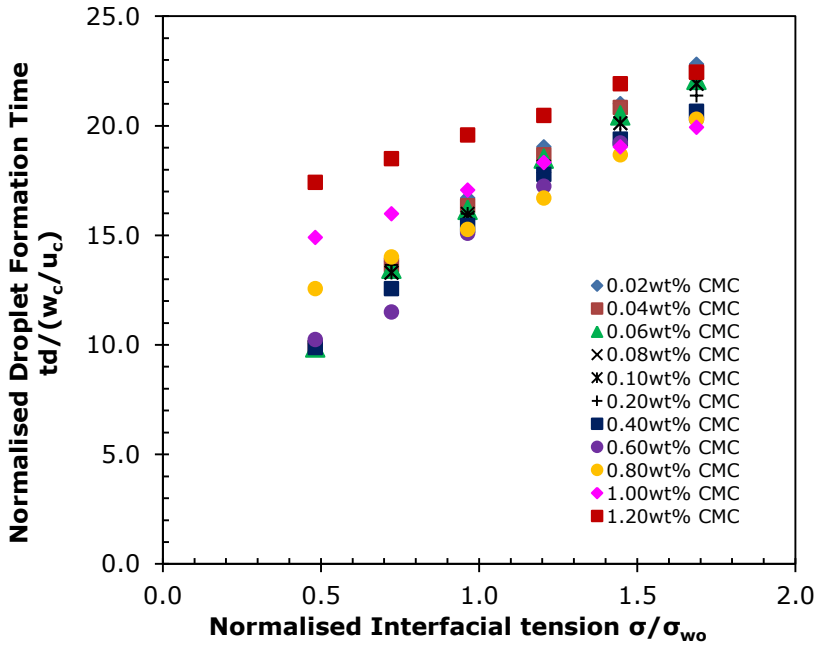


Figure 6.24: Effect of interfacial tension on the normalised droplet formation time of CMC solutions (σ_{wo} =0.02074 N/m).

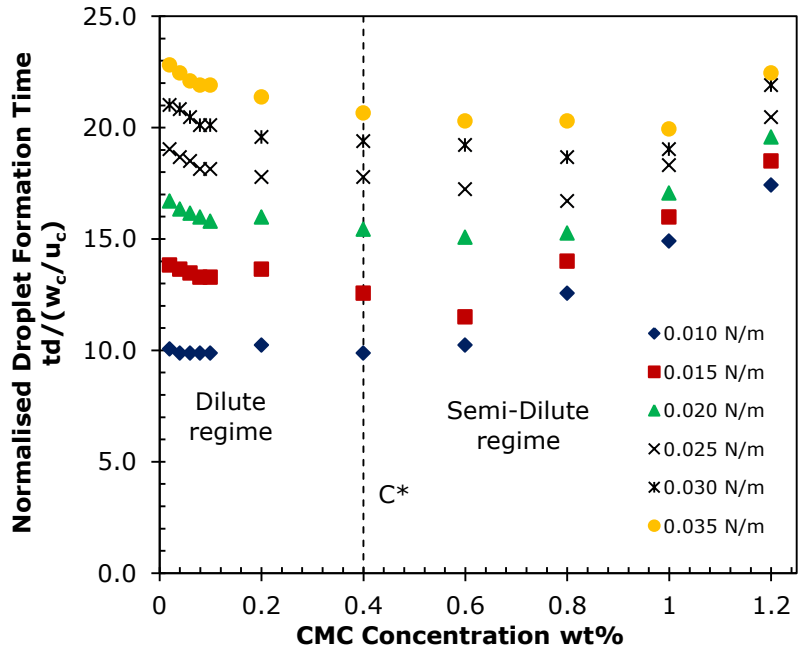


Figure 6.25: Variation in normalised droplet formation time of CMC droplets for various CMC concentrations at each interfacial tension.

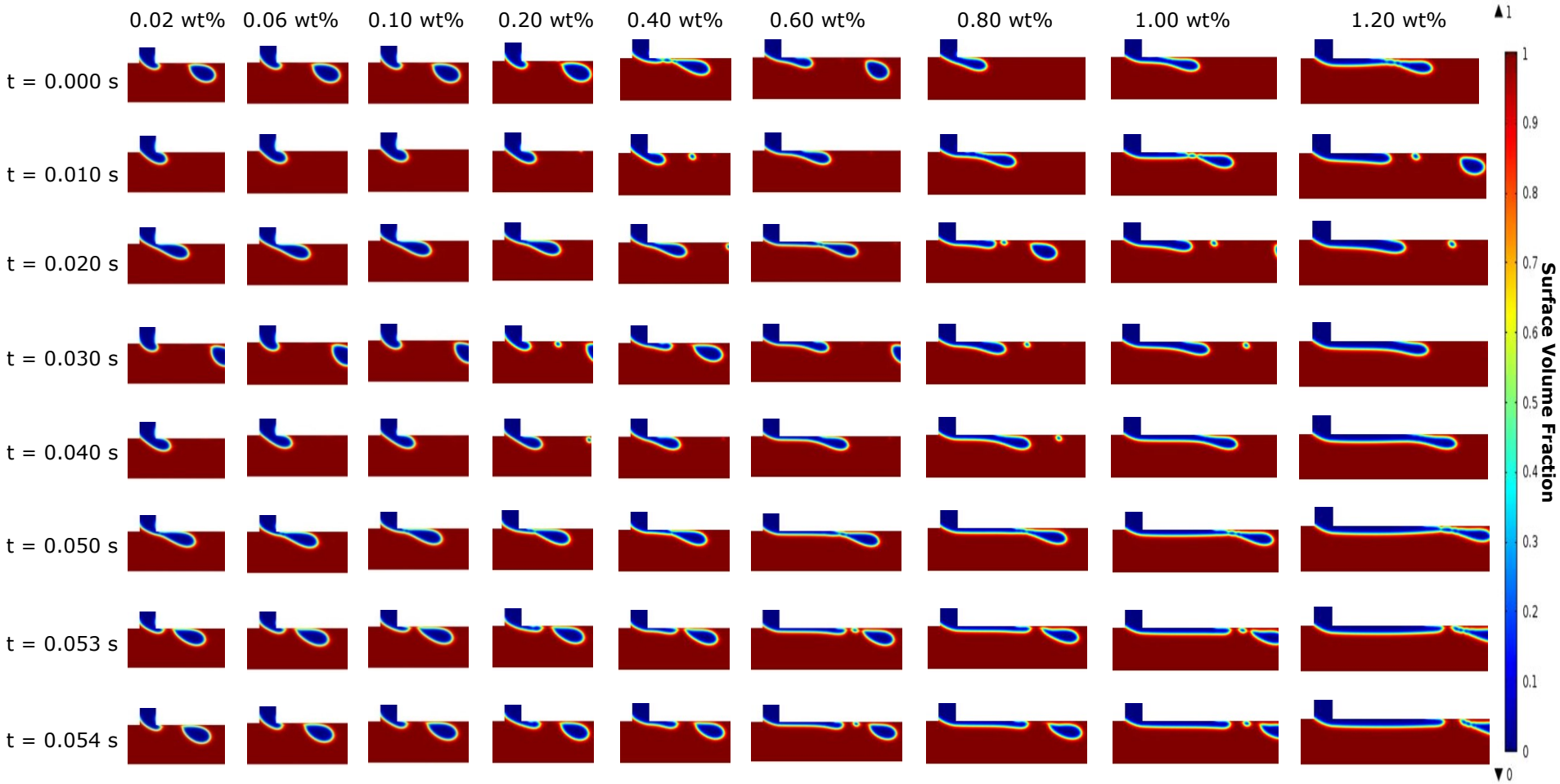


Figure 6.26: Snapshots of two-dimensional (2D) simulation of the effect of interfacial tension on CMC-in-olive oil droplet breakup process for different CMC concentration (for system: σ=0.010 N/m, Q_d/Q_c=0.05).

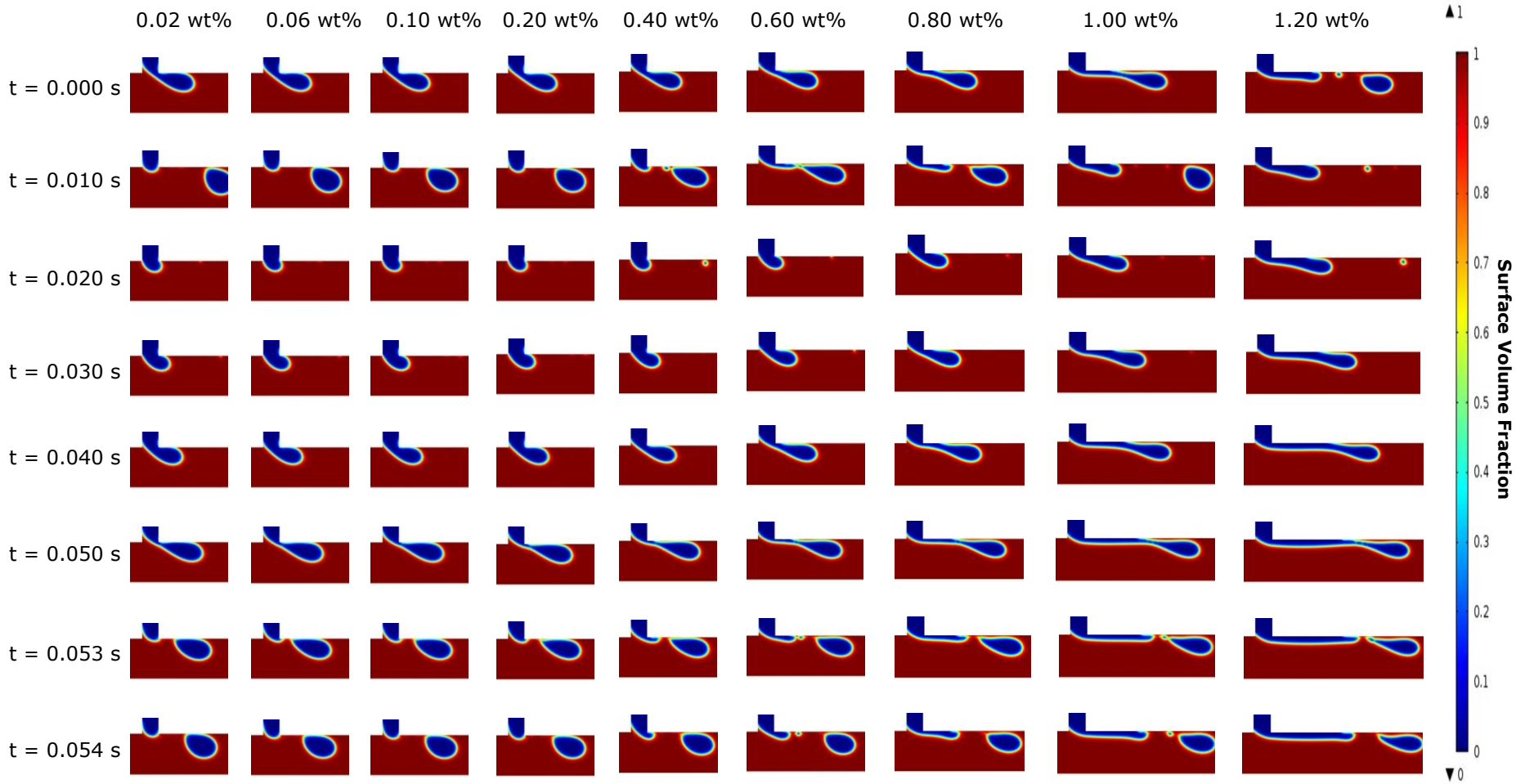


Figure 6.27: Snapshots of two-dimensional (2D) simulation of the effect of interfacial tension on CMC-in-olive oil droplet breakup process for different CMC concentration (for system: σ=0.020 N/m, Q_d/Q_c=0.05).

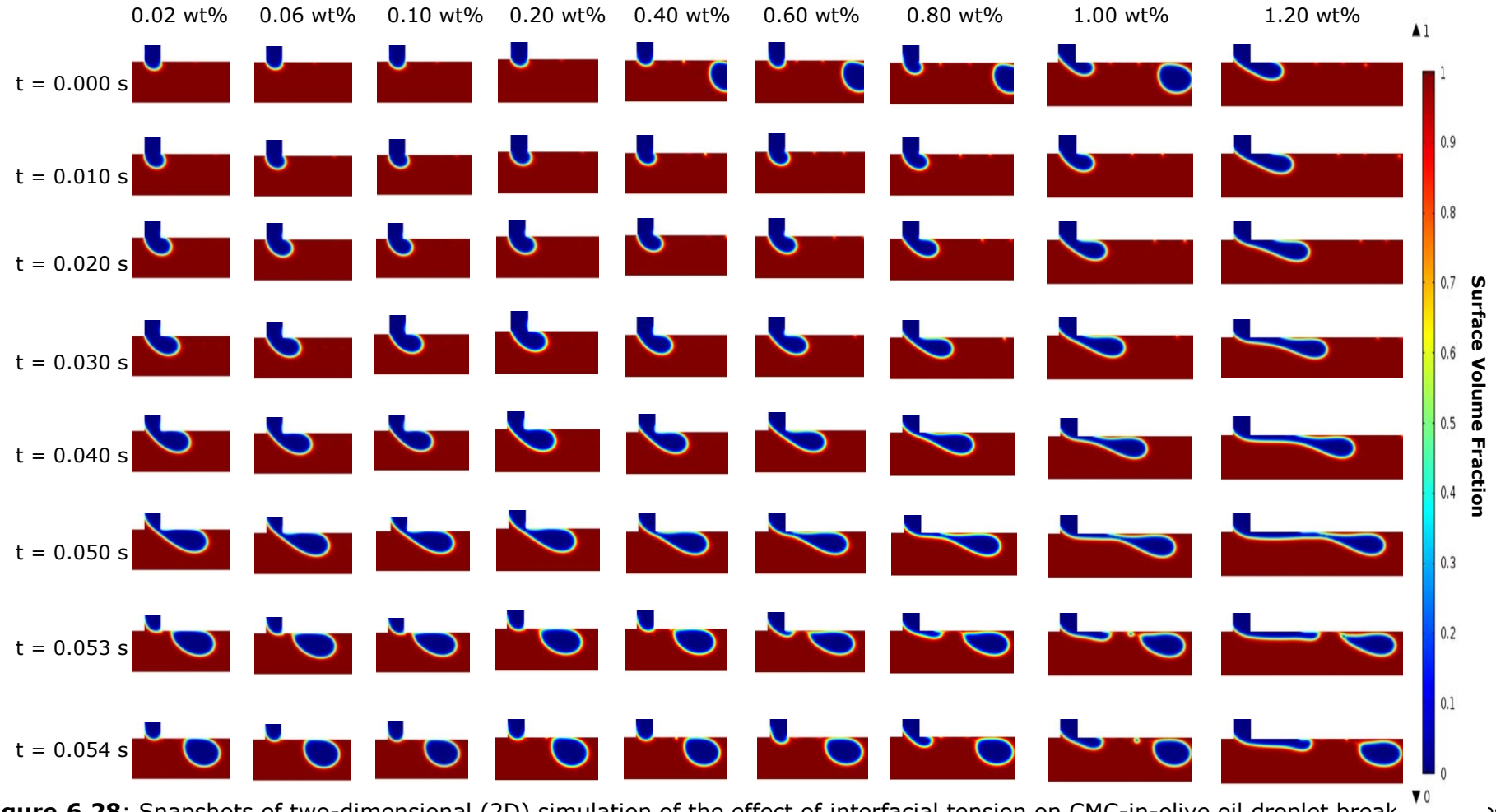


Figure 6.28: Snapshots of two-dimensional (2D) simulation of the effect of interfacial tension on CMC-in-olive oil droplet breakup process for different CMC concentration (for system: σ=0.035 N/m, Q_d/Q_c=0.05).

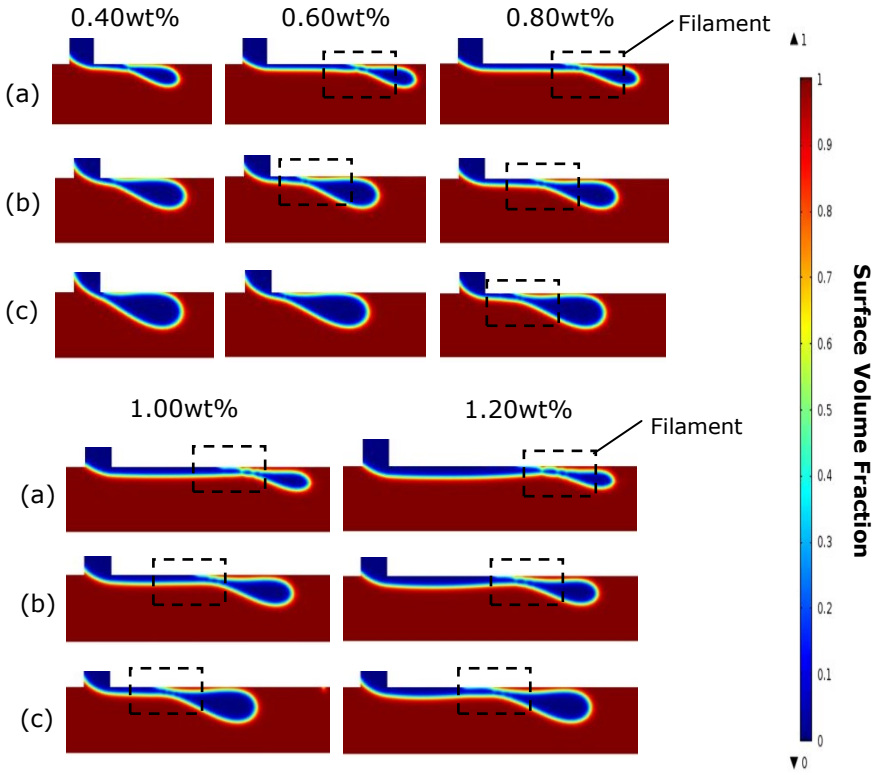


Figure 6.29: Jet and filament formation profile prior to pinch-off for CMC concentrations above 0.4wt% at interfacial tension: (a) 0.010 N/m, (b) 0.020 N/m, (c) 0.035 N/m (for system: Q_d/Q_c=0.05).

The diameter growth of the CMC droplet as function of time, for various CMC concentrations at different interfacial tension, is illustrated in Figures 6.30 to 6.32. As elucidated in these diagrams, the droplets grow with time and reach a plateau often with a small overshoot. This means the local flow mandates a maximum droplet size, occurring when the resisting and driving forces approach equilibrium. Additionally, Figures 6.30, 6.31 and 6.32 show a delayed growth curve of the CMC droplet diameter for CMC concentrations above 0.40wt%. This phenomenon is possible whenever the viscosity dominates over interfacial tension. At fixed interfacial tension, as the dispersed phase viscosity increases, the flow is increasingly dominated by viscosity effects. In addition, it becomes sufficiently large to counteract the interfacial tension effect for the higher CMC concentration (C>C*).

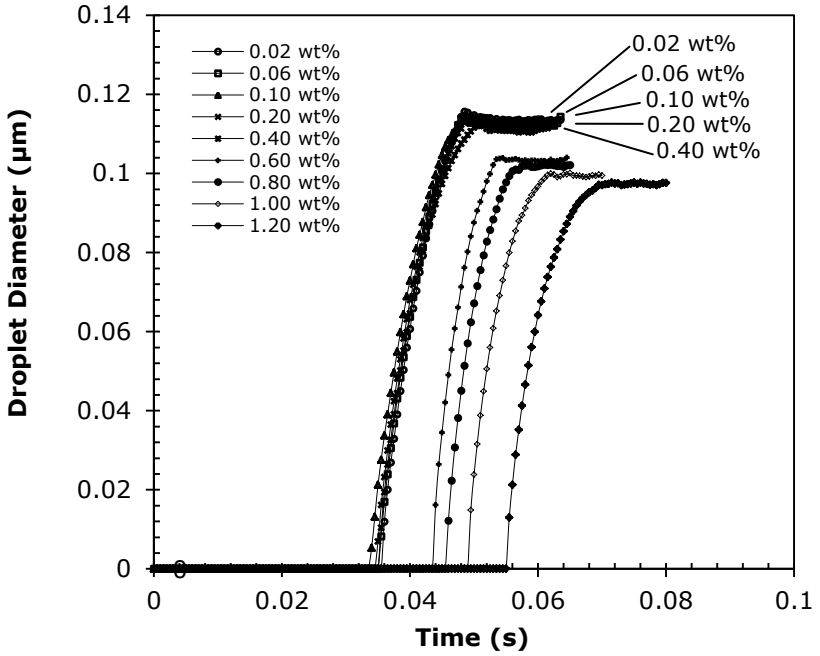


Figure 6.30: Diameter growth of CMC droplet as function of time for various CMC concentrations during the droplet formation process (for system: σ=0.010 N/m, Q_d/Q_c=0.05).

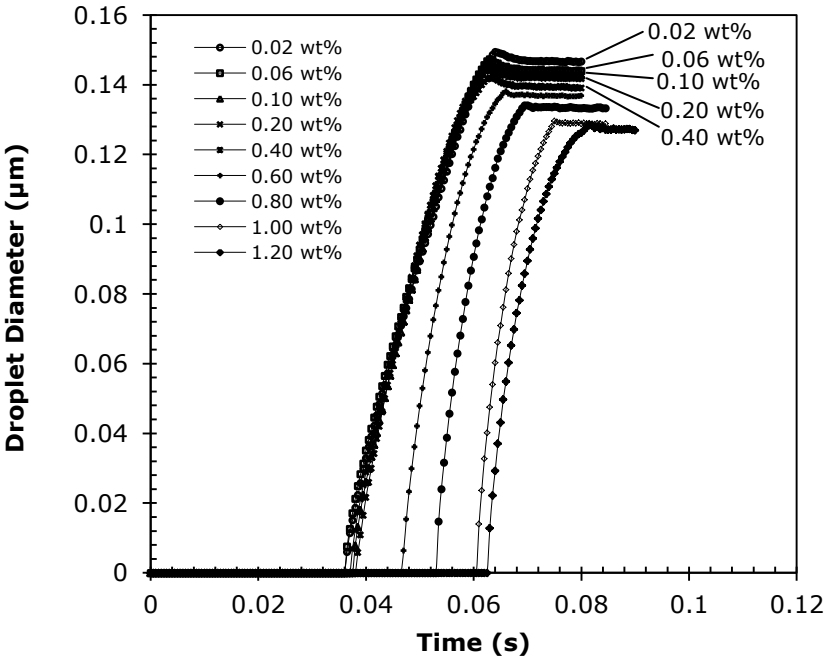


Figure 6.31: Diameter growth of CMC droplet as function of time for various CMC concentrations during the droplet formation process (for system: σ=0.020 N/m, Q_d/Q_c=0.05).

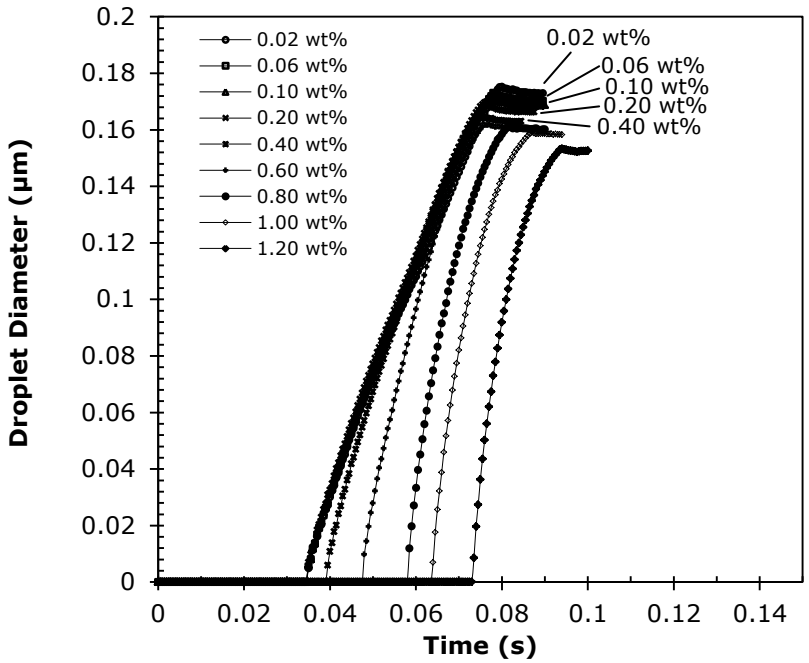


Figure 6.32: Diameter growth of CMC droplet as function of time for various CMC concentrations during the droplet formation process (for system: σ=0.035 N/m, Q_d/Q_c=0.05).

6.2.10 Effect of Interfacial Tension on Droplet Generation Frequency

When the interfacial tension becomes larger, the breakup time for a droplet is increased, resulting in a decreased generation frequency and increased diameter for the droplets, correspondingly at fixed Q (see Figure 6.33). This exhibits the similar observations to the studies made by Peng *et al*. (2011) and Bashir *et al*. (2011) who focused on Newtonian water-oil (w/o) emulsions in flow-focusing and cross-flowing microfluidics devices, respectively. In two distinct regimes according to CMC concentration, the droplet formation frequency at each fixed interfacial tension has been investigated (see Figure 6.34). In the dilute concentration regime(C<C*), droplet breakup time reduction is observed to occur when the concentration is increased. In contrast, the production frequency is reduced in the semi-dilute concentration regime (C>C*)because it takes a longer time for the dispersed phase viscous force to be overcome by the opposing inertial force and shear stress induced by the continuous phase, which delays the dynamic breakup process, as we have previously discussed.

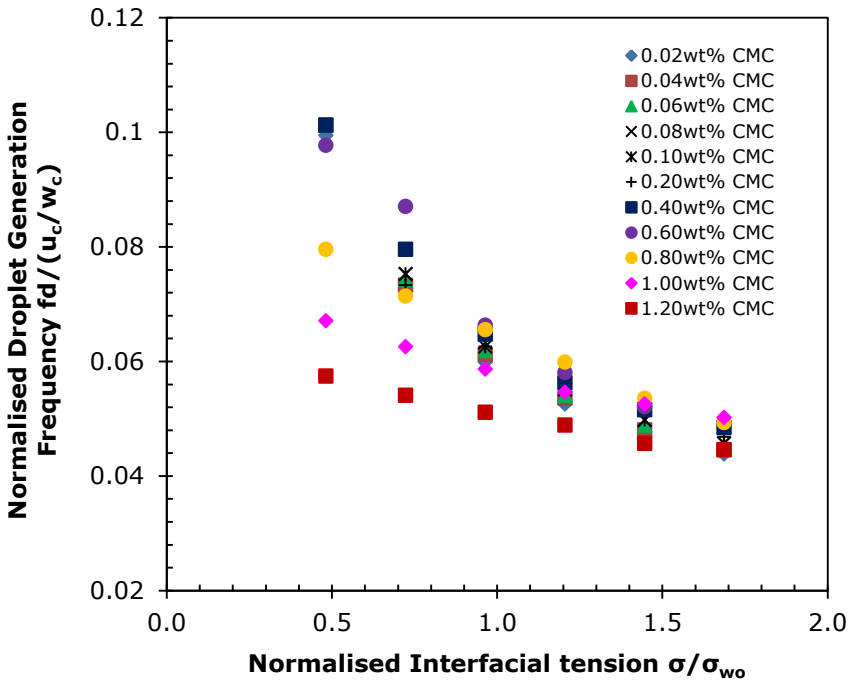


Figure 6.33: Effect of interfacial tension on the normalised droplet generation frequency of CMC solutions (σ_{wo} (=0.02074 N/m) denotes the interfacial tension between de-ionized water and olive oil).

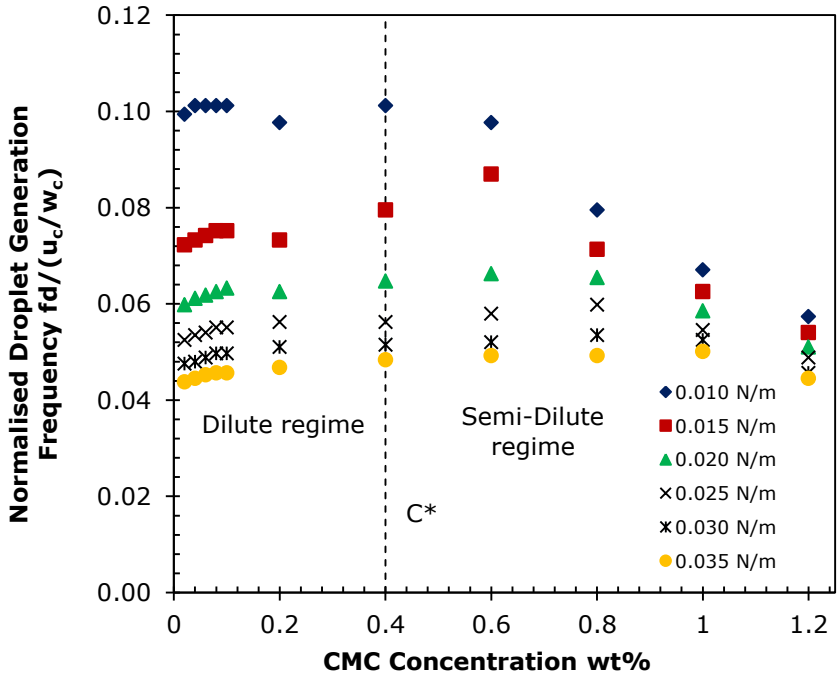


Figure 6.34: Variation in normalised droplet generation frequency of CMC droplets for various CMC concentrations at each interfacial tension.

6.3 Summary

Due to the existence of a high surface-to-volume ratio within a microscaled device, the governing physical parameters of the interface are leverage factors in the physical process of non-Newtonian droplet generation, motion, and breakup. Nevertheless, the flow behaviour of non-Newtonian shear-thinning fluids in microfluidics flow is still poorly understood. The results are of interest in view of the essential role of the viscosities, surface wettability and interfacial tension in determining the behaviour of shear-thinning CMC droplets in the emulsification process. The aim of the present work is to systematically investigate the evolution of the effective droplet diameter, breakup time, and the droplet production frequency, which is effectively governed by the physical properties of the tested fluids, using conservative two-phase level set formulation. Collectively, this information is an important first step towards constructing an extensive understanding of non-Newtonian droplet formation.

In present work, the numerical simulation data predicted that the effective droplet diameter is found to be dependent on these interface parameters for various CMC concentrations. Some conclusions are summarized as follows:

(1) For the combined effect of continuous and dispersed phase viscosity at fixed viscosity ratio of 1, there is a reduction in CMC droplet diameter with increasing CMC concentration and breakup time when the continuous phase and dispersed phase viscosity are comparable.

(2) Neglecting fixed viscosity ratio of 1, the role of surface wettability and interfacial tension on the size of CMC shear-thinning droplet has been highlighted in present simulation. For both studies, olive oil was selected as the continuous phase fluid with constant shear viscosity while the CMC polymer was used as the dispersed phase fluid. The present simulation data revealed that the droplet diameter increases as the interfacial tension increases. Conversely, the droplet diameter decreases with increasing

dispersed phase contact angle from 130° to 150°, especially for lower CMC concentration (C<0.80wt%). When contact angle increases above 150°, the larger contact angle has no significant influence on the CMC droplet diameter. Additionally, for larger CMC concentration (C>0.80wt%), the droplet diameter remains almost constant for different wetting condition when the shear-thinning effect becomes pronounced. Nevertheless, in both cases, the droplet formation time and the generation frequency have a striking non-monotonic with the CMC polymer concentration. By considering the CMC concentrations, the dependence of the droplet breakup time on concentration is distinctly different in two concentration regimes, namely dilute and semi-dilute. The existence of these two regimes is due to the considerable effect of the concentration of CMC polymer. As the concentration increases, the effect of concentration crosses over from the dilute regime to the semi-dilute regime. In the dilute regime (C<C*~0.40wt%), the droplet breakup time decreases as the CMC concentration increases, when the contact angle and interfacial tension were held constant, respectively. While in the semi-dilute regime (C>C*~0.40wt%), droplet breakup time increases as the CMC concentration increases. This phenomenon can be explained because the dispersed phase viscous force may begin to dominate the breakup behaviour. As CMC concentration increases, a laminar elongated dispersed thread is formed connecting to the primary droplet due to the high viscous pressure, and thus the droplet breakup point moves progressively downstream of the outlet channel. Hence, the presence of highly polymer molecules in the dispersed phase leads to an elongated fluid thread and a delay in breakup time.

Above all, it can be concluded that the viscosities of dispersed and continuous phase, contact angle, and interfacial tension are important physical properties that markedly influence the droplet breakup phenomena. In contrast to previous

findings, this work excluded the effect of elastic properties of CMC fluid in the process of microdroplets formation. Nevertheless, we still observed many features that were previously attributed to elastic effects including elasticity still remains a defining challenge, especially for higher CMC concentration. Future works are recommended to integrate the elastic stress model with level-set method, in order to investigate the effect of fluid elasticity on breakup process.

CHAPTER 7

The Effect of Fluid Flow Characteristics on Shear-Thinning Microdroplets Formation and Breakup Dynamics

7.1 Introduction

The understanding of the non-Newtonian droplets generation mechanism is lacking and proposed models lack generality for microfluidic devices under different flow conditions. Most studies of drop formation and pinch-off concern Newtonian liquids mainly in theoretical, experimental and computational analysis. As a result, a number of droplet breakup studies have been devoted to the idea of flow rate and viscosity variation in investigating the breakup mechanism. Christopher *et al*. (2008) studied experimentally the formation of water droplets in a silicone oil-based continuous phase at microfluidics T-junction by varying the flow rate ratio and viscosity ratio of two phases. Garstecki *et al*. (2005) reviewed the mechanism of formation of droplets and bubbles which governed by the rate of the flow of liquids in a T-junction microfluidics device. Gupta *et al*. (2009) numerically investigated the effect of the continuous and dispersed phase rate and the viscosity ratio of both phases on the droplet breakup using lattice Boltzmann (LB) method. DeMenech *et al*. (2008) used diffuse interface method to numerically investigate the regime of droplet breakup in T-junction microchannel, focusing on the effect of capillary (Ca) number and flow rate ratio. Glawdel *et al*. (2012) has presented a model validation and numerical investigation on the formation of droplets for several T-junction configurations across a range of flow rate and viscosity ratios. Besides, Zhang *et al*. (2009) has also analysed the impact of flow rate ratio on determining the nanoliter droplet volume and formation time. All cited studies confirmed the control of droplets

motion and formation in microfluidics can be significantly manipulated by altering the fluid volumetric flow rates or by changing the relative viscosity between the continuous and dispersed phases. Nevertheless, little is known about how to conduct numerical work using non-Newtonian nature of polymer solution.

7.2 Parametric Studies of the Variations in Controlling Flow Rate and Concentration of Continuous and Dispersed Phase

In spite of extensive studies investigating mechanisms for Newtonian nature of droplet formation, physical models predicting the droplet size, uniformity and production frequency as a function of the relevant control parameters such as flow rate and fluid concentration are still unsatisfactory for non-Newtonian fluids with different flow conditions in microchannels. To address this lack of understanding, the effects of dispersed phase flow rate, continuous phase flow rate, dispersed phase concentration and continuous phase viscosity in tailoring the droplet size, formation time and generation frequency were numerically investigated. The droplet formation process were captured at a time step of 0.0005 seconds and a contact angle of 180^{o} represents the complete repulsions of working liquid by the PDMS surface was applied. The previous *Chapter 4* dealt with comparison test between the numerical and experimental model at different flow rate ratio *Q*. The results revealed that the numerical model is reasonably acceptable for low *Q*; however, the trend curves show in similar way for both models (see *Figure 4.9*). Thus, the idea of subsequent section 7.2.1 to 7.2.6 examines the possibility of the evolution of droplet diameter, generation frequency and formation time at different *Q*.

7.2.1 Effect of Dispersed Phase Flow Rate on Effective Droplet Diameter

In the first series of numerical simulations, the effect of dispersed phase flow rate on droplet diameter was systematically examined for CMC mixture with concentrations ranging from 0wt% to 1.20wt% which the controllable fluid behaves as a non-Newtonian shear-thinning fluid. For a constant Q_c at 2.00 ml/hr, the droplet size was measured with the variation in Q_d (0.05 ml/hr to 0.25ml/hr, see *Appendix A.3*, *Table A.8*), with results shown in Figure 7.1. At 0wt% CMC (water, η_d=0.00093 kg/m.s) the emulsions exhibit Newtonian behaviour, the results reveal that the length of the dispersed droplets increased when dispersed flow rate increased. In comparison to non-Newtonian droplet formation, a similar phenomenon to the Newtonian system was found.

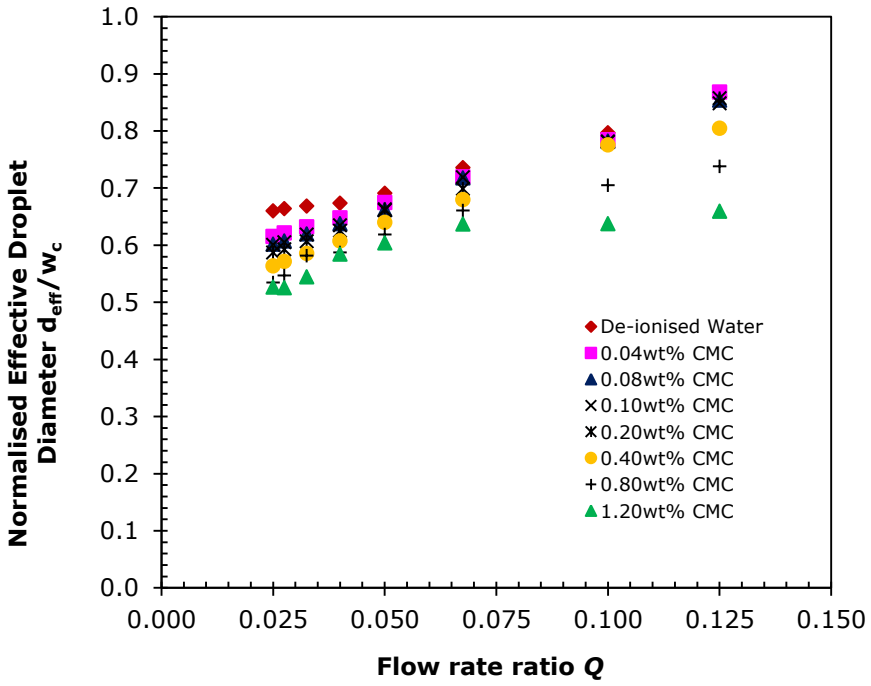


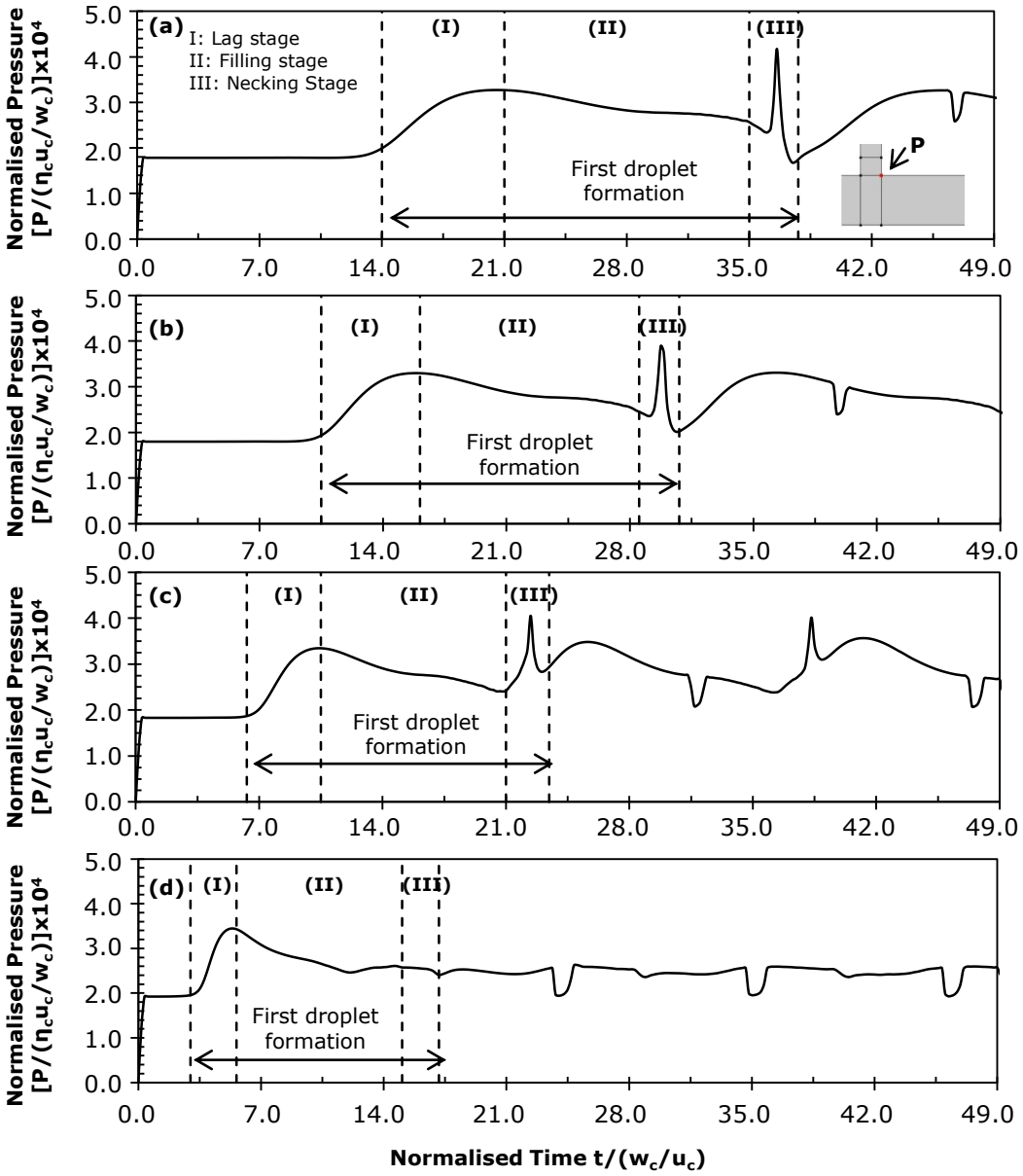
Figure 7.1: Effect of dispersed phase flow rate on the effective droplet diameter of CMC solutions for various CMC concentrations at different flow rate ratio Q (=Q_d/Q_c) (for system: Q_c: fixed 2.00 ml/hr; Q_d: 0.05 ml/hr to 0.25ml/hr)

Figure 7.1 illustrates that the Q_d plays important role in tailoring droplet diameter. When Q_c>Q_d, droplet does not have time to elongate and breakup occurs immediately after a droplet length is formed, and the droplet detachment

occurs at the junction (Bashir *et al*., 2011). This predictions also supported by Tan *et al*. (2008) who reported that shear force from the continuous phase is sufficiently high to induce the dispersed phase to form droplets at T-junction of the microchannel at the low dispersed phase rates. As Q_d increases, more dispersed phase fluids enter the main channel before the dispersed thread is pinched off at the outlet corner and the inertial force of the dispersed phase generated during the droplet formation process are greatly enough to resist the opposing shear force which moves the interfacial boundary of the two liquids towards the T-junction corner pinch point resulting in formation of droplet. Therefore, larger droplets are being created when a higher Q_d is employed.

The pressures at the corner where the two channels meet for CMC droplets breakup at different flow rate ratios, Q were systematically investigated and the simulation outputs were graphically plotted in Figure 7.2. Generally, the droplets formation process has been divided into three stages, namely lag, filling, and necking stage (Glawdel *et al*., 2012). At the necking stage, the pressure forces overwhelm the droplet leading to detachment. As elucidated in Figure 7.2, the build-up pressure for droplets breakup at the corner of junction decreases as the dispersed phase flow rate increases. Moreover, the magnitude of pressure is dependent on the specific location of necking and breaking of the droplets. When the Q_d is small, the droplets are pinched off at the T-junction corner at the same continuous phase flow rate. The pressure is recognized as the dominant factor for the droplet detachment at the corner of T-junction. When Q_d increases, it is evident that the pressure peak becomes smaller as the increasing Q_d will force the detachment point to move from the corner to a point downstream. The detachment points gradually moves downstream and form a long neck before droplets are sheared off with the increasing of Q_d. This can be concluded that the pressure plays less dominant role when the dispersed phase rate becomes larger. Figure 7.3 demonstrates the snapshots of effect of dispersed phase flow rate on

the droplet formation for CMC concentrations ranging from 0wt% to 1.20wt%. As seen in Figure 7.3, the necking of the dispersed phase is initiated once the continuous phase intrudes into the upstream of the lateral channel. With the increase in dispersed phase flow rate (0.05 ml/hr to 0.25 ml/hr) in the same change of continuous phase rate, the droplet diameter increases and the position of necking and detachment point is affected and shifted towards jetting phenomenon where a long neck of dispersed thread is developed before droplets are sheared off in the main channel. This phenomenon becomes more drastic for the larger concentration of CMC solutions (C>C*~0.40wt%). Fu *et al*. (2012) has investigated experimentally that larger droplets are being generated caused by the higher flow rate of the dispersed phase which induces more resistance to the continuous phase. Gupta and Kumar (2010) have also reported that increasing of the flow rate of dispersed phase can lead to a shift in the droplet detachment point.



	Q_d (ml/hr)	$Q(=Q_d/Q_c)$	Pressure Peak (Pa)	Periods (s)	Snapshots
(a)	0.050	0.0250	1670.07	0.0715	
(b)	0.065	0.0325	1555.92	0.0585	
(c)	0.100	0.0500	1620.45	0.0455	
(d)	0.200	0.1000	999.72	0.0325	

Figure 7.2: Pressure profile of 0.20wt% for the effects of dispersed phase rate on droplet breakup process at each flow rate ratio (for system: fixed Q_C=2.00 ml/hr). P denotes the pressure at the corner of T-junction. The sharp pressure peak in the given data values reflects the droplet breakup point as shown in the extracted images. The pressure profile demonstrated an abrupt fall in pressure caused by the balance of surface tension and viscous force dictates the droplet movement after the first droplet formation. This phenomenon is applied to all cases. The maximum magnitudes of the pressure peak and the formation periods under different dispersed phase rate are listed above.

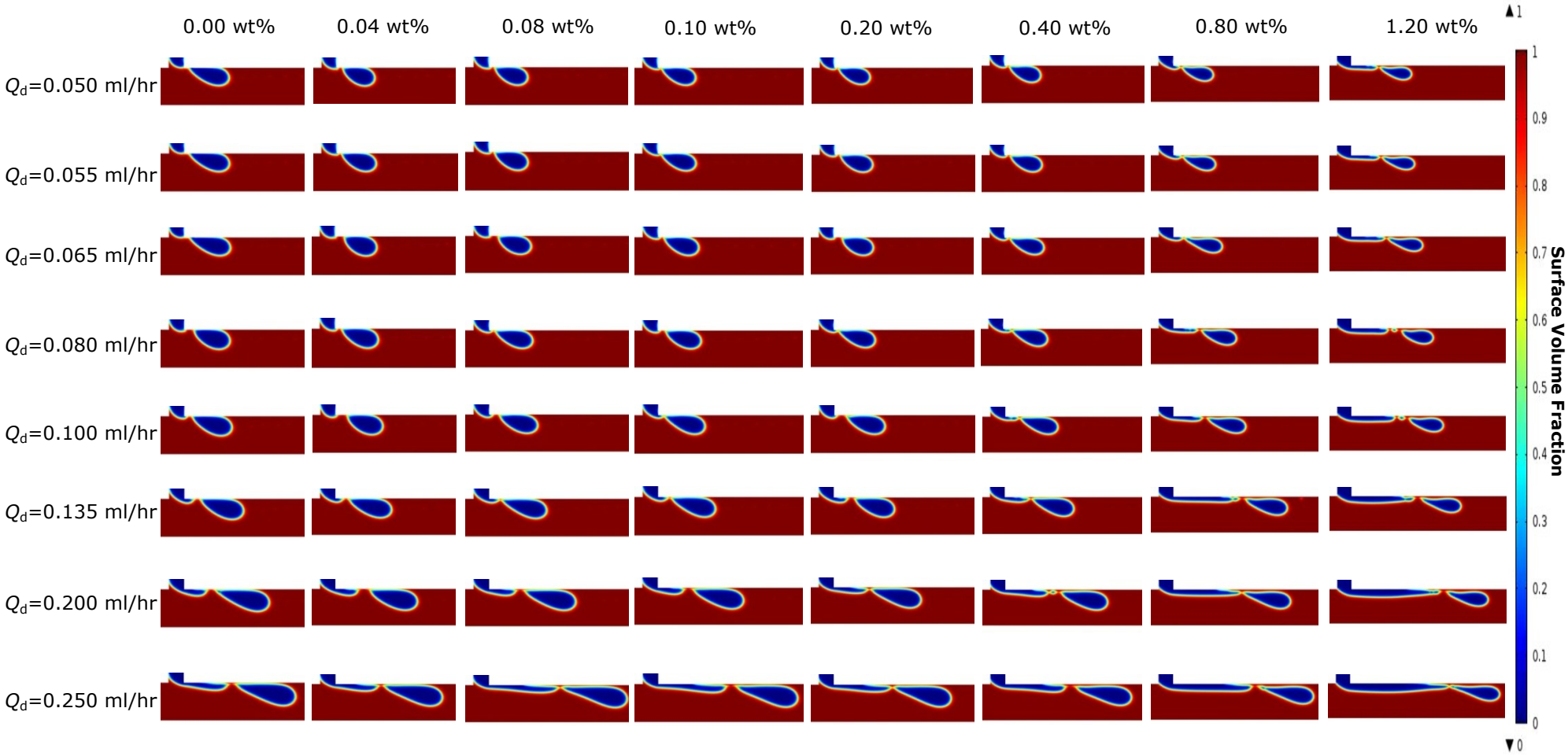


Figure 7.3: Snapshots of two-dimensional (2D) simulation of the effect of dispersed phase rate on CMC-in-olive oil droplet breakup process for different CMC concentrations (for system: Q_c=2.00 ml/hr).

7.2.2 Effect of Dispersed Phase Flow Rate on Droplet Formation Time

The influence of Q_d the on normalised droplet formation time was examined and the results are plotted graphically in Figure 7.4. The droplet formation time show dependence on Q_d regardless of variation in CMC concentration. With the increase in Q_d (increase in Q), the time taken for a droplet to form and detach is reduced for a fixed Q_c. As Q_d increases, the larger internal flow rates lead to more volume entering a droplet prior to breakup in the main channel resulting in a higher growth rate of dispersed thread and thus increase of breakup (Garstecki *et al*., 2006; Tan *et al*., 2008; Bashir *et al*., 2011, Fu *et al*., 2012). Davidson and Cooper-White (2006) reported that the rate at which a shear-thinning pendant drop pinch-off becomes more abrupt as the Weber number increases which means the inertial force becomes more prominent as the rate of dispersed thread increases. As Figure 7.4 shows, when the CMC concentration is increased above C*, different decreasing trend in droplet formation time was found. This is because the abrupt changes in viscosity properties when the polymer disentanglement occurs beyond the C* causes retardation of breakup process.

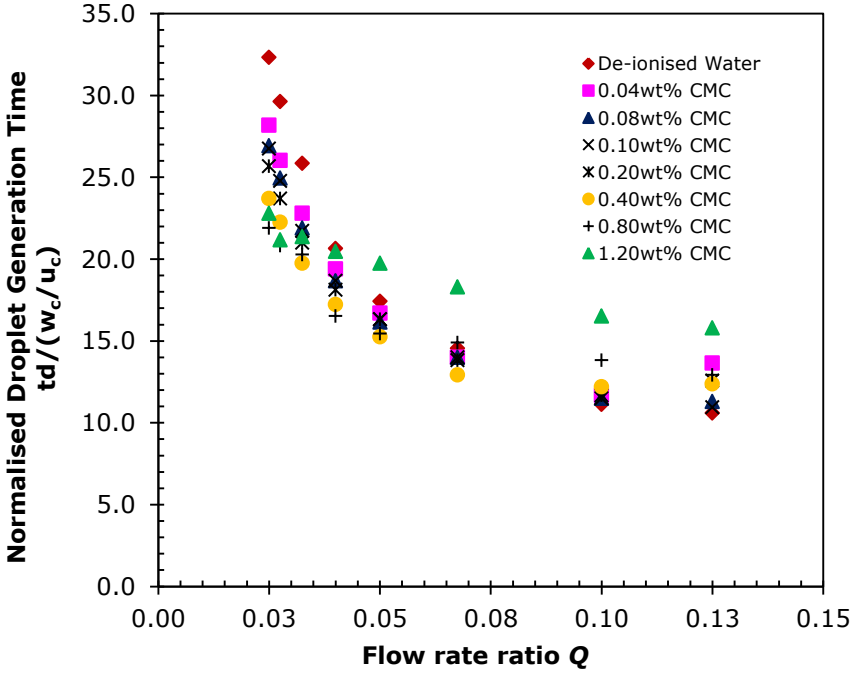


Figure 7.4: Effect of dispersed phase flow rate on the normalised droplet formation time of CMC solutions for various CMC concentrations at different flow rate ratio Q (=Q_d/Q_c) (for system: Q_c: fixed 2.00 ml/hr; Q_d: 0.05 ml/hr to 0.25ml/hr).

7.2.3 Effect of Dispersed Phase Flow Rate on Droplet Generation Frequency

The droplet generation frequency could be tuned by controlling the rates of dispersed phase. The normalised droplet formation frequency is proportionally increased with the dispersed phase flow rate as illustrated in Figure 7.5. For both Newtonian and shear-thinning solution, the use of a higher dispersed phase flow rate leads to a rise in CMC droplet diameter (see Figure 7.1) and a corresponding increase in the frequency of droplet formation, enabling high throughput. However, the results showed a dissimilar increasing trend of generation frequency for data in Figure 7.5 when C>C*~0.40wt% owing to the viscosity effect, as noted in previous section.

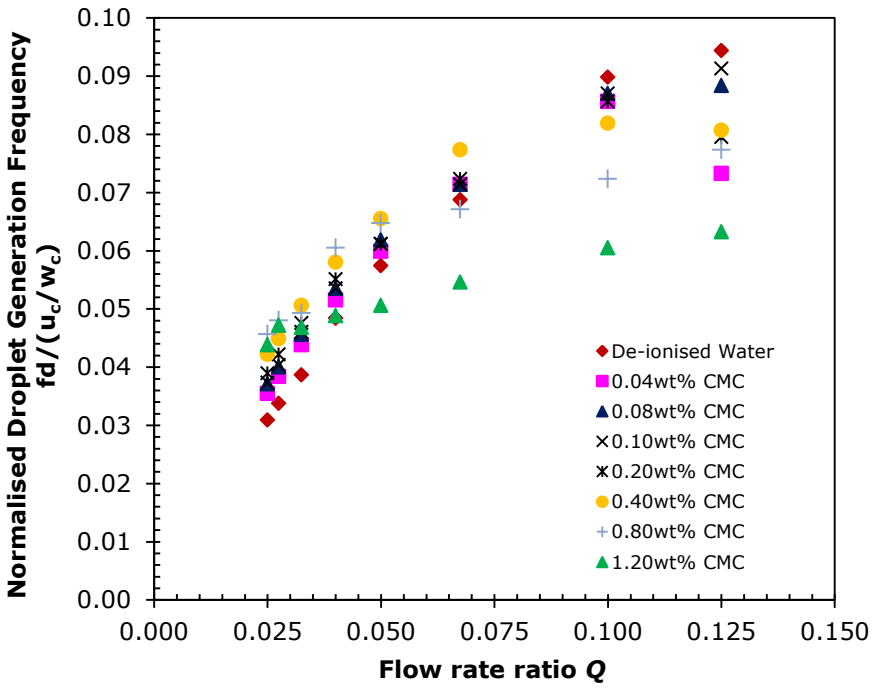


Figure 7.5: Effect of dispersed phase flow rate on normalised droplet generation frequency of CMC solutions for various CMC concentrations at different flow rate ratio Q ($=Q_d/Q_c$) (for system: Q_c: fixed 2.00 ml/hr; Q_d: 0.05 ml/hr to 0.25ml/hr).

7.2.4 Effect of Continuous Phase Flow Rate on Effective Droplet Diameter

Droplet formation process is dominated by the balancing of interfacial force and viscous stresses imposed by the continuous phase and also the viscosity of the dispersed phase. The size of the droplets can be tuned by changing the

continuous phase flow rate, which may alter the viscous stresses on the droplets (DeMenech *et al*., 2008). Since the channel width of continuous phase (w_c≈221 μm) is larger than the dispersed phase channel width (w_d≈90 μm), the dispersed phase stream does not occupy the entire width of the channel downstream of T-junction, and thus the breakup is mainly dominated by the local shear-stress of the continuous phase acting on the stream of dispersed phase thread.

For a constant Q_d at 0.20 ml/hr, the droplet size was measured with the variation in continuous phase flow rate, Q_c (1.50 ml/hr to 4.00 ml/hr), with results shown in Figure7.6. Figure 7.6 reveals that CMC droplet size can be discerned in the T-junction microchannel by varying the flow rates of the continuous phase when the disperse phase is kept constant, with the data tabulated in Table A.9 (see Appendix A.3). As the Q_c is increased, the simulations show a reduction in droplet size as illustrated graphically in Figure 7.6. As expected, the graph shows that the diameter of CMC droplet decreases as the continuous phase flow speed increases, as at higher Q_c, the shearing effect on the dispersed phase is larger, and droplets will pinch off before reaching a significant size. According to Husney *et al*. (2003), this behaviour can be interpreted by the fact that at a higher cross flow velocity, a higher shear force near the wall is presented. Consequently, this leads to a decrease in the drop growth and detachment time, resulting in a reduction in final drop volume. Both Thorsen *et al*. (2001) and Tan *et al*. (2008) also reported that the droplet size of the Newtonian fluids is decreased with increasing Q_c. Hong and Cooper-White (2009) studied that the non-Newtonian properties affected the droplet formation dynamics in a flow-focusing device which responsible for variation in droplet size. As Q_c is further increased, the droplet size increases as viscosity ratio increases due to the impact of non-Newtonian properties (Hong and Cooper-White, 2009). As compared to the Newtonian dispersion, the increase of CMC concentration was shown to cause reduction in droplet diameters for a fixed Q_c. This is mainly

due to the fact that the extent of shear-thinning in the emulsion becomes more pronounced when its concentration increases, leading to a reduction in droplet diameter once the shear stress induced by continuous phase exerted on the interface. Besides, as dispersed phase concentration increases, the increase of the viscosity contributes to an increase in viscous pressure in the dispersed thread which opposes the capillary pressure and suppress the growth of the deformation of droplets resulting in longer threads but contains less material being formed and thus a smaller droplets are being created (Zhang and Basaran, 1995; Nunes *et al*., 2013). The variation in normalised effective droplet diameter of CMC solution could be also correlated to the flow rate ratio, Q of both phases in T-junction microfluidics as demonstrated in Figure 7.7. As Q increases, the normalised droplet diameter is increased when the continuous phase rate is decreased with the same change of dispersed phase. This prediction was found similar to the previous observations in a T-junction microfluidics (Gu and Liow, 2011). Figure 7.8 demonstrates the snapshots of effect of Q_c on the CMC droplet flow pattern for various CMC concentrations. Liu and Zhang (2011) have systematically investigated the flow pattern of droplet formation process as function of flow rate ratio in a cross-flowing microfluidics using lattice Boltzmann approach. At low Q, the droplets breakup occurs near the corner of cross-junction, whereas the breakup point is shifted further downstream in the main channel when the Q is increasing. This phenomenon has been found similar to the simulation predictions for all CMC concentrations as illustrated in Figure 7.8.

Figure 7.9 illustrates the evolution of pressure of the entire droplets formation process for 0.20wt% CMC dispersed liquid at each flow rate ratio. As demonstrated in Figure 7.9, it is clearly shown that the increase in the averaged pressure profile with sharp pressure step for the higher rate of continuous phase. As Q_c increases, the gap between the emerging droplet and main channel wall is increased due to the emerging dispersed tip does not have sufficient time to

obstruct the main channel caused by the significant increase in pressure at the corner of T-junction resulting in immediate breakup, which in similar to the corresponding Newtonian fluid.

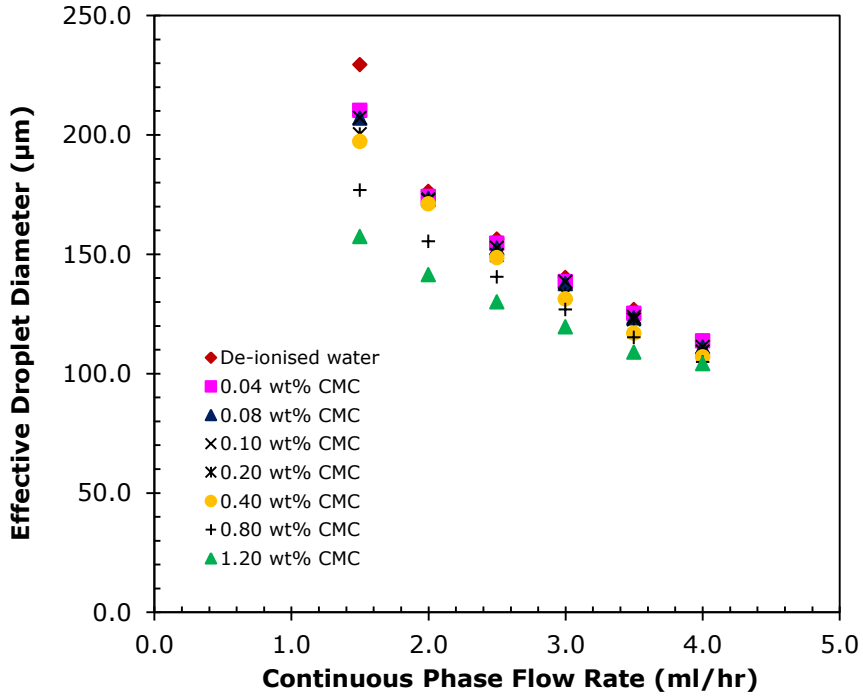


Figure 7.6: Effect of continuous phase flow rate on effective droplet diameter of CMC solutions for various CMC concentrations (for system: fixed Q_d=0.20 ml/hr).

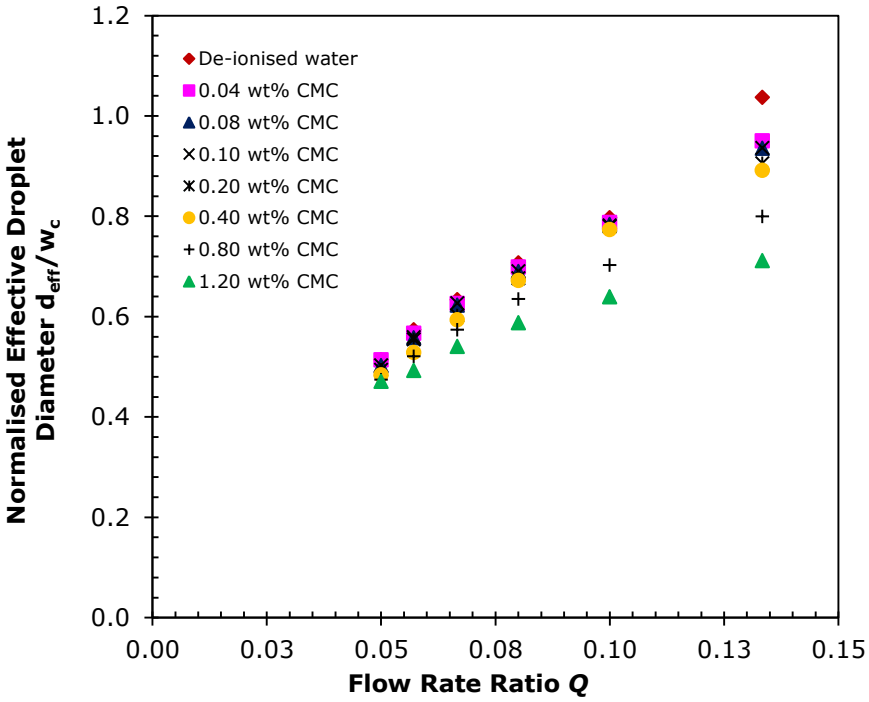


Figure 7.7: Effect of flow rate ratio Q ($=Q_d/Q_c$) on normalised effective droplet diameter of CMC solutions for various CMC concentrations (for system: fixed Q_d=0.20 ml/hr; Q_c=1.50 ml/hr to 4.00 ml/hr).

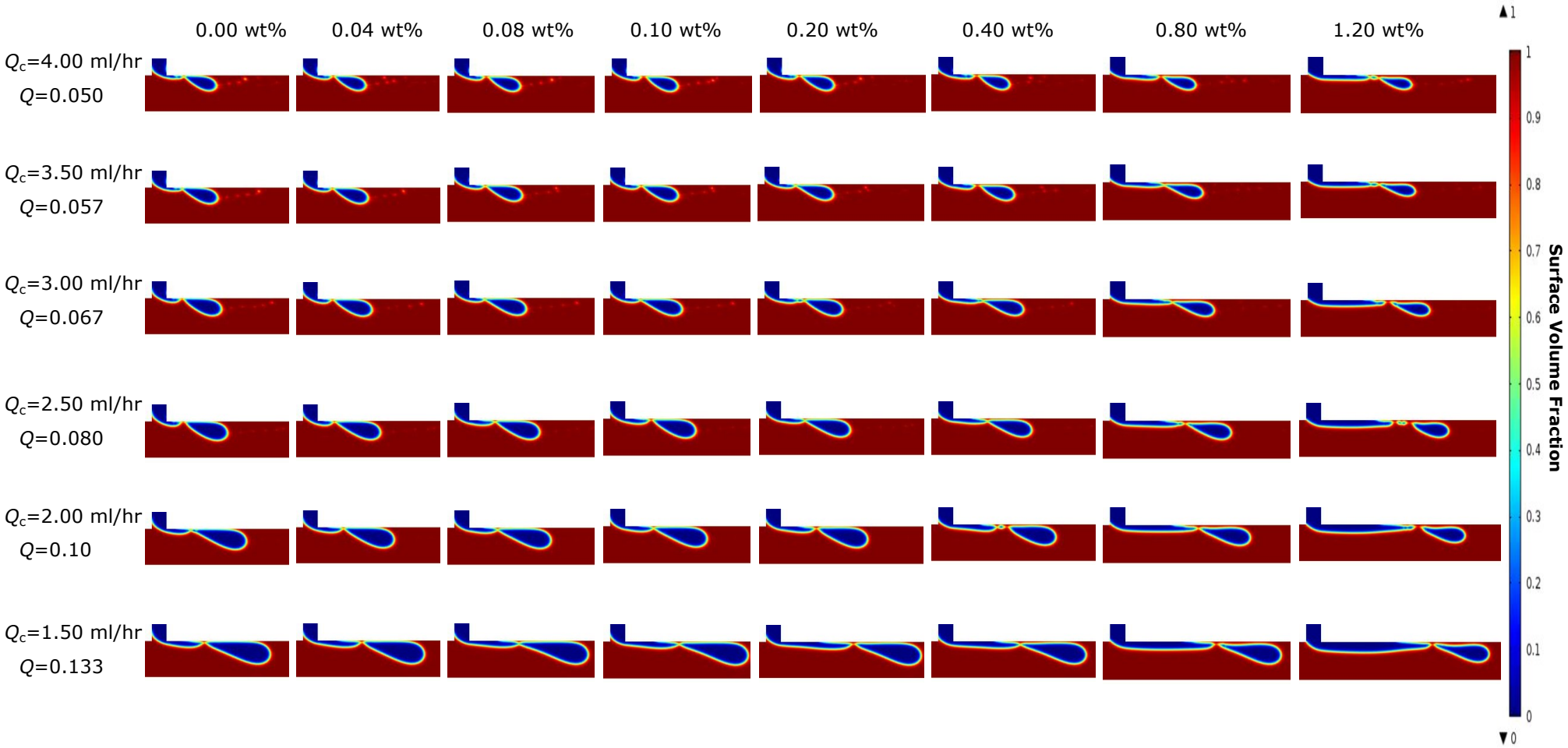
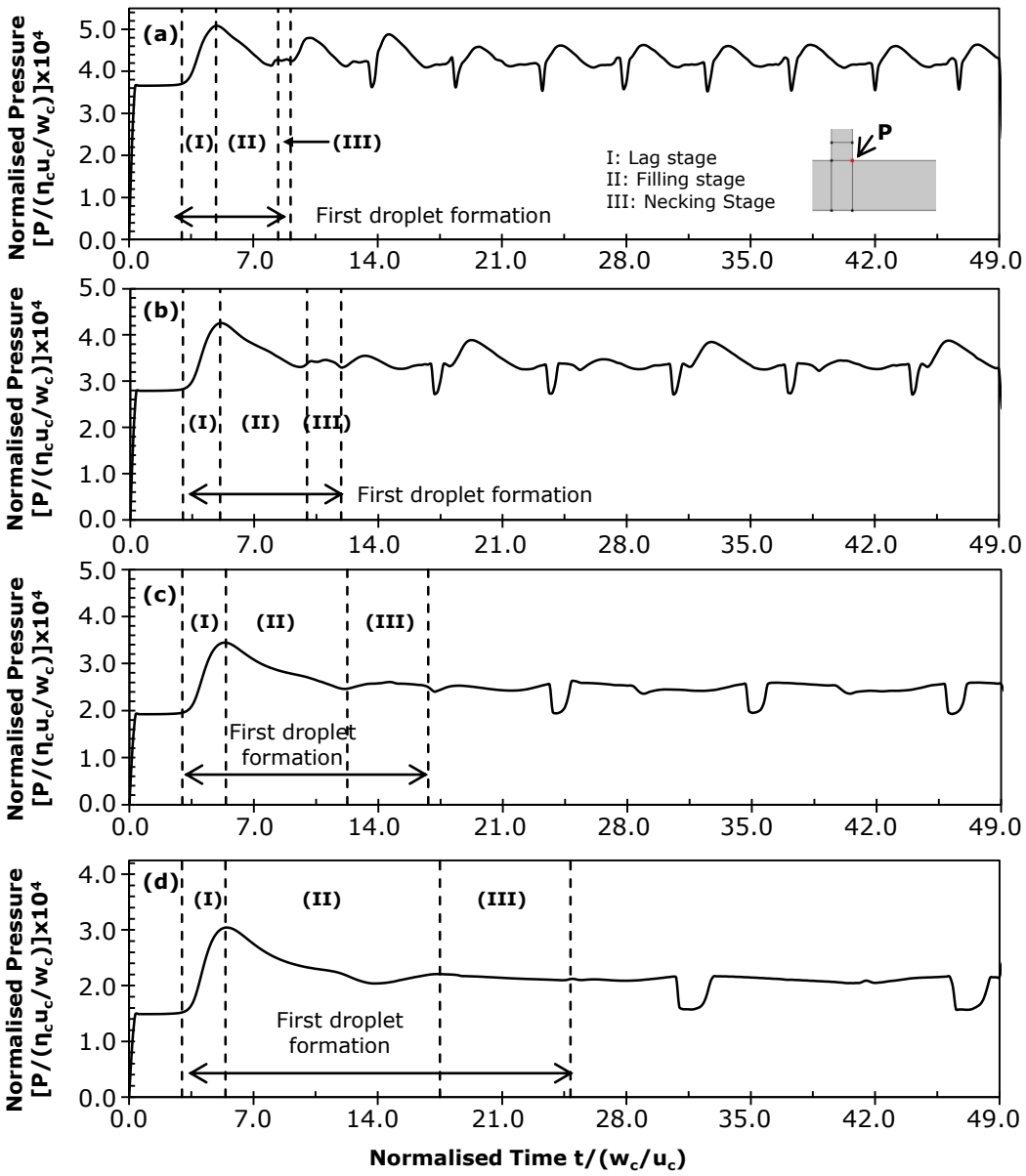


Figure 7.8: Snapshots of two-dimensional (2D) simulation of the effect of continuous phase flow rate on CMC-in-olive oil droplet breakup process for different CMC concentrations (for system: Q_d=0.20 ml/hr).



	Q_c (ml/hr)	$Q(=Q_d/Q_c)$	Pressure Peak (Pa)	Periods (s)	Snapshots
(a)	4.00	0.0500	1705.11	0.0130	
(b)	3.00	0.0667	1317.69	0.0180	
(c)	2.00	0.1000	999.72	0.0330	
(d)	1.50	0.1333	839.01	0.0475	

Figure 7.9: Pressure profile of 0.20wt% for the effects of continuous phase rate on droplet breakup process at each flow rate ratio Q (for system: Q_d=0.20 ml/hr). P denotes the pressure at the corner of T-junction. After the first droplet is pinched off, the pressure fluctuates abruptly and repeatedly. The insignificant sharp pressure peak reflects the detachment point is located downstream of the junction. The pressure profile demonstrated an abrupt fall in pressure caused by the balance of surface tension and viscous force dictates the droplet movement after the first droplet formation. This phenomenon is applied to all cases.

7.2.5 Effect of Continuous Phase Flow Rate on Droplet Formation Time

In numerical aspect, the droplet formation time was systematically predicted with the variation in Q_c for a constant Q_d. The droplet formation time is the time taken by the rear interface travelling from the starting position to near downstream corner of the T-junction (Zhang *et al*., 2009). At the higher flow rate of continuous phase, the resultant droplet formation time decreases exponentially when the local shear-stress acting on interface becomes larger (see Figure 7.10). As compared to the previous experimental works, Cramer *et al*. (2004) performed an investigation on the effect of flow rates on the polyethylene glycol droplets formation over time in the dripping regime using a co-flowing structure. They have reported that the increase of continuous phase flow velocity leads to a reduction in droplet detachment time. As Q_c increases, higher viscous stresses acting on emerging dispersed thread causing more rapidly pinch-off when the early-onset equilibrium between interfacial force and hydrodynamics force is attained (Cramer *et al*., 2004). Besides, Gu and Liow (2011) have experimentally observed the similar phenomenon. Zhang *et al*. (2009) has proposed empirical correlations for predicting the droplet formation time. His empirical model has predicted that the droplet formation time is decreased with increasing of Q_c. The variation in normalised droplet formation time could be also correlated to the flow rate ratio as demonstrated in Figure 7.11. As elucidated in Figure 7.11, the resultant droplet formation time increases as the flow rate ratio increases at the fixed Q_d. This phenomenon is in agreement with Van der Graaf *et al*. (2006) who have reported that higher shear rate exerted by the continuous phase causes shorter necking time and rapid droplet formation for various Q_c at constant Q_d.

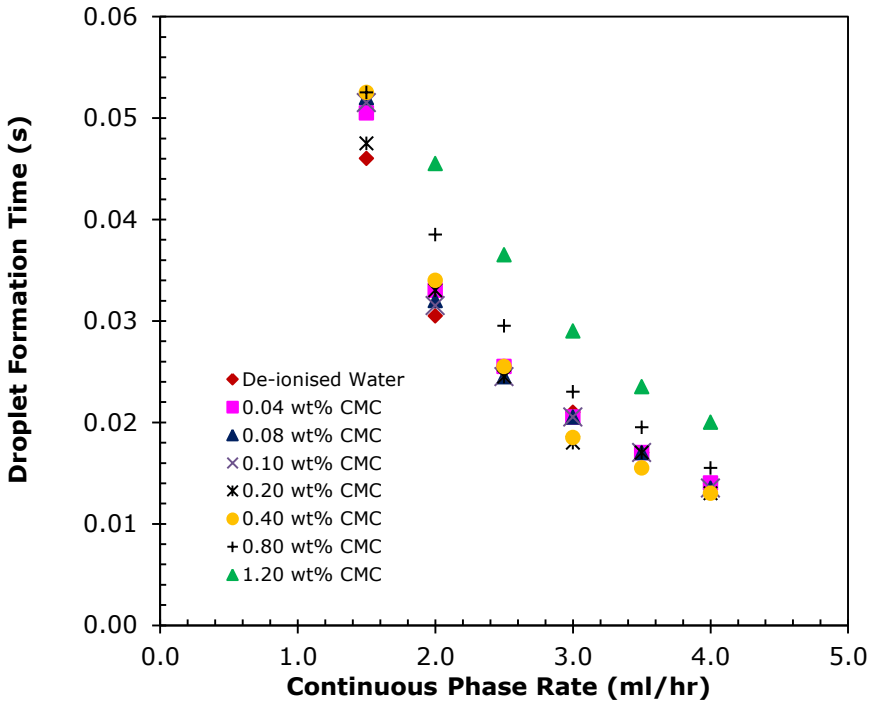


Figure 7.10: Effect of continuous phase flow rate on the droplet formation time of CMC solutions for various CMC concentrations (for system: fixed Q_d=0.20 ml/hr).

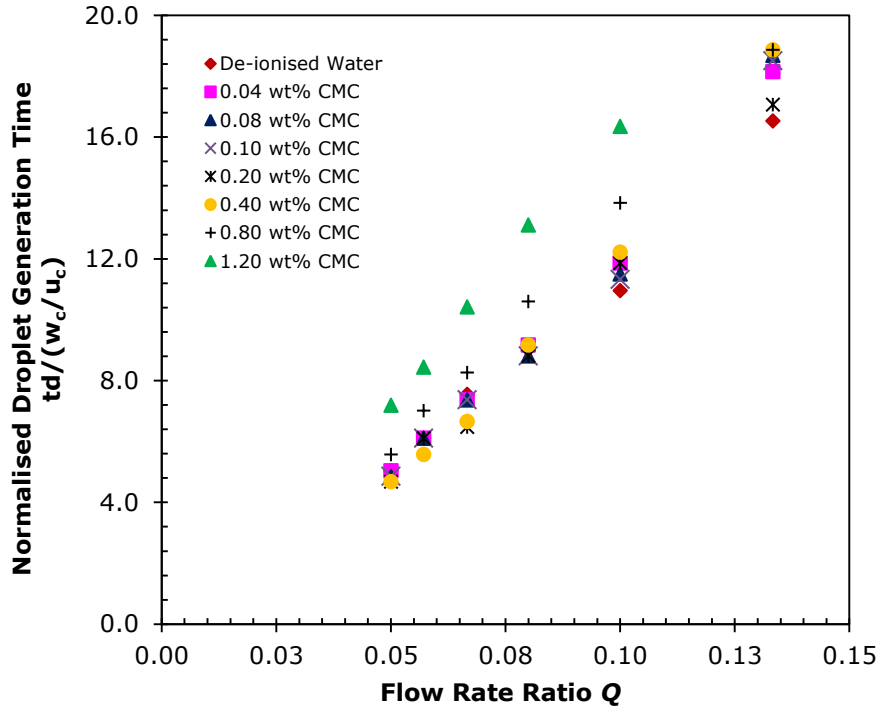


Figure 7.11: Effect of flow rate ratio Q ($=Q_d/Q_c$) on the normalised droplet formation time of CMC solutions for various CMC concentrations (for system: fixed Q_d=0.20 ml/hr; Q_c=1.50 ml/hr to 4.00 ml/hr).

As seen in Figure 7.10, the droplet formation time increases as CMC concentration increases owing to the increase of dispersed phase viscosity. This observation has been reported and described by Zhang and Basaran (1995),

Cooper-White *et al*. (2002), and Hong and Cooper-White (2009). On the other hand, Tirtaatmadja*et al*. (2006) studied experimentally the effect of polymer concentration on the dynamic of droplet formation. The results revealed that the viscous and elastic effects are important to prevent the rapid formation of the pinch region due to the enhancement of chain-chain interaction when the concentration increases. However, according to our numerical model without elasticity effect, a similar observation was found for the non-Newtonian fluid with purely shear-thinning behaviour.

7.2.6 Effect of Continuous Phase Flow Rate on Droplet Generation Frequency

The droplet generation can be governed by the shear-stress and the interfacial tension in microfluidic device. In present study, the variation of interfacial tension with increasing CMC concentration is very narrow (see Table 3.3). Therefore, the surface tension remains almost constant. While the interfacial tension acts to restore the deformation of interface, the shear-stress induced by the continuous phase acts to deform the dispersed thread. By employing a constant value of Q_d, the droplet generation frequency is controlled by regulating the continuous phase flows. Figure 7.12 illustrates the effect of continuous phase rate on the droplet generation frequency for different CMC concentration. As Q_c increases, the generation frequency is increased due to the rapid deformation of fluid interface towards pinch-off. The normalised droplet generation frequency as function of Q is also graphically plotted in Figure 7.13. The results show that as Q decreases, the droplets are rapidly generated owing to higher shear-rate that allows for the shorter breakup time. These findings can be supported by the previous experimental works from other researchers (Cramer *et al*., 2004; Van der Graaf *et al*., 2006; Zhang *et al*., 2009; Gu and Liow, 2011). Interestingly, the generation frequency increases when C>C*. As mentioned previously, this is referred to as the high concentration induce large viscous pressure in the thread

which oppose the breakup process (Zhang and Basaran, 1995; Cooper-White *et al*., 2002; Tirtaatmadja*et al*., 2006; Hong and Cooper-White, 2009).

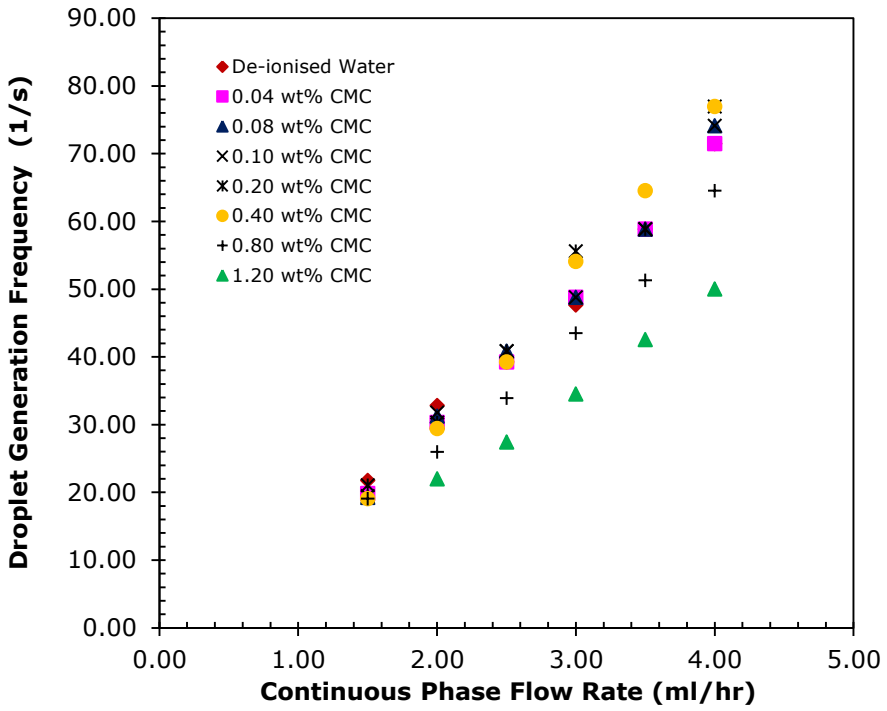


Figure 7.12: Effect of continuous phase flow rate on the CMC droplet generation frequency for various CMC concentrations (for system: fixed Q_d=0.20 ml/hr).

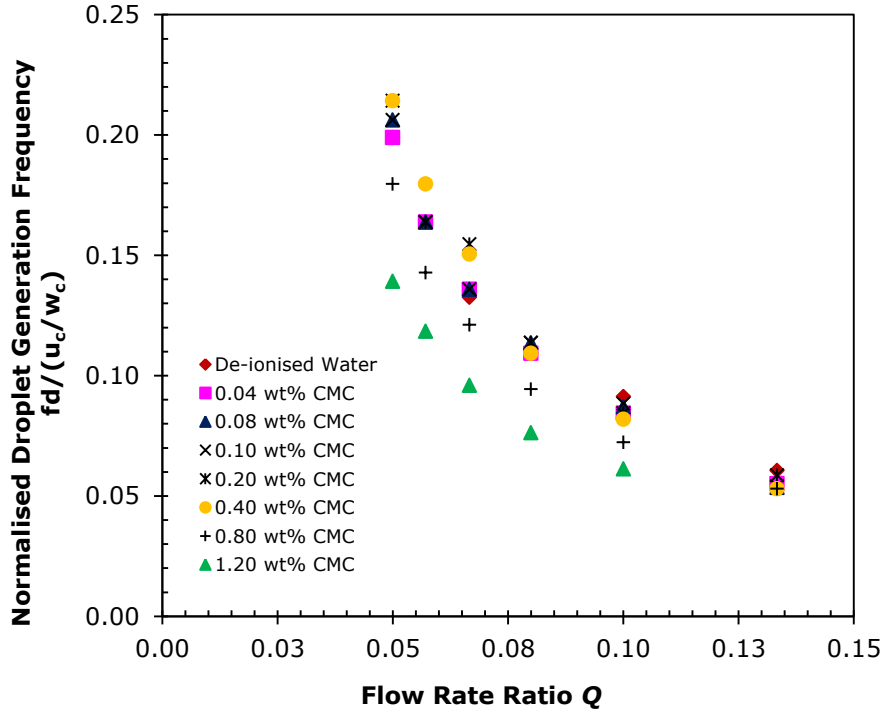


Figure 7.13: Effect of flow rate ratio Q ($=Q_d/Q_c$) on the normalised droplet generation frequency of CMC solutions for various CMC concentrations (for system: fixed Q_d=0.20 ml/hr; Q_c=1.50 ml/hr to 4.00 ml/hr).

7.2.7 Effect of Sodium Carboxymethylcellulose (CMC) Concentration on Effective Droplet Diameter

The present study was designed to determine the influence of the dispersed phase concentration on generated droplet size and the results of prediction data are illustrated in Figure 7.14. As elucidated in Figure 7.14, the results indicate that the larger concentration of CMC dispersed fluid brings the significant effect on reducing the size of generated droplet at Q of 0.05. For instance, when the concentration of dispersed fluid is increased in a series of simulations from 0.00wt% to 1.20wt% for a constant value of Q of 0.05 caused a decrease in droplet diameter from 152.88 μm to 126.68 μm is observed. This is due to the change in the zero shear viscosity η_o from 0.00693 to 10.2644 kg/m.s.

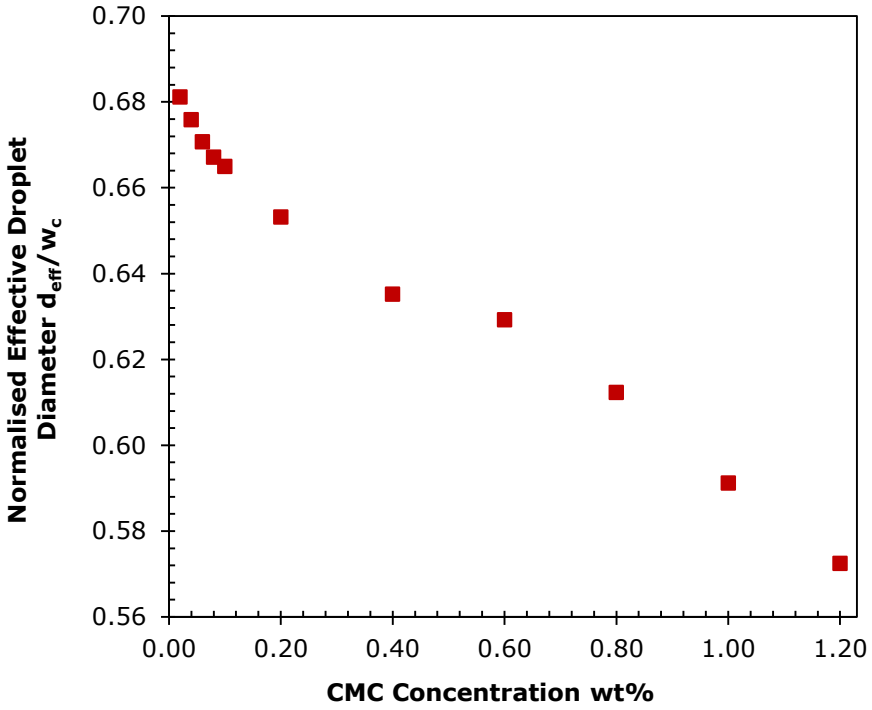


Figure 7.14: Effect of CMC Concentration on normalised effective droplet diameter of CMC droplets (for system: Q_d/Q_c=0.05).

As illustrated in Figure 7.15, the normalised droplet diameter is also strongly influenced by the concentration of shear-thinning CMC solution. These phenomena could be interpreted by the fact that the viscosity effects of the two phases contribute to the droplet formation. Viscosity of a polymer solution depends on concentration and the molecular weight of dissolved polymer. By

taking account of viscosity effects, when the dispersed phase liquid is more viscous than the continuous phase, the viscous force becomes more dominant over the inertial force exerted by the continuous phase on the forming interface. Besides, the shear-thinning effect of CMC solution increases with the concentration. The greater shear-thinning effect exhibit a decrease in viscosity upon the application of shear due to the inertial force. A study made by Davidson and Cooper-White (2006) has reported that the larger effect of shear-thinning will tend to reduce the resulting droplet length at higher viscosity. The effect of dispersed phase concentration can be examined by comparing the CMC droplet size obtained at different flow rate ratio (see Figure 7.15).

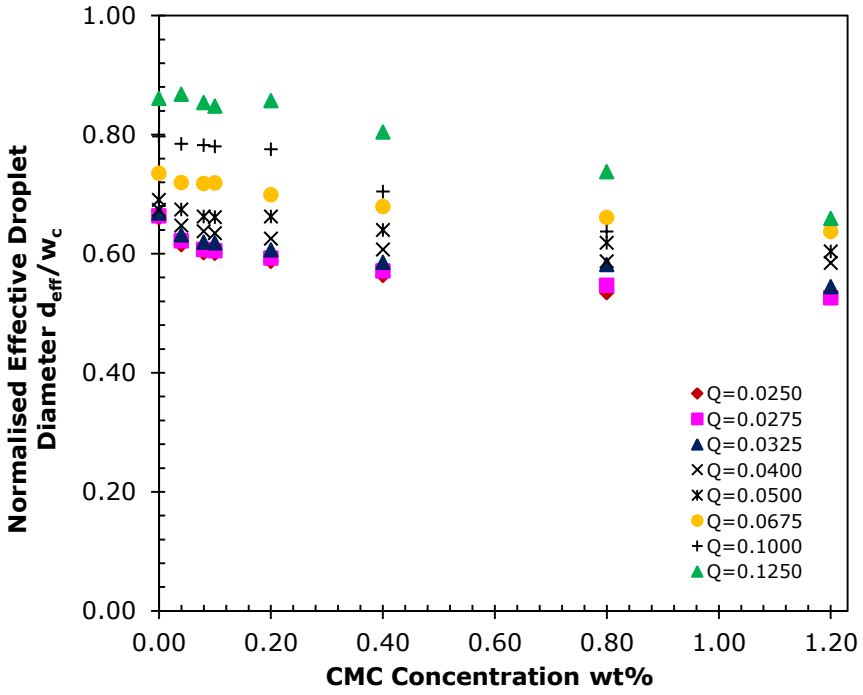
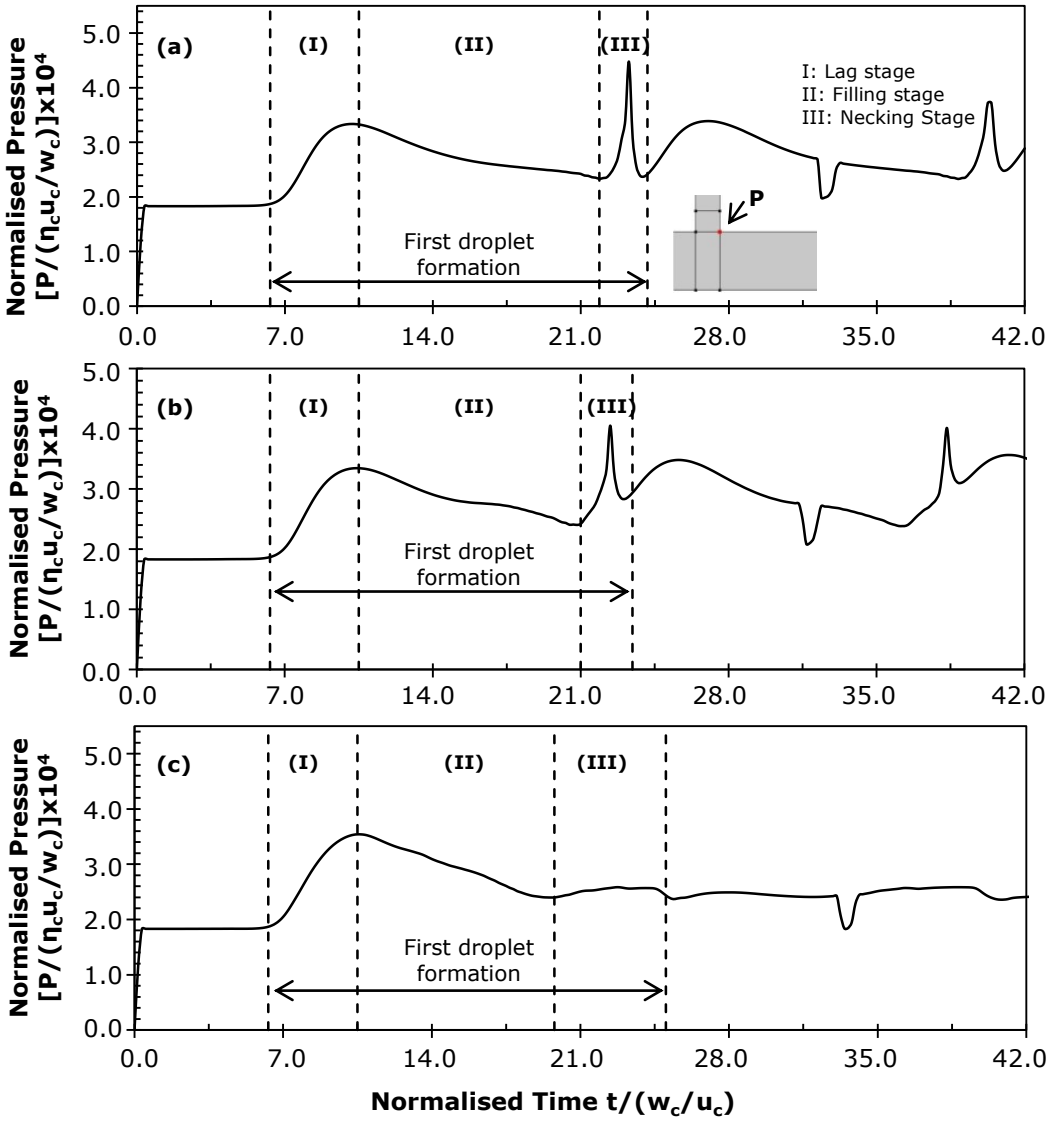


Figure 7.15: Variation in normalised effective droplet diameter of CMC droplets for various CMC concentrations at each flow rate ratio.

Theoretical predictions of the viscosity effect on droplet diameter are found dissimilar to the previous empirical observations for dispersed fluid with different non-Newtonian properties. For instance, Husny and Cooper-White (2006) reported that larger droplet was produced for solutions containing higher polyethylene oxide (PEO) molecular weights and viscosity. Besides, this similar empirical observation to the viscoelastic fluid was also observed by Steinhaus

and Shen (2007). A study has made by Gu and Liow (2011) has reported that a larger diameter droplet diameters was observed for larger viscosity of shear-thinning xanthan gum solution in a T-junction microchannel. Different type of non-Newtonian fluids always displays a rich variety of characteristic that may contrast to these observations; thus, dissimilar phenomena may be accounted due to the complex nature and interactions of non-Newtonian properties. Nevertheless, the current computational studies have been established as a framework that provides reasonable starting points for empirical studies in future applications. More numerical and experimental research studies of nonlinear rheological behaviour of non-Newtonian fluids that impart unusual characteristics to their flow in microfluidics are needed to gather sufficient evidence and provide a further understanding of the breakup dynamics and deformation of non-Newtonian droplets.

Figure 7.16 demonstrates the normalised pressure distribution of droplet breakup process at the T-junction corner for the concentration of 0.00wt%, 0.20wt% and 0.80wt% CMC solution. For the fixed flow rate ratio *Q* of 0.05, the droplets pinch off nearer to the corner of junction result in sharp pressure peaks when the CMC concentration is lower. However, a progressive necking and breakup of the dispersed thread occurs downstream results in less pressure peaks when higher concentration are encountered. This is mainly due to the fact that higher concentration of dispersed phase contributes to flow resistance that enable the formation of a stable and laminar thread before the droplet is being generated. Consequently, sharp pressure peaks are less marked with the dynamic breakup occurring at the corner of T-junction.



	CMC Concentration	Pressure Peak (Pa)	Periods (s)	Snapshots
(a)	0.00wt%	1790.25	0.0485	
(b)	0.20wt%	1620.45	0.0455	
(c)	0.80wt%	974.25	0.0425	

Figure 7.16: Pressure profile of (a) 0.0wt%, (b) 0.20wt%, (c) 0.80wt%for droplet breakup process (for system: Q_d/Q_c=0.05). P denotes the pressure at the corner of T-junction. The sharp pressure peak in the given data values reflects the droplet breakup point as shown in the extracted images. The insignificant sharp pressure peak reflects the detachment point is located downstream of the junction. The pressure profile demonstrated an abrupt fall in pressure caused by the balance of surface tension and viscous force dictates the droplet movement after the first droplet formation. This phenomenon is applied to all cases. The maximum magnitudes of the pressure peak and the formation periods under different CMC concentration are listed above.

7.2.8 Effect of Sodium Carboxymethylcellulose (CMC) Concentration on Droplet Formation Time

As illustrated in Figure 7.17, as the CMC concentration increases, the formation time of CMC droplets increases with the increase of shear-thinning effect. The effect of CMC concentrations were also examined by comparing the CMC droplet breakup time obtained at different flow rate ratio as illustrated in Figure 7.18. As seen in both figures, the distribution of breakup time evolution can be discerned in two distinct concentration regimes, namely dilute regime and semi-dilute regime (see section 3.5.2). In dilute regime, the breakup time decreases as CMC concentration (0.02wt% to 0.40wt% (≈C*)) increases. Within this regime, the solution was dilute with weak chain-chain interactions. Moreover, the droplets pinch-off in lower viscosity fluids for which the inertial effects are amplified. Tirtaatmadja*et al*. (2006) studied the dynamics pinching process for low viscosity of elastic pendant drop. They reported that viscous and elastic stress become irrelevant when the dynamics controlled by inertial-capillary balance contributes in rapid formation of pinch region. It could be envisaged that the lower the dispersed phase viscosity, the higher the dominance inertial force by the continuous phase over interfacial forces. While the solution enters semi-dilute regime (0.60wt% to 1.20wt%), the breakup time increases drastically when the increasing of chain concentration, which in consequences causes an significant increase in viscous pressure to prevail over the Laplace pressure and retard the breakup process. At concentrations well above the critical concentration (C*~0.40wt%) of polymer, the onset of the intermolecular hydrodynamic interaction occurs between the polymer coil. This is because the flow incident on a chain is perturbed by the segments of the neighbouring chains. Therefore, a sharp increase in viscosity leads to marked increase in resistance to flow. Hence, the breakup process is substantially retarded. This retardation of breakup mechanism due to the high viscous pressure in thread was adequately explored in many works that has been published (Zhang and Basaran, 1995; Cooper-

White *et al*., 2002; Tirtaatmadja*et al*., 2006; Arratia *et al*., 2009; Hong and Cooper-White, 2009).

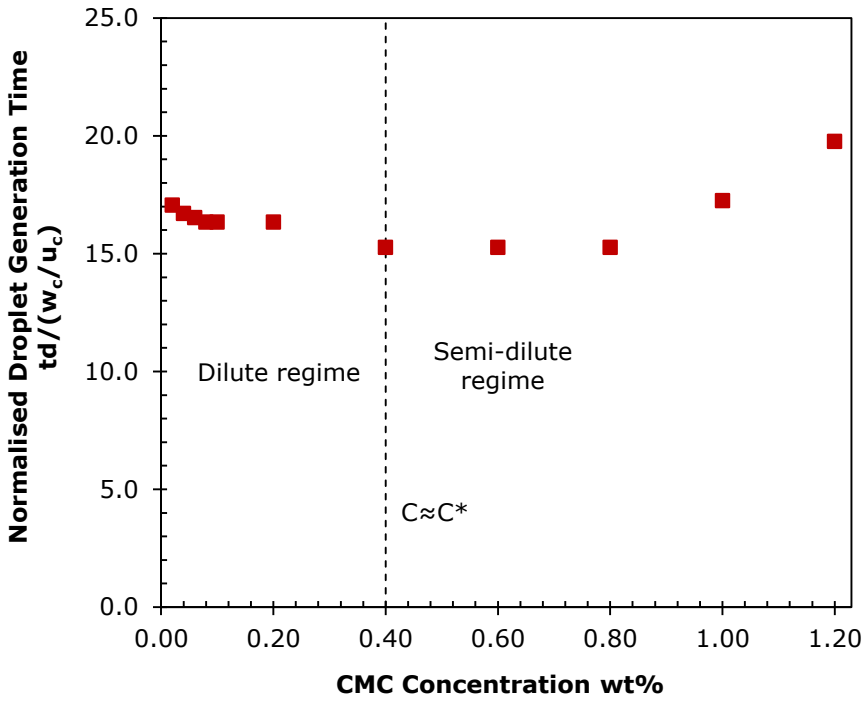


Figure 7.17: Effect of CMC Concentration on droplet formation time of CMC droplets (for system: Q_d/Q_c=0.05).

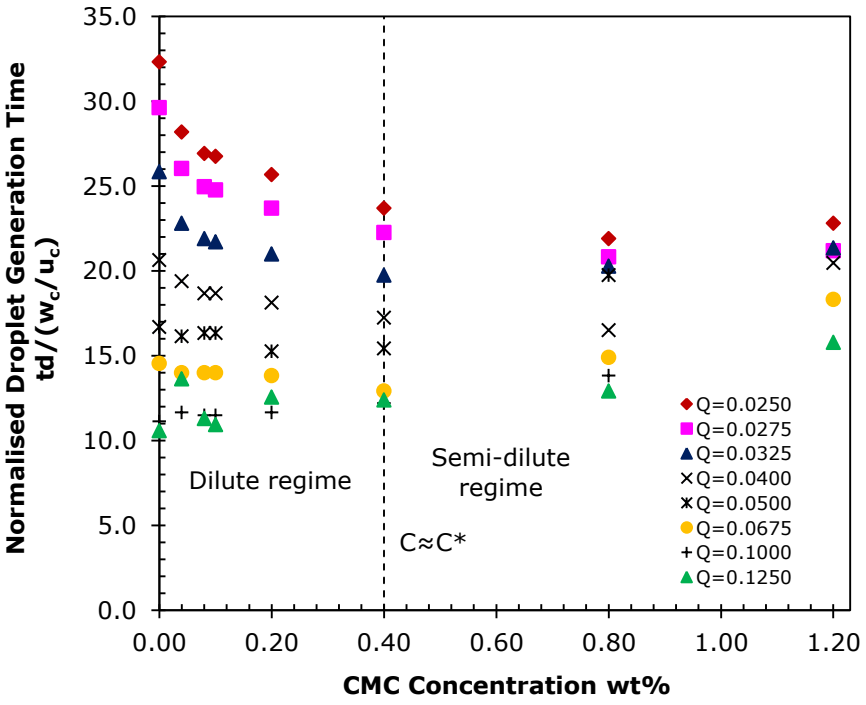


Figure 7.18: Variation in droplet formation time of CMC droplets for various CMC concentrations at each flow rate ratio.

7.2.9 Effect of Sodium Carboxymethylcellulose (CMC) Concentration on Droplet Generation Frequency

The influence of the dispersed phase concentration on normalised f_d was examined and the results are plotted graphically in Figure 7.19. The effect of dispersed phase concentration can be examined by comparing the normalised f_d obtained at different flow rate ratio (see Figure 7.20). As seen in Figure 7.19, when the solution in dilute regime (C<C*~0.40wt%), the frequency of droplet generation is increased. With the increase of CMC concentration, a significant effect of shear-thinning behaviour results in a faster growth rate of droplets. While at each viscosity of dispersed phase fluid, it has been found that the higher frequency of droplet generation and the shorter time of droplets formation caused the larger diameter of the droplets as it is fully compensated by faster growth rate of droplets when the rate of dispersed phase flow. When C>C*~0.40wt%, the reduction in frequency of droplet formation was observed when the viscosity of CMC polymer fluid is further increased to 1.20wt% owing to considerable viscosity effect of the dispersed phase, as we have previously discussed (see section 7.2.8).

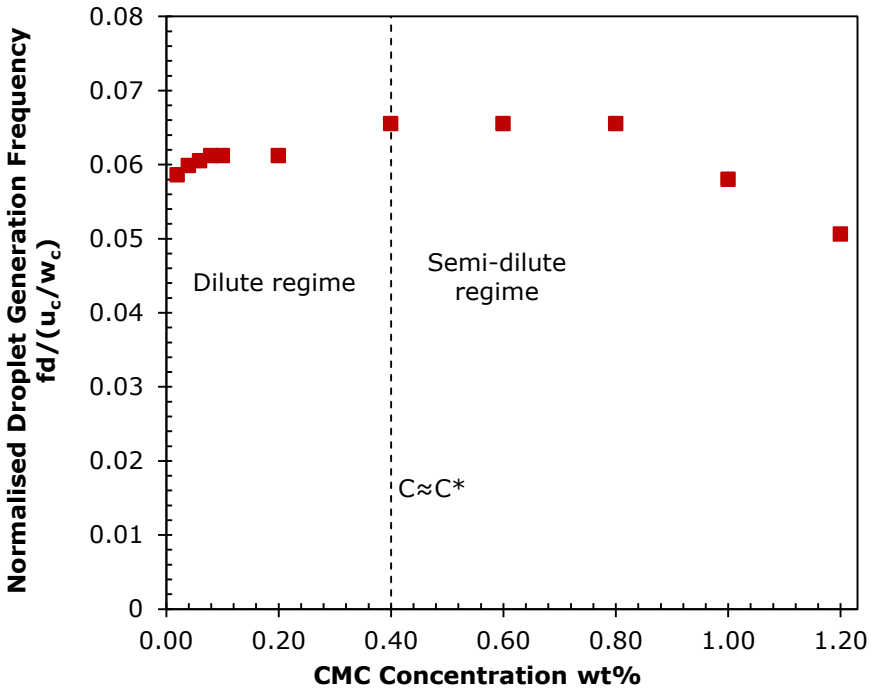


Figure 7.19: Effect of CMC concentration on normalised droplet generation frequency of CMC droplets (for system: Q_d/Q_c=0.05).

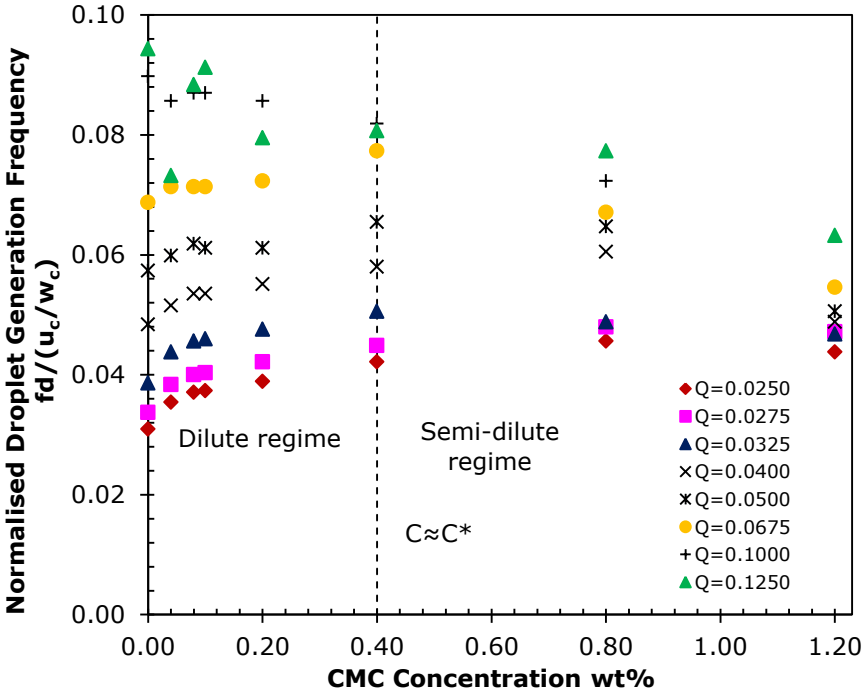


Figure 7.20: Variation in normalised droplet generation frequency of CMC droplets for various CMC concentrations at each flow rate ratio.

7.2.10 Effect of Continuous Phase Viscosity on Effective Droplet Diameter

Apart from the influence of dispersed phase viscosity, the continuous phase viscosity η_c is also an important factor in controlling the dispersion stability. This study set out with the aim of accessing the role of the continuous phase viscosity on CMC droplets in the context of droplet size distribution at each CMC concentrations and these results are plotted in Figure 7.21.Three different viscosities, 0.0354 kg/m.s (mineral oil), 0.068 kg/m.s (olive oil), and 0.0988 kg/m.s (peanut oil) of continuous phase (From data in Loizou *et al*. (2014)) were employed for current studies on droplet breakup process. Numerical simulations were performed at a constant flow rate ratio Q of 0.05 (where Q_c: 2.00 ml/hr, Q_d: 0.10 ml/hr).

Figure 7.21 illustrates that droplet diameter decreases as continuous phase viscosity increases. Decreasing the continuous phase viscosity (or increasing

viscosity ratio λ, quotient of η_o with the η_c), a higher viscosity ratio indicates that smaller shear force on penetrating dispersed phase thread and thus a higher likelihood of leading to more stable thread. Husny and Cooper-White (2006) supported the argument that the increasing the continuous phase viscosity results in decreasing of the droplets size. The findings of current study are also consistent with those earlier experimental studies (Garstecki *et al*., 2006; Yeom and Lee, 2011; Gu and Liow, 2011). Nevertheless, the present results still differed from other published findings (Gupta and Kumar, 2010), which stated that the volume of droplet is increased with increasing the continuous phase viscosity.

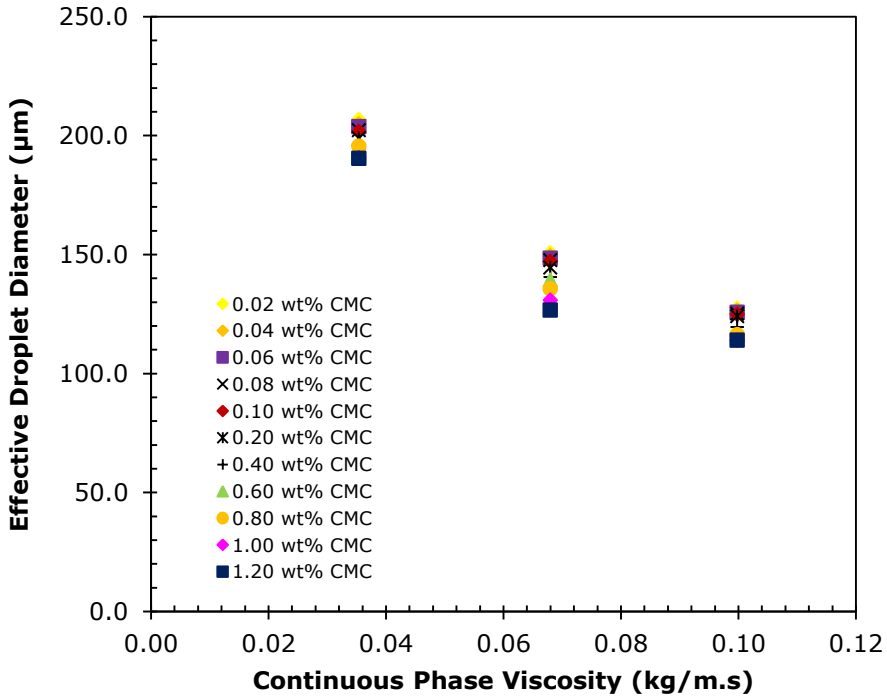


Figure 7.21: Effect of continuous phase viscosity on effective droplet diameter of CMC droplets (for system: Q_d/Q_c=0.05).

Figure 7.22 illustrates the effect of continuous phase viscosity on normalised droplet diameter for various CMC concentrations. In accordance with the present results, previous studies (see section 7.2.7) have demonstrated that the droplet diameter decreases as the increase of the concentration of dispersed fluid at a constant η_c of 0.068 kg/m.s. As seen in Figure 7.22, it is clearly show that the

results has attributes similar to different type of oil properties on controlling the droplet size at each CMC concentration. Prior studies have noted that the volume (relative to droplet size) of a final droplet at the end of the growth and detachment stages is determined by the forces balance at the detachment point. The droplet is generated when the equilibrium of forces is achieved (Husny *et al*., 2003). Surface tension force, shear-stress force (force induced by continuous phase), and resistance force (force induced by dispersed phase) are the dominant forces that generally acting on emerging tip of dispersed thread as reported by Garteski *et al*. (2006). At fixed *Q* and dispersed phase concentration, the droplet diameter is reduced with the increasing of η_c. Figure 7.23 illustrates normalised droplet diameter as function of viscosity ratio for fixed flow rate ratio. At lower η_c (or higher viscosity ratio), viscous shear-stress seems appear to be minimised and surface tension (mineral oil, 41.37±2.90 mN/m>olive oil, 20.74±0.47 mN/m> peanut oil, 18.80±1.31 mN/m, from empirical data in Loizou *et al*., (2014)) becomes increasingly dominant on breakup process. While increasing η_c, shear-stress force exerted on the interface by continuous phase could largely increases. This effect becomes more effective when larger Q_c is involved.

The pressure profile of 0.20wt% CMC droplets under different η_c at fixed flow rate ratio are illustrated in Figure 7.24. As observed from Figure 7.24, the build-up pressure at the corner of junction increases as the η_c decreases. The simulations indicated that the averaged pressure peaks are less marked in the case of larger η_c. A possible explanation for this might be that, the larger viscosity of continuous phase, corresponding to the larger magnitude of the viscous drag forces acting on the immiscible tip is sufficiently high to cause the flow goes farther downstream (see Figure 7.25) and thus the droplets are being sheared off in the main channel. Consequently, sharp peaks were clearly observed when η_c is smaller.

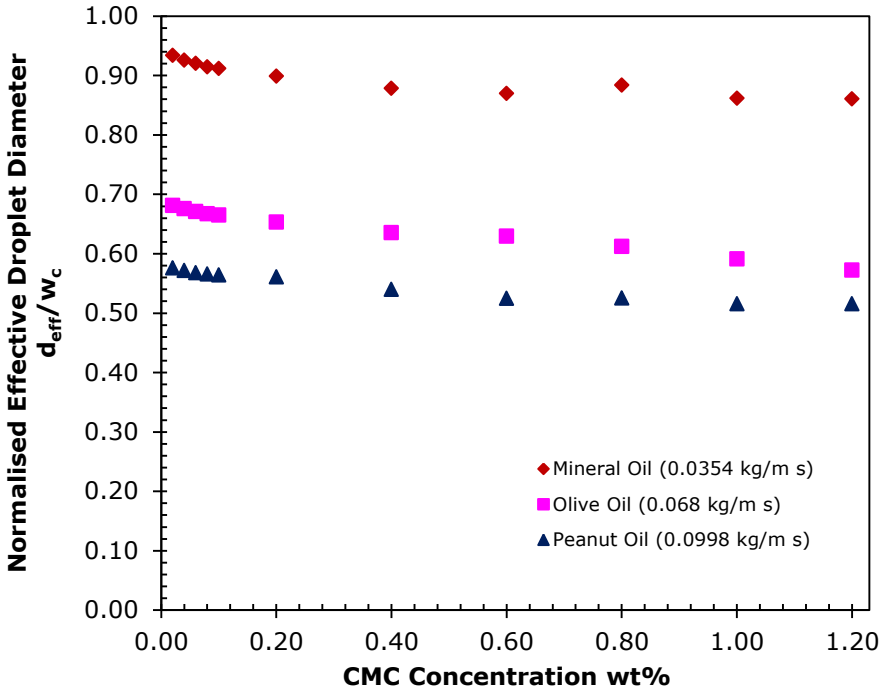


Figure 7.22: Effect of continuous phase viscosity on effective droplet diameter for different CMC concentration (for system: Q_d/Q_c=0.05).

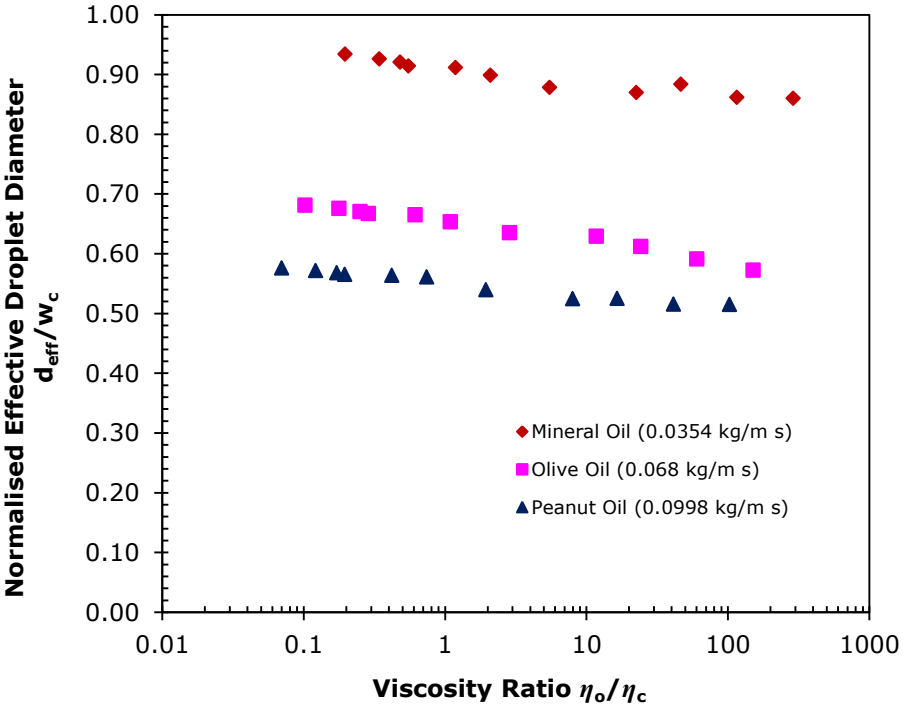
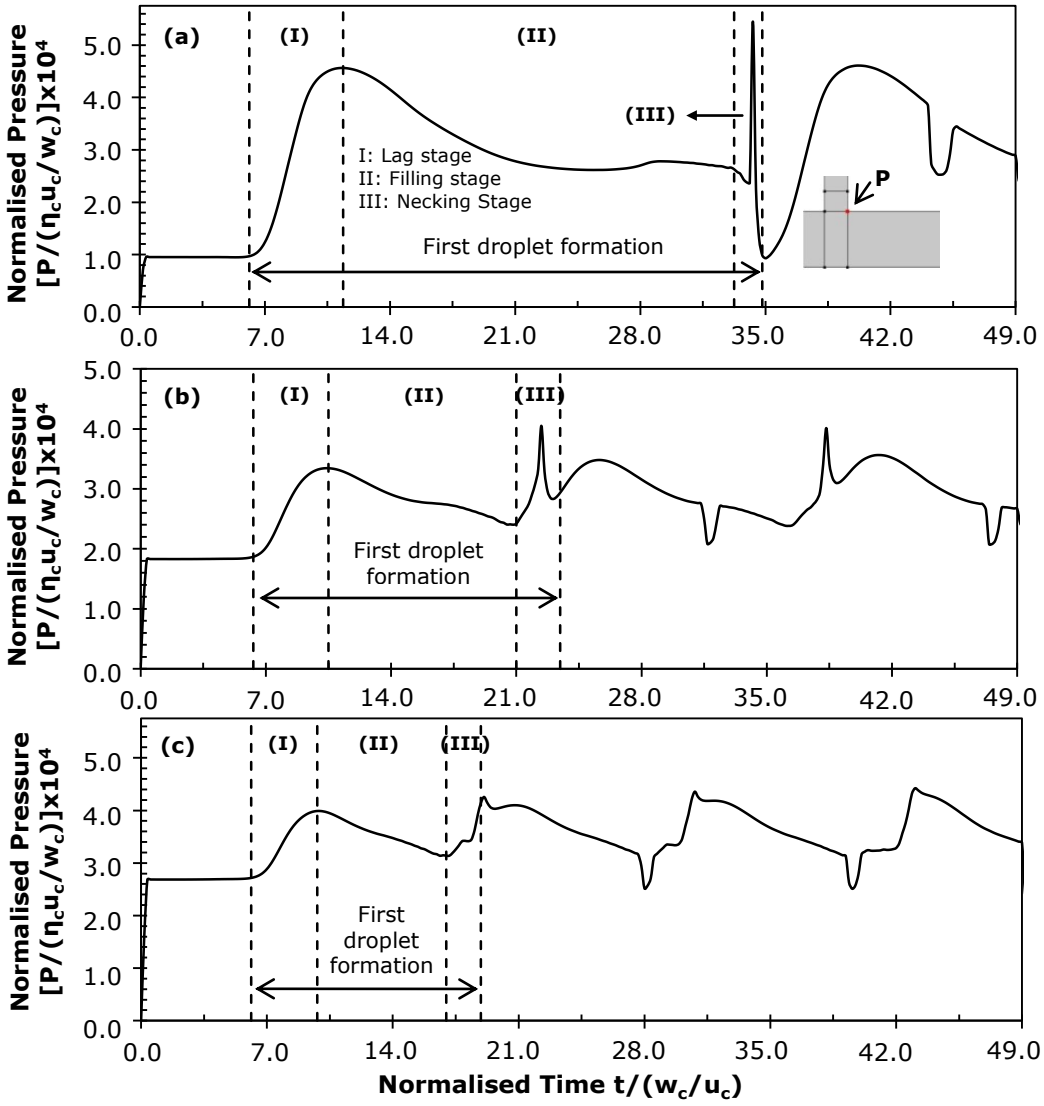


Figure 7.23: Effect of viscosity ratio on effective droplet diameter of CMC droplets for different continuous phase viscosity (for system: Q_d/Q_c=0.05).



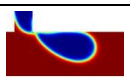
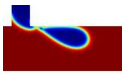
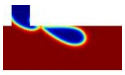
η_c (kg/m.s)	Pressure Peak (Pa)	Periods (s)	Snapshots
0.0354	2179.94	0.0825	
0.0680	1620.45	0.0455	
0.0998	1564.84	0.0330	

Figure 7.24: Pressure profile of 0.20wt% CMC droplets breakup at the system with different continuous phase viscosity: (a) 0.0354kg/m.s, (b) 0.068kg/m.s, (c) 0.0998 kg/m.s(for system: Q_d/Q_c=0.05). P denotes the pressure at the corner of T-junction. The sharp pressure peak in the given data values reflects the droplet breakup point as shown in the extracted images. The insignificant sharp pressure peak reflects the detachment point is located downstream of the junction. The pressure profile demonstrated an abrupt fall in pressure caused by the balance of surface tension and viscous force dictates the droplet movement after the first droplet formation. This phenomenon is applied to all cases. The maximum magnitudes of the pressure peak and the formation periods under different continuous phase viscosity are listed above.

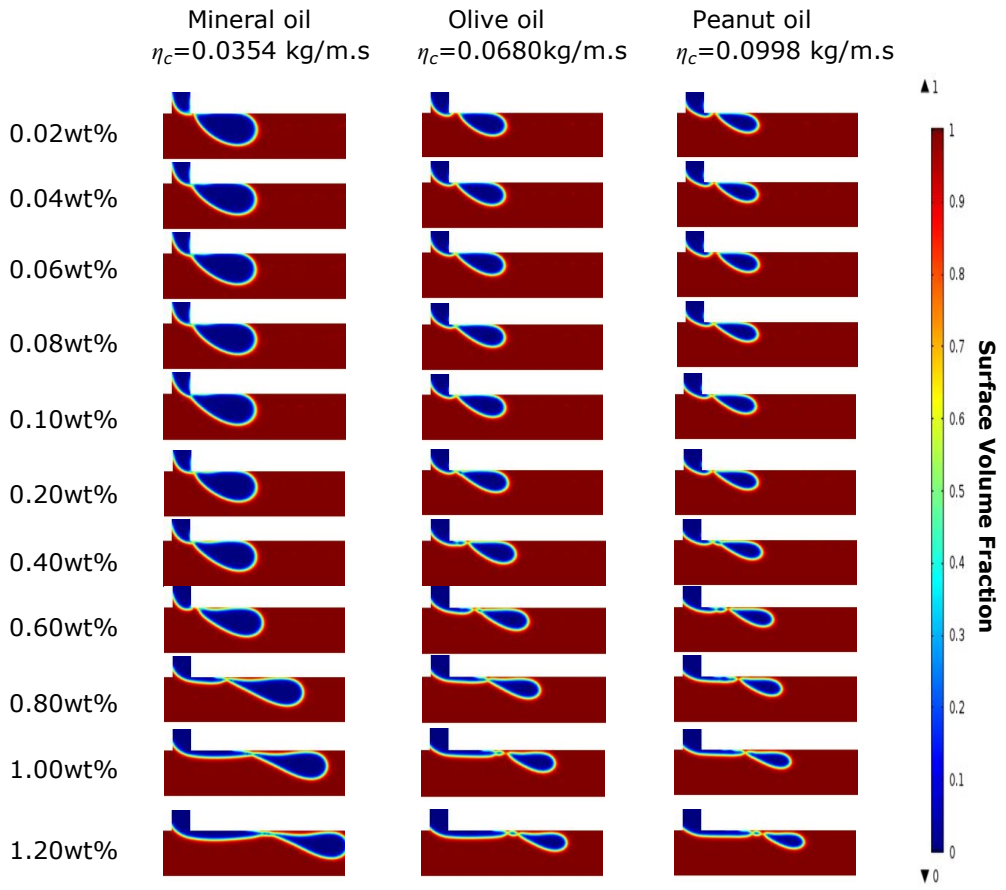


Figure 7.25: Snapshots of two-dimensional (2D) simulation of the effect of continuous phase viscosity on CMC-in-olive oil droplet breakup process for different CMC concentration (for system: Q_d/Q_c=0.05).

7.2.11 Effect of Continuous Phase Viscosity on Droplet Formation Time

The aim in present studies sought to determine the effect of η_c on the droplet breakup process over time. For a fixed η_c, results provide the similar findings which stated that the evolution of breakup time are discerned in two distinct concentration regimes as previously discussed in section 7.2.8.Figure 7.26 illustrates that the droplet formation time decreases as the CMC concentration increases in dilute regime. When the concentration is further increased above a critical overlap concentration, resistance force induced by dispersed phase become pronounce and dominate over the viscous shear-stress acting on forming interface and thus delay the breakup process. However, further work is required to establish this phenomenon focuses on the elastic and viscous component due to the complex rheological properties of shear-thinning CMC

liquid. At fixed CMC concentration, the results clearly show that the droplet formation time decreases as η_c increases (see Figure 7.27).This accord with our earlier observations in section 7.2.10, which showed that higher shear-stress, corresponding to an increasing η_c, leads to rapid breakup and detachment of droplet(Garstecki *et al*., 2006; Husny and Cooper-White, 2006; Yeom and Lee, 2011). The strengthen shear-stress force squeezes the neck of emerging dispersed tip thus shorten breakup process (reduce the formation time).

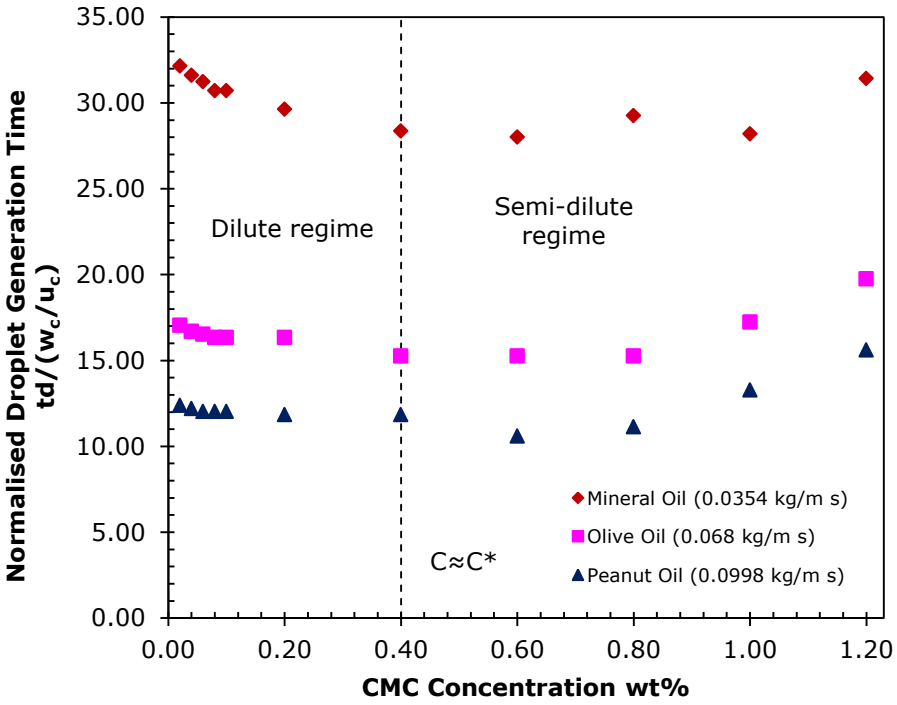


Figure 7.26: Effect of continuous phase viscosity on normalised droplet formation time of CMC droplets for various CMC concentrations (for system: Q_d/Q_c=0.05).

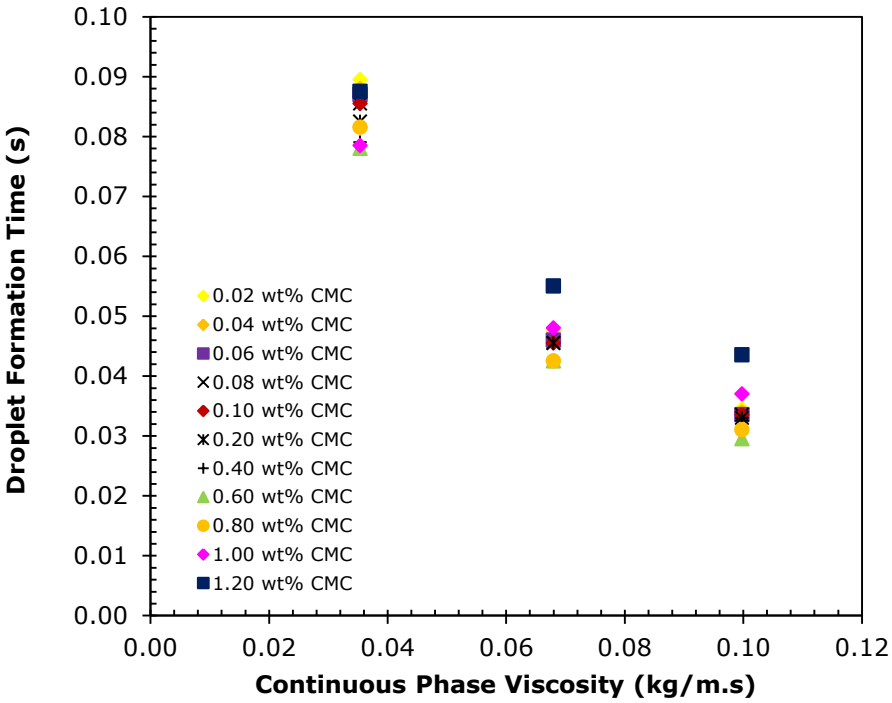


Figure 7.27: Effect of continuous phase viscosity on droplet formation time of CMC droplets (for system: Q_d/Q_c=0.05).

7.2.12 Effect of Continuous Phase Viscosity on Droplet Generation Frequency

In present numerical study, the droplet generation frequency (f_d) as a function of η_c has been systematically investigated and these results are shown in Figure 7.28 and 7.29. In this section, the numerical studies has been carried out considering different type of oils (mineral oil, olive oil, and peanut oil) as continuous phase with different CMC solutions as dispersed phase. As expected, the simulations show that two strong dissimilarities of the evolution of droplet generation frequency were found across the dilute and semi-dilute regime (see Figure 7.28). In dilute regime, C<C*~0.40wt%, the results predicted that the normalised generation frequency increases monotonically as the CMC concentration increases. When C>C*~0.40wt%, the normalised droplet generation frequency decreases with further increasing of CMC concentration, especially for the higher viscosity of continuous system containing olive oil or peanut oil (see Figure 7.28). This is believed due to the fact that high viscous

pressure in the dispersed thread becomes prevailing in the entire breakup process.

Figure 7.29 illustrates the influence of η_c on droplet generation frequency at each CMC concentrations. For a given CMC concentration, the frequency of formation increases as the continuous phase viscosity increases. At low frequency of droplet formation, where the interfacial tension is expected to dominate, droplets behave similarly regardless of dispersed phase concentration. While increasing the η_c, the high viscous shearing force induced by the continuous phase accelerates the breakup process and thus increase the rate of generation.

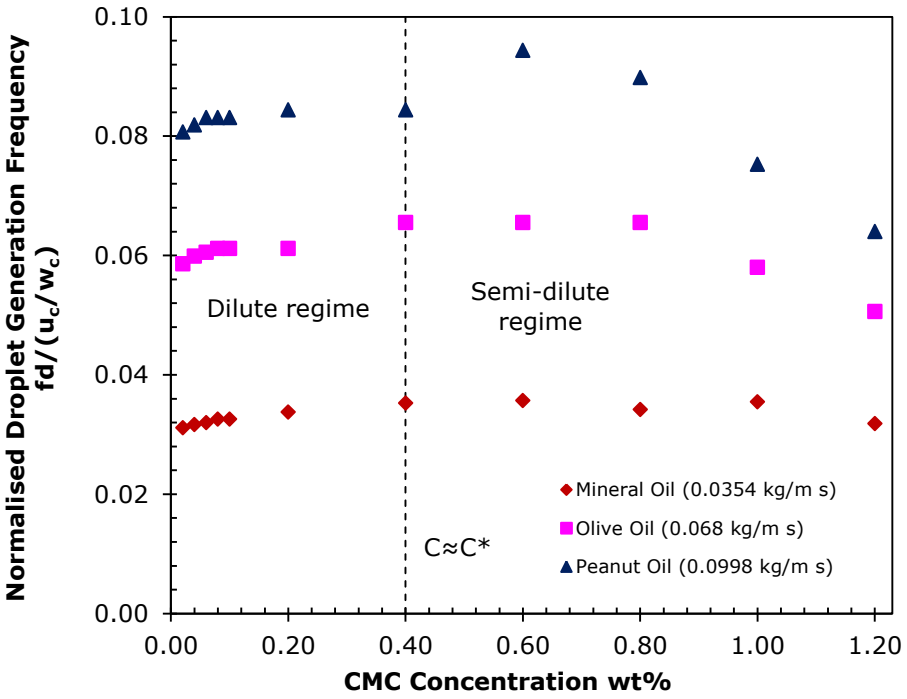


Figure 7.28: Effect of continuous phase viscosity on normalised droplet generation frequency of CMC droplets for various CMC concentrations (for system: Q_d/Q_c=0.05).

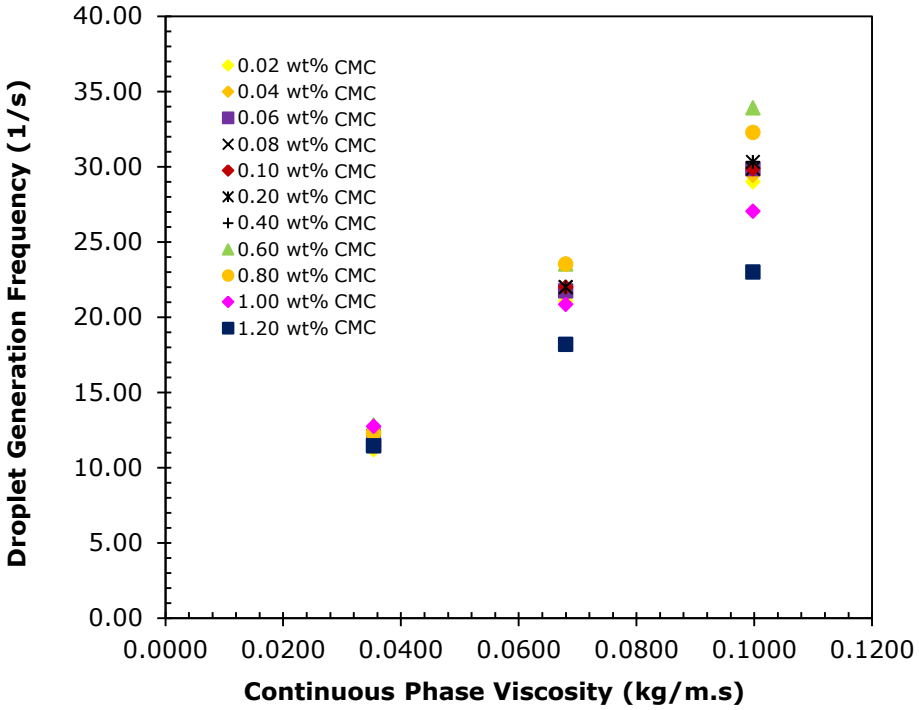


Figure 7.29: Effect of continuous phase viscosity on droplet generation frequency of CMC droplets (for system: Q_d/Q_c=0.05).

7.3 Summary

In this chapter, a conservative level-set approach coupled with Carreau-Yasuda stress model has been employed to study the shear-thinning CMC droplet breakup process at different conditions and variation of controlling parameters. Systematic set of numerical investigation is demonstrated to monitor the evolution of droplet diameter, formation time, generation frequency and pressure distribution as function of different operating parameters such as flow rate of continuous and dispersed phase, shear-thinning polymer concentration, and continuous phase viscosity. This number of key parameters controlling the sodium carboxymethlycellulose (CMC) shear-thinning microdroplets formation has not been established solidly. This findings reported in this chapter may become important implications for future applications. Moreover, this chapter eventually provide a way of computing the dynamics of droplets breakup process and meanwhile characterising the shear-thinning (pseudo plastic) properties in a micro-scaled devices when non-Newtonian effects are properly taken into account.

Preliminary investigation focuses on the effect of Q_d on the deformation and breakup process. This effect was observed numerically for CMC mixture with a concentration ranging from 0wt% to 1.20wt% which behaves as a shear-thinning fluid. With the increase in Q_d, larger droplets are being generated. The time taken for droplet formation and detachment is reduced as Q_d increases. Larger internal flow rates of dispersed phase results in a higher growth rate of dispersed thread and thus accelerates dramatically the breakup. These results match those observed in earlier studies (Davidson and Cooper-White, 2006; Garstecki *et al*., 2006; Tan *et al*., 2008; Bashir *et al*., 2011, Fu *et al*., 2012).

By varying the flow rates of continuous phase (Q_c), the effective droplet diameter was tuned in a controlled manner. When Q_d was held constant, the shear-thinning droplet diameter was found to decrease when increasing the Q_c. The increase of Q_c, relative to flow velocity, leads to a reduction in droplet breakup time due to higher viscous stresses acting on forming interface causing more rapidly pinch-off and thus increase the rate of droplet production. The present findings seem to be consistent with those empirical investigations (Cramer *et al*., 2004; Van der Graaf *et al*., 2006, Zhang *et al*., 2009, Gu and Liow, 2011).

Flow pattern obtained as a consequence of two-immiscible fluids interacting at T-junction have been analysed for influence of Q_d and Q_c, respectively. The position of necking and detachment point was found to be dependent on Q_d and Q_c through numerical observations. Dripping mechanisms for droplet formation were observed for lower Q_d at fixed Q_c when $Q_c > Q_d$ (or larger Q_c at fixed Q_d), where the shearing force dominates over the interfacial tension force. Jetting phenomenon was seen to occur for larger Q_d (or smaller Q_c) where dripping is not the dominant mechanism for droplet formation. In jetting phenomenon, a long neck of dispersed thread is being developed before droplets are sheared off

downstream in the main channel. However, this phenomenon becomes more drastic for the larger concentration of CMC dispersion.

Considering the dispersed phase concentration, numerical predictions revealed that the increasing CMC concentration (a corresponding increase in shear-thinning viscosity) resulting in decreasing the size of non-Newtonian droplet for a fixed η_c at each constant value of *Q*. Contrary to expectations, these findings are in disagreement with some published experimental data (Hunsy and Cooper-White, 2006; Steinhaus and Shen, 2007; Gu and Liow, 2011). The complexity of non-Newtonian flow behaviour may induce the dissimilar phenomenon in present study. Another possible explanation for this section is that smaller droplets are being generated due to high viscous effect temper the onset of Rayleigh-Plateau instability when the dispersed thread undergoes breakup. In contrast to Newtonian-Newtonian system, there was limited evidence for the study of rheological effects on droplet formation in microfluidic device. Therefore, future research studies of nonlinear rheological behaviour of non-Newtonian fluids are required to understand non-Newtonian complex behaviour in microscaled channel. The evolution of droplet formation time and frequency of formation are having dissimilar phenomenon in two distinct concentration regime (dilute and semi-dilute regime) due to the chain-chain interaction that will induce growth retardation when the increasing of dispersed phase concentration.

A series of oils of different viscosity classes with Newtonian properties were employed as continuous phase in this non-Newtonian/Newtonian multiphase system. Increasing η_c was found to produce smaller shear-thinning droplets for each CMC concentration at constant flow rate ratio. Continuous phase with larger viscosity is accompanied by shorter breakup time and a corresponding increase in generation frequency. In accordance with the present results, previous studies have demonstrated that shear-stress force exerted on the interface by

continuous phase becomes increasingly dominant on breakup process when the increasing of η_c (Garstecki *et al*., 2006; Husny and Cooper-White, 2006; Yeom and Lee, 2011, Gu and Liow, 2011). Additionally, this effect becomes drastically pronounced if larger Q_c is employed. However, there are some discrepancy between the present findings and the numerical observation reported by Gupta and Kumar (2010).

CHAPTER 8

Conclusion and Recommendation

8.1 Conclusion and Summary of Key Findings

The development of microfluidic systems which allow for the formation of microdroplets is crucial for applications in many fields, especially medical and biological research such as point-of-care diagnostics testing, purification of biological sample, or in vivo monitoring for disease and conditions. Nevertheless, many fluids of interest to lab-on-chip devices in this area exhibit complex micro-structure and non-Newtonian behaviour. Previous studies have considered mostly Newtonian fluids and their importance in the field of microfluidics. However, the theoretical understanding of controlled formation of aqueous phase droplets with viscous non-Newtonian fluids in a T-junction microscaled channel is still limited. A numerical simulation of sodium carboxymethlycellulose (CMC) microdroplets formation with shear-thinning properties in a microfluidics T-junction has been carried out. Current computational studies have been established as a conceptual framework for future empirical studies.

Numerical Modelling Setup

Numerical prediction was an essential tool to track precisely the fluid-fluid interface between two immiscible fluids in the present work. In the preliminary research stage, the simulation setup, consisting of a T-junction in two-dimensions (2D) was constructed based on the prescribed geometry size. Here sodium carboxymethlycellulose (CMC) was selected as the dispersed phase, while olive oil (Newtonian fluid) was selected as the continuous phase. For the system that neglects the Marangoni effect, the process of droplet formation in

across-flowing immiscible liquid was reasonably predicted. A two-phase conservative Level-Set approach (LS) effectively captured the dynamics of the droplet breakup process. The proposed numerical model incorporated a Carreau-Yasuda stress model together with front-tracking scheme in computational fluid dynamics (CFD). In the present work, the fluid of interest, CMC solution with concentrations ranging from 0wt% to 1.20wt%, was modelled as a purely viscous non-Newtonian fluid obeying the Carreau-Yasuda stress model in order to examine the effect of shear-thinning behaviour on the breakup process. This numerical simulation model consists of the LS equation which was coupled to the incompressible Navier-Stokes equation and the continuity equation. These governing partial differential equations (PDE) have been formulated in the strong and weak formulation.

Experimental Model Setup

Data for rheological and physical property measurements were obtained to support the computation work. Prior to validation of the proposed numerical model, an experimental model was designed. A PDMS-based microfluidic device with a channel dimension of 221 μm x 90 μm x 76 μm was fabricated in-house via photolithography and soft-lithography. This was used for empirical studies of microdroplet formation. Each working solution of desired concentration was prepared accordingly. The rheological and physical properties of each continuous phase and dispersed phase solution were empirically characterized and determined respectively. In particular, the surface/interfacial tension and contact angle measurements were effectively determined using our in-house pendant and sessile drop apparatus. The images of pendant and sessile drop were collected and successfully analysed with application of MATLAB as a method of image processing analysis. Density and viscosity measurements were carried out using a densitometer and an Ostwald viscometer. All these obtained data were

validated with those published in the literature data prior to the startup of laboratory experiments.

Numerical Model Validation and Numerical Predictability

Experimental Implementation: The dispersed and continuous flow rates were applied separately using an infusion pump to the developed system. The system was allowed to reach steady-state for at least 20 minutes. Images and video of the microdroplet formation were recorded and used for image processing analysis. A MATLAB code was developed for droplet diameter measurement. From the imported images, the droplet was successfully traced and the size was computed with an adequate accuracy.

Grid Refinement Analysis: In the present developed numerical model, a grid convergence study was carried out to achieve a highly reliable predictive model and optimal grid resolution by refining the grid size of 2D mapped mesh.

Model Validation: A comparison between numerical and experimental results was presented at different flow rate ratios (Q). The experimental model was initially applied to a Newtonian/Newtonian system. The discrepancy between numerical and experimental results of droplet size was decreased when a lower Q is applied due to the reduced effect of numerical dissipation in advection step of the fluid simulation. This finding is in agreement with Bashir *et al*. (2011). The present computation work was studied based on a low flow rate ratio of 0.05.

Effect of Controlling Parameters on Droplet Breakup Process

A series of systematic parametric studies were established:(a) to investigate and understand the dynamics of droplet formation and propagation, and (b) monitor the evolution of non-Newtonian shear-thinning droplet diameter, formation time,

generation frequency, velocity and pressure distribution as function of following different operating parameters:

Varying η_o/η_∞: The ratio η_o/η_∞ determines the total amount of shear-thinning that is possible in the Carreau-Yasuda model. The potential of η_o/η_∞ in controlling the droplet diameter and flow behaviour has never been systematically determined. η_o and η_∞ are important parameters in Carreau-Yasuda rheological model. Each η_o of CMC concentration was held constant accordingly and η_∞ was varied. Changes in η_∞ represent changes in η_o/η_∞. Droplet diameters were found to be dependent on η_o/η_∞ for the Carreau-Yasuda fluid used at fixed Q of 0.05. Increasing η_o/η_∞ gives rise to larger droplet diameter and this phenomenon has become more pronounced for higher CMC concentration. As η_o/η_∞ is further increased, a plateau region was observed in the evolution of droplet diameter. The range of typical shear rate associated with this microfluidics geometry was the dominant factor in controlling the dynamic breakup process and this limits the effect of η_o/η_∞ as if η_∞ is further increased, the additional shear-thinning occurs outside the range of typical shear rates.

Varying λ_{CY}: Apart from η_o and η_∞, λ_{CY} is another important parameter as it controls the onset shear rate for shear-thinning. Variation in λ_{CY} exhibits a major effect on CMC droplet diameter. Predictions revealed that diameter of CMC droplets increases as the λ_{CY} increases (critical shear rate, $1/\lambda_{CY}$ decreases) at a fixed Q of 0.05. When λ_{CY} is further increased, the evolution of the droplet diameter reaches a constant value. The shear-thinning nature of the dispersed phase becomes prominent as λ_{CY} increases. The velocity profile in the core region of the dispersed phase flow is shown as evidence of effect of the shear-thinning behaviour.

Varying η_c and η_o (at fixed λ of 1): The λ is defined as the quotient of η_o with the η_c. Considering a fixed λ of 1, the η_c is adjusted to match the value of η_o for a given CMC concentration in polymer solution. This aims to examine the effects of CMC concentration on the formation and detachment of shear-thinning CMC droplets with concentrations ranging from 0.04wt% to 0.40wt%, while eliminating the rapid change of η_c with respect to η_o when the concentration changes. The resultant droplet diameter decreases as the equivalent viscosity of both phases increases. For a fixed λ of 1, by considering η_c, an increase in η_c leads to reduction in droplet breakup time and thus increases in generation frequency, which is in agreement with previous literature data. This is mainly due to the fact that higher shearing force acts on the forming interface, resulting in higher pressure along the neck of emerging tip. When η_c is larger, viscous-stress effects dominate over interfacial ones. By taking account of CMC concentration, the greater the shear viscosity the larger intermolecular friction between dispersed particles, which results in more resistance to flow and thus affects the flow pattern and mechanism. Two different breakup regimes (dripping and jetting phenomenon) have been observed due to the viscosity effects of the two phases. Larger droplets are formed in the dripping mode while smaller droplets are created in jetting mode.

Varying θ: Prior studies investigated the role of the contact angle (θ) shows major effects on the dynamics of Newtonian microdroplets formation. The influence of θ on the formation CMC shear-thinning droplets in microfluidic device has not been available in preceding analysis. The θ of the CMC droplet at the channel walls was varied from 130^o (partial wetting) to 180^o (complete wetting). Larger θ tends to minimize the adhesion force between the dispersed fluids with the channels wall, causing larger shear force to result in rapid droplet breakup and thus generate smaller droplets. This finding is consistent with previous publications. By taking account of CMC concentration, a turning point in

the dependence of the droplet formation time and frequency of droplet generation on the CMC concentration was found in between the dilute and semi-dilute regime. This turning point displays a non-monotonic profile which is mainly caused by the considerable viscosity effect of CMC polymer solution when its concentration increases above a critical value.

Varying σ: Surface tension is a resisting force that stabilized the forming droplet. Six groups of cases with increasing values of σ from 0.010 N/m to 0.035 N/m were numerically analysed. As σ increases, the intermolecular forces become greater and tend to resist the droplet breakup, resulting in larger droplets size. CMC droplet diameters can be markedly influenced by the σ. By considering the viscous stress (induced by the dispersed phase) combined with the interfacial tension, the influence of the CMC concentration on droplet breakup time and generation frequency at fixed σ was examined. Predictions revealed that the CMC concentration plays a key role in controlling the dynamic breakup process when a larger dispersed phase shear viscosity was encountered.

Varying Q_d: This work focused on the analysis of the effect of Q_d on the evolving droplet size. For a fixed Q_c (2.0 ml/hr), the droplet diameter was examined with variation of Q_d (0.05 ml/hr to 0.25 ml/hr). In the case of $Q_c > Q_d$, as Q_d increases, a larger internal flow rate leads to a larger volume of thread entering the main channel, resulting in a higher growth rate of thread and thus accelerating the breakup process (or shorter breakup time), which is consistent with previous observations. Distilled water was used as the Newtonian reference dispersed fluid for comparison.

Varying Q_c: The results revealed that droplet diameter is highly dependent on Q_c. Increasing Q_c (1.50 ml/hr to 4.00 ml/hr) was found to produce smaller droplet size at fixed Q_d (0.20 ml/hr).As the continuous phase flow speed increases, the

rate of size reduction decreases due to the larger shearing effect on the forming interface. When compared to the Newtonian dispersion, the extent of shear-thinning in the dispersion becomes prominent for higher CMC concentration, leading to a reduction in droplet diameter. Thus, a shorter breakup time and higher generation frequency was observed.

Varying CMC concentrations: The time and frequency of droplet formation show a non-monotonic behaviour as the CMC concentration was varied. CMC polymer solution demonstrates two modes of concentration regime, namely the dilute state (C<C*) and the semi-dilute state (C>C*).When C<C*,the droplet breakup time decreases with increasing CMC concentration. Conversely, when C>C*, the breakup time increases with increasing CMC concentration. For higher CMC concentrations, the intermolecular hydrodynamic interaction between polymer coils becomes larger. Thus, when C>C*, the viscosity of CMC polymer solution rapidly increases and starts playing a role in retarding the breakup process. Besides, the flow pattern transits from dripping mode to jetting mode when the concentration is increased. As the CMC concentration increases, the CMC droplet diameter decreases monotonically. However, this theoretical prediction is different from the previous experimental observations that focused on dispersed fluid with viscoelastic properties. Prior studies has reported that the more elastic the polymer solution, the larger the droplets generated. However, the elasticity is not included in the present constitutive model. Future work is necessary to understand the fluid elasticity of a shear-thinning fluid.

Varying η_c: Prior studies revealed that η_c is an important factor in controlling the dispersion stability. This study was set up to access the role of the η_c on CMC droplets in the context of droplet size. Three types of continuous phase with different viscosities classes (0.00354 kg/m.s, 0.068 kg/m.s, and 0.0988 kg/m.s) were employed. At larger η_c, the size of droplets generated is smaller. At low η_c,

the interfacial tension dominates over viscous shear-stress regardless of dispersed phase concentration. Larger η_c induced a higher viscous shearing force on the penetrating dispersed phase thread and thus reduces the breakup time of droplet generation.

8.2 Recommendation and Future Works

The following is a list of key recommendations for future work to be carried out subsequent to the studies described in the previous sections of this dissertation:

- Emulsification of non-Newtonian/Newtonian systems whose behaviour and performance in different geometries/configurations have not been widely investigated. In the simulation aspect, further numerical studies may be necessary to focus on different microsystems for droplet generation such as co-flowing stream, flow-focusing stream (elongational strained flow), or, microchannel emulsification. These are common microfluidics configurations in prior studies for Newtonian microdroplets formation based on different physical mechanisms. This study will advance our understanding of the complex behaviour of non-Newtonian fluids under different conditions in different types of micro-scaled devices.
- Performing a parametric study investigating the effect of geometric dimensions on droplet formation performance in a T-junctions microfluidics. This will provide a platform to understand the degree of confinement on the deformation and detachment of non-Newtonian droplets.
- Proper choice of a constitutive equation is essential to describe the rheological behaviour. In the present simulation work, CMC solutions exhibit shear-thinning characteristic at the prescribed concentrations and thus the Carreau-Yasuda rheological model is adopted for the shear-thinning CMC fluid. Nevertheless, the elasticity of fluids was not determined experimentally. As the CMC concentrations increases, the level of fluid elasticity in polymer solution may be higher. Hence, a White-Metzner model, in which incorporates

elasticity as well as both viscosity and relaxation time with shear-thinning function, is suggested for numerical studies in future works.

- An investigation into various operating parameters to further understand the effect of dimensionless numbers such as the Deborah number (De) and the Weissenberg number (Wi) on the non-Newtonian CMC shear-thinning droplet formation process. These can be linked to the above described computational work.
- Extensive analysis is necessary to rheologically characterise the CMC polymer solutions to obtain material properties such as polymer relaxation time and elasticity to allow more detailed constitutive models to be used for modelling of droplet formation for these non-Newtonian materials.
- Numerical investigations into the rich variety of behaviour in non-Newtonian fluids such as shear-thickening, viscoplastic, time-dependent, and viscoelastic fluids can be carried out and compared with the behaviour of purely shear-thinning fluids on governing the dynamics of the droplet breakup process.
- Present parametric analyses were implemented based on two-dimensional (2D) CFD simulations to reduce the computational complexity of the problem. However, 2D numerical simulations may not fully capture underlying physics quantitatively and may deceptively mislead. Further work is needed, identifying the viability of moving to three-dimensional (3D) modelling, which considers the velocity field in all three coordinates' directions. This would enable a detailed comparison to be made between 2D and 3D numerical analysis.
- Prior studies have identified scaling law for the size of droplet for Newtonian fluids and have led to some elegant models for quantitatively predicting the droplet length and volume of droplets based on different breakup mechanism or formation mode. Future work is suggested to develop a specific model to predict the droplet length of non-Newtonian shear-thinning fluids.

- Flow rate ratios are limited to a certain range due to the difficulties of numerical dissipation in the advection step of the fluid simulation. Improved numerical methods are required to control the numerical dissipation and stabilize the solution.
- Experiments performing a series of similar parametric studies such as flow rates and viscosities of both phases, as well as the surface tension on the shear-thinning droplets formation process, to compare with the developed numerical model.

References

Abate, A.R., Kutsovsky, M., Seiffert, S., Windbergs, M., Pinto, L.F.V, Rotem, A., Utada, A.S., and Weitz, D.A. (2011). Synthesis of monodisperse microparticles from non-Newtonian polymer solutions with microfluidic devices. *Advanced Material*, 23, 1-4.

Abate, A.R., Lee, D.Y., Do, T., Holtze, C., and Weitz, D.A. (2008). Glass coating for PDMS microfluidic channels by sol-gel methods*. Lab on Chip*, 2008, 516-518.

Abate, A.R., and Weitz, D.A. (2011). Faster multiple emulsification with drop splitting. *Lab on Chip*, 11, 1911-1915.

Adamson, A. W., and Gast, A. P. (1997). *Physical Chemistry of Surfaces,* Wiley: New York. Sixth edition, 4-35.

Ãlvarez, M.C., Ayuso, D.F.P., and Granda, M.G. (2008). Critical points in the fabrication of microfluidic devices on glass substrates. *Sensors and Actuators B*, 130, 436-448.

Ambravaneswaran, B., Subramani, H.J., Phillips, S.D. and Basaran, O.A. (2004). Dripping-Jetting Transitions in a Dripping Faucet. *Physical Review Letter*, 93, 034501.

Anna, S.L., Bontoux, N., and Stone, H.A. (2003). Formation of dispersions using ''flow-focusing'' in microchannels. *Applied Physics Letter*, 82,363–364.

Anna, S.L., and Mayer, H.C. (2006). Microscale tip streaming in a microfluidic flow focusing device. *Physics of fluids*, 18, 121512.

Anwar, K., Han, T., and Kim, S.M. (2010). Reversible sealing techniques for microdevice application. *Sensors and Actuators B: Chemical*, 153, 301-311.

Arashiro, E.Y., and Demarquette, N.R. (1999). Use of the pendant drop method to measure interfacial tension between molten polymers. *Materials Research*, 2, 23-32.

Arratia, P.E., Cramer, L.A., Gollub, J.P., and Durian, D.J. (2009). The effects of polymer molecular weight on filament thinning and drop breakup in microchannels. *New Journal of Physics*, 11, 115006, 1-18.

Aryanti, N., Williams, R.A.,, Hou, R.Z., and Vladisavljevic´, G.T. (2006). Performance of rotating membrane emulsification for o/w production. *Desalination*, 200, 572-574.

ASTM International (2012, August 15). *Standard specifications and operating instructions for glass capillary kinematic viscometers*. Retrieved from http://www.che.utah.edu/department_equipment/Projects_Lab/A_Viscometers/SOP2_Glass_Capillary.pdf.

Aubin, J., Ferrando, M., and Jiricny, V. (2010). Current methods for characterising mixing and flow in microchannels. *Chemical Engineering Science*, 65, 2065-2093.

Baroud, C.N., Gallaire, F., and Dangl, R. (2010). Dynamics of microfluidic droplets .*Lab Chip*, 2010, 10, 2032-2045.

Bashforth, F., & Adams, J. C. (1883). *An attempt to test the theories of capillary action: by comparing the theoretical and measured forms of drops of fluid*. University Press.

Bashir, S., Rees, J.M., and Zimmerman, W.B. (2011). Simulations of microfluidics droplet formation using the two-phase level set method. *Chemical Engineering Science*, 66, 4733-4741.

Beebe, D.J., Mensing, G.A., and Walker, G.M. (2002). Physics and application of microfluidics in biology. *Annual Review of Biomedical Engineering*, 4, 261-286.

Benchabane, A., and Bekkour, K. (2008). Rheological properties of carboymethyl cellulose (CMC) solutions. *Colloid and Polymer Science*, 286, 1171-1180.

Berthier, J., and Silberzan, P. (2009). *Microfluidics for biotechnology*. Norwood: Artech House.

Bonometti, T., and Magnaudet, J. (2007). An interface-capturing method for incompressible two-phase flows. Validation and application to bubble dynamics. *International Journal of Multiphase Flow*, 33, 109-133.

Bubendorfer, A., Liu, X., and Ellis, A.V. (2007). Microfabrication of PDMS microchannels using SU-8/PMMA mouldings and their sealing to polystyrene substrates. *Smart Materials and Structures*, 16, 367-371.

Chen, S., and Doolen, G.D. (1998). Lattice Boltzmann method for fluid flows. Annual Review of Fluid Mechanics, 30, 329-364.

Chhabra, R.P., and Richardson J.F. (2008). *Non-Newtonian flow and applied rheology*, *2nd ed*. Oxford: Butterworth-Heinemann.

Cho, Y.I., and Hartnett, J.P. (1985).*Non-Newtonian Fluids, Handbook of Heat Transfer Applications, 2nd ed. Fluids.* New York: McGraw-Hill.

Chung, C.K., Hulsen, M.A., Kim, J.M, Ahn, K.H., and Lee, S.J. (2008). Numerical study on the effect of viscoelasticity on drop deformation in simple shear and 5:1:5 planar contraction/expansion microchannel. *Journal of Non-Newtonian Fluid Mechanics*, 155, 80-93.

Christopher, G.F., Bergstein, J., End, N.B., Poon, M., Nguyen, C., and Anna, S.L. (2009). Coalescence and splitting of confined droplets at microfluidic junctions. *Lab on a Chip*, 9, 1102-110.

Christopher, G.F., Noharuddin, N.N., Taylor, J.A., and Anna, S.L. (2008). Experimental observations of the squeezing-to-dripping transition in T-shaped microfluidic junctions. *Physical Review*, 78, 036317,1-12.

COMSOL Multiphysics 4.2a (2011). *Chapter 7: Finite Element Method*. COMSOL Multiphysics, Reference Guide.

Cooper-White, J.J., Fagan, J.E., Tirtaatmadja, V., Lester, D.R., and Boger, D.V. (2002). Drop formation dynamics of constant low-viscosity, elastic fluids. *Journal of Non-Newtonian Fluid*, 106, 29-59.

Cramer, C., Fischer, P., and Windhab, E.J. (2004). Drop formation in a co-flowing ambient fluid. *Chemical Engineering Science*, 59, 3045 -3058.

Cubaud, T., and Mason, T.G. (2008). Capillary threads and viscous droplets in square microchannels*. Physics of Fluids*, 20, 1-10.

Davidson, M.R., and Cooper-White, J.J. (2006). Pendant drop formation of shear-thinning and yield stress fluids. *Applied Mathematics Modelling*, 30, 1392–1405.

Davidson, M.R., Cooper-White, J.J., and Tirtaatmadja, V. (2004). Shear-thinning drop formation. *ANZIAM Journal*, 450, 405-418.

DeMenech, M., Garstecki, P., Jousse, F., and Stone, H.A. (2008). Transition from squeezing to dripping in a microfluidic T-shaped junction. *Journal of Fluid Mechanics*, 595,141-161.

Deshpande, K.B., and Zimmerman, W.B. (2006). Simulation of interfacial mass transfer by droplet dynamics using the level set method. *Chemical Engineering Sciences*, 61, 6486-6498.

Drelich, J., Fang, Ch., and White, C.L. (2002). Measurement of interfacial tension in fluid-fluid systems. *Encyclopedia of Surface and Colloid Science*, 3152-3166.

Fischer, P., and Erni, P. (2007). Emulsion drops in external flow fields – The role of liquid interfaces. *Current Opinion in Colloid & Interface Science*, 12, 196–205.

Fu, T.T., Ma, Y.G., Funfschilling, D., Zhu, C.Y., and Li, H.Z. (2010). Squeezing-to-dripping transition for bubble formation in a microfluidics T-junction. *Chemical Engineering Science*, 65, 3739-3748.

Fu, T.T, Wu, Y.N, Ma, Y.G., and Li, H.Z. (2012). Droplet formation and breakup dynamics in microfluidic flow focusing devices: From Dripping to Jetting. *Chemical Engineering Science*, 84, 207-217.

Garstecki, P., Stone, H.A. and Whitesides, G.M. (2005). Mechanism for Flow-Rate Controlled Breakup in Confined Geometries: A Route to Monodisperse Emulsions. *Physical Review Letters*, 94, 164501-1-164501-4.

Garstecki, P., Fuerstman, M.J., Stone, H.A. and Whitesides, G.M. (2006) .Formation of droplets and bubbles in a microfluidic T-junction-scaling and mechanism of breakup. *Lab Chip*, 6, 437-446.

Ghannam, M.T., Esmail, M.N. (1997). Rheological properties of carboxyl methyl cellulose. *Journal of Applied Polymer Science*, 64, 289-301.

Glatzel, T., Litterst, C., Cupelli, C., Lindemann, T., Moosmann, C., Niekrawietz, R., Streule, W., Zengerle, R., and Koltay, P. (2008). Computational fluid dynamics (CFD) software tools for microfluidic applications - A case study. *Computers & Fluids*, 37, 218-235.

Glawdel, T., Elbuken, C., and Ren, C.L. (2012). Droplet formation in microfluidic T-junction generators operating in the transitional regime. II. Modelling. *Physical Review*, 85, 016323-1-016323-12.

Grace, H.P. (1982). Dispersion phenomena in high-viscosity immiscible fluid systems and application of static mixers as dispersion devices in such systems. *Chemical Engineering Communication*, 14, 225–277.

Gu, H., Duits, M.H.G, and Mugele, F. (2011). Droplets Formation and Merging in Two-Phase Flow Microfluidics. *International Journal of Molecular Sciences*, 12, 2572-2597.

Gu, Z.P., and Liow, J.L. (2011). Microdroplet formation in a T-junction with xanthan gum solutions. *Chemeca:Australasian Conference on Chemical Engineering.*

Gupta, R., Fletcher, D.F., and Haynes, B.S. (2009). On the CFD modelling of Taylor flow in microchannels. *Chemical Engineering Science*, 64, 2941-2950.

Gupta, A., Murshed, S.M.S., and Kumar, R. (2009).Droplet formation and stability of flows in a microfluidic T-junction. *Applied Physics Letters*, 94, 164107 (1-3).

Gupta, A., and Kumar, R. (2010). Flow regime transition at high capillary numbers in a microfluidic T-junction: Viscosity contrast and geometry effect. *Physics of Fluids*, 22, 122001, 1-11.

Hessel, V., Renken, A., Schouten, J.C., and Yoshida, J. (2009). *Micro Process Engineering: A Comprehensive Handbook, Volume 1: Fundamental, Operations and Catalysts*. Weinheim: Wiley-VCH.

Hirt, C.W., and Nichols, B.D. (1981). Volume of fluid (VOF) method for the dynamics of free boundaries. *Journal of computational physics,* 39(1), 201-225.

Hirt, C.W., Nichols, B.D., & Romero, N.C. (1975). SOLA: A numerical solution algorithm for transient fluid flows. *NASA STI/Recon Technical Report N*, *75*, 32418.

Hong, J.S., and Cooper-White, J. (2009). Drop formation of Carbopol dispersions displaying yield stress, shear thinning and elastic properties in a flow-focusing microfluidic channel. *Korea-Australia Rheology Journal*, 21, 269-280.

Hong, Y.P, and Wang, F.J. (2007). Flow rate effect on droplet control in co-flowing microfluidic device . Microfluidics and Nanofluidics, 3, 341-346.

Hou, T.Y.; Lowengrub, J.S.; and Shelley, M.J. (2001). Boundary integral methods for multicomponent fluids and multiphase materials. *Journal of Computational Physics*, 169, 302-362.

Hung, L.H., and Lee, A.P. (2007). Microfluidic Devices for the Synthesis of Nanoparticlesand Biomaterials. *Journal of Medical and Biological Engineering*, 27, 1-6.

Husny, J., Jin, H.Y., Harvey, E., and Cooper-White, J.J. (2003). Dynamics of Shear-Induced Drop Formation in T-Shaped Microchannels. *Seventh International Conference on Miniaturized Chemical and Biochemical Analysts Systems*, 1 113-116.

Husny, J., and Cooper-White, J.J. (2006). The effect of elasticity on drop creation in T-shaped microchannels. *Journal of Non-Newtonian Fluid Mechanics*, 137, 121-136.

Janssen, J.M.H., and Meijer, H.E.H. (1993). Droplet breakup mechanisms: Stepwise equilibrium versus transient dispersion. *Journal of Rheology*, 37, 597-608.

Kim, S.H., Jeon, S.J., Jeong, W.C., Park, H.S., and Yang, S.M. (2008). Optofuildic synthesis of electroresponsive photonic Janus balls with isotropic structural colours. *Advanced Materials*, 20, 4129-4134.

Kim, S.H., Sim, J.Y., Lim, J.M., and Yang, S.M. (2010). Magnetoresponsive microparticles with nanoscopic surface structures for remote controlled locomotion. *Angewandte Chemie International Edition*, 49, 3786-3790.

Kobayashi, I., Mukataka, S., and Nakajima, M. (2005). High Performance Flow Focusing Geometry For Spontaneous Generation Of Monodispersed Droplets. *Industrial and Engineering Chemistry Research*, 44, 5852-5856.

Kobayashi, I., Nakajima, M., and Mukataka, S. (2003). Preparation characteristics of oil-in-water emulsions using differently charged surfactants in straight-through microchannel emulsification. *Colloids and Surfaces A: Physicochemical and Engineering Aspects*, 229, 33-41.

Kobayashi, I., Nakajima, M., Chun, K., Kikuchi, Y., and Fukita, H. (2002). Silicon Array of Elongated Through-Holes for Monodisperse Emulsion Droplets. *AIChE Journal*, 48, 1639-1644.

Kostic, M. (1993). Influence of viscosity function simplification on non-Newtonian velocity and shear rate profiles in rectangular ducts. *International Communications in Heat and Mass Transfer*, 20, 515-525.

Kumar, V., Paraschivoiu, M., and Nigam, K.D.P. (2010). Single-phase fluid flow and mixing in microchannels. *Chemical Engineering Science*, 66, 1329-1373.

Kumacheva, E., and Garstecki, P. (2011). *Microfluidic Reactors for Polymer Particles,* Wiley: New York.

Lee, S.J. (2004). Flow behaviour of high internal phase emulsions and preparation to microcellular foam. *Korea-Australia Rheology Journal*, 16, 153-160.

Lee, S.J.J., and Saudrarajan, N. (2010). *Microfabrication for microfluidics*. Norwood: Artech House.

Lee, T., and Lin, C.L. (2005). A stable discretization of the lattice Boltzmann equation for simulation of incompressible two-phase flows at high density ratio. *Journal of Computational Physics*, 206, 16-47.

Leshansky, A.M., and Pismen, L.M. (2009). Breakup of drops in a microfluidic T-junction. *Physics of Fluids*, 21, 023303 (1-6).

Li, J., and Renardy, Y. (2000). Numerical study of flows of two immiscible liquids at low Reynolds number. *SIAM Review*, 42, 417-439.

Li, Z., Li-ya, H., and Wei-yi, Z. (2010). A new fabrication method for glass microfluidic devices used in micro chemical system. *Sensors and Actuators B*, 148, 135-146.

Liu, J. and Nguyen, N.T. (2010). Numerical simulation of Droplet-Based Microfluidics-A Review .*Micro and Nanosystems*, 2, 193-201.

Liu, H., and Zhang, Y. (2011). Lattice Boltzmann simulation of droplet generation in a microfluidic cross-junction. *Communications in computational physics*, 9, 5, 1235-1256.

Liu, H., and Zhang, Y. (2009). Droplet formation in T-shaped microfluidic junction. *Journal of Applied Physics*, 106, 034906, 1-8.

Loizou, K., Thieleman, W., and Hewakandamby, B.N. (2013). *Effect of Geometry on Droplet Generation in a Microfluidic T-Junction*. ASME 2013 Fluids Engineering Division Summer Meeting.

Loizou, K.,Wong, V.L**.**, Thielemans, W., and Hewakandamby, B.N. (2014). *Effect of Fluid Properties on Droplet Generation in a Microfluidic T-junction*. Proceedings of the ASME 4th Joint US-European Fluids Engineering Division Summer Meeting, Chicago, Illinois, August 3-8, 9pp.

Manz, A., Graber, N., and Widmer, H.M. (1990). Miniaturized total chemical analysis systems: a novel concept for chemical sensing. *Sensors and Actuators B*, 1, 244-248.

McDonald, J.C., and Whitesides, G.M. (2002).Poly(dimethylsiloxane) as a material for fabricating microfluidic devices. *Accounts of chemical research*, 35, 491-499.

McDonald, J.C., Duffy, D.C., Anderson, J.R., Chiu, D.T., Wu, H., Schueller, O.J.A., and Whitesides, G.M. (2000). Fabrication of microfluidic system in poly(dimethylsiloxane). *Electrophoresis*, 21, 27-40.

Misak, M.D (1968). Equations for determining 1/H versus S values in computer calculations of interfacial tension by pendent drop method. *Journal of Colloid and Interface Science*, 27, 141-142.

Moon, S.K., Cheong, I.W., and Choi, S.W. (2014). Effect of flow rates of the continuous phase on droplet size in dripping and jetting regimes in a simple fluidic device for coaxial flow. *Colloids and Surfaces A: Physicochemical and Engineering Aspects*, 454, 84-88.

Moreno, J.M., and Quero, J.M. (2010). A novel single-use SU-8 microvalve for pressure-driven microfluidic applications. *Journal of Micromechanics and Microengineering*, 20, 1-11.

Mott, D.R., Howell, P.B., Jr., Golden, J.P., Kaplan, C.R., Ligler, F.S. and Oran, E.S. (2006). Toolbox for the design of optimized microfluidic components. *Lab Chip*, 6, 540-549.

Mulligan, M.K. and Rothstein, J.P. (2012). Scale-up and control of droplet production in coupled microfluidic flow-focusing geometries. *Microfluidics and Nanofluidics*, 13, 65-73.

Murshed, S.M.S., Tan, S.H., and Nguyen, N.T. (2008). Temperature dependence of interfacial properties and viscosity of nanofluids for droplet-based microfluidics. *Journal of Physics D: Applied Physics*, 41(8).

Ng, K.C., Yusoff, M.Z., Yusaf, T.F., and Hussein, I. (2005). Development status of indigenous computational fluid dynamics software for arbitrary complex geometry. *The Institution of Engineers, Malaysia*, 66, 15-22.

Nguyen, N.T. and Wereley, S.T. (2002). *Fundamentals and applications of microfluidics*. Boston, Mass.: Artech House.

Nisisako, T., Torii, T., and Higuchi, T. (2002). Droplet formation in a microchannel network. *Lab on Chip*, 2(1), 24-26.

Nisisako, T., Torii, T., and Higuchi, T. (2004). Novel microreactors for functional polymer beads. *Chemical Engineering Science*, 101, 23–29.

Nunes, J.K., Tsai, S.S.H., Wan, J., and Stone, H.A. (2013). Dripping and jetting in microfluidic multiphase flows applied to particle and fibre synthesis. *Journal of Physics D: Applied Physics*, 46, 114002 (20pp).

Olsson, E., and Kreiss, G. (2005). A conservative level set method for two phase flow. *Journal of Computational Physics*, 210, 225-246.

Olsson, E., Kreiss, G., Zahedi, S. (2007). A conservative level set method for two phase flow II. *Journal of Computational Physics*, 225(1), 785-807.

Osher, S., and Sethian, J.A. (1988). Fronts propagating with curvature-dependent speed: algorithms based on Hamilton-Jacobi formulations. *Journal of Computational Physics*, 79, 12-49.

Papautsky, I., Gale, B.K., Mohanty, S., Ameelc, T. A., and Frazier, A.B. (1999). *Effects of Rectangular Microchannel Aspect Ratio on Laminar Friction Constant*. Santa Clara, CA: SPIE Conference on Microfluidic Devices and Systems II.

Peng, L., Yang, M., Guo, S.S., Liu, W. and Zhao.X.Z. (2011). The effect of interfacial tension on droplet formation in flow focusing microfluidic device. *Biomedical Microdevices*, 13, 559-564.

Pipe, C.J., and McKinley, G.H. (2009). Microfluidic rheometry. *Mechanics Research Communications*, 36, 110-120.

Qiu, D.M., Silva, L., Tonkovich, A.L., and Arora, R. (2010). Micro-droplet formation in non-Newtonian fluid in a microchannel. *Microfluidics and Nanofluidics*, 8, 531-548.

Raj, R., Mathur, N., and Buwa, V.V. (2010). Numerical simulations of liquid-liquid flows in microchannels. *Industrial and Engineering Chemistry Research*, 49, 10606-10614.

Rawool, A.S., Mitra, S.K., and Kandlikar, S.G. (2005). Numerical simulation of flow through microchannels with designed roughness. *Microfluidics and Nanofluidics*, 2, 215-221.

Rider, W.J., and Kothe, D.B. (1998). Reconstructing volume tracking. *Journal of Computational Physics*, 141, 112 - 152.

Rosengarten, G., Harvie, D.J.E., and Cooper-White, J. (2006). Contact angle effects on microdroplet deformation using CFD. *Applied Mathematical Modelling*, 30, 1033-1042.

Saha, A.A., and Mitra, S.K. (2008). Modeling and Simulation of Microscale Flows.In G. Petrone and G. Cammarata (Ed.), *Modelling and simulation* (pp. 283-316). United Kingdom: Intech.

Sankaranarayanan, K., Shan, X., Kevrekidis, I.G., and Sundaresan, S. (2002). Analysis of drag and virtual mass forces in bubbly suspensions using an implicit formulation of the lattice Boltzmann method. *Journal of Fluid Mechanics*. 452, 61-96.

Sang, L., Hong, Y.P., and Wang, F.J. (2009). Investigation of viscosity effect on droplet formation in T-shaped microchannels by numerical and analytical methods. *Microfluidics and Nanofluidics*, 6, 621-635.

Schechter, R.S. (1961). On the Steady Flow of a Non-Newtonian Fluid in Cylinder Ducts. *American Institute of Chemical Engineers Journal*, 7, 445-448.

Sethian J.A. (1999). *Level Set Methods and Fast Marching Methods: Evolving Interfaces in Computational Geometry, Fluid Mechanics, Computer Vision and Materials Sciences*. Cambridge, MA: Cambridge University Press Second Edition.

Shilpiekandula, V., Burns, D.J., Rifai, K.E., Toumi, K.Y., Guang, L.S., Reading, I., and Yoon, S.F. (2006). Metrology of microfluidic devices: a review. *ICOMM: International Conference of Micromanufacturing*.

Shui, L.L, Berg, A.V.D., and Eijkel, J.C.T. (2009). Interfacial tension controlled W/O and O/W 2-phase flows in microchannel. *Lab Chip*, 9, 795-801.

Sin, M.L.Y., Gao, J., Liao, J.C., and Wong, P.K. (2011). System Integration-A Major Step toward Lab on a Chip. *Journal of Biological Engineering*, 5:6, 1-21.

Sinton, D., Erickson, D., and Li, D.Q. (2002). Photo-injection based sample design and electroosmotic transport in microchannels. *Journal of Micromechanics and Microengineering*, 12, 898-904.

Smolka, L.B., and Belmonte, A. (2003). Drop pinch-off and filament dynamics of wormlike micellar fluids. *Journal of Non-Newtonian Fluid Mechanics*, 115, 1-25.

Song, H., Tice, J.D., and Ismagilov, R.F. (2003). A microfluidic system for controlling reaction networks in time. *Angewandte Chemie International Edition*, 42,767–772.

Squires, T.M., and Quake, S.R. (2005). Microfluidics: Fluid physics at the nanoliter scale. *Reviews of modern physics*, 77, 977-1024.

Steinhaus, B., and Shen, A.Q. (2007). Dynamics of viscoelastic fluid filaments in microfluidic devices. *Physics of Fluids*, 18, 073103, 1-13.

Stokes, G. (1851). On the Effect of the Internal Friction of Fluids on the Motion of Pendulums. *Transactions of the Cambridge Philosophical Society*, 9, 8-106.

Stone, H.A., Stroock, A.D., Ajdari, A. (2004). Engineering flows in small devices: microfluidics toward lab-on-a-chip. *Annual Review Fluid Mechanics*, 36,381-411.

Srinivasan, S., Mckinley, G.H., and Cohen, R.E. (2011). Assessing the accuracy of contact angle measurements for sessile drops on liquid-repellent surfaces. *Langmuir*, 27(22), 13582-13589.

Sugiura, S., Nakajima, M., Iwamoto, S., and Seki, M. (2001). Interfacial Tension Driven Monodispersed Droplet Formation from microfabricated channel array. *Langmuir*, 17, 5562-5566.

Sun, M., Du, W.B., and Fang, Q. (2006). Microfluidic liquid–liquid extraction system based on stopped-flow technique and liquid core waveguide capillary. *Talanta*, 70, 392–396.

Sussman, M., Smereka, P., and Osher, S. (1994). A level set approach for computing solutions to incompressible two-phase flow. *Journal of Computational Physics*, 114, 146-159.

Takada, N., Misawa, M., Tomiyama, A., and Fujiwara, S. (2000). Numerical simulation of two- and three-dimensional two phase fluid motion by Lattice Boltzmann method. *Computer Physics Communications*, 129, 233-246.

Takagi, M., Maki, T., Miyahara, M., and Mae, K. (2004). Production of titania nanoparticles by using a new microreactor assembled with same axle dual pipe. *Chemical Engineering Journal*, 101, 269-273.

Tan, S.H, Murshed, S.M.S., Nguyen, N.T., Wong, T.N., and Yobas, L. (2008). Thermally controlled droplet formation in flow focusing geometry: formation regimes and effect of nanoparticle suspension. *Journal of Physics D: Applied Physics*, 41, 165501.

Tanyeri, M., Ranka, M., Stipolkul, N., and Schroeder, C.M. (2011). A microfluidic-based hydrodynamic trap: Design and implementation. *Lab Chip*, 11, 1786-1794.

Taylor, G.I. (1932). The viscosity of a fluid containing small drops of another fluid. *Proceedings of the Royal Society of London Series A*, 138, 41-48.

Taylor, G.I. (1934). The formation of emulsions in definable fields of flow. *Proceedings of the Royal Society of London Series A*, 146, 501-523.

Teh, S.Y., Lin, R., Hung, L.H., and Lee, A.P. (2008).Droplet microfluidics. *Lab Chip*, 8, 198-220.

Terry, S.C., Jerman, J.H., and Angell, J.B. (1979). A gas chromatograph air analyser fabricated on a silicon wafer. *IEEE Transaction on Electron Devices*, 26, 1880-1886.

Tezduyar,T.E. (2004). *Finite element methods for fluid dynamics with moving boundaries and interfaces, in: E. Stein, R. De Borst, T.J.R. Hughes (Eds)*. Encyclopedia of Computational Mechanics, Fluids, 3, John Wiley & Sons, London (Chapter 17).

Thorsen, T., Roberts, R. W., Arnold, F. H. and Quake, S.R. (2001). Dynamic Pattern Formation in a Vesicle- Generating Microfluidic Device. *Physical Review Letters,* 86(16), 4163-4166.

Tice, J.D., Lyon, A.D., and Ismagilov, R.F. (2004). Effects of viscosity on droplet formation and mixing in microfluidic channels. *Analytica Chimica Acta*, 507, 73-77.

Tirtaatmadja,V., McKinley, G.H., and Cooper-White, J.J. (2006). Drop formation and breakup of low viscosity elastic fluids: Effects of molecular weight and concentration*. Physics of Fluids*, 18, 043101, 1-18.

Tostado, C.P., Xu, J.H., Luo, G.S. (2011).The effects of hydrophilic surfactant concentration and flow ratio on dynamic wetting in a T-junction microfluidic device. *Chemical Engineering Journal*, 171, 1340-1347.

Tryggvason, G.; Bunner, B.; Esmaeeli, A.; Juric, D.; Al-Rawahi, N.; Tauber, W.; and Jan, Y. J. (2001). A front-tracking method for the computations of multiphase flow. *Journal of Computational Physics*, 169(2), 708-759.

Umbanhowar, P.B., Prasad, V., and Weitz, D.A. (2000). Monodisperse emulsion generation via drop break off in a coflowing stream. *Langmuir*, 16, 347-351.

Unverdi, S.O., and Tryggvason, G. (1992). A Front Tracking Method for Viscous Incompressible Flows. *Journal ofComputational Physics*, 100, 25-37.

Utada, A.S., Fernandez-Nieves, A., Stone, H.A., and Weitz, D.A. (2007). Dripping to Jetting Transitions in Coflowing Liquid Streams. *Physical Review Letter*, 99, 094502.

Vananroye, A., Puyvelde, P.V., and Moldenaers, P. (2006).Effect of Confinement on Droplet Breakup in Sheared Emulsions. *Langmuir*, 22,3972-3974.

Van der Graaf, S., Nisisako, T., Schroeen, C.G.P.H., Van der Sman, R.G.M., and Boom, R.M. (2006). Lattice Boltzmann Simulations of Droplet Formation in a T-Shaped Microchannel. *Langmuir*, 22, 4144-4152.

Van der Zwan, E., Schroen, K., and Boom, R. (2009). A Geometric Model for the Dynamics of Microchannel Emulsification. *Langmuir*, 25(13), 7320–7327.

Van Steijn, V., Kleijn, C. R., & Kreutzer, M. T. (2010). Predictive model for the size of bubbles and droplets created in microfluidic T-junctions. *Lab Chip*,*10*, 2513-2518.

Verschueren, M., van de Vosse, F.N., Meijer, H.E.H.(2001). Diffuse-interface modelling of thermocapillary flow instabilities in a Hele-Shaw cell. *Journal of Fluid Mechanics*, 434, 153–166.

Villanueva, W., and Amberg, G. (2006). Some generic capillary-driven flows. *International Journal of Multiphase Flow*, 32(9), 1072-1086.

Wang, R.J. (2013). Nanoparticles influence droplet formation in a T-shaped microfluidic. *Journal of Nanoparticles Research*, 15:2128, 1-9.

Wang, K., Lu, Y.C., Xu, J.H., and Luo, G.S. (2009). Determination of dynamic interfacial tension and its effect on droplet formation in the T-shaped microdispersion process. *Langmuir*, 25, 2153-2158.

Webster, A., Dyer, C.E., Haswell, S.J., and Greenman, J. (2010). A microfluidic device for tissue biopsy culture and interrogation. *Analytical Methods*. 2(8), 1005-1007.

Wehking, J.D., Gabany, M., Chew, L., and Kumar, R. (2014). Effects of viscosity, interfacial tension, and flow geometry on droplet formation in a microfluidic T-junction. *Microfluidics and Nanofluidics*, 16, 441-453.

Weigl, B.H., Bardell, R.L., and Cabrera, C.R. (2003).Lab on a chip for drug development.*Advanced Drug Delivery Reviews*, 55, 349-377.

Whitesides, G.M. (2006). The origins and the future of microfluidics. *Nature*, 442, 368-373.

Xu, J.H., Li, S.W., Tan, J., and Luo, G.S. (2008). Correlations of droplet formation in T-junction microfluidics devices: from squeezing to dripping. *Microfluidics and Nanofluidics*, 5, 711-717.

Xu, J.H., Li, S.W., Tan, J., Wang, Y.J., and Luo, G.S. (2006a). Controllable preparation of monodisperse O/W and W/O emulsions in the same microfluidic device. *Langmuir*, 22, 7943-7946.

Xu, J.H., Li, S.W., Tan, J., Wang, Y.J., and Luo, G.S. (2008). Preparation of Highly Monodisperse Droplet in a T-Junction Microfluidic Device. *American Institute of Chemical Engineers Journal*, 52, 3005-3010.

Xu, J.H., Luo, G.S., Li, S.W., and Chen, G.G. (2006b). Shear force induced monodisperse droplet formation in a microfluidic device by controlling wetting properties. *Lab on Chip*, 6, 131-136.

Yang, G.H., Lin, Y.S., Huang, K.S., Huang, Y.C., Wang, E.C., Jhong, J.Y., and Kuo, C.Y.(2008). Microfluidics emulsification and sorting assisted preparation of monodisperse chitosan microparticles. *Lab Chip*, 9, 145-150.

Yeom, S., and Lee, S. Y. (2011). Size prediction of drops formed by dripping at a micro T-junction in liquid–liquid mixing. *Experimental Thermal and Fluid Science*, 35, 2, 387-394.

Young, T. (1805). An Essay on the Cohesion of Fluids. *Philosophical Transactions of the Royal Society of London*, 95, 65-87.

Zhang, X. (1999). Dynamics of growth and breakup of viscous pendant drops into air. *Journal of Colloid and Interface Science*, 212, 107-122.

Zhang, X., and Basaran, O.A. (1995). An experimental study of dynamics of drop formation. *Physics of Fluids*, 7, 1184-1203.

Zhang, Y.X., Fan, J., and Wang, L.Q. (2009). Formation of Nanoliter Droplets in a Confined Microfluidic T-shaped Junction: Formation time and Droplet Volume. *Current Nanoscience*, 5, 519-526.

Zhao, C.X., and Middelberg, A.P.J. (2011). Two-phase microfluidic flows. *Chemical Engineering Science*, 66, 1394-1411.

Zhao, Y.J., Zhao, X.W., Sun, C., Li, J., Zhu, R., and Gu, Z.Z. (2008). Encoded silica colloidal crystal beads as supports for potential multiplex immunoassay. *Analytical Chemistry*, 80, 1598-1605.

Zheng, B., Tice, J.D., Roach, L.S., Ismagilov, R.F. (2004). A droplet-based, composite PDMS/glass capillary microfluidic system for evaluating protein crystallization conditions by microbatch and vapor diffusion methods with on-chip X-ray diffraction. *Angewandte Chemie International Edition*, 43, 2508-2511.

Zheng, H.W., Shu, C., and Chew, Y.T. (2006). A Lattice Boltzmann for Multiphase flows with large density ratio. *Journal of Computational Physics*, 218, 353-371.

Appendix A.1: Table Data for Chapter 5

Table A.1: Data for Figure 5.2.

CMC Concentration	η_o (kg/m.s)	η_∞(kg/m.s)	η_o/η_∞	d_{eff} (μm)
0.02wt%	0.00698	0.00007	99.76	148.77
		0.00014	49.88	148.83
		0.00028	24.57	148.92
		0.00056	12.47	148.68
		0.00112	6.23	148.41
		0.00224	3.12	147.85
		0.00448	1.56	146.93
0.04wt%	0.01214	0.00007	173.39	147.40
		0.00014	86.70	147.22
		0.00028	43.35	146.84
		0.00056	21.67	147.05
		0.00112	10.84	146.76
		0.00224	5.42	146.36
		0.00448	2.71	145.49
		0.00896	1.35	144.54
0.06wt%	0.01710	0.00007	244.29	145.90
		0.00014	122.14	146.13
		0.00028	61.07	145.94
		0.00056	30.54	145.62
		0.00112	15.27	145.49
		0.00224	7.63	145.39
		0.00448	3.82	144.93
		0.00896	1.91	144.04
0.08wt%	0.01954	0.00007	279.14	146.67
		0.00014	139.57	146.40
		0.00028	69.79	146.37
		0.00056	34.89	145.51
		0.00112	17.45	145.48
		0.00224	8.72	145.21
		0.00448	4.36	144.61
		0.00896	2.18	143.70
		0.01792	1.09	143.94
0.10wt%	0.04195	0.00007	599.31	144.96
		0.00014	299.65	144.90
		0.00028	149.83	144.72
		0.00056	74.91	144.59
		0.00112	37.46	144.43
		0.00224	18.73	144.16
		0.00448	9.36	143.91
		0.00896	4.68	144.09
		0.01792	2.34	143.06
		0.03584	1.17	139.84
0.20wt%	0.07417	0.00007	1059.64	143.52
		0.00014	529.82	143.61
		0.00028	264.91	143.57
		0.00055	134.86	143.82
		0.00112	66.23	143.63
		0.00224	33.11	143.59
		0.00448	16.56	143.50
		0.00896	8.28	143.26
		0.01792	4.14	142.13
		0.03584	2.07	139.66
		0.07168	1.03	134.54

Table A.1: (Continued).

CMC Concentration	η_o (kg/m.s)	η_∞(kg/m.s)	η_o/η_∞	d_{eff} (μm)
0.40wt%	0.19461	0.00007	2780.18	139.66
		0.00014	1390.09	139.73
		0.00028	695.04	139.83
		0.00056	347.52	139.63
		0.00112	173.76	139.47
		0.00224	86.88	139.28
		0.00448	43.44	139.11
		0.00896	21.72	139.51
		0.01792	10.86	139.27
		0.03584	5.43	137.42
		0.07168	2.72	132.97
		0.14336	1.36	129.26
0.60wt%	0.79948	0.00007	11421.21	138.94
		0.00014	5710.60	138.94
		0.00028	2855.30	139.06
		0.00056	1427.65	138.83
		0.00112	713.83	138.83
		0.00223	358.82	138.82
		0.00448	178.46	136.75
		0.00896	89.23	136.11
		0.01792	44.61	135.32
		0.03584	22.31	133.67
		0.07168	11.15	131.23
		0.14336	5.58	124.82
		0.28672	2.79	116.88
0.80wt%	1.64696	0.00007	23528.05	135.92
		0.00014	11764.02	135.92
		0.00028	5882.01	135.87
		0.00055	2941.01	135.93
		0.00112	1470.50	135.71
		0.00224	735.25	135.61
		0.00448	367.63	135.21
		0.00896	183.81	134.75
		0.01792	91.91	133.63
		0.03584	45.95	132.45
		0.07168	22.98	127.83
		0.14336	11.49	123.19
		0.28672	5.74	115.80
		0.57344	2.87	109.78
1.00wt%	4.11430	0.00007	58775.71	131.01
		0.00014	29387.86	131.00
		0.00028	14693.93	131.18
		0.00056	7346.96	131.17
		0.00112	3673.48	131.20
		0.00224	1836.74	130.97
		0.00448	918.37	130.75
		0.00896	459.19	130.29
		0.01792	229.59	129.06
		0.03584	114.80	127.76
		0.07168	57.40	124.95
		0.14336	28.70	121.62
		0.28672	14.35	114.48
		0.57344	7.17	109.45
1.20wt%	10.26440	0.00007	14663.29	126.84
		0.00014	73317.14	126.80
		0.00028	36658.57	126.69
		0.00056	18329.29	126.63
		0.00112	9164.64	126.47
		0.00224	4582.32	126.32
		0.00448	2291.16	126.16

Table A.1: (Continued).

CMC Concentration	η_o (kg/m.s)	η_∞(kg/m.s)	η_o/η_∞	d_{eff} (μm)
1.20wt%	10.26440	0.00896	1145.58	125.79
		0.01792	572.79	125.26
		0.03584	286.40	124.09
		0.07168	143.20	121.56
		0.14336	71.60	117.06
		0.28672	35.80	114.66
		0.57344	17.90	108.40

Table A.2: Data for Figure 5.10.

CMC Concentration	η_o/η_∞	$\dot{\gamma}_\infty$ (1/s)
0.02wt%	99.76	219672028.62
	49.88	19770796.17
	24.57	1689164.16
	12.47	160114.39
	6.23	14381.44
	3.12	1267.59
	1.56	89.57
0.04wt%	173.39	1637737518.74
	86.70	149793666.33
	43.35	13700695.14
	21.67	1253117.37
	10.84	114614.80
	5.42	10482.80
	2.71	957.18
	1.35	78.64
0.06wt%	244.29	991049020.46
	122.14	115523089.00
	61.07	13466118.83
	30.54	1569697.46
	15.27	182972.94
	7.63	21325.94
	3.82	2480.15
	1.91	276.21
0.08wt%	279.14	4239084.00
	139.57	1093018.76
	69.79	281814.68
	34.89	72645.50
	17.45	18708.19
	8.72	4796.11
	4.36	1203.42
	2.18	270.13
	1.09	17.70
0.10 wt%	599.31	430142277.91
	299.65	67946751.33
	149.83	10719113.02
	74.91	1685734.88
	37.46	263113.93
	18.73	40321.59
	9.36	5904.34
	4.68	767.42
	2.34	69.33
	1.17	0.71
0.20 wt%	1059.64	11054694.11
	529.82	3708169.48
	264.91	1229961.09
	134.86	412888.36
	66.23	127142.15
	33.11	38578.60

Table A.2: (Continued).

CMC Concentration	η_o/η_∞	$\dot{\gamma}_\infty$ (1/s)
0.20 wt%	16.56	10873.77
	8.28	2688.61
	4.14	512.07
	2.07	49.92
	1.03	0.01
0.40 wt%	2780.18	7795049.27
	1390.09	2824490.49
	695.04	1021715.23
	347.52	368495.56
	173.76	132209.00
	86.88	46994.69
	43.44	16427.58
	21.72	5568.99
	10.86	1780.75
	5.43	505.11
	2.72	107.33
	1.36	7.28
0.60 wt%	11421.21	7673227.39
	5710.60	3181607.54
	2855.30	1311956.09
	1427.65	536850.05
	713.83	217323.25
	358.82	87166.45
	178.46	33800.82
	89.23	12775.14
	44.61	4606.15
	22.31	1544.22
	11.15	459.64
	5.58	110.45
	2.79	16.71
0.80 wt%	23528.05	11809169.73
	11764.02	4709372.54
	5882.01	1875999.99
	2941.01	746045.82
	1470.50	295903.22
	735.25	116879.86
	367.63	45868.55
	183.81	17817.47
	91.91	6809.04
	45.95	2534.10
	22.98	902.38
	11.49	297.51
	5.74	84.77
	2.87	17.43
1.00wt%	58775.71	30365559.18
	29387.86	11481329.88
	14693.93	4339590.96
	7346.96	1639284.27
	3673.48	618658.25
	1836.74	233120.66
	918.37	87623.87
	459.19	32800.65
	229.59	12195.88
	114.80	4484.28
	57.40	1618.23
	28.70	565.57
	14.35	186.77
	7.17	55.42
1.20wt%	14663.29	24511710.77
	73317.14	9950038.28

Table A.2: (Continued).

CMC Concentration	η_o/η_∞	$\dot{\gamma}_\infty$ (1/s)
1.20wt%	36658.57	4035817.40
	18329.29	1635067.81
	9164.64	661311.48
	4582.32	266810.39
	2291.16	107256.98
	1145.58	42887.83
	572.79	17014.67
	286.40	6671.55
	143.20	2570.32
	71.60	964.02
	35.80	346.70
	17.90	116.49

Table A.3: Data for Figure 5.12.

CMC Concentration	η_o (kg/m.s)	η_∞(kg/m.s)	η_o/η_∞	d_{eff} (μm)
0.02wt%	0.00698	0.00028	24.57	148.92
0.04wt%	0.01214		43.35	146.84
0.06wt%	0.01710		61.07	145.94
0.08wt%	0.01954		69.79	146.37
0.10wt%	0.04195		149.83	144.72
0.20wt%	0.07417		264.91	143.57
0.40wt%	0.19461		695.04	139.83
0.60wt%	0.79948		2855.30	139.06
0.80wt%	1.64696		5882.01	135.87
1.00wt%	4.11430		14693.93	131.18
1.20wt%	10.26440		36658.57	126.69
0.02wt%	0.00698	0.00056	12.47	148.68
0.04wt%	0.01214		21.67	147.05
0.06wt%	0.01710		30.54	145.62
0.08wt%	0.01954		34.89	145.51
0.10wt%	0.04195		74.91	144.59
0.20wt%	0.07417		134.86	143.82
0.40wt%	0.19461		347.52	139.63
0.60wt%	0.79948		1427.65	138.83
0.80wt%	1.64696		2941.01	135.93
1.00wt%	4.11430		7346.96	131.17
1.20wt%	10.26440		18329.29	126.63
0.02wt%	0.00698	0.00112	6.23	148.41
0.04wt%	0.01214		10.84	146.76
0.06wt%	0.01710		15.27	145.49
0.08wt%	0.01954		17.45	145.48
0.10wt%	0.04195		37.46	144.43
0.20wt%	0.07417		66.23	143.63
0.40wt%	0.19461		173.76	139.47
0.60wt%	0.79948		713.83	138.83
0.80wt%	1.64696		1470.50	135.71
1.00wt%	4.11430		3673.48	131.20
1.20wt%	10.26440		9164.64	126.47
0.02wt%	0.00698	0.00224	3.12	147.85
0.04wt%	0.01214		5.42	146.36
0.06wt%	0.01710		7.63	145.39
0.08wt%	0.01954		8.72	145.21
0.10wt%	0.04195		18.73	144.16
0.20wt%	0.07417		33.11	143.59
0.40wt%	0.19461		86.88	139.28
0.60wt%	0.79948		358.82	138.82
0.80wt%	1.64696		735.25	135.61
1.00wt%	4.11430		1836.74	130.97

Table A.3: (Continued).

CMC Concentration	η_o (kg/m.s)	η_∞(kg/m.s)	η_o/η_∞	d_{eff} (μm)
1.20wt%	10.26440	0.00224	4582.32	126.32
0.02wt%	0.00698	0.00448	1.56	146.93
0.04wt%	0.01214		2.71	145.49
0.06wt%	0.01710		3.82	144.93
0.08wt%	0.01954		4.36	144.61
0.10wt%	0.04195		9.36	143.91
0.20wt%	0.07417		16.56	143.50
0.40wt%	0.19461		43.44	139.11
0.60wt%	0.79948		178.46	136.75
0.80wt%	1.64696		367.63	135.21
1.00wt%	4.11430		918.37	130.75
1.20wt%	10.26440		2291.16	126.16

Table A.4: Data for Figure 5.14.

CMC Concentration	η_o (kg/m.s)	η_∞(kg/m.s)	λ_{CY}(s)	d_{eff} (μm)
0.02wt%	0.00698	0.00028	0.80	150.83
			0.60	150.54
			0.40	150.39
			0.20	149.89
			0.10	149.44
			0.08	149.36
0.04wt%	0.01214	0.00001	0.80	149.84
			0.60	149.69
			0.40	149.41
			0.20	148.72
			0.10	148.13
			0.08	147.83
0.06wt%	0.01717	0.00000	0.80	149.66
			0.60	149.03
			0.40	148.74
			0.20	148.49
			0.10	147.78
			0.08	147.45
0.08wt%	0.01954	0.00278	0.80	148.11
			0.60	148.12
			0.40	147.91
			0.20	147.89
			0.10	147.46
			0.08	147.39
0.10wt%	0.04195	0.00069	0.80	147.69
			0.60	147.34
			0.40	146.85
			0.20	145.97
			0.10	145.40
			0.08	145.04
0.20wt%	0.07417	0.00055	0.80	150.59
			0.60	150.23
			0.40	149.71
			0.20	148.80
			0.10	147.98
			0.08	147.59
0.40wt%	0.19461	0.00402	0.80	146.05
			0.60	145.87
			0.40	145.70
			0.20	144.62
			0.10	144.83
			0.08	144.52

Table A.4: (Continued).

CMC Concentration	η_o (kg/m.s)	η_∞(kg/m.s)	λ_{CY}(s)	d_{eff} (μm)
0.60wt%	0.79948	0.00223	0.80	146.61
			0.60	145.82
			0.40	145.16
			0.20	144.39
			0.10	143.47
			0.08	142.95
0.80wt%	1.64696	0.00565	0.80	143.64
			0.60	143.59
			0.40	140.28
			0.20	139.37
			0.10	136.91
			0.08	136.62
1.00wt%	4.11430	0.00313	0.80	139.79
			0.60	139.44
			0.40	136.96
			0.20	133.82
			0.10	127.13
			0.08	124.96
1.20wt%	10.26440	0.00000	0.80	138.21
			0.60	136.65
			0.40	132.85
			0.20	126.20
			0.10	122.17
			0.08	119.23

Appendix A.2: Table Data for Chapter 6

Table A.5: Data for Figure 6.1, 6.3 and 6.6 at fixed viscosity ratio (λ) of 1.

CMC Concentration	η_c (kg/m.s)	η_o (kg/m.s)	t_d (s)	f_d (1/s)	d_{eff} (μm)
0.04wt%	0.0121	0.0121	0.0950	10.53	213.67
0.06wt%	0.0171	0.0171	0.0855	11.70	202.25
0.08wt%	0.0195	0.0195	0.0805	12.42	195.93
0.10wt%	0.0420	0.0420	0.0580	17.24	166.37
0.20wt%	0.0680	0.0680	0.0430	23.26	142.73
0.40wt%	0.1946	0.1946	0.0195	51.28	132.46

Table A.6: Data for Figure 6.8, 6.13 to 6.15, and Figure 6.19 to 6.20.

CMC Concentration	θ	t_d (s)	f_d (1/s)	d_{eff} (μm)
0.02wt%	130°	0.0555	18.02	161.82
	140°	0.0550	18.18	161.43
	150°	0.0535	18.69	160.29
	160°	0.0495	20.20	153.62
	170°	0.0485	20.62	151.44
	180°	0.0475	21.05	150.74
0.06wt%	130°	0.0530	18.87	158.90
	140°	0.0530	18.87	158.74
	150°	0.0495	20.20	153.68
	160°	0.0480	20.83	150.32
	170°	0.0465	21.51	149.06
	180°	0.0460	21.74	148.42
0.10wt%	130°	0.0525	19.05	157.52
	140°	0.0525	19.05	158.34
	150°	0.0480	20.83	151.30
	160°	0.0475	21.05	149.11
	170°	0.0455	21.98	147.57
	180°	0.0455	21.98	147.15
0.20wt%	130°	0.0530	18.87	158.67
	140°	0.0485	20.62	151.54
	150°	0.0470	21.28	149.79
	160°	0.0645	21.51	147.16
	170°	0.0455	21.98	144.84
	180°	0.0455	21.98	144.55
0.40wt%	130°	0.0470	21.28	149.20
	140°	0.0465	21.51	147.95
	150°	0.0450	22.22	143.90
	160°	0.0440	22.73	142.01
	170°	0.0445	22.47	141.75
	180°	0.0425	23.53	140.56
0.60wt%	130°	0.0525	19.05	149.21
	140°	0.0455	21.98	142.84
	150°	0.0425	23.53	139.55
	160°	0.0420	23.81	138.61
	170°	0.0430	23.26	139.18
	180°	0.0425	23.53	139.24
0.80wt%	130°	0.0550	18.18	143.56
	140°	0.0490	20.41	135.37
	150°	0.0470	21.28	134.96
	160°	0.0440	22.73	135.74
	170°	0.0430	23.26	135.57
	180°	0.0425	23.53	135.50

Table A.6: (Continued).

CMC Concentration	θ	t_d (s)	f_d (1/s)	d_{eff} (μm)
1.00wt%	130°	0.0570	17.54	132.06
	140°	0.0530	18.87	130.04
	150°	0.0510	19.61	130.19
	160°	0.0490	20.41	130.23
	170°	0.0480	20.83	131.17
	180°	0.0480	20.83	130.82
1.20wt%	130°	0.0625	16.00	124.75
	140°	0.0585	17.09	125.08
	150°	0.0570	17.54	125.89
	160°	0.0555	18.02	126.46
	170°	0.0550	18.18	126.51
	180°	0.0550	18.18	126.68

Table A.7: Data for Figure 6.21, 6.23 to 6.25, and Figure 6.33 to 6.34.

CMC Concentration	σ (N/m)	t_d (s)	f_d (1/s)	d_{eff} (μm)
0.02wt%	0.010	0.0280	35.71	113.78
	0.015	0.0385	25.97	135.18
	0.020	0.0465	21.51	149.65
	0.025	0.0530	18.87	160.17
	0.030	0.0585	17.09	168.16
	0.035	0.0635	15.75	175.06
0.04wt%	0.010	0.0275	36.36	113.61
	0.015	0.0380	26.32	134.29
	0.020	0.0455	21.98	147.67
	0.025	0.0520	19.23	158.77
	0.030	0.0580	17.24	166.51
	0.035	0.0625	16.00	173.38
0.06wt%	0.010	0.0275	36.36	112.95
	0.015	0.0375	26.67	133.72
	0.020	0.0450	22.22	146.89
	0.025	0.0515	19.42	157.42
	0.030	0.0570	17.54	165.84
	0.035	0.0615	16.26	172.49
0.08wt%	0.010	0.0275	36.36	112.76
	0.015	0.0370	27.03	132.04
	0.020	0.0445	22.47	145.19
	0.025	0.0505	19.80	155.72
	0.030	0.0560	17.86	163.88
	0.035	0.0610	16.39	171.01
0.10wt%	0.010	0.0275	36.36	112.19
	0.015	0.0370	27.03	131.82
	0.020	0.0440	22.73	144.85
	0.025	0.0505	19.80	155.70
	0.030	0.0560	17.86	163.61
	0.035	0.0610	16.39	170.44
0.20wt%	0.010	0.0285	35.09	112.06
	0.015	0.0380	26.32	129.30
	0.020	0.0445	22.47	144.82
	0.025	0.0495	20.20	153.21
	0.030	0.0545	18.35	160.07
	0.035	0.0595	16.81	168.17
0.40wt%	0.010	0.0275	36.36	103.86
	0.015	0.0350	28.57	126.37
	0.020	0.0430	23.26	137.98
	0.025	0.0495	20.20	152.04
	0.030	0.0540	18.52	160.01
	0.035	0.0575	17.39	165.32

Table A.7: (Continued).

CMC Concentration	σ (N/m)	t_d (s)	f_d (1/s)	d_{eff} (μm)
0.60wt%	0.010	0.0285	35.09	102.98
	0.015	0.0320	31.25	122.34
	0.020	0.0420	23.81	136.99
	0.025	0.0480	20.83	148.96
	0.030	0.0535	18.69	157.27
	0.035	0.0565	17.70	163.30
0.80wt%	0.010	0.0350	28.57	99.19
	0.015	0.0390	25.64	120.56
	0.020	0.0425	23.53	135.51
	0.025	0.0465	21.51	145.37
	0.030	0.0520	19.23	154.28
	0.035	0.0565	17.70	161.85
1.00wt%	0.010	0.0415	24.10	96.49
	0.015	0.0445	22.47	118.65
	0.020	0.0475	21.05	132.00
	0.025	0.0510	19.61	140.10
	0.030	0.0530	18.87	153.34
	0.035	0.0555	18.02	158.33
1.20wt%	0.010	0.0485	20.62	92.74
	0.015	0.0515	19.42	119.00
	0.020	0.0545	18.35	132.26
	0.025	0.0570	17.54	135.55
	0.030	0.0610	16.39	149.61
	0.035	0.0625	16.00	158.72

Appendix A.3: Table Data for Chapter 7

Table A.8: Data for Figure 7.1 and Figure 7.4 to 7.5.

CMC Concentration	Q_c (ml/hr)	Q_d (ml/hr)	Q	t_d (s)	f_d (1/s)	d_{eff} (μm)
0.00wt%	2.00	0.050	0.0250	0.0900	11.11	146.15
		0.055	0.0275	0.0825	12.12	146.95
		0.065	0.0325	0.0720	13.89	147.96
		0.080	0.0400	0.0575	17.39	149.13
		0.100	0.0500	0.0485	20.62	152.88
		0.135	0.0675	0.0405	24.69	162.80
		0.200	0.1000	0.0310	32.26	176.40
		0.250	0.1250	0.0295	33.90	190.56
0.04wt%	2.00	0.050	0.0250	0.0785	12.74	136.18
		0.055	0.0275	0.0725	13.79	137.59
		0.065	0.0325	0.0635	15.75	139.85
		0.080	0.0400	0.0540	18.52	143.38
		0.100	0.0500	0.0465	21.51	149.33
		0.135	0.0675	0.0390	25.64	159.25
		0.200	0.1000	0.0325	30.77	173.67
		0.250	0.1250	0.0380	26.32	192.15
0.08wt%	2.00	0.050	0.0250	0.0750	13.33	133.26
		0.055	0.0275	0.0695	14.39	134.42
		0.065	0.0325	0.0610	16.39	137.16
		0.080	0.0400	0.0520	19.23	141.16
		0.100	0.0500	0.0450	22.22	146.64
		0.135	0.0675	0.0390	25.64	158.94
		0.200	0.1000	0.0320	31.25	173.19
		0.250	0.1250	0.0315	31.75	189.07
0.10wt%	2.00	0.050	0.0250	0.0745	13.42	132.95
		0.055	0.0275	0.0690	14.49	133.97
		0.065	0.0325	0.0605	16.53	136.88
		0.080	0.0400	0.0520	19.23	140.52
		0.100	0.0500	0.0455	21.98	146.39
		0.135	0.0675	0.0390	25.64	159.13
		0.200	0.1000	0.0320	31.25	173.07
		0.250	0.1250	0.0305	32.79	187.76
0.20wt%	2.00	0.050	0.0250	0.0715	13.99	130.04
		0.055	0.0275	0.0660	15.15	131.24
		0.065	0.0325	0.0585	17.09	134.28
		0.080	0.0400	0.0505	19.80	138.45
		0.100	0.0500	0.0455	21.98	146.69
		0.135	0.0675	0.0385	25.97	154.71
		0.200	0.1000	0.0325	30.77	172.78
		0.250	0.1250	0.0350	28.57	189.76
0.40wt%	2.00	0.050	0.0250	0.0660	15.15	124.81
		0.055	0.0275	0.0620	16.13	126.48
		0.065	0.0325	0.0550	18.18	129.63
		0.080	0.0400	0.0480	20.83	134.42
		0.100	0.0500	0.0425	23.53	141.70
		0.135	0.0675	0.0360	27.78	150.41
		0.200	0.1000	0.0340	29.41	171.71
		0.250	0.1250	0.0345	28.99	178.10
0.80wt%	2.00	0.050	0.0250	0.0610	16.39	118.32
		0.055	0.0275	0.0580	17.24	121.09
		0.065	0.0325	0.0570	17.70	128.77
		0.080	0.0400	0.0460	21.74	129.95
		0.100	0.0500	0.0430	23.26	136.91

Table A.8: (Continued).

CMC Concentration	Q_c (ml/hr)	Q_d(ml/hr)	Q	t_d (s)	f_d (1/s)	d_{eff} (μm)
0.80wt%	2.00	0.135	0.0675	0.0415	24.10	146.26
		0.200	0.1000	0.0385	25.97	155.97
		0.250	0.1250	0.0360	27.78	163.39
1.20wt%	2.00	0.050	0.0250	0.0635	15.75	116.58
		0.055	0.0275	0.0590	16.95	116.38
		0.065	0.0325	0.0595	16.81	120.59
		0.080	0.0400	0.0570	17.54	129.36
		0.100	0.0500	0.0550	18.18	133.70
		0.135	0.0675	0.0510	19.61	141.02
		0.200	0.1000	0.0460	21.74	141.10
		0.250	0.1250	0.0440	22.73	145.96

Table A.9: Data for Figure 7.6 to 7.7 and Figure 7.10 to 7.13.

CMC Concentration	Q_c (ml/hr)	Q_d (ml/hr)	Q	t_d (s)	f_d (1/s)	d_{eff} (μm)
0.00wt%	4.00	0.20	0.0500	0.0140	71.429	113.65
	3.50		0.0571	0.0170	58.824	126.88
	3.00		0.0667	0.0210	47.619	140.20
	2.50		0.0800	0.0255	39.216	156.41
	2.00		0.1000	0.0305	32.787	176.34
	1.50		0.1333	0.0460	21.739	229.46
0.04wt%	4.00	0.20	0.0500	0.0140	71.429	113.67
	3.50		0.0571	0.0170	58.824	125.29
	3.00		0.0667	0.0205	48.780	138.53
	2.50		0.0800	0.0255	39.216	154.56
	2.00		0.1000	0.0330	30.303	174.20
	1.50		0.1333	0.0505	19.802	210.26
0.08wt%	4.00	0.20	0.0500	0.0135	74.04	111.10
	3.50		0.0571	0.0170	58.824	123.37
	3.00		0.0667	0.0205	48.780	137.77
	2.50		0.0800	0.0245	40.816	152.61
	2.00		0.1000	0.0320	31.520	173.35
	1.50		0.1333	0.0520	19.231	207.03
0.10wt%	4.00	0.20	0.0500	0.0135	74.074	111.21
	3.50		0.0571	0.0170	58.824	123.71
	3.00		0.0667	0.00205	48.780	138.58
	2.50		0.0800	0.0245	40.816	152.71
	2.00		0.1000	0.0315	31.746	173.01
	1.50		0.1333	0.0515	19.417	207.14
0.20wt%	4.00	0.20	0.0500	0.0130	76.923	109.31
	3.50		0.0571	0.0170	58.824	122.68
	3.00		0.0667	0.0180	55.556	133.33
	2.50		0.0800	0.0245	40.816	149.62
	2.00		0.1000	0.0330	30.303	172.59
	1.50		0.1333	0.0475	21.053	200.41
0.40wt%	4.00	0.20	0.0500	0.0130	76.923	106.97
	3.50		0.0571	0.0155	64.516	116.93
	3.00		0.0667	0.0185	54.054	131.34
	2.50		0.0800	0.0255	39.216	148.59
	2.00		0.1000	0.0340	29.412	171.17
	1.50		0.1333	0.0525	19.048	197.21
0.80wt%	4.00	0.20	0.0500	0.0155	64.516	104.92
	3.50		0.0571	0.0195	51.282	115.13
	3.00		0.0667	0.0230	43.478	126.87
	2.50		0.0800	0.0295	33.898	140.50
	2.00		0.1000	0.0385	25.974	155.44
	1.50		0.1333	0.0525	19.048	176.90

Table A.9: (Continued).

CMC Concentration	Q_c (ml/hr)	Q_d (ml/hr)	Q	t_d (s)	f_d (1/s)	d_{eff} (μm)
1.20wt%	4.00	0.20	0.0500	0.0200	50.000	104.24
	3.50		0.0571	0.0235	42.553	108.96
	3.00		0.0667	0.0290	34.483	119.60
	2.50		0.0800	0.0365	27.397	130.07
	2.00		0.1000	0.0455	21.978	141.41

Table A.10: Data for Figure 7.14 to 7.15 and Figure 7.18 to 7.20.

CMC Concentration	η_0 (kg/m.s)	η_c (kg/m.s)	λ	t_d (s)	f_d (1/s)	d_{eff} (μm)
0.00wt%	0.00093	0.0680	0.014	0.0485	20.62	152.88
0.02wt%	0.00698		0.103	0.0475	21.05	150.74
0.04wt%	0.01214		0.179	0.0465	21.51	149.56
0.06wt%	0.01710		0.252	0.0460	21.74	148.42
0.08wt%	0.01954		0.287	0.0455	21.98	147.63
0.10wt%	0.04195		0.617	0.0455	21.98	147.15
0.20wt%	0.07417		1.091	0.0455	21.98	144.55
0.40wt%	0.19461		2.862	0.0425	23.53	140.56
0.60wt%	0.79948		11.757	0.0425	23.53	139.24
0.80wt%	1.64696		24.220	0.0425	23.53	135.50
1.00wt%	4.11430		60.504	0.0480	20.83	130.82
1.20wt%	10.26440		150.947	0.0550	18.18	126.68

Table A.11: Data for Figure 7.21 to 7.23 and Figure 7.27 to 7.29.

CMC Concentration	η_0 (kg/m.s)	η_c (kg/m.s)	λ	t_d (s)	f_d (1/s)	d_{eff} (μm)
0.02wt%	0.00698	0.0354	0.197	0.0895	11.17	206.70
0.04wt%	0.01214		0.343	0.0880	11.36	204.91
0.06wt%	0.01710		0.483	0.0870	11.49	203.71
0.08wt%	0.01954		0.552	0.0855	11.70	202.33
0.10wt%	0.04195		1.185	0.0855	11.70	201.76
0.20wt%	0.07417		2.095	0.0825	12.12	198.87
0.40wt%	0.19461		5.497	0.0790	12.66	194.38
0.60wt%	0.79948		22.584	0.0780	12.82	192.52
0.80wt%	1.64696		46.524	0.0815	12.27	195.54
1.00wt%	4.11430		116.223	0.0785	12.74	190.69
1.20wt%	10.26440		289.955	0.0875	11.43	190.41
0.02wt%	0.00698	0.0680	0.103	0.0475	21.05	150.74
0.04wt%	0.01214		0.179	0.0465	21.51	149.56
0.06wt%	0.01710		0.252	0.0460	21.74	148.42
0.08wt%	0.01954		0.287	0.0455	21.98	147.63
0.10wt%	0.04195		0.617	0.0455	21.98	147.15
0.20wt%	0.07417		1.091	0.0455	21.98	144.55
0.40wt%	0.19461		2.862	0.0425	23.53	140.56
0.60wt%	0.79948		11.757	0.0425	23.53	139.24
0.80wt%	1.64696		24.220	0.0425	23.53	135.50
1.00wt%	4.11430		60.504	0.0480	20.83	130.82
1.20wt%	10.26440		150.947	0.0550	18.18	126.68
0.02wt%	0.00698	0.0998	0.070	0.0345	28.99	127.49
0.04wt%	0.01214		0.122	0.0340	29.41	126.57
0.06wt%	0.01710		0.171	0.0335	29.85	125.71
0.08wt%	0.01954		0.196	0.0335	29.85	125.18
0.10wt%	0.04195		0.420	0.0335	29.85	124.85
0.20wt%	0.07417		0.743	0.0330	30.30	124.17
0.40wt%	0.19461		1.950	0.0330	30.30	119.52

Table A.11: (Continued).

CMC Concentration	η_0 (kg/m.s)	η_c (kg/m.s)	λ	t_d (s)	f_d (1/s)	d_{eff} (μm)
0.60wt%	0.79948	0.0998	8.011	0.295	33.90	116.15
0.80wt%	1.64696		16.503	0.0310	32.26	116.28
1.00wt%	4.11430		41.225	0.0370	27.03	114.07
1.20wt%	10.26440		102.850	0.0435	22.99	114.06

Appendix A.4: MATLAB Code Function for Surface and Interfacial Tension Measurement

```
%*********************************************************************
%**   Determining Surface/Interfacial Tension of A Pendant Drop   **
%*********************************************************************
%*********************************************************************
%** Surface/Interfacial Tension Program code                        **
%**Created by Katerina Loizou (2011)                               **
%** Multiphase Flow Research Group                                  **
%** University of Nottingham, United Kingdom                        **
%*********************************************************************
%*********************************************************************
%**                  Clean up and Initialization                  **
%*********************************************************************

clc;                    % Clear the command window.
close all;              % Close all figures (except those of imtool.)
imtool close all;       % Close all imtool figures.
clear;                  % Erase all existing variables.
workspace;              % Make sure the workspace panel is showing.
fontSize = 15;

[filename, pathname] = ...
uigetfile({'*.tif';'*.jpg';'*.gif';'*.*'},'Select an image');  %Open
standard dialog box for retrieving files

unfilteredimage = imread([pathname,filename]);

%*********************************************************************
%**          Identify Droplet and Crop Region of Interest         **
%*********************************************************************

myfilter = fspecial('gaussian',[5 5], 1);

myfilteredimage = imfilter(unfilteredimage, myfilter);

N = myfilteredimage;
cropped=imcrop (N);          %Crop the region of interest
I=cropped;                   %Image of Droplet on a Substrate
imshow(I)

%*********************************************************************
%**             Convert to Grayscale and Binary Image             **
%*********************************************************************

K= rgb2gray(I);
level = graythresh(K);

imshow([pathname,filename]); % Display image and filtered image
imshow(myfilteredimage);

%Converting a grey5scale image to a binary image
BW = im2bw(I,level);
```

```
BW2 = edge(BW,'sobel');
figure,imshow(BW2);

%*********************************************************************
%**             Identify Substrate and Contact Point              **
%*********************************************************************

imshow(BW2);            %Manually select the starting point
[x, y] = ginput(1);
xp=round (x);

[s,t]= size(BW2);       %Size of image in terms of pixels
col1 = xp;
row1 = min(find(BW2(:,col1)));

boundary1 = bwtraceboundary(BW2, [row1, col1], 'N', 8,
inf); %Tracing the boundaries

[p,q]= size(boundary1); %Size of the resulting matrix

B = sortrows(boundary1); %Sorts the rows of the matrix X in
ascending order as a group

%From matrix to dataset

data = B;

data_fields= {'Ypix','Xpix'};

S=dataset ();

for i=1:length(data_fields);

S.(data_fields{i})=data(:,i);

end

for i=1:1:t
            Si=S(S.Ypix==i, ...  % sub dataset
         { 'Ypix' 'Xpix'});
     Si1=S(S.Ypix==i+1, ...
{ 'Ypix' 'Xpix'});
     Di= double (Si);   %dataset array to matrix to get max and min
     Di1=double (Si1);
mxi=max(Di (:,2)); % max value of  new matrix from subdataset
     mxi1= max (Di1 (:,2));
mni=min (Di (:,2));  % min value of  new matrix from subdataset
mni1=min (Di1 (:,2));
     d=mxi-mni;
di1=mxi1-mni1;

     a=d;   % comparing d
     b=di1;
if b>a;
de=b;
else d=a; % d so that if b<a it wont overwrite the max val of b
end
```

```
end
firstset= B(1:p,2);
Secondset=B(1:p,1);

p1= plot(firstset,Secondset,'o');
set(gca,'YDir','reverse'); % to change origin position of y axis to
match BW2

% diameter of the needle in terms of pixels
S1=S(S.Ypix==1, ...
{ 'Ypix' 'Xpix'});
D1= double (S1);
mx1=max(D1 (:,2));
mn1=min (D1 (:,2));
d1=mx1-mn1;

m=max(B (:,1)); %to read max pixel number of edge (needed for ds)

l=m-de;  % to get ds
Sl=S(S.Ypix==l, ...
{ 'Ypix' 'Xpix'});
Dl= double (Sl);
mxl=max(Dl (:,2));
mnl=min (Dl (:,2));
ds=mxl-mnl;

Sa=ds/de;
Sp=Sa;

%**********************************************************************
%**            Surface/Interfacial Tension Calculation            **
%**********************************************************************

% J = 1/H
% from Misak, M.D., 1967. Equations for Determing 1/H versus S
values in
% Computer Calucations of Interfacial Tension by the Pendant drop
method.
% Journal of Colloid and Interface Science, Vol.27, No.1., p. 141-
142.

%Determine Drop Shape Factor
if .401<=Sp<=.46
    J = (0.32720/(Sp^2.56651))-(0.97553*(Sp^2))+(0.94059*Sp)-0.18069
elseif .46<=Sp<=.59
    J = (0.31968/(Sp^2.59725))-(0.46898*(Sp^2))+(0.50059*Sp)-0.13261
elseif .59<=Sp<=.68
    J = (0.31522/(Sp^2.62435))-(0.11714*(Sp^2))+(0.15756*Sp)-0.05285
elseif .68<=Sp<=.90
    J = (0.31345/(Sp^2.64267))-(0.09155*(Sp^2))+(0.14701*Sp)-0.05877
else
    .9<=Sp<=1;
    J = (0.30715/(Sp^2.84636))-(0.69116*(Sp^3))+(1.08315*(Sp^2))-
0.18341*Sp...
        -0.20970
end

R = input('density1');          %Density of fluid phase 1
R2 = input('density2');         %Density of fluid phase 2
R3= input('needle diameter in meters');
```

```
deltarho= abs (R-R2);           %Difference of densities between two
phases
v=R3;

% Calibration using the needle diameter form pixels to meters
de1= (v*(de/d1))

g= 9.81; % Acceleration of gravity

% Determine surface tension of a pendant drop
Surface_tension=g*deltarho*(de1.^2)*J

%*********************************************************************
```

Appendix A.5: MATLAB Code Function for Contact Angle Measurement

```
%**********************************************************************
%**        Determining Contact Angle of A Sessile Drop               **
%**********************************************************************
%**********************************************************************
%** Contact Angle Measurement Program code                           **
%** Regenerated by Voon Loong (2012)                                 **
%** Reference: Srinivasan et al. (2011)                              **
%** Multiphase Flow Research Group                                   **
%** University of Nottingham, United Kingdom                         **
%**********************************************************************
%**********************************************************************
%**                  Clean up and Initialization                     **
%**********************************************************************

clc;                    % Clear the command window.
close all;              % Close all figures (except those of imtool.)
imtool close all;       % Close all imtool figures.
clear;                  % Erase all existing variables.
workspace;              % Make sure the workspace panel is showing.
fontSize = 15;

[filename, pathname] = ...
uigetfile({'*.tif';'*.jpg';'*.gif';'*.*'},'Select an image');  %Open
standard dialog box for retrieving files

unfilteredimage = imread([pathname,filename]);

myfilter = fspecial('disk',3);

myfilteredimage = imfilter(unfilteredimage, myfilter);

%**********************************************************************
%**          Identify Droplet and Crop Region of Interest            **
%**********************************************************************
N = myfilteredimage;
cropped=imcrop (N);
I=cropped;
figure,imshow(I);

%**********************************************************************
%**                Threshold Computing and Detection                 **
%**********************************************************************

[rows, columns, numberOfColorBands] = size(I);
if numberOfColorBands > 1
    I = rgb2gray(I);
end
% Display the original image.
subplot(2, 4, 1);
imshow(I, []);
title('Original GrayScale Image', 'FontSize', fontSize);
set(gcf, 'units','normalized','outerposition',[0 0 1 1]);
```

```
% Compute and display the histogram.
[pixelCount, grayLevels] = imhist(I, 256);
subplot(2, 4, 5);
bar(pixelCount);
grid on;
title('Histogram Original Droplet', 'FontSize', fontSize);
xlim([0 grayLevels(end)]); % Scale x axis manually.

% Extract left half of droplet image
middleColumn = floor(columns/2);
leftHalfImage = I(:, 1:middleColumn);
subplot(2, 4, 2);
imshow(leftHalfImage, []);
title('Left Half Droplet', 'FontSize', fontSize);

% Compute and display the histogram.
[pixelCountL, grayLevelsL] = imhist(leftHalfImage, 256);
subplot(2, 4, 6);
bar(pixelCountL);
grid on;
title('Histogram Left Half', 'FontSize', fontSize);
xlim([0 grayLevels(end)]); % Scale x axis manually.

% Extract right half of droplet image
middleColumn = floor(columns/2);
rightHalfImage = I(:, middleColumn+1:end);
subplot(2, 4, 3);
imshow(rightHalfImage, []);
title('Right Half Droplet', 'FontSize', fontSize);

% Compute and display the histogram.m.
[pixelCountR, grayLevelsR] = imhist(rightHalfImage, 256);
subplot(2, 4, 7);
bar(pixelCountR);
grid on;
title('Histogram Right Half', 'FontSize', fontSize);
xlim([0 grayLevels(end)]); % Scale x axis manually.

% Subtract the histograms:
diffHistogram = int16(pixelCountL - pixelCountR);
% Display it
subplot(2, 4, 8);
bar(diffHistogram, 'BarWidth', 1);
title('Difference Histograms', 'FontSize', fontSize);

% Now let's do an Otsu thresholding on it.
thresholdLevel = 230 * graythresh(diffHistogram);

% Place vertical bar on histogram to show threshold
yl = ylim();
line([thresholdLevel, thresholdLevel], [yl(1), yl(2)], ...
    'Color', 'r', 'LineWidth', 2);

BW2 = I > thresholdLevel;
title('Above thresholdlevel', 'FontSize', fontSize);
BW3 = imfill( 1-BW2, 'holes');
subplot(2, 4, 4);
imshow(BW3,[]);
title('Binary Image After Threshold','FontSize', fontSize);
```

```
figure, imshow(BW3);
set(gcf, 'units','normalized','outerposition',[0 0 1 1]);

%*********************************************************************
%**                    Droplet Image Truncation                     **
%*********************************************************************

[x_coordinates y_coordinates Pixel_vals] = ginput;
rot_line = polyfit(x_coordinates ,y_coordinates ,1 );
rot_point = polyval( rot_line, 1 );
rot_angle = atan( rot_line(1) );
BW4 = BW3(1:rot_point,:);
BW5 = imrotate(BW4, rot_angle*180/pi );
figure;
subplot(1,3,1);
imshow(BW3,[]);
title('Binary Image Before Truncation','FontSize', fontSize);
set(gcf, 'units','normalized','outerposition',[0 0 1 1]); %Enlarge
to Full Screen
subplot(1, 3, 2);
imshow(BW5,[]);
title('Binary Image After Truncation','FontSize', fontSize);

%*********************************************************************
%**          Dimension Measurement of a Sessile Drop                **
%*********************************************************************

%Find the maximum height and width of sessile drop
labeledImage = bwlabel(BW5);
measurements = regionprops(labeledImage,'Area','BoundingBox');
allAreas = [measurements.Area];
biggestBlobIndex = find(allAreas == max(allAreas));
keeperBlobsImage = ismember(labeledImage, biggestBlobIndex);
boundaries = bwboundaries(keeperBlobsImage);
M1 = measurements(biggestBlobIndex).BoundingBox;
blobBoundary = boundaries{1};

%Plot the BoundingBox
subplot(1, 3, 3);
imshow(BW5,[]);
title('Identification','FontSize', fontSize);
hold on
rectangle('position',M1,'edgecolor','g','linewidth',1);
hold off;

%% To get the information for calculations:
R1 = input('Surface/InterfacialTension(N/m) =');
R2 = input('Density(kg/m^3) =');
calibFactor = 1e-3/730.28; %length/pixel
g = 9.81;

%*********************************************************************
%**           O'Brien's Singular Pertubation Solution to           **
%**                    Bashforth-Adams Equation                    **
%*********************************************************************

%Calculate parameters using respective equation (Srinivasan et
al.,2010 using pertubation method):
a = sqrt(R1/(R2*g));
h = M1(4)*calibFactor;
l = (M1(3)/2)*calibFactor;
```

```
R = l/a;
Z = h/a;

param=[R Z];

%using function to operate
phi2=fsolve(@(phi) ...
zphi(phi,param),4*pi/10,optimset('Algorithm','trust-region-
reflective','Display','iter'));
phi3=(180/pi)*phi2;
disp(['The apparent contact angle determined is '
num2str(round(phi3)) ' degrees']);
zs=zsens(phi3*(pi/180),param);
disp(['The sensitivity is ' num2str(zs,3) ' radians']);

%*********************************************************************

%*********************************************************************
%**    Dimensionless Volume of Liquid Drop Derivative Equation    **
%*********************************************************************

function y=zphi(phi,param)
R=param(1);
Z=param(2);
phi1=(pi-phi)/R;
if(phi==pi)
X=(2/3)^(1/2)*R^2;
y=2*R+(1/3)*R^3*(-1-log(6))+(2/3)*R^3*log(R)-Z;
P=2/R-R/3+R^3*(1/3*log(2)-1/6);
else
z_outer=R*(1-cos(phi))+R^3*((1/3)*cos(phi)-
(1/3)*(cos(phi))^2+(2/3)*log(cos(phi/2)));
z_inner=2*R+(2/3)*R^3*(log(R))+R^3*((-
1/4)*phi1*(phi1^2+8/3)^(1/2)+(2/3)*log(phi1+(phi1^2+8/3)^(1/2))-
1/4*phi1^2+(2/3)*(-2*log(2)-1/2));
z_cp=2*R-(1/2)*R*(pi-phi)^2 - (2/3)*R^3 + (2/3)*R^3*log(pi-phi) -
(2/3)*R^3*log(2);
y=z_inner+z_outer-z_cp-Z;
end
end

%*********************************************************************

%*********************************************************************
%**     Dimensionless Sensitivity of Apparent Contact Angles      **
%*********************************************************************

function y=zsens(phi,param)
R=param(1);
Z=param(2);
phi1=(pi-phi)/R;
y=1/(2*R^3/(3*(pi-phi))+4*R^3*(pi-phi)/(8*R^2+(pi-phi)*(3*(pi-phi)-
sqrt(24*R^2+9*(pi-phi)^2))) - R*(pi-phi)+R*sin(phi)-
(R^3/3)*(sin(phi)-sin(2*phi)+tan(phi/2)));
end

%*********************************************************************
```

Appendix A.6: MATLAB Code Function for Threshold Detection Measurement

```
%**********************************************************************
%**                Threshold Detection Measurement                   **
%**********************************************************************
%**********************************************************************
%** Threshold Detection Measurement Program code                      **
%** Regenerated by Voon Loong (2012)                                  **
%** Multiphase Flow Research Group                                    **
%** University of Nottingham, United Kingdom                          **
%**********************************************************************
%**********************************************************************
%**                  Clean up and Initialization                     **
%**********************************************************************

clc;                    % Clear the command window.
close all;              % Close all figures (except those of imtool.)
imtool close all;       % Close all imtool figures.
clear;                  % Erase all existing variables.
workspace;              % Make sure the workspace panel is showing.
fontSize = 15;

[filename, pathname] = ...
uigetfile({'*.tif';'*.jpg';'*.gif';'*.*'},'Select an image');  %Open
standard dialog box for retrieving files

unfilteredimage = imread([pathname,filename]);

myfilter = fspecial('disk',3);

myfilteredimage = imfilter(unfilteredimage, myfilter);

%**********************************************************************
%**          Identify Droplet and Crop Region of Interest            **
%**********************************************************************
N = myfilteredimage;
cropped=imcrop (N);
I=cropped;
figure,imshow(I);

%**********************************************************************
%**                Threshold Computing and Detection                 **
%**********************************************************************

[rows, columns, numberOfColorBands] = size(I);
if numberOfColorBands > 1
    I = rgb2gray(I);
end
% Display the original image.
subplot(2, 4, 1);
imshow(I, []);
title('Original GrayScale Image', 'FontSize', fontSize);
set(gcf, 'units','normalized','outerposition',[0 0 1 1]);
```

```
% Compute and display the histogram.
[pixelCount, grayLevels] = imhist(I, 256);
subplot(2, 4, 5);
bar(pixelCount);
grid on;
title('Histogram Original Droplet', 'FontSize', fontSize);
xlim([0 grayLevels(end)]); % Scale x axis manually.

% Extract left half of droplet image
middleColumn = floor(columns/2);
leftHalfImage = I(:, 1:middleColumn);
subplot(2, 4, 2);
imshow(leftHalfImage, []);
title('Left Half Droplet', 'FontSize', fontSize);

% Compute and display the histogram.
[pixelCountL, grayLevelsL] = imhist(leftHalfImage, 256);
subplot(2, 4, 6);
bar(pixelCountL);
grid on;
title('Histogram Left Half', 'FontSize', fontSize);
xlim([0 grayLevels(end)]); % Scale x axis manually.

% Extract right half of droplet image
middleColumn = floor(columns/2);
rightHalfImage = I(:, middleColumn+1:end);
subplot(2, 4, 3);
imshow(rightHalfImage, []);
title('Right Half Droplet', 'FontSize', fontSize);

% Compute and display the histogram.m.
[pixelCountR, grayLevelsR] = imhist(rightHalfImage, 256);
subplot(2, 4, 7);
bar(pixelCountR);
grid on;
title('Histogram Right Half', 'FontSize', fontSize);
xlim([0 grayLevels(end)]); % Scale x axis manually.

% Subtract the histograms:
diffHistogram = int16(pixelCountL - pixelCountR);
% Display it
subplot(2, 4, 8);
bar(diffHistogram, 'BarWidth', 1);
title('Difference Histograms', 'FontSize', fontSize);

% Now let's do an Otsu thresholding on it.
thresholdLevel = 230 * graythresh(diffHistogram);

% Place vertical bar on histogram to show threshold
yl = ylim();
line([thresholdLevel, thresholdLevel], [yl(1), yl(2)], ...
    'Color', 'r', 'LineWidth', 2);

BW2 = I > thresholdLevel;
title('Above thresholdlevel', 'FontSize', fontSize);
BW3 = imfill( 1-BW2, 'holes');
subplot(2, 4, 4);
imshow(BW3,[]);
title('Binary Image After Threshold','FontSize', fontSize);
figure, imshow(BW3);
```

```
set(gcf, 'units','normalized','outerposition',[0 0 1 1]);

%**********************************************************************
```

Appendix A.7: MATLAB Code Function for Droplet Diameter Measurement

```
%**********************************************************************
%**                Generated Droplet Size Measurement                **
%**********************************************************************
%**********************************************************************
%** Effective Droplet Diameter Program Code                           **
%** Regenerated by Voon Loong (2011)                                  **
%** Multiphase Flow Research Group                                    **
%** University of Nottingham, United Kingdom                          **
%**********************************************************************

%**********************************************************************
%**                   Clean-up and Initialization                    **
%**********************************************************************

clc;                    % Clear the command window.
close all;              % lose all figures (except those of imtool.)
imtool close all;       % Close all imtool figures.
clear;                  % Erase all existing variables.
workspace;              % Make sure the workspace panel is showing.
fontSize = 15;

%**********************************************************************
%**                      Size Calibration                            **
%**********************************************************************

%Open standard dialog box for retrieving files
[filename, pathname] = ...
uigetfile({'*.jpg';'*.tif';'*.gif';'*.*'},'Select an image');
rgbImage = imread([pathname,filename]);
imshow(rgbImage); % Display image
figure; imagesc(rgbImage);
colormap(gray)
axis image

h = imdistline(gca);
api = iptgetapi(h);
%pause -- move the edges of the segment and then press a key to
continue
api.setLabelVisible(false);
pause();                                %get the distance
dist = api.getDistance();
knownLength = 1000;
calibFactor = knownLength/dist;         %calibrationFactor

%**********************************************************************
%**    Calculate Major and Minor Length of A Generated Droplet       **
%**********************************************************************

myFolder = 'C:\Users\enxvw\Desktop\22.10.12Image\Run0.6';

if ~isdir(myFolder)
```

```
errorMessage = sprintf('Error: The following folder does not
exist:\n%s', myFolder);
uiwait(warndlg(errorMessage));
return;
end

filePattern = fullfile(myFolder, '*.tif');
jpegFiles = dir(filePattern);

for k = 1:length(jpegFiles)
baseFileName = jpegFiles(k).name;
fullFileName = fullfile(myFolder, baseFileName);
fprintf(1, 'Now reading %s\n', fullFileName);
imageArray = imread(fullFileName);
  %imshow(imageArray);  % Display image.
drawnow; % Force display to update immediately.

%Get the dimensions of the image. numberOfColorBands should be = 3.
[rows columns numberOfColorBands] = size(imageArray);
% Display the original color image.
subplot(2, 3, 1);
imshow(imageArray, []);
title('Original color Image', 'FontSize', fontSize);
% Enlarge figure to full screen.
set(gcf, 'Position', get(0,'Screensize'));

cropped=imcrop  (imageArray, [528.2 610.5 100.6 100.6])

% Extract the individual red color channel.
redChannel = cropped(:, :, 1);
% Display the red channel image.
subplot(2, 3, 2);
imshow(redChannel, []);
title('Red Channel Image', 'FontSize', fontSize);

% Binarize it
binaryImage = redChannel <128; % Based on Image Pixel Coverage
% Display the image.
subplot(2, 3, 3);
imshow(binaryImage, []);
title('Thresholded Image', 'FontSize', fontSize);

BW = imfill( binaryImage, 'holes' ); % Fill In Holes in Image

% Get rid of the top junk
se = strel('disk', 5);
BW = imopen(BW, se);
% Display the cleaned image.
subplot(2, 3, 4);
imshow(BW, []);
title('Opened Image', 'FontSize', fontSize);

labeledImage = bwlabel(BW)

measurements =
regionprops(labeledImage,'Area','MajorAxisLength','MinorAxisLength')

% Find the largest blob.
allAreas = [measurements.Area]
```

```
biggestBlobIndex = find(allAreas == max(allAreas))

% Extract only the largest blob.
% Note how we use ismember() to do this.
keeperBlobsImage = ismember(labeledImage, biggestBlobIndex);

% Display the original color image.
subplot(2, 3, 5);
imshow(cropped, []);
hold on; % Prevent plot() from blowing away the image.
title('Original Color Image with Droplet Outlined',
   'FontSize',fontSize);

% Get its boundary and overlay it over the original image.
boundaries = bwboundaries(keeperBlobsImage);
blobBoundary = boundaries{1};
plot(blobBoundary(:,2), blobBoundary(:,1), 'r-', 'LineWidth', 3);
hold off;

X = measurements(biggestBlobIndex).MajorAxisLength;
Y = measurements(biggestBlobIndex).MinorAxisLength;
MajorAxis{k,:} = X*calibFactor;
MinorAxis{k,:} = Y*calibFactor;

end

%**********************************************************************
```